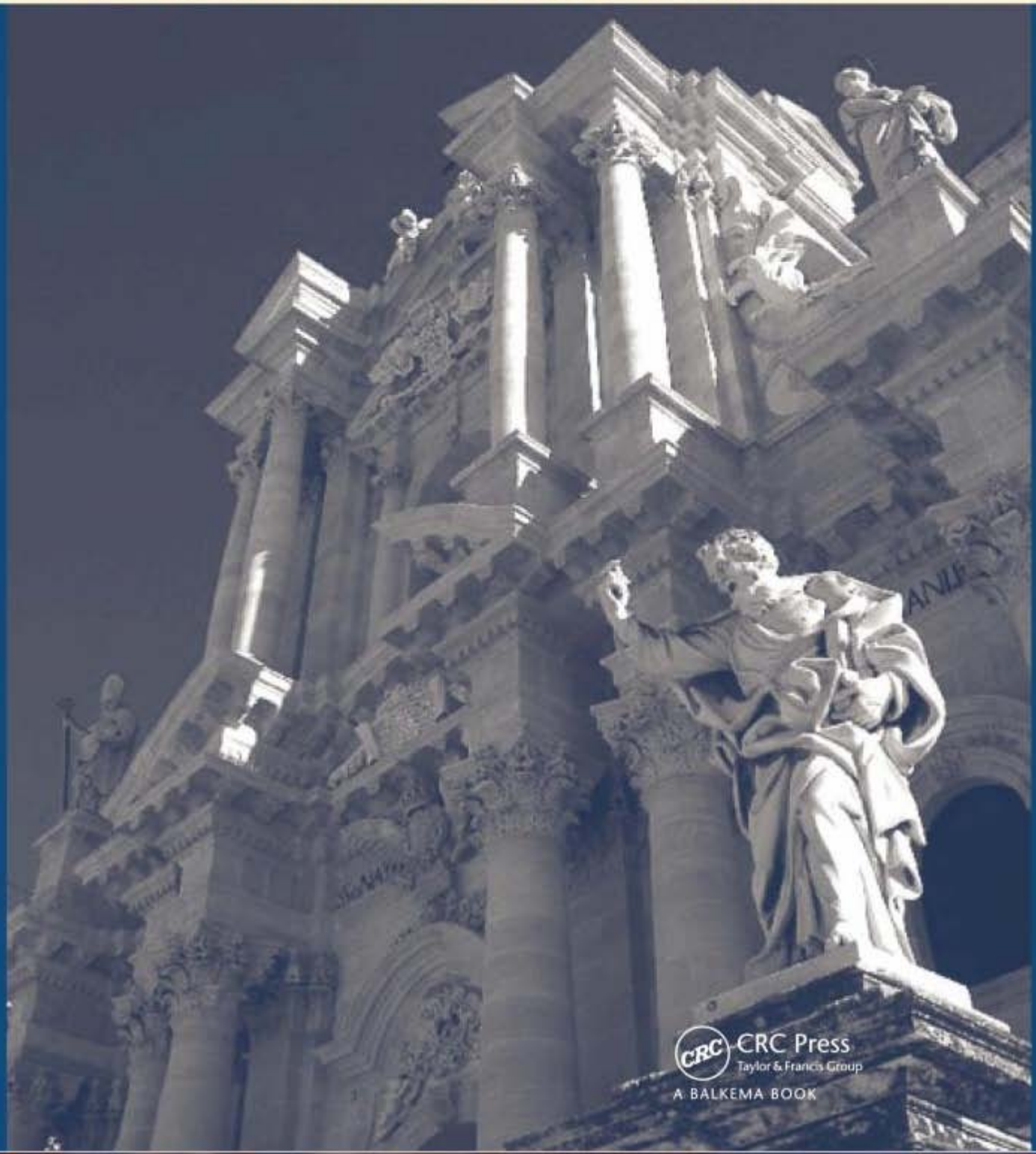
# ACOUSTIC EMISSION AND CRITICAL PHENOMENA

## FROM STRUCTURAL MECHANICS TO GEOPHYSICS

ALBERTO CARPINTERI & GIUSEPPE LACIDOGNA – EDITORS



CRC Press
Taylor & Francis Group
A BALKEMA BOOK

# Acoustic Emission and Critical Phenomena

© 2008 Taylor & Francis Group, London, UK

# Acoustic Emission and Critical Phenomena:
## From Structural Mechanics to Geophysics

*Edited by*
Alberto Carpinteri & Giuseppe Lacidogna
*Department of Structural Engineering & Geotechnics, Politecnico di Torino, Italy*




CRC Press
Taylor & Francis Group
Boca Raton London New York Leiden

CRC Press is an imprint of the
Taylor & Francis Group, an **informa** business

A BALKEMA BOOK

© 2008 Taylor & Francis Group, London, UK

Cover photograph: The Cathedral of Syracuse whose structures were monitored with the Acoustic Emission technique.
Photograph taken from the paper: "Multidimensional Approaches to Study Italian Seismicity", by A. Carpinteri, G. Lacidogna and G. Niccolini.

*CRC Press/Balkema is an imprint of the Taylor & Francis Group, an informa business*

© 2008 Taylor & Francis Group, London, UK

Kanji Ono, Structural Intergrity Evaluation by Means of Acoustic Emission, pp. 13–28,
Copyright © 2008 Kanji Ono

Typeset by Charon Tec Ltd (A Macmillan Company), Chennai, India
Printed and bound in Great Britain by Antony Rowe (CPI-group), Chippenham, Wiltshire

All rights reserved. No part of this publication or the information contained herein may be reproduced, stored in a retrieval system, or transmitted in any form or by any means, electronic, mechanical, by photocopying, recording or otherwise, without written prior permission from the publishers.

Although all care is taken to ensure integrity and the quality of this publication and the information herein, no responsibility is assumed by the publishers nor the author for any damage to the property or persons as a result of operation or use of this publication and/or the information contained herein.

Published by: CRC Press/Balkema
P. O. Box 447, 2300 AK Leiden, The Netherlands
e-mail: Pub.NL@taylorandfrancis.com
www.crcpress.com – www.taylorandfrancis.co.uk – www.balkema.nl

*Library of Congress Cataloging-in-Publication Data*

Acoustic emission and critical phenomena : from structural mechanics to geophysics / Alberto Carpinteri & Giuseppe Lacidogna (editors).
p. cm.
Includes index.
ISBN 978-0-415-45082-9
1. Fracture mechanics–Congresses. 2. Concrete–Cracking–Congresses.
3. Buildings–Earthquake effects–Congresses. 4. Acoustic emission testing–Congresses.
I. Carpinteri, A. II. Lacidogna, Giuseppe. III. Title.

TA409.A32 2008
624.1′762–dc22 2008016521

ISBN13: 978-0-415-45082-9 (Hardback)
ISBN13: 978-0-203-89222-0 (e-book)

© 2008 Taylor & Francis Group, London, UK

*Acoustic Emission and Critical Phenomena – Carpinteri & Lacidogna (eds)*
*© 2008 Taylor & Francis Group, London, ISBN 978-0-415-45082-9*

# Contents

Preface VII

Acknowledgements IX

Introduction 1

**1 Acoustic Emission and Critical Structural States**

*1.1 Space-time characterization of AE sources*

STRUCTURAL INTEGRITY EVALUATION BY MEANS OF ACOUSTIC EMISSION 13
*K. Ono*

SOME OBSERVATIONS ON ACOUSTIC EMISSION/STRESS/TIME RELATIONSHIPS 29
*A. A. Pollock*

LOCALIZATION AND MODE DETERMINATION OF FRACTURE EVENTS BY ACOUSTIC EMISSION 41
*H.W. Reinhardt, C.U. Grosse and J. H. Kurz*

SOURCE CHARACTERIZATION OF FRACTURE IN QUASI-BRITTLE MATERIALS 67
*C.S. Kao, F.C.S. Carvalho, G. Rosati, S. Cattaneo and J.F. Labuz*

*1.2 AE detection of failure processes in concrete structures*

ACOUSTIC EMISSION ANALYSIS OF CONCRETE FOR CORROSION, DAMAGE AND CRACKING MECHANISM 87
*M. Ohtsu, Y. Tomoda and T. Suzuki*

LOCALIZATION ACCURACY OF MICROCRACKS IN DAMAGED CONCRETE STRUCTURES 103
*A. Carpinteri, G. Lacidogna and A. Manuello*

*1.3 AE damage quantification in civil structures*

CONTRIBUTION OF AE MONITORING TO THE NEW ERA OF SUSTAINABLE CIVIL STRUCTURES 127
*T. Shiotani*

© 2008 Taylor & Francis Group, London, UK

ACOUSTIC EMISSION ANALYSIS DURING TEST LOADING OF EXISTING STRUCTURES 155
*G. Kapphahn and V. Slowik*

ACOUSTIC EMISSION MONITORING OF A CONCRETE HINGE JOINT BRIDGE STRUCTURE 167
*R. Pullin, K. M. Holford, R. J. Lark and J. J. Hensman*

**2 Seismic Mechanics and Critical Behaviours**

*2.1 Critical state transition in earthquake dynamics*

NUCLEATION AND CRITICAL PHENOMENA, DAMAGE, AND CHARACTERISTIC EARTHQUAKES 187
*D.L. Turcotte, J.B. Rundle, M. Yoder, S.G. Abaimov and W. Klein*

ACCELERATING MOMENT RELEASE BEFORE LARGE EARTHQUAKES 205
*C. G. Sammis and A. Kositsky*

*2.2 Scale invariant behaviour in earthquake occurrence*

SCALING AND UNIVERSALITY IN THE DYNAMICS OF SEISMIC OCCURRENCE AND BEYOND 225
*Á. Corral*

MULTIDIMENSIONAL APPROACHES TO STUDY ITALIAN SEISMICITY 245
*A. Carpinteri, G. Lacidogna and G. Niccolini*

© 2008 Taylor & Francis Group, London, UK

*Acoustic Emission and Critical Phenomena – Carpinteri & Lacidogna (eds)*
*© 2008 Taylor & Francis Group, London, ISBN 978-0-415-45082-9*

# Preface

The Acoustic Emission (AE) technique uses ad hoc transducers to detect AE events caused by crack growth in a structure under external loading. This technique is similar to the one employed in earthquake control, where seismic waves reach the monitoring stations placed on the surface of the Earth. Though they take place on very different scales, these two families of phenomena – damage in structural materials and earthquakes in geophysics- are very similar: in either case, in fact, we have a release of elastic energy from sources located inside a medium.

This volume includes works by scholars of international stature in the fields of seismicity and acoustic emissions. The contributions proposed basically consist of those presented at the Post-Conference Workshop on "Acoustic Emission and Critical Phenomena: From Structural Mechanics to Geophysics", held in Catania (Italy) on June 22, 2007, during the 6th International Conference on Fracture Mechanics of Concrete and Concrete Structures (FraMCoS-6).

This volume goes to print about one year after the publication, in 2007, of the book entitled "Earthquakes and Acoustic Emission", by the same publishing group, Taylor & Francis, and the same editors. The publication of two volumes on this topic so close in time and by such a prestigious publishing group reflects the great interests of scholars in this field of research and is evidence of the high pace of progress in this area.

During the last few years, in fact, numerous experimental techniques have been employed to evaluate fracture processes, and a number of modelling approaches have been developed to predict fracture behaviour. The non-destructive method based on the Acoustic Emission (AE) technique has proved highly effective, especially in determining and measuring the damage phenomena that take place inside a structure subjected to mechanical loading.

An earthquake is a sudden movement of the ground caused by the release of elastic energy stored in the Earth's Crust. It causes vibrations that propagate outwards from the source as seismic waves. The events of a similar nature that occur – on a different scale – in structural materials under loading are analysed by means of the AE technique. Since the signals time series recorded in seismology and acoustic emission technique are caused by the same phenomenon, the AE method can use analysis techniques similar to those adopted in earthquake control, including the localization of the sources or the inversion of source parameters.

© 2008 Taylor & Francis Group, London, UK

Both earthquakes and AE signals can be viewed as *Critical Phenomena* and satisfy the Guttenberg-Richter frequency-magnitude relationship under a wide variety of conditions. The number of earthquakes and AE signals scales as a power-law of the area of the rupture zone, and a fractal scaling is proposed for the spatial and temporal distributions of earthquakes and AEs. Earthquakes are also taken as an example of the notion of self-organized criticality introduced by P. Bak in 1988. There is a continuous input of strain energy through the relative motion of tectonic plates; this energy is then dissipated in a fractal distribution of earthquakes. In 1991 argued C.H. Scholz that the entire Earth's crust is in a state of self-organized criticality. The notion of self-organized criticality describes the spontaneous organization of the dynamics of a system towards a very particular state, analogous to the critical point found in equilibrium phase transitions. It is also pointed out that brittle failure phenomena, as identified through AE monitoring in concrete, masonry and rocks, can be likened to critical phenomena.

The contributions presented in this book have been subdivided into two parts: Acoustic Emission and Critical Structural States (Part 1), and Seismic Mechanics and Critical Behaviours (Part 2), with the aim of bringing together the latest achievements at world-wide level in fields ranging from the mechanics of materials to geophysics, and outlining the potential of the AE technique in terms of practical applications (non-destructive testing and failure evaluation) and theoretical developments (critical phenomena in complex systems).

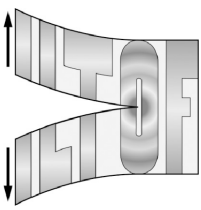
Alberto Carpinteri & Giuseppe Lacidogna
Turin, Italy
January 2008

© 2008 Taylor & Francis Group, London, UK

*Acoustic Emission and Critical Phenomena – Carpinteri & Lacidogna (eds)*
*© 2008 Taylor & Francis Group, London, ISBN 978-0-415-45082-9*

# Acknowledgements

This Volume was edited in the framework of the ILTOF Project (EU Leonardo da Vinci Programme for Education and Culture):
Innovative Learning and Training On Fracture.
The support of the European Union (EU) is gratefully acknowledged.




www.iltof.org

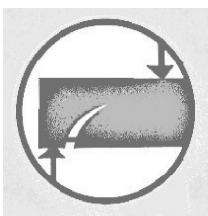





Leonardo da Vinci




www.polito.it



www.framcos6.org

© 2008 Taylor & Francis Group, London, UK

*Acoustic Emission and Critical Phenomena – Carpinteri & Lacidogna (eds)*
*© 2008 Taylor & Francis Group, London, ISBN 978-0-415-45082-9*

# INTRODUCTION*

**A. Carpinteri and G. Lacidogna**
Department of Structural Engineering & Geotechnics, Politecnico di Torino,
10129 Torino, Italy

An earthquake is a sudden movement of the ground caused by the release of elastic energy stored in the Earth's Crust. It causes vibrations that propagate outwards from the source as seismic waves. A similar phenomenon occurs – on a different scale – in structural materials under loading and is called Acoustic Emission (AE), see Figs. 1–3 [1–3]. While the techniques used in seismology have been well developed over the years, the AE technique has not been fully defined. It can be shown, on the other hand, that the AE method can utilize different seismic analysis techniques, including the localization of the sources or the inversion of source parameters [4–6].

During the last few years, numerous experimental techniques have been employed to evaluate fracture processes, and a number of modelling approaches have been developed to predict fracture behaviour. The non-destructive method based on the Acoustic Emission (AE) technique has proved highly effective, especially to check and measure the damage phenomena that take place inside a structure subjected to mechanical loading. The acoustic emission is a consequence of micro-cracks forming and propagating in the material and should thus provide an indirect measure of the damage accumulating in the system. For this reason, AE is often used as a non-destructive tool in material testing and evaluation [7,8]. Beside these practical applications, understanding the statistical properties of AE has become a challenging theoretical problem. The distribution of AE amplitudes follows a power-law, suggesting an interpretation in terms of critical phenomena and scaling theories [9–13]. This behaviour has been observed in several materials such as concrete, masonry and rocks, to name just a few (Figs. 4–6).

On the other hand, another common and familiar example of this behaviour is the occurrence of earthquakes in a particular seismic zone, where the event amplitudes span from the smallest almost imperceptible vibrations of the crust to the largest destructive catastrophic events (Fig. 7). The AE monitoring technique is similar to the one employed in earthquake control, where seismic waves reach

* With this introduction, the first author opened the FraMCoS-6 Post-Conference Workshop on "Acoustic Emission and Critical Phenomena: From Structural Mechanics to Geophysics", Catania (Italy), June 22, 2007.

© 2008 Taylor & Francis Group, London, UK

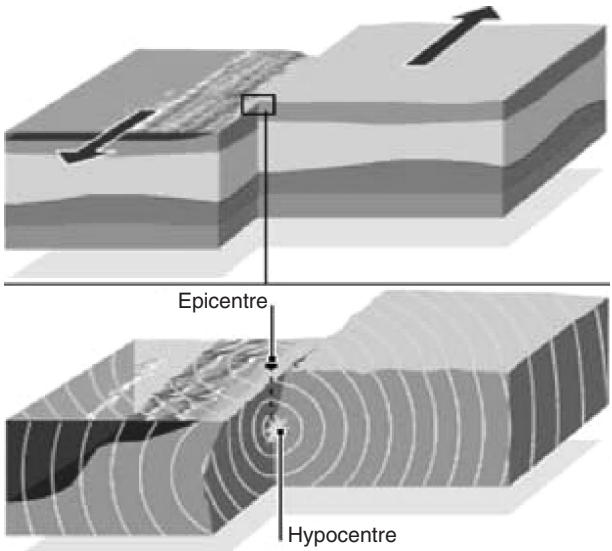



Figure 1: When a fault is displaced by a sudden movement of the Earth's Crust, the adjacent crust plates move abruptly relative to one another: Two types of vibration propagate from the hypocentre, the deep-seated point of origin of the earthquake: *P* waves that compress and expand the rock, and *S* waves, that shake the rock sideways. The seismographs of the entire world record these vibrations, enabling the geologists to locate the hypocentre and the point on the surface directly above it, the epicentre.

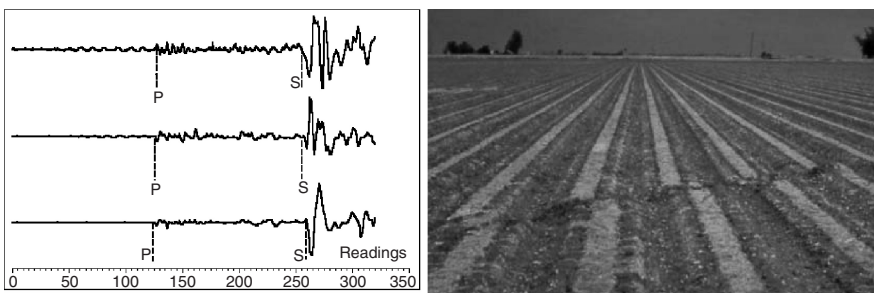



Figure 2: The pressure waves (*P*) and the shear waves (*S*) reaching the surface of the earth are generally strongest in the proximity of the fault concerned. (a) Typical signals obtained by a seismograph, showing the distinction between *P* and *S*-waves. (b) A conspicuous displacement of the ground at the epicentre of the quake.

© 2008 Taylor & Francis Group, London, UK

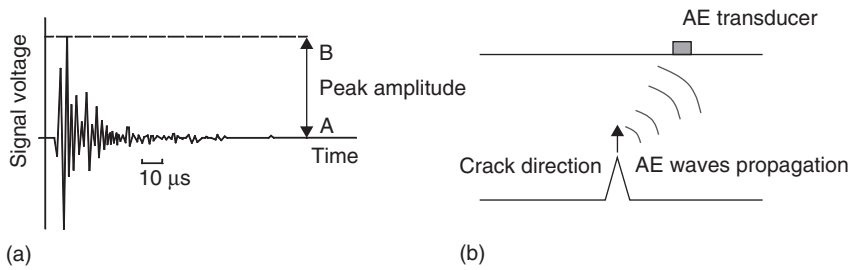



Figure 3: The AE sensors are transducers that convert the mechanical waves into electrical signals. This is similar to seismicity, where sesmic waves reach the seismographic stations placed on the Earth's surface. (a) Typical AE signal identified by the AE transducers. (b) Schematic view of a structure undergoing damage.

the monitoring stations placed on the surface of the Earth [1–3]. Though they take place on very different scales, these two families of phenomena – damage in structural materials and earthquakes in geophysics – are very similar: in either case, in fact, we have a release of elastic energy from sources located inside a medium (Fig. 8) [9].

The contributions presented at the Workshop, that include works by some of the most prominent world experts in the fields of seismicity and acoustic emission, have been collected in this volume.

The contributions have been grouped into two parts: Acoustic Emission and Critical Structural States (Part 1), and Seismic Mechanics and Critical Behaviours (Part 2), with the aim of bringing together the latest achievements at world-wide level in fields ranging from the mechanics of materials to geophysics, and outlining the potential of acoustic emission monitoring in terms of applications (non-destructive testing and failure evaluation) and theoretical developments (critical phenomena in complex systems).

Part 1, Section 1.1, contains works on "Space-time characterization of AE sources".

K. Ono provides an overall examination of the AE technique and its correlations with critical phenomena. The location and characterization of AE sources are discussed from the theoretical viewpoint and examples are given of the assessment of structural integrity. The proposed systematic approach to damage quantification uses NDT and fracture mechanics.

A.A. Pollock explains the physical meaning of acoustic emission events and then examines the redistribution over time of the elastic energy accumulated in the structures, as measured through the AE technique. Information on cascades, the equivalent of earthquake foreshocks and aftershocks, during delamination processes is also presented.

© 2008 Taylor & Francis Group, London, UK

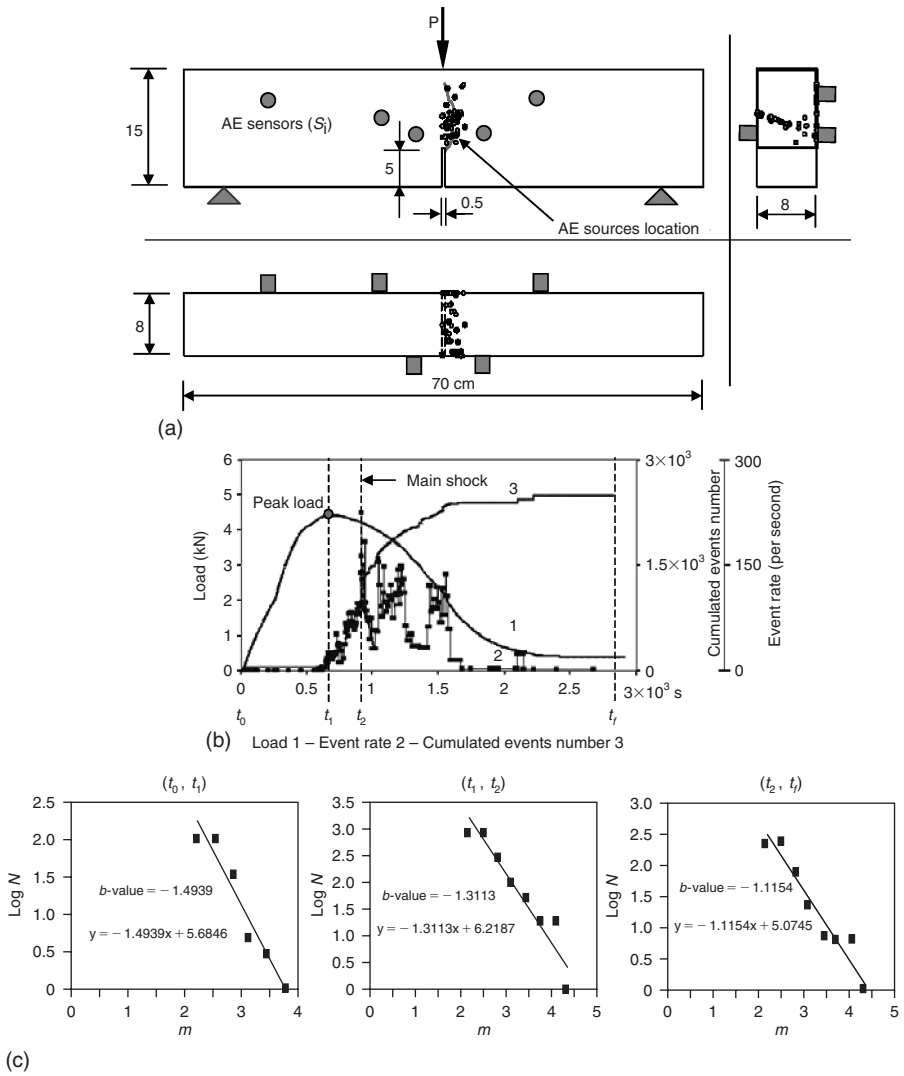



Figure 4: Three bending point test [14]. (a) Identification of the fracture process zone by the AE technique. (b) Load vs. time curve and AE activity. (c) *b*-values of the Gutenberg-Richter law obtained during the test.

H.W. Reinhardt, C.U. Grosse and J.H. Kurz discuss modern quantitative or signal-based AE techniques. They point out the similarities and differences between acoustic emission waves and seismograms, in order to present their progress made in the localisation of AE sources and in fracture mechanics studies based on moment tensor analysis.

C.S. Kao, F.C.S. Carvalho, G. Rosati, S. Cattaneo and J.F. Labuz focus on the calibration of AE transducers through a simplified methodology which utilizes

© 2008 Taylor & Francis Group, London, UK

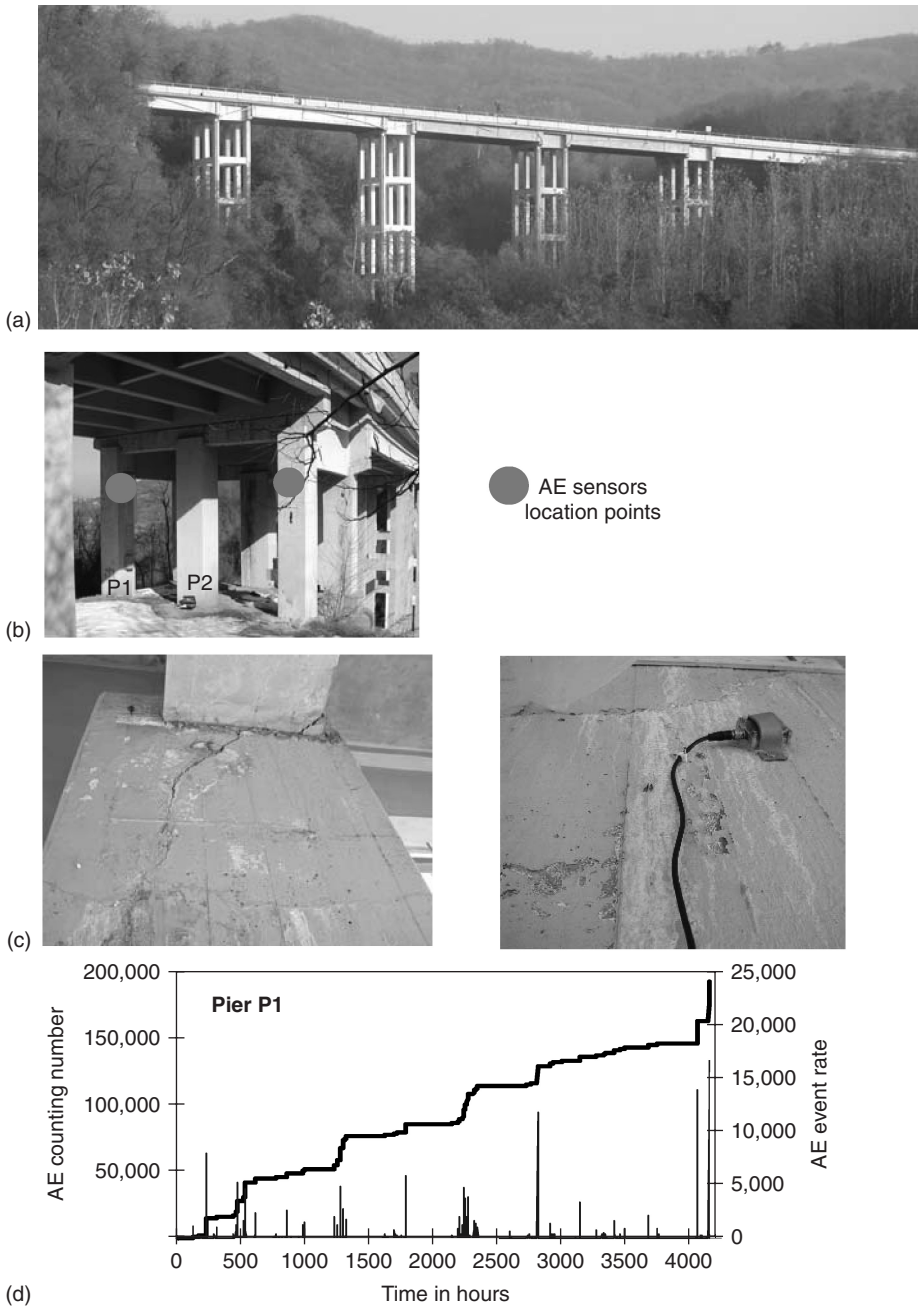



Figure 5: (a) AE monitoring of a highway viaduct built in the 1950s [15]. (b) The viaduct and piers monitored, P1 and P2. (c) Cracks in pier P1 and the applied sensor. (d) Pier P1 monitoring data.

© 2008 Taylor & Francis Group, London, UK

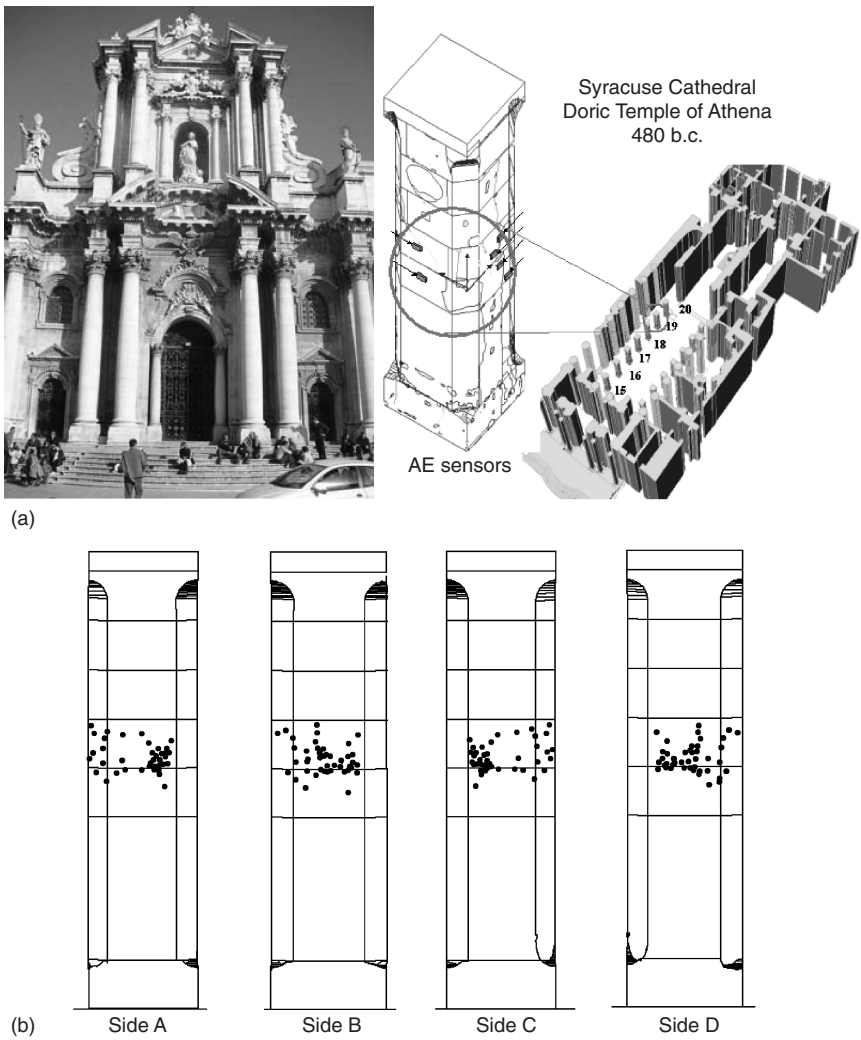



Figure 6: (a) This image provides a summary view of a study conducted by the authors [16] in which the AE technique was used to determine the damage level in a pillar that was part of the vertical bearing structure of the Cathedral of Syracuse (Sicily). The AE technique is non invasive and non destructive and therefore is ideally suited for the control of historic and monumental structures in seismic areas. (b) Localisation of AE sources (microcracks) in one of the pillars monitored.

the sensor response up to the first peak associated with the *P*-wave arrival. The aim is to optimise the determination of displacements through moment tensor analysis.

Section 1.2 deals with "AE detection of failure processes in concrete structures".

© 2008 Taylor & Francis Group, London, UK

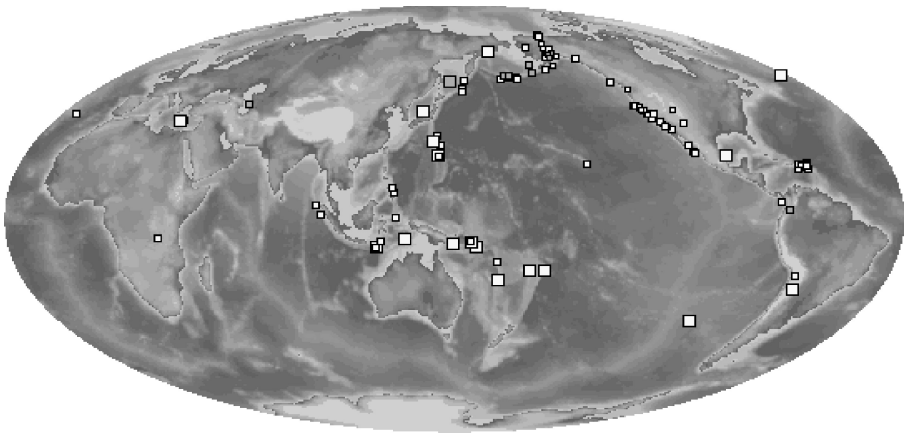


Figure 7: The distribution of earthquakes on the surface of the earth is an intrinsically random and chaotic phenomenon. By looking at a seismic map it can be seen at a glance that the faults are not arranged according to regular, orderly paths. Fractured and unstable, the Earth's Crust is subject to extremely high stresses, which the sudden movement of a fault may transfer to the adjacent faults. The latest theories regarding these phenomena come from the science of complexity and critical phenomena [17].

M. Ohtsu, Y. Tomoda and T. Suzuki interpret crack kinematics by the SiGMA procedure based on the AE moment tensor analysis. Then they use this technique to obtain a quantitative assessment of cracking mechanisms and damage of concrete members in service, as well as corrosion activity in reinforced concrete structures.

A. Carpinteri, G. Lacidogna and A. Manuello use the AE monitoring method to analyse, through three-point bending tests conducted in the laboratory, the processes leading to failure by shear or delamination of FRP reinforced concrete beams.

Section 1.3 is about "AE damage quantification in civil structures".

In his study focusing on the general concepts of structural safety, T. Shiotani emphasizes that the assessment of the current health status of civil structures, which should necessarily be conducted with an appropriate NDT, can be rationally evaluated with AE testing. AE monitoring, in fact, has great potential for global monitoring of large civil structures in the new era of sustainable civil structures.

G. Kapphahn, V. Slowik argue that the experimental safety evaluation of existing concrete and masonry structures should always include AE analysis. Then they discuss the effective use of the AE technique *in situ* to valuate the load-bearing capacity of civil structures and the ultimate conditions leading to collapse.

© 2008 Taylor & Francis Group, London, UK

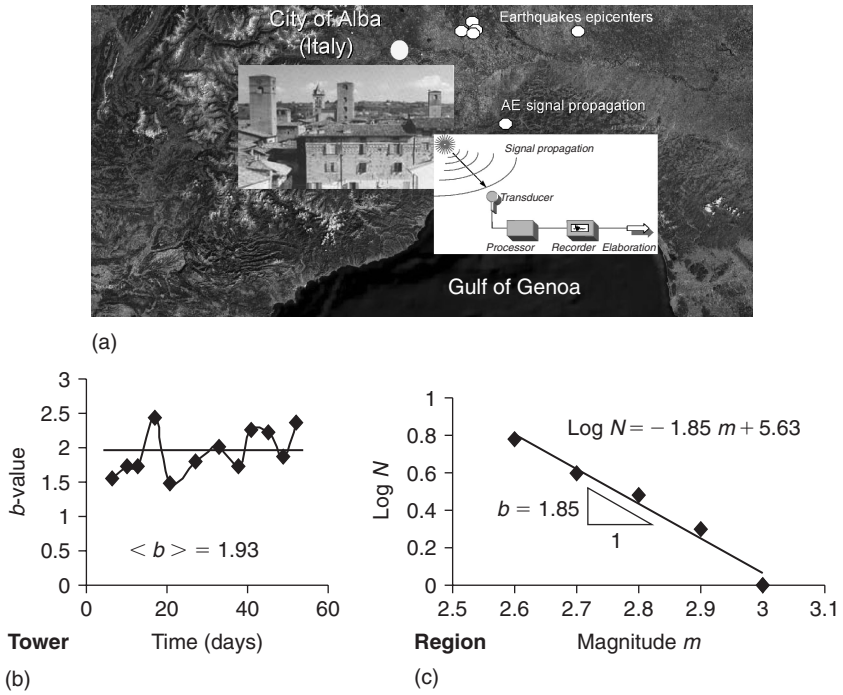



Figure 8: Figure (a) provides an overview of a study conducted by the authors [18] on the structural stability of three medieval towers rising in the centre of Alba, a characteristic town in Piedmont (Italy). During the monitoring period a correlation between peaks of AE activity in the masonry of these towers and regional seismicity was found. Earthquakes always affect structural stability. Besides that, the towers behaved as sensitive earthquake receptors. Through this type of analysis it is possible to assess experimentally the analogies between the seismic events occurring in the territory and the acoustic emission phenomena occurring in a structure. In figures (b) and (c) the Gutenberg-Richter *b*-values calculated for AEs in the tower are compared with the *b*-values describing regional seismicity.

R. Pullin, K. M. Holford, R. J. Lark and J. J. Hensman illustrate an interesting application of AE monitoring to a concrete hinge joint bridge structure, using surface mounted sensors. The aim was to detect hinge joint deterioration including corrosion induced fatigue cracking of the steel reinforcement bars.

Part 2, Section 2.1, contains papers regarding "Critical state transition in earthquake dynamics".

D.L. Turcotte, J.B. Rundle, M. Yoder, S.G. Abaimov and W. Klein compare the behaviour of typical earthquakes with the behaviour of a slider-block model with the aim to interpret the behaviour in terms of damage mechanics and critical phenomena. Drawing an analogy between an earthquake-induced rupture and a

© 2008 Taylor & Francis Group, London, UK

first-order phase transition, it is possible to demonstrate that rupture may occur with and without damage. In the presence of rapid damage accumulation, the rupture is equivalent to an equilibrium phase change. The fault does not enter a metastable state. Without damage, the rupture is equivalent to a spinodal phase change. The fault remains in a metastable state until the applied stress is sufficient to overcome the energy barrier to rupture.

C. G. Sammis and A. Kositsky deal with earthquake prediction, which continues to be a controversial issue. If large earthquakes are predictable, then the most promising approach to prediction appears to lie in the spatial and temporal patterns of regional seismicity. Epidemic Type Aftershock Sequence (ETAS) methods that evaluate the probability of future large events in time and space based on past seismicity, by using Omori's law and the Gutenberg-Richter distribution, have been shown to give better probabilistic predictions than those based on a random Poisson distribution. Whether or not precursory patterns of seismicity, such as Accelerating Moment Release AMR methods, can be developed to yield a robust deterministic predictor is still a subject of debate.

Section 2.2 contains works on the topic of "Scale invariant behaviour in earthquake occurrence".

A. Corral presents a review of recent findings about scale-invariant behaviour in the structure of earthquake occurrence in time and size, leading to the proposal of a striking universal scaling law that has also been shown to describe fracture phenomena. The connections between critical phenomena, crackling noise, self-organized criticality, and the possible existence of universality and out-of-equilibrium universality classes are mentioned as well.

A. Carpinteri, G. Lacidogna and G. Niccolini present two case studies of monumental buildings subjected to AE monitoring and located in two areas of Italy characterised by different levels of seismicity. The correlation between AE activity in these buildings and regional earthquakes during the monitoring period is investigated. The aim is to explore the analogies between these two phenomena and the possibility that AEs from structures can be regarded as seismic precursors.

## References

[1] C. H. Scholz, "The Mechanics of Earthquakes and Faulting", 2nd ed., Cambridge Univ. Press, New York, 2002.

[2] J. B. Rundle, D. L. Turcotte, R. Shcherbakov, W. Klein and C. Sammis, "Statistical physics approach to understanding the multiscale dynamics of earthquake fault systems", *Rev. Geophys*., vol. 41, pp. 1–30, 2003.

[3] A. Carpinteri and G. Lacidogna (Editors), "Earthquakes and Acoustic Emission", Taylor & Francis (Balkema), London, 2007.

© 2008 Taylor & Francis Group, London, UK

[4] S. P. Shah and Z. Li, "Localization of microcracking in concrete under uniaxial tension", *ACI Materials Journal*, vol. 91, pp. 372–38, 1994.
[5] M. Shigeishi and M. Ohtsu, "Acoustic emission moment tensor analysis: development for crack identification in concrete materials", *Construct. Build. Mater*., vol. 15, pp. 311–319, 2001.
[6] C. U. Grosse, H. W. Reinhardt and F. Finck, "Signal-based acoustic emission techniques in civil engineering", *J. of Materials in Civil Engineering* (*ASCE*), vol. 15, pp. 274–279, 2003.
[7] A. A. Pollock, "Acoustic emission-2: acoustic emission amplitudes", *Non-Destructive Testing*, vol. 6, pp. 264–269, 1973.
[8] M. Ohtsu, "The history and development of acoustic emission in concrete engineering", *Magazine of Concrete Research*, vol. 48, pp. 321–330, 1996.
[9] H. Scholz, "The frequency-magnitude relation of microfracturing in rock and its relation to earthquakes," *Bull. Seismo. So. America*, vol. 58, pp. 399–415, 1968.
[10] D. A. Lockner, J. D. Byerlee, V. Kuksenko, A. Ponomarev and A. Sidorin, "Quasi-static fault growth and shear fracture energy in granite", *Nature,* vol. 350, pp. 39–42, 1991.
[11] Petri, G. Paparo, A. Vespignani, A. Alippi and M. Costantini, "Experimental evidence for critical dynamics in microfracturing processes", *Phys. Rev. Lett*., vol. 73, pp. 3423–3426, 1994.
[12] T. Shiotani, Z. Li, S. Yuyama and M. Ohtsu, "Application of the AE improved *b*-value to quantitative evaluation of fracture process in concrete materials," *Journal of AE*, vol. 19, pp. 118–133, 2001.
[13] R. Shcherbakov and D.L. Turcotte, "Damage and self-similarity in fracture", *Theor. Appl. Fract.Mech*., vol. 39, pp. 245–58, 2003.
[14] A. Carpinteri, G. Lacidogna and G. Niccolini, "Critical behaviour in concrete structures and damage localization by acoustic emission", *Key Engineering Materials*, vol. 312, pp. 305–310, 2006.
[15] A. Carpinteri, G. Lacidogna and N. Pugno, "Structural damage diagnosis and life-time assessment by acoustic emission monitoring", *Engineering Fracture Mechanics*, vol. 74, pp. 273–289, 2007.
[16] A. Carpinteri, G. Lacidogna, A. Manuello and L. Binda, "Monitoring the structures of the ancient temple of Athena incorporated into the cathedral of Syracuse", *Proc. of the 14th Int. Brick and Block Masonry Conference*, Sydney, Australia, 2008.
[17] P. Tosi, V. De Rubeis, V. Loreto and L. Pietronero, "Space-time combined correlation integral and earthquake interactions", *Annals of Geophysics*, vol. 47, pp. 1849–1854, 2004.
[18] A. Carpinteri, G. Lacidogna and G. Niccolini, "Acoustic emission monitoring of medieval towers considered as sensitive earthquake receptors", *Natural Hazards and Earth System Sciences*, vol. 7, pp. 1–11, 2007.

© 2008 Taylor & Francis Group, London, UK

# 1 Acoustic Emission and Critical Structural States

## *1.1 Space-time characterization of AE sources*

© 2008 Taylor & Francis Group, London, UK

*Acoustic Emission and Critical Phenomena – Carpinteri & Lacidogna (eds)*
*© 2008 Kanji Ono, ISBN 978-0-415-45082-9*

# STRUCTURAL INTEGRITY EVALUATION BY MEANS OF ACOUSTIC EMISSION

**Kanji Ono**
Department of Materials Science and Engineering, University of California, Los Angeles, California 90095 USA

## ABSTRACT

This article examines the methodology used in acoustic emission (AE) testing of structures such that we can improve this important application of AE technology. Numerous successful AE tests of structures have been completed, but details are quite often obscured for commercial reasons. Here, we attempt to organize the AE methodology in four steps. 1. AE Sources: Primary sources of brittle fracture, micro- or macro-cracks, are distinguished from secondary sources of friction or fretting, rust, etc. The latter can be as important as primary ones in finding flaw. Materials effects are discussed separately. 2. Kaiser effects, arising from the irreversibility of AE, allow the detection of prior loading level and of damage states. 3. Source location: Using zone, 2D- and 3D-source location methods or via embedded waveguides, this approach identifies the area of integrity loss. 4. Source characterization: Many methods are practiced here, including combined AE parameters, attenuation-corrected signal amplitude, signal frequency, waveform analysis, pattern recognition analysis and moment tensor analysis. Avenues for better AE technology include: to accumulate basic data on structures with standardized procedures, to devise combinatorial approach between localized damage evaluation and long-range detection and to develop regional or global database under international cooperation. The final goal of determining the structural integrity is attainable only with systematic approach with damage quantification via NDT and with the use of fracture mechanics.

## 1 INTRODUCTION

Acoustic emission (AE) testing of structures in modern era began with rocket development work (Green [1]). AE technology has since been applied extensively in structural monitoring. The goal of quantifying the structural integrity and remaining lifetime, however, remains elusive. Current status of AE testing of structures is reviewed here to advance this important application.

© 2008 Taylor & Francis Group, London, UK

AE's connection to the Critical Phenomena (CP) has been an implicit one. Early on, the power-law dependence of AE parameters (AE counts, events, energy, etc.) on stress or stress-intensity factor was recognized and formed the basis of fracture prediction. We in the AE field interpreted it on a deterministic term per *Tetelman* [2], correlating the volume of fracture-process zone to external loading; $N \propto K_I^n$. See Fig. 1 for the case of $n = 4$. The rapid increase in AE from a few concentrated sources forms the basis of our method in finding if the failure of a structure is imminent. The power-law AE was recently given a stochastic basis by *Johansen and Sornette* [3], who re-plotted the final parts of composite tank AE data into CP-based power laws. Another formulation refers to the fracture (critical) point $\tau'$ and cumulative AE "energy" $E \propto [(\tau' - t)/\tau']^{-\gamma}$, with time t and an universal critical exhibitor without dimension, $\gamma$ (*Guarino et al.* [4]). Figure 1 includes such CP curves with $\gamma$–values of 0.025 to 1. A theoretical value is 0.27 (*Guarino et al.* [4]), but obviously the curves fit a power law only locally. Thus, the current CP approach needs refinements in analyzing fracture. Practical benefit from the CP approach is also unclear, but better insight may be expected eventually.

AE testing of structures consists of detecting active AE signals (often with the use of Kaiser effect), identifying the locations of AE sources, grouping them to clusters and ranking the clusters according to the criticality of the AE

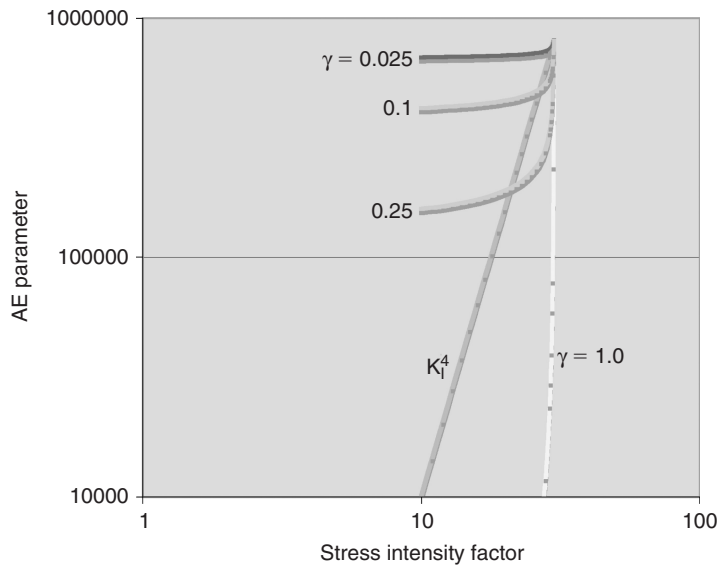



Figure 1: The power-law AE correlation of $N \propto K_I^n$ for the case of $n = 4$ and the CP formulation of AE "energy" $E \propto [(\tau' - t)/\tau']^{-\gamma}$, with the fracture (critical) point $\tau'$, time t and an universal critical exhibitor without dimension, $\gamma$ (1, 0.25, 0.1 and 0.025 shown).

© 2008 Taylor & Francis Group, London, UK

sources. In the last stages, collective AE characteristics are compared with empirical database and lead to integrity evaluation. We will examine each stage in order.

## 2 AE SIGNALS AND SOURCES

Some AE signals in structural testing originate directly from brittle fracture and other fast-moving cracks (primary sources) of structures under test. In steels, these include brittle fracture, low-energy tear, intergranular and inclusion fracture, various embrittlement modes (hydrogen, stress corrosion), weld flaws and heat-affected zone failure. These generate AE with low b-values in amplitude distribution and high-amplitude signals. Plastic deformation plays a minor role as its AE is hard to separate from noise, but nonmetallic inclusions are active sources of AE (*Ono* [5]).

Concrete and rock produce brittle cracks and accompanying AE signals (*Hardy* [6], *Yuyama and Ohtsu* [7]). In micro-seismic testing, seismic magnitude has been correlated to crack sizes (*Lei* [8]). Distinction of AE from micro-cracks and macro-cracks exhibits changing b-values and amplitude ranges (See Fig. 2; *Shiotani et al.* [9]). In composite structures like tanks, vessels and piping, matrix cracks, interlaminar failure and fiber failures are of main sources of AE, but fiber layout, section thickness and resin types affect the detectability of AE signals (*Fowler et al.* [10], *Hamstad* [11]).

Secondary AE sources in structural tests include those from friction at joints and from fretting of crack faces and can be useful in locating harmful discontinuities. Rust in steel cracks acts in similar manner. Rust, oxidation and corrosion products can be active emitters, as demonstrated by *Cho and Takemoto* [12]. However, some others interfere with proper AE testing. Structural noise from bearings and joints can be loud requiring its elimination before AE analysis. Finding gas and fluid leaks is by itself an important goal of AE testing, but leaks must be stopped for AE testing of structure proper. Weather-induced noise can also be a serious obstacle in field tests.

## 3 EFFECTS OF MATERIALS

Structural materials affect the attenuation of AE waves and determine the effective range of detection frequency and sensor spacing. In typical metallic alloys, the attenuation is low and primary AE signals at 100 kHz–2 MHz can be routinely utilized. It is often found that secondary AE signals have their main contents below 100 kHz, allowing frequency-based discrimination (*Dunegan* [13]). In metallic tanks, pressure vessels and pipes filled with liquids, the usable range is reduced to 30–100 kHz. This comes from the loss of wave energy dissipated

© 2008 Taylor & Francis Group, London, UK

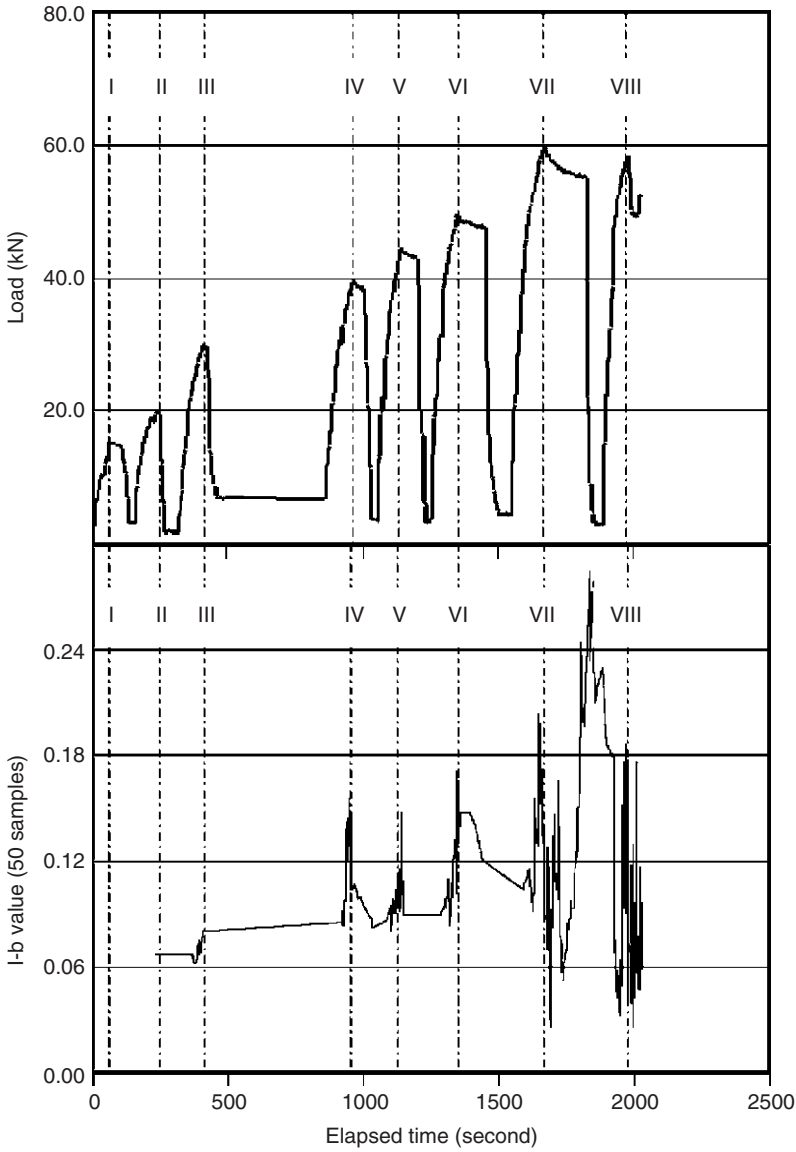



Figure 2: Loading curves of concrete L-shape with corresponding I(improved)-b values. Stage VI nears yielding with an increase in I-b, stages VII and VIII show I-b below 0.05 indicating macro-damages beyond yielding. (*Shiotani et al*. [9]) ©AE Group.

into liquid via dispersion and absorption. Heterogeneous concrete, bricks and rocks have high attenuation and the detection frequency is at 10–60 kHz. Even at this range, *Shiotani et al.* [14] showed the frequency-based discrimination is possible between cracking and fretting signals.

© 2008 Taylor & Francis Group, London, UK

Geological materials have high attenuation and their typically large sizes further limit the usable frequency to sub-kHz range. In the low-frequency range, however, 3-axis sensing becomes practical and this allows detailed evaluation of sources (*Niitsuma* [15]). In geological cases, the large size of propagation media allows the use of body waves. This is in contrast to industrial structures, where guided waves are common and boundaries wield strong effects on the signals reaching sensors. Until the work of *Gorman and Prosser* [16], the guided waves were long ignored in AE studies, especially in field AE testing, in part due to the difficulties of analyzing them. By now, Lamb (plate) waves have proven the utility in field inspection and cylindrical waves are beginning to be used (*Uchida et al.* [17]). Expanded uses of guided-wave analysis should be seriously considered in AE testing.

Wide-frequency signals in low-attenuation materials provide more detailed waveform analysis and better source characterization. Reverberation presents a challenge in sorting out the original signals, especially in smaller shapes. By combining with source location, exact waveform analysis is possible and source parameters can be determined (*Suzuki et al.* [18]). Such laboratory scale scheme is difficult to scale up to the industrial level, but increased capability of Lamb-wave simulation should enable this to happen.

In structures with high-attenuation materials, limited sound transmission forces the use of lower detection frequency. Low frequency implies wavelength larger than the scale of inhomogeneity, thus reducing attenuation. While longer transmission becomes possible, low frequency waveforms carry less information regarding the sources and limit the capability of source characterization.

## 4 KAISER EFFECT

Kaiser effect enables the detection of the prior loading level and in assessing the state of structural damages. AE emitted below the prior load (Felicity effect) implies the presence of damages, although other measures are needed to characterize the damages. In metallic structures, a clear re-start of AE is usually indicated in the absence of flaws. Crack-face cohesion and fretting provide under-preload AE indication of the crack presence, especially under cyclic loading. Oxidation and corrosion products amplify this effect.

Successful use of Kaiser effect in determining the pre-existing stresses in under-sea rocks 30 years ago pioneered this AE application (*Kanagawa and Nakasa* [19]). Large background AE is always present in geologic materials and careful test procedures are required in correct prior-stress assessment (*Yoshikawa and Mogi* [20]).

*Wood* [21] has been using Kaiser effect (by defining "structural integrity index" as percent of the prior load where AE starts) in the evaluation of various structures. He reported successful predictions of failure based on expected time to

© 2008 Taylor & Francis Group, London, UK

reach the critical value of the structural integrity index (80 for metals, 90 for FRP and geologic/concrete materials and 100 being the sound condition). Figure 3 shows an example, where this area is predicted to fail at 250 days upon reaching SII of 90. Global definition of such an index must take proper account of critical components, and is difficult to verify. However, this approach is worthy of further consideration in integrity assessment.

In AE tests of composites, Felicity effect has played the central role in identifying the damaged states (*Fowler et al*. [10], *Hamstad* [11]). Felicity ratio is defined as the ratio of the load at AE start in reloading to the prior load. This parameter was important along with the magnitude of strong emissions (severity index) and rates of change in AE intensity (historic index). In concrete testing, other parameters have been defined for damage evaluation. (*Ohtsu and Yuyama* [22]) For repeating loading tests of concrete, "Load ratio" was defined (as in the case of Felicity ratio):

**Load ratio** = load at the onset of AE activity under the repeated loading/previous load.

Another term, "Calm ratio" was defined as

**Calm ratio** = the number of cumulative AE activity during unloading/total AE activity at the previous maximum loading cycle.

In concrete, crack face rubbing generates unload emissions, which are indicator of the presence of cracks in a structure. By cross plotting these two ratios, three levels of concrete damage can be identified. This procedure was incorporated

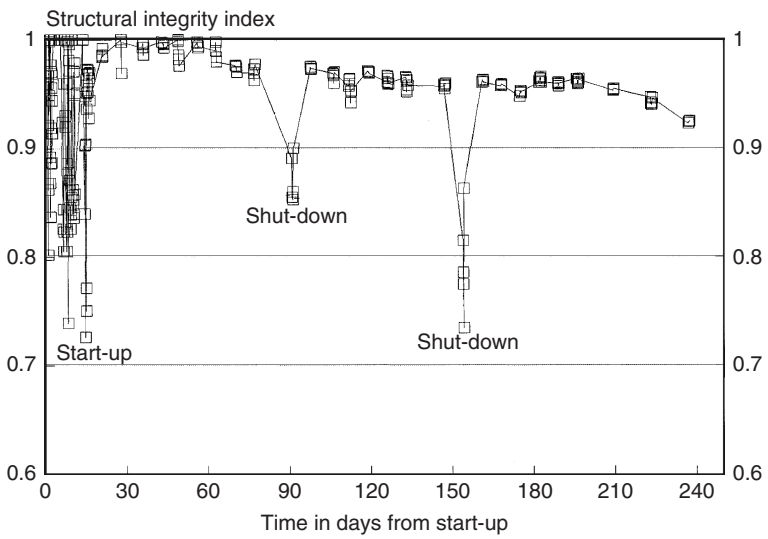



Figure 3: The structural integrity index from continuous AE monitoring of a defective area during plant operation (*Wood et al*. [21]). ©AE Group.

© 2008 Taylor & Francis Group, London, UK

in a Japanese industrial standard, NDIS2421. It is also noted that this standard defined RA ratio as

**RA ratio** = rise time of an AE signal/amplitude in V.

This parameter is essentially the inverse of rise time slope, except the latter uses dB-scale so these are not directly invertible. Ohtsu and coworkers [23] originally developed RA ratio and utilized it in conjunction with average frequency to correlate the tensile vs. shear nature of AE sources. Recently, *Takuma et al*. [24] used RA ratio for the evaluation of tool wear successfully, so this parameter should be considered in many other applications.

## 5 SOURCE LOCATION

Source location identifies the area of integrity loss. Zone location method has been used in structures with high attenuation materials. AE activities at the first-arriving sensor are associated with this sensor location and the "zone" surrounding it. While not as precise as triangulation, it identifies the regions of high AE activity.

The positions of emitting defects are located by triangulation of AE signals arriving at strategically positioned sensors. Techniques used in seismology are adapted to engineering structures with typically complicated boundaries. *Ge* [24] thoroughly reviewed available source location algorithms with theoretical background. These are applicable to both 2D- and 3D-source location.

These methods rely on prior knowledge of wave propagation speed. In many cases, empirical mapping of wave speed is useful, while liquid-filled structures typically need to consider two or more propagation paths and speeds (Nakamura *et al.* [25]). When AE signals travel in shells, Lamb wave modes are dominant. As these waves are dispersive, the frequency of the waves must be taken into account. Recently introduced wavelet transform (Suzuki et al. [26]) is a valuable addition to source location strategy since it can identify signal arrivals at a given frequency (Yamada *et al.* [27], *Kurokawa et al.* [28]). This is a powerful tool in dealing with dispersive wave propagation. See an example given in Fig. 4.

Source location results using Lamb waves detected by sensors placed on the annular plate of a 32-m diameter, 10 Ml tank are shown in Fig. 5. *Takemoto et al.* [29] utilized $A_0$-Lamb mode waves in this monitoring by threshold-crossing arrival-time difference method. Corresponding view of ultrasonic testing (UT) for thickness reduction is also given, indicating reasonably good matching.

Source location in an anisotropic propagation medium such as CFRP requires special consideration. Applications of affine transformation are examples of such effort (*Kurokawa et al.* [28]). The affine transformation together with wavelet transform speeds up 2-D source location algorithm in orthotropic plates by three orders of magnitude.

© 2008 Taylor & Francis Group, London, UK

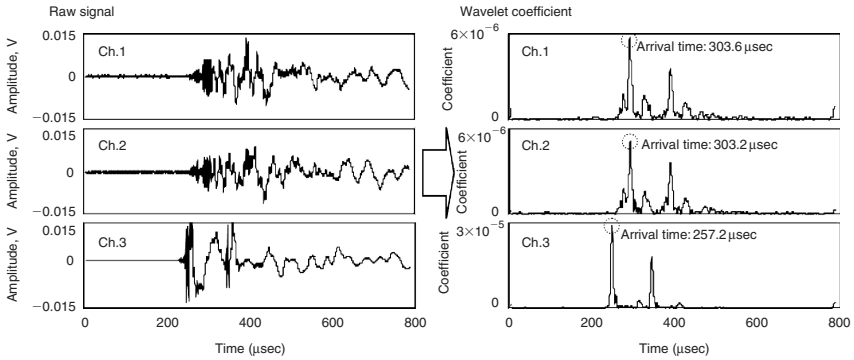



Figure 4: Examples of simulated signals in a CFRP plate and their wavelet transforms. Arrival times are indicated in the figure. Frequency was chosen at 4% of the maximum intensity (*Kurokawa et al.* [28]). ©AE Group.

Most current AE equipment incorporates the software for source location and clustering scheme and displays results in various user interfaces. High AE activity at a given area of a structure, or a cluster, implies the possible presence of flaw. The criteria of "high" activity always need careful attention; AE hit counts and rates, amplitude, and energy have formed the basis for the grading of clusters. In addition to the visualization of clusters, the grading of the clusters further identifies the degree of damage present. In highly successful CARP procedures, developed initially for composite vessels (*Fowler et al.* [10]), the grading utilized severity and historic indices representing cumulative intensity and sudden AE activity jump. Here, zone-location method was used to indicate the flawed regions in an FRP vessel because of high wave attenuation that precluded the use of multiple-sensor triangulation.

For very high attenuation media, embedded waveguides provide an effective means of narrowing the zone of AE activities. Waveguides are also used in tests under extreme environment, but often cause severe waveform distortion.

## 6 SOURCE CHARACTERIZATION

Direct methods of AE signal characterization are inverse (deconvolution) analysis and source simulation analysis (*Ono* [30]). These provide source rise time and magnitude for Mode-I cracks. However, the inverse analysis requires theoretical Green's function and cannot be used for AE from structures. The source simulation analysis, in principle, works on complex shapes, but its field applications must await further development.

Many indirect methods are practiced to determine the nature of AE origins, including combined AE parameters, attenuation-corrected signal amplitude and

© 2008 Taylor & Francis Group, London, UK

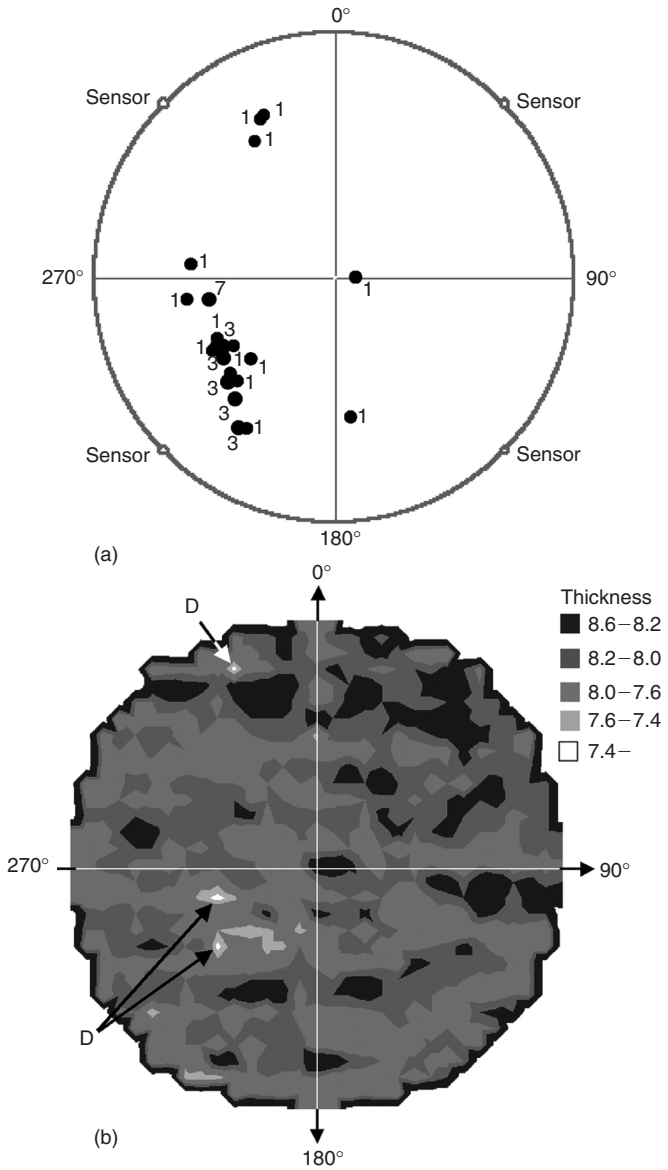



Figure 5: An example of Lamb-wave source location using sensors placed on the annular plate of a 32-m diameter, 10 Ml tank. UT thickness reduction data agrees with AE locations (*Takemoto et al.* [29]). ©AE Group.

its distribution, signal frequency, waveform analysis and moment tensor analysis. Invariably, materials study accompanies AE examination and empirical deduction leads to AE characterization (although some are prone to proclaim mechanisms by intuition). Of these, methods using selected AE parameters

© 2008 Taylor & Francis Group, London, UK

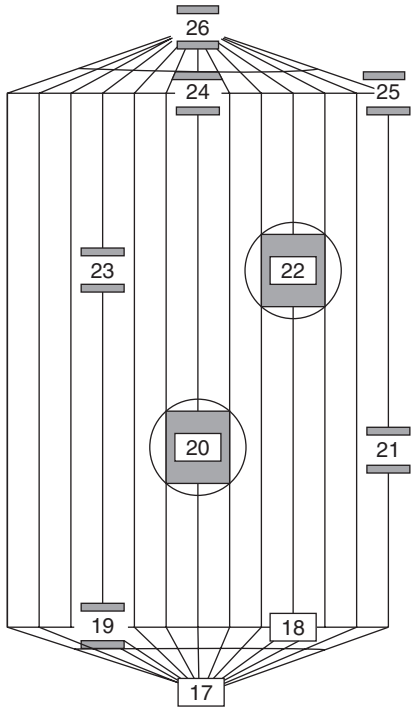



Figure 6: A display of grading after a CARP test of first pressurization test of a hydrocracker reactor. Sensor zones 20 and 22 are rated "D", requiring immediate follow-up inspection (*Fowler et al*. [10]). ©AE Group.

(hit rates, amplitude, and their time history, being the typical) have been the most common approach used in combination with a source location scheme (*Vahaviolos et al.* [31], *van de Loo and Cole* [32]). Signal frequency remains controversial as to its effectiveness in source characterization. It is tempting to assign an AE mechanism to its characteristic frequency. It should be pointed out that the direct signal characterization methods have clearly shown that source rise times of a given type of cracking vary by a factor of ten or more so that a single "characteristic frequency" of cracking does not exist (*Ono* [30]).

Moment tensor analysis (MTA) is useful in characterizing the nature of AE sources. This identifies the magnitude and orientation of displacement vector of an AE source. From its geological origin, *Ohtsu and Ono* [33, 34] set forth this method in AE context initially using theoretical simulation. They set a framework for deducing the crack characteristics using only surface AE observations. *Ohtsu* [35, 36] developed the MTA further, applying to real AE observations in concrete structures with great success. MTA software has been available with a major AE system. The MTA provides the classification of AE signals due to tension (crack-opening) and shear mode of fracture. However, this analysis requires the

© 2008 Taylor & Francis Group, London, UK

detection of weak, initial P-wave arrivals and sensor spacing cannot be large. It is expected that the MTA of localized sources is the first step of integrating this valuable technique into large-scale structural AE tests.

Another technique useful in AE testing of structures is pattern recognition analysis (PRA). PRA has long been studied in evaluating AE observations (*Ohtsu and Ono* [37]), but recent improvements in data-processing speed allow this to be integrated with multi-channel location software (*Anastasopoulos* [38]). *Godinez et al.* [39] used a supervised PRA scheme to detect flaw in helicopter tail gearbox in real time. The energy content of different frequency bands was used as the basis for classification features. K-nearest-neighbor and neural-network classifiers are often used in PRA to cluster signals into separate groups based on combinations of "features". Since various schemes of artificial intelligence compare and deduce matching patterns, independent validation is needed to provide appropriate AE context to PRA results. This is especially keen for neural-network results. These are obtained from a "black-box", which was trained by feeding inputs and outputs.

Wideband waveforms of AE signals are useful in analyzing the displacement-time function at the source, but such a detailed study of AE sources is of limited utility in structural testing. In AE sensor selection, high sensitivity has taken precedence over wideband detection capability. Thus, while wave propagation modes have dominant effects on the waveforms received, any information on a source or the propagation path is lost when a narrow-band sensor is used. In order to improve the source characterization capability, we need a comprehensive approach. One should note that some commonly used resonant AE sensors respond at multiple frequency bands. Newer wideband sensors also have increased sensitivity. These can work with higher functionality of modern AE processing equipment and provide us with a better data set for new AE parameters. Recognizing different modes of guided waves in thin-wall structures is another avenue for vast improvement in interpreting observations. This may lead to the nature of AE sources even under limited frequency band detection.

## 7 AE IN STRUCTURAL INTEGRITY ASSESSMENT

Acoustic emission has been used widely in the US since the 1970s as a means of monitoring the structural integrity of large pressurized vessels and structures. This statement describes the current state reasonably well in that AE has successfully evaluated thousands of structures and alerted conditions of potential failure. Further refining this approach is prudent for AE technology in the near future. Yet, AE is not seriously contributing to "structural integrity assessment" of critical structures. Here, the "assessment" implies far more ambitious goal of predicting remaining lifetime and calculating failure probability.

© 2008 Taylor & Francis Group, London, UK

The procedures for structural integrity assessment require three main groups of input data: 1. material: constitutive (stress-strain) behavior with time and temperature dependence, fracture toughness and fatigue parameters; 2. load: loading regime of primary stresses, residual stresses; 3. geometry: geometry of structure, geometry of flaw. The last item is the most difficult to obtain unless its size is large enough for UT or radiographic testing (RT) or surface-breaking and accessible. Improvement of NDE technology is the most urgent needs in structural integrity assessment. This is where AE can contribute in identifying the position of active flaw. Flaw (or crack) sizing is probably beyond current AE techniques. Digesting the input with various rounds of analysis via finite-element codes, fracture mechanics, material damage and loading schemes, probabilistic lifetime prediction emerges. Thus, unless AE can address AE source characterization issue in structural testing, AE cannot hope for assuming a key role in structural integrity assessment. As suggested earlier, combining global flaw evaluation with localized AE source study is a right first step.

Past attempts for structural integrity assessment by AE have been reported (e.g., *Runow* [40], *Jeong et al.* [41]). However, meaningful progress has been difficult.

Another front is the standardization, where many "international" standards appeared instead of consolidation of existing documents. *Brunner and Bohse* [42] assessed them and concluded that irrespective of the area of AE test procedure, well-documented evaluation criteria must be available for the success of the procedure. From the US-side, ISO seems to have become an irrelevant regional organization. On the other side, ASTM tries to prevail over the whole world. This certainly is not an ideal state.

In order to advance structural testing of AE, it is necessary to increase cooperative endeavor when such a test is conducted in non-commercial environment. Most such tests are done without access to academic researchers and little is published. Intra-European projects under COST [43] are encouraging. In Japan, *Takemoto* group [29] recently tested several large oil storage tanks. It is hoped that more structural tests become open to researchers and this area expands vigorously in years to come.

## 8 CONCLUDING REMARKS

To push AE technology into the center stage of structural integrity assessment, we must improve it from several fronts. We need to better characterize AE sources; to extract more from AE signals reaching sensors; to devise effective AE parameters (like RA); to combine available analysis methods such as WT, MTA, and PRA; to include simulation tools in analysis; to accumulate basic data on structures with standardized procedures; to devise combinatorial approach between localized damage evaluation and long-range detection and to develop regional or global

© 2008 Taylor & Francis Group, London, UK

database under international cooperation. Using systematic approach along with NDT, fracture mechanics, etc., improved AE can make substantial inroads to the domain of structural integrity assessment.

## References

[1] A.T. Green, Me and AE – The early years 1962–1982, *Advanced Materials Research*, vol. 13–14, pp. 3–14, 2006.
[2] A.S. Tetelman, Acoustic emission and fracture mechanics testing of metals and composites, in *Proc. US-Japan Joint Symposium on Acoustic Emission*, Engl. volume, pp. 1–46, Japan Industrial Plan. Assoc., 1972.
[3] A. Johansen and D. Sornette, Critical ruptures, *Eur. Phys. J. B*, vol. 18, pp. 163–181, 2000.
[4] A. Guarino and A. Garcimartin, S. Ciliberto. An experimental test of the critical behaviour of fracture precursors, *Eur. Phys. J. B,* vol. 6, pp. 13–24, 1998.
[5] K. Ono, New goals for AE in materials research, in *Acoustic Emission – Beyond the Millennium*, pp. 57–76, Elsevier, 2000.
[6] H.R. Hardy Jr, *Acoustic Emission Microseismic Activity, Vol. 1: Principles, Techniques and Geotechnical Applications,* Taylor & Francis, 292 p., 2003.
[7] S. Yuyama and M. Ohtsu, AE evaluation in concrete, in *Acoustic Emission – Beyond the Millennium*, pp. 187–213, Elsevier, 2000.
[8] X. Lei, O. Nishizawa, A. Moura and T. Satoh, Hierarchical fracture process in brittle rocks by means of high-speed monitoring of AE hypocenter, *J. of Acoustic Emission*, vol. 23, pp. 102–112, 2005.
[9] T. Shiotani, S. Yuyama, Z. W. Li and M. Ohtsu. Application of AE improved *b*-value to quantitative evaluation of fracture process in concrete materials, *J. of Acoustic Emission*, vol. 19, pp. 118–133, 2001.
[10] T.J. Fowler, J.A. Blessing, P.J. Conlisk and T.L. Swanson, The MONPAC system, *J. of Acoustic Emission,* vol. 8, pp. 1–10, 1989.
[11] M.A. Hamstad, 30 years of advances and some remaining challenges in the application of AE to composite materials, in *Acoustic Emission – Beyond the Millennium*, Elsevier, pp. 77–91, 2000.
[12] H. Cho and M. Takemoto, Acoustic emission from rust in stress corrosion cracking, *J. of Acoustic Emission*, vol. 22, pp. 224–235, 2004.
[13] H.L. Dunegan, Modal analysis of acoustic emission signals, *J. of Acoustic Emission*, vol. 15, pp. 53–61, 1997.
[14] T. Shiotani, Y. Nakanishi, K. Iwaki, X. Luo and H. Haya, Evaluation of reinforcement in damaged railway concrete piers by means of AE, *J. of Acoustic Emission*, vol. 23, 260–271, 2005.
[15] H. Niitsuma, *Acoustic Emission – Beyond the Millenium*, pp. 109–125, Elsevier, 2000.

© 2008 Taylor & Francis Group, London, UK

[16] M. R. Gorman and W. H. Prosser, AE source orientation by plate wave analysis, *J. of Acoustic Emission*, vol. 9, pp. 283–288, 1990.
[17] F. Uchida, H. Nishino, M. Takemoto and K. Ono, Cylinder wave analysis for ae source location and fracture dynamics of stress corrosion cracking of brass tube, *Journal of Acoustic Emission*, vol. 19, pp. 75–84, 2001.
[18] H. Suzuki, M. Takemoto and K. Ono, The fracture dynamics in a dissipative glass-fiber/epoxy model composite with AE source simulation analysis, *Journal of Acoustic Emission*, vol. 14, pp. 35–50, 1996.
[19] T. Kanagawa and H. Nakasa H. *Method of estimating ground pressure*. U.S. Patent No. 4107981; 1978.
[20] B.R.A. Wood, R.W. Harris and E.L. Porter, Structural integrity and remnant life evaluation using acoustic emission techniques, *J. of Acoustic Emission*, vol. 17, pp. 121–126, 1999.
[21] M. Ohtsu and S. Yuyama, Recommended practice for in situ monitoring of concrete structures by acoustic emission, *J. of Acoustic Emission*, vol. 19, pp. 184–190, 2001.
[22] N. Tsuji, M. Uchida, T. Okamoto and M. Ohtsu, Application of acoustic emission technique to evaluation of cracking in concrete structures, in *Progress in Acoustic Emission X*, pp. 189–194, JSNDI, 2000.
[23] M. Takuma, N. Shinke, T. Nishiura and K. Akamatu, Study on evaluation system of tool life for shearing – wavelet transform and chaos time series analysis of AE signals, in *Progress in Acoustic Emission XIII*, pp. 109–116, JSNDI. 2006.
[24] M. Ge, Analysis of source location algorithms, Parts I and II, *J. of Acoustic Emission*, vol. 21, 14–28 and 29–51, 2003.
[25] H. Nakamura, T. Arakawa, M. Yamada, Examination of AE wave propagation routes in a small model tank, *J. of Acoustic Emission*, 23, pp. 243–248, 2005.
[26] H. Suzuki, T. Kinjo, Y. Hayashi, M. Takemoto and K. Ono with Appendix by Y. Hayashi, Wavelet transform of acoustic emission signals, *J. of Acoustic Emission*, vol. 14, pp. 69–84, 1996.
[27] H. Yamada, Y. Mizutani, H. Nishino, M. Takemoto and K. Ono, Lamb-wave source location of impact on anisotropic plates, *J. of Acoustic Emission*, vol. 18, pp. 51–60, 2000.
[28] Y. Kurokawa, Y. Mizutani and M. Mayuzumi, Real-time executing source location system applicable to anisotropic thin structures, *J. of Acoustic Emission*, vol. 23, pp. 224–232, 2005.
[29] M. Takemoto, H. Cho and H. Suzuki, Lamb-wave acoustic emission for condition monitoring of tank bottom plates, *J. of Acoustic Emission*, vol. 24, pp. 12–21, 2006.
[30] K. Ono, Current understanding of mechanisms of acoustic emission, *J. of Strain Analysis*, vol. 40, pp. 1–15, 2005.

© 2008 Taylor & Francis Group, London, UK

[31] S.J. Vahaviolos, R.K. Miller, D.J. Watts, V.V. Shemyakin and S.A. Strizkov, Detection and location of cracks and leaks in buried pipelines using AE, *J. of Acoustic Emission*, vol. 19, pp. 172–183, 2001.
[32] P.T. Cole and P.J. van de Loo, *Acoustic Emission – Beyond the Millenium*, pp. 169–178, Elsevier, 2000.
[33] M. Ohtsu and K. Ono, Crack orientations and moment tensor solutions in acoustic emission, in *Progress in Acoustic Emission III*, pp. 771–778, JSNDI, 1986.
[34] M. Ohtsu and K. Ono, AE source location and orientation determination of tensile cracks from surface observation, *NDT International*, vol. 21, pp. 143–152, 1988.
[35] M. Ohtsu, Determination of crack orientation by acoustic emission, *Materials Evaluation*, vol. 45, pp. 1070–1075, 1987.
[36] M. Ohtsu, Moment tensor analysis of AE and SiGMA code, *Acoustic Emission – Beyond the Millennium*, pp. 19–34, Elsevier, 2000.
[37] M. Ohtsu and K. Ono, Pattern recognition analysis of magneto-mechanical acoustic emission signals, *J. of Acoustic Emission*, vol. 3, pp. 69–80, 1984.
[38] A. Anastasopoulos, Pattern recognition techniques for acoustic emission based condition assessment of unfired pressure vessels, *J. of Acoustic Emission*, vol. 23, pp. 318–330, 2005.
[39] V. Godinez, F. Shu, A. Anastasopoulos, R. Finlayson and B. O'Donnell, Real time classification of acoustic emission signals for drive system coupling crack detection, in *Progress in Acoustic Emission XII,* pp. 7–14, JSNDI, 2004.
[40] P. Runow, The use of acoustic emission methods as aids to the structural integrity assessment of nuclear power plants, Defense Technical Information Center, ADD320141, 51 p., 1985.
[41] H.D. Jeong, H. Takahashi and Y. Murakami, On-line evaluation procedure for structural integrity by acoustic emission frquency analysis, in *Progress in Acoustic Emission IV,* pp. 428–438, JSDNI, 1986.
[42] A.J. Brunner and J. Bohse, Acoustic emission standards and guidelines 2002: a comparative assessment and perspectives, NDT.net – vol. 7 No. 09, September 2002; http://www.ndt.net/article/v07n09/21/21.htm.
[43] COST, European cooperation in the field of scientific and technical research, Action 534, Workshop of COST on NTD assessment and new systems in pre-stressed concrete structures, Kielce Tech. University, Poland, 252 p., 2005.

© 2008 Taylor & Francis Group, London, UK

*Acoustic Emission and Critical Phenomena – Carpinteri & Lacidogna (eds)*
*© 2008 Taylor & Francis Group, London, ISBN 978-0-415-45082-9*

# SOME OBSERVATIONS ON ACOUSTIC EMISSION/STRESS/TIME RELATIONSHIPS

**A. A. Pollock**
Physical Acoustics Corporation, Princeton Junction, New Jersey, USA

## ABSTRACT

Stress and energy are discussed first in the context of the individual AE event. The AE wave redistributes the elastic energy stored in the structure. The propagation of the wave restores equilibrium to a system whose equilibrium has been momentarily disturbed. On a longer timescale, the occurrence of multiples acoustic emission events during loading and load holds is also indicative of the material and structure seeking equilibrium in response to stress challenges. The response of the material takes time. AE data from FRP-wrapped air flasks is presented to illustrate the AE behaviour of damaged and undamaged composite material with respect to global stress, local stress and time. During high-pressure hold periods, damaged material produces much more AE than undamaged material, but the AE decays more rapidly. This is explained in terms of the higher stresses that are present in damaged regions. Information on cascades (the equivalent of earthquake foreshocks and aftershocks) during delamination processes is also presented. There is evidence that damaged material is more likely to produce cascades than undamaged material, and an explanation is offered. The time intervals between the events in the cascades in this case are on the order of $10^{-2}$ s.

## 1 STRESS AND ENERGY: THE INDIVIDUAL AE EVENT

Acoustic emission events are the smaller-scale relatives of earthquakes. Like their larger relatives, they result from sudden local disturbances of material during which elastic energy is released.

The released elastic energy propagates through the material in the form of an acoustic wave. The term "stress wave emission" was used in the past, to emphasize the fact that the wave is associated with the release of stress. Stress is indeed an integral aspect of the dynamics of the wave propagation process, along with strain, velocity, displacement and acceleration.

It is useful to consider the energy terms involved in the AE source process. Suppose that the material, in which the disturbance takes place, is part of a

© 2008 Taylor & Francis Group, London, UK

test body that is under stress due to externally applied forces. There will be a definite amount of elastic energy stored within the test body. This amount will depend on the geometry of the body, the material stiffness and the stress field within it. There is a moment when the disturbance starts and a moment when it ends. There will be a certain amount of stored elastic energy at the moment the disturbance starts, and a different amount after the system has regained equilibrium. The difference will depend on (a) the change in geometry at the source of the disturbance, and (b) the external boundary conditions. We will express this change by the equation:

$$E_a = E_b + W - \Delta E \tag{1}$$

where $E_a$ is the stored elastic energy after the system has regained equilibrium, $E_b$ is the stored elastic energy before the disturbance, and W is any work done by the external forces during the disturbance. $\Delta E$ is essentially a balancing term which shows the amount of energy made available from the elastic field due to the disturbance. There are several ways this energy $\Delta E$ can go. First, if the disturbance creates new surface within the material, there is surface energy to be supplied. Second, energy may be used up in the forceful, plastic deformation of material in the immediate neighbourhood of the source. Finally, if there is surplus energy left over after these needs have been taken care of, the disturbance will be rapid and the surplus energy will be released in the form of acoustic emission. These three energy terms are indicated in the equation:

$$\Delta E = \Delta E_s + \Delta E_p + \Delta E_{ae} \tag{2}$$

This equation highlights the fact that the acoustic emission is a variable fraction of the total energy released by the disturbance. $\Delta E_s$ and $\Delta E_{ae}$ may be best termed *acoustic emission event energy* (*ASTM Book of Standards,* [1]) and *acoustic emission wave energy* respectively. For a given disturbance – a given amount of crack growth, for example – it is possible that $\Delta E$ will be hardly greater than $(\Delta E_s + \Delta E_p)$. In this case the deformation will take place slowly (quasi-equilibrium conditions) and there will be little or no AE. This is the case for ductile tearing in steels. If on the other hand $\Delta E$ is substantially greater than $(\Delta E_s + \Delta E_p)$, then the source event will take place rapidly and there will be substantial AE. This is what happens with brittle materials. Further analysis of the relationships between these terms may be found in (*Pollock,* [2]).

At the moment the acoustic emission (AE) event takes place, the mechanical equilibrium of the material is disturbed. The propagation of the wave serves to restore the material to mechanical equilibrium. This is the nature of acoustic waves in general. Wave motion is the response of material to unbalanced forces. After the wave has propagated, reflected, dispersed and eventually dissipated, the material is again at rest. The transient nature of the AE process makes us

© 2008 Taylor & Francis Group, London, UK

particularly aware of this aspect of the process. At most if not all points in the material, the stress field after the event is slightly different from what it was before the event. The change is permanent, and nowhere greater than at the source.

Most commonly in laboratory and industrial practice, the stimulus for the AE is mechanical stress applied by human agency. Examples of this, in the world of AE application, include the pressurization of vessels and dams, and the loading of highway bridges by traffic. Other times the stress may occur naturally, as in earthquakes or the weathering of rocks (Figure 1). In the weathering of rocks, the operative stress field is produced by thermal gradients rather than by directly applied mechanical forces. Thermally induced stress waves can also be induced by pulsing the test object with a laser, but the mechanism is different. In the case of the rock, the thermal gradient sets up a quasi-static stress field which provokes sudden small, local breakdowns of the rock at points of stress concentration. In the case of laser stimulation, the heat application is abrupt and the thermal expansion itself launches the stress wave.

Directly applied forces and thermal gradients are by no means the only kinds of stimulus that can produce AE. In the application of AE to detect corrosion on the floors of oil storage tanks, the source of stress energy is ultimately chemical. The corrosion product is formed by oxygen entering the metal lattice and dilating it. The material swells; the oxide has a much lower density than the parent metal. The resulting stresses lead to AE of remarkably high amplitude as the oxide cracks and spalls. Under the adverse chemical conditions often found in oil storage tanks, this process is continually at work, even when the tank is under nominally steady state conditions.



Figure 1: Cracks from Weathering of Rock (Cape Neddick, Maine).

© 2008 Taylor & Francis Group, London, UK

In the manifestations of AE so far discussed, the event takes place in a material that is already under high stress, that stress being the cause of the AE. The stress may be either global (as in a pressure vessel) or local (as in spalling of corrosion products). In some other manifestations of AE, phase transformations for example, the presence of pre-existing stress is more debatable.

In all these situations, the source event must be sudden if there is to be appreciable wave energy released. The upper limit of the frequency spectrum of the wave is inversely related to the duration of the source event (*Pollock*, [2]). The simplest case is when the disturbance at the source is completed in a time that is short compared to the period of the wave motion under consideration, and short compared to the time taken by a wave to dampen out, or to travel across the dimension of the test object. This is often the case in practice. But it is also quite common for source disturbances to last longer than this, leading to variety and complexity in AE waveforms. In the extreme, the AE signal can even be modulated by vibrations of the test object while a crack is running (*Pollock*, [3]).

The above considerations apply to individual AE events. Normally when we monitor AE, we are recording many such events that take place over an extended period of time. The main part of this paper discusses relationships between AE, load and time in this larger context.

## 2 AE AND STABILIZATION OF MATERIAL AND STRUCTURE

Materials under applied stress seek stability. The path to stability often includes plastic (permanent) deformation. Since this involves the re-arrangement of atomic bonds, it is ultimately a chemical process. Theories of chemical kinetics are applicable, as well as mechanical considerations (*Krausz and Eyring*, [4]). As is well known, chemical reactions proceed at definite rates that depend on activation energies, temperature and other factors. Deformation of materials is therefore also a time-dependent phenomenon.

In the growth of AE technology, it was a major step when the developers of test procedures stepped beyond the Kaiser effect (which is linked with *instantaneously* plastic materials) and paid serious attention to the existence of AE during load holds and AE on repeated loadings (*Fowler*, [5]). It is helpful to see these time-dependent "effects" as manifestations of the structure's search for stability. The higher the stress, the longer it takes the structure to stabilize and the more persistent the emission.

The main rationale for using AE technology as a non-destructive test method is that flaws act as stress risers, therefore when a structure is stressed it is predominantly the flaws that emit. This applies both to the quantities of emission and to the persistence of emission during load holds.

It is interesting to see how the emission process operates in relation to stress and stability, over different timescales. Composite materials are particularly

© 2008 Taylor & Francis Group, London, UK

interesting to study because their extreme heterogeneity leads to a stress field that on the microscopic scale is very non-uniform, especially when the material is damaged. Therefore as an illustration, we will look at some AE tests performed during the development of an AE test procedure for fiber reinforced composite wrapped pressure vessels. These are DOT Class 3 "air flasks", high pressure (23 MPa) cylinders used to hold compressed air supplies for divers working underwater. The AE test pressure is 10% higher than the working pressure. The burst pressure is about three times higher than the working pressure. Figure 2 shows a vessel that was pressurized to burst after the AE test, as part of the procedure validation process (*Godinez*, [6]).

We will show illustrative data from two of the flasks, out of a total of about 50 vessels used during the development program. Figure 3 shows AE from two flasks, one in good condition (monitored by channel 7, upper graphs) and the other damaged by dropping from a height (monitored by channel 3, lower



Figure 2: Aluminum-Lined, Composite-Wrapped Air Flask after Pressurization to Burst.

© 2008 Taylor & Francis Group, London, UK

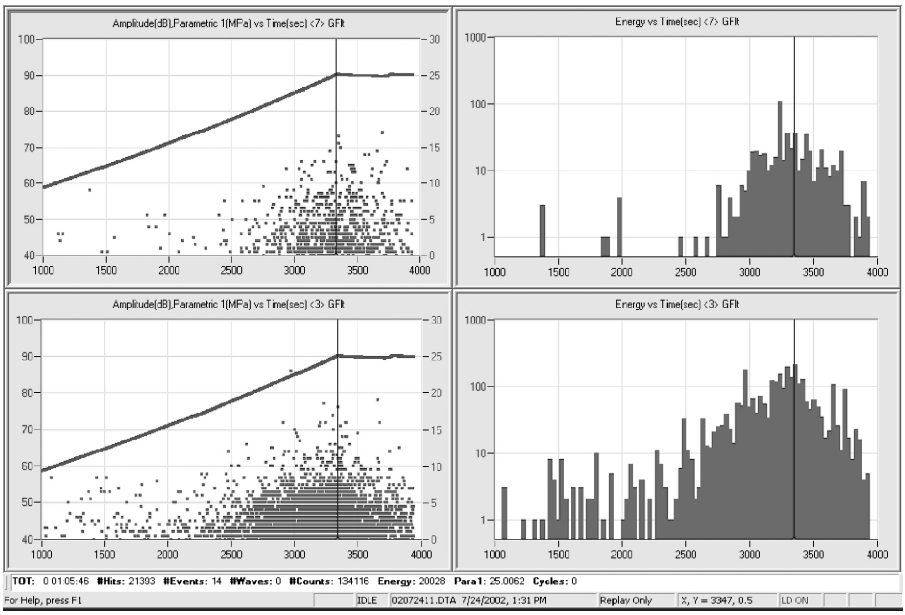



Figure 3: AE Amplitude Point Plots with Pressure, and Energy Histograms for Undamaged Flask (Upper Graphs) and Damaged Flask (Lower Graphs).

graphs). Both flasks are being pressurized from the same source at the same time. The pressure is ramped up steadily and then held for 10 minutes. The damaged flask gives much more emission than the undamaged flask, at all stages of the test. The emission rises during the pressure ramp and persists, slowly diminishing, during the hold at peak pressure. This is standard behaviour for AE from fibre-reinforced composite materials.

The longest timescale of interest for purposes of this paper is a few minutes, which is the timescale of the hold period during which the pressure is essentially constant. In this period the flasks are stabilizing, in response to a stress challenge of a magnitude that they have not seen for a very long time (maybe years; this is an overpressure test). Comparing the AE from the undamaged and damaged flasks as shown in the graphs on the right hand side of Figure 3, it is striking that the rate of decay of the emission during pressure hold is much greater for the damaged flask. For the damaged flask, the AE falls in an exponential manner from 70 to 7 energy counts per second, a factor of 10 in the first five minutes of the hold period. For the undamaged flask, the AE rate falls from 10 to 4 energy counts per second in the same period, a much smaller factor. This difference has its origin in the nature of the stress field and the way it is relieved by the ongoing damage. In the case of the damaged flask, the search for stability involves the relief of exceptionally high stresses in the small damage region (size on the order of tens of millimetres). In these high-stress regions the viscoelastic flow

© 2008 Taylor & Francis Group, London, UK

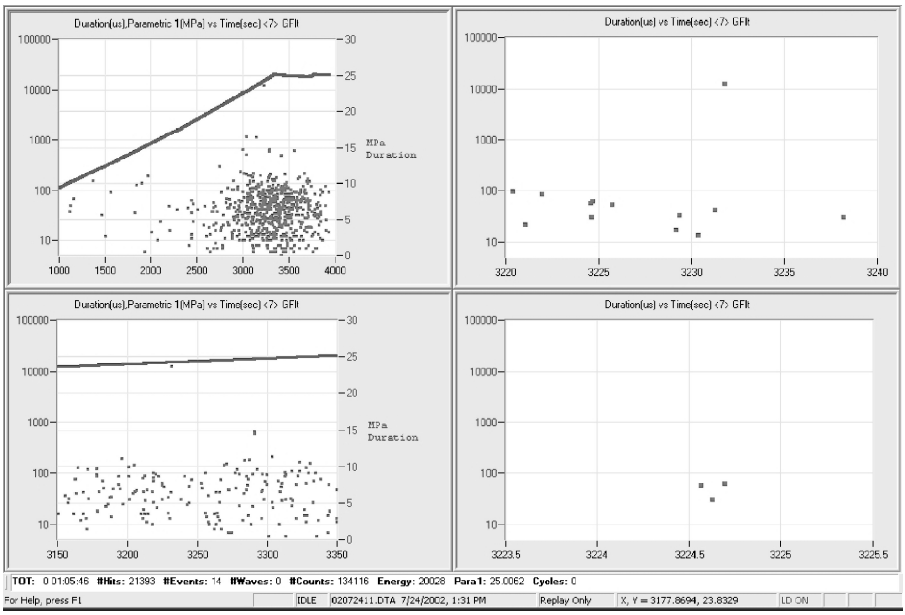



Figure 4: AE (Signal Duration vs Time) from Undamaged Flask, Four Different Timescales.

of the matrix is relatively rapid, and so is the accompanying stabilization. In the case of the undamaged flask, the emission most likely comes from widely distributed sources, not from a single concentrated high stress region. Again, it is viscoelastic flow of the matrix that stimulates AE following microstructural stress adjustments. But in the basically undamaged, more homogeneous material the stresses are more uniform. The matrix flow is slower and the emission, though less in quantity, is more persistent.

It is also of interest to examine AE behaviour over shorter timescales. Along with summary data from the whole test, Figures 4 and 5 show data for selected intervals lasting 200 s, 20 s and 2 s, for the undamaged and damaged flasks respectively. Presented here is a short study of a phenomenon sometimes called "cascades". This is the AE equivalent of earthquake foreshocks and aftershocks. True cascades indicate a causal relationship between their component events, which is interesting in terms of the structure's search for stability. In concept, one event causes a local redistribution of stress, triggering another event after only a short activation time. It takes several events to stabilize the local region. At the end of the process, stresses may have been transferred out to other nearby regions, but evidently those regions are able to sustain them. Material heterogeneity has a dominant influence on processes of this kind, which have been much discussed in the literature since the early work of researchers such as Mogi and Scholz (reviewed in *Pollock* [7]).

© 2008 Taylor & Francis Group, London, UK

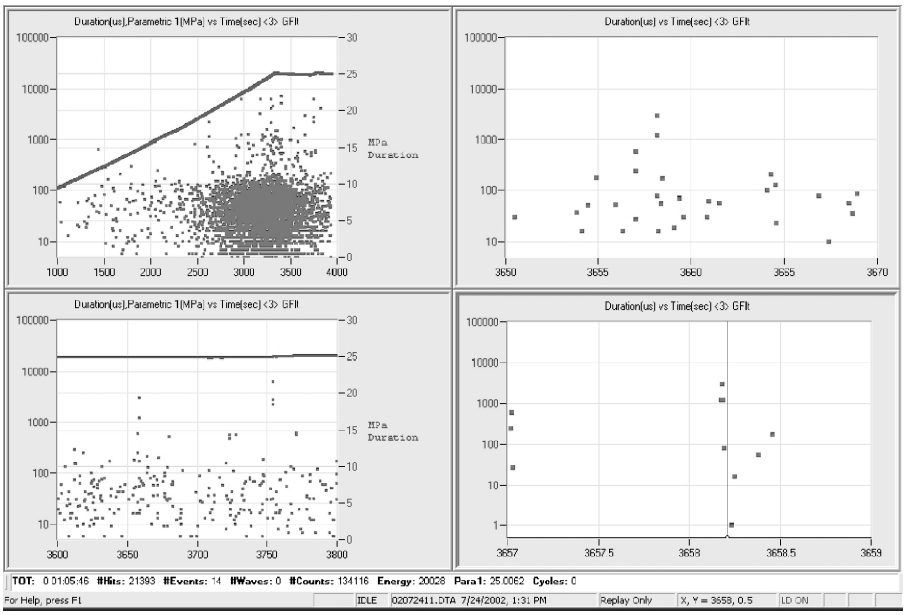



Figure 5: AE (Signal Duration vs Time) from Damaged Flask, Four Different Timescales.

In this illustration of AE cascades, the 200 s intervals for Figures 4 and 5 were selected to have approximately equal levels of AE activity (lower left hand graphs). To accomplish this, the interval selected for the undamaged flask was during rising pressure, while the interval for the damaged flask was during the pressure hold.

The 200 s AE plots from the two flasks look quite similar. Both show apparently random distributions of AE events with respect to their duration (y-axis, in microseconds) and time (x-axis, in seconds). Of particular interest are delamination events, which are characterized by long signal durations, typically several milliseconds. The undamaged flask shows one of these, and the damaged flask shows two.

These delamination events are included in the 20 s AE plots (the upper right-hand plots of Figures 4 and 5). Here a difference appears. In the undamaged flask, the delamination event appears to be isolated. The event that preceded it was 560 ms earlier, the event that followed it was 6.3 s later – just 3 events in 7 seconds. In the damaged flask, there were 21 events in the 10 seconds surrounding the delamination event. This can be compared to 1.5 events per second, which is the average for the 200 s interval we are considering.

On the 2 s plots it becomes clear that the delamination event on the damaged flask was part of a true cascade. The lower right-hand plot in Figure 5 shows six hits which all occurred in a 71 ms interval. The first of these had the largest

© 2008 Taylor & Francis Group, London, UK

Table 1: AE Hits from Damaged Air Flask, Including Cascades.

| Time of hit (s) | Risetime (μs) | Counts | Energy (ec) | Duration (μs) | Amplitude (dBae) |
|---|---|---|---|---|---|
| 3650.485 | 14 | 5 | 0 | 30 | 51 |
| 3653.820 | 3 | 4 | 0 | 37 | 42 |
| 3654.125 | 12 | 2 | 0 | 16 | 42 |
| 3654.468 | 35 | 8 | 0 | 51 | 47 |
| 3654.878 | 67 | 28 | 5 | 181 | 56 |
| 3655.946 | 16 | 8 | 0 | 54 | 47 |
| 3656.344 | 7 | 2 | 0 | 16 | 43 |
| 3657.021 | 64 | 30 | 8 | 248 | 62 |
| 3657.024 | 22 | 12 | 2 | 590 | 50 |
| 3657.027 | 2 | 3 | 0 | 27 | 41 |
| 3658.178 | 55 | 66 | 56 | 1208 | 78 |
| 3658.181 | 6 | 57 | 13 | 3007 | 57 |
| 3658.186 | 19 | 10 | 3 | 1200 | 48 |
| 3658.190 | 16 | 7 | 1 | 81 | 48 |
| 3658.234 | 1 | 1 | 0 | 1 | 40 |
| 3658.249 | 12 | 3 | 0 | 16 | 42 |
| 3658.379 | 8 | 10 | 0 | 55 | 48 |
| 3658.457 | 40 | 25 | 5 | 169 | 59 |
| 3659.103 | 16 | 3 | 0 | 19 | 45 |
| 3659.384 | 22 | 8 | 0 | 72 | 48 |
| 3659.638 | 16 | 4 | 0 | 31 | 45 |
| 3660.843 | 14 | 5 | 0 | 30 | 50 |
| 3660.961 | 32 | 9 | 0 | 63 | 49 |

amplitude, so the other five could be classified as aftershocks. The data is listed in Table 1. Typically there are hundreds of milliseconds between consecutive events. The time intervals between the six hits starting at 3658.178 s are so small that there is no doubt that they have a common physical cause. Given the way this AE equipment measures signals, the first four hits are not totally distinct from one another, and may arguably have come from the same event. However there is no doubt that the last two hits in the cascade came from distinct events. In the time intervals separating the last few hits, the acoustic waves died down and the material came to rest. The last two hits were separated by 45 ms and 17 ms, respectively, from their predecessors in the cascade. So it is demonstrated that in the very-short-term, local stabilization that occurred around this delamination event in the high-stress damage region, there were aftershocks separated by times on the order of tens of milliseconds.

© 2008 Taylor & Francis Group, London, UK

The aftershock process is conveniently explained by reference to the notion of "latent sites" introduced in 1974 (*Pollock*, [8]). In this concept a material contains a distribution of latent sites (latent AE sources), each having a probability of activation that can be expressed as a decay time $\tau_i$, which is itself a function of the local stress $\tau_i(\sigma_i)$. The cascade phenomenon can be discussed in the following terms. Each event in the cascade alters the stresses $\sigma_i$ at latent sites nearby. In general some of the $\sigma_i$ will be reduced but others will be raised. At the latent sites where $\sigma_i$ is raised, $\tau_i$ will be shortened and thus the next event in the cascade will be stimulated. What we are seeing here is $\tau_i$ on the order of $10^{-2}$ s for stresses on the order of the interlaminar failure stress.

## 3 CONCLUSIONS

1. Upon comparing the AE during the hold at the test pressure, from the damaged and undamaged flasks, it was found that the damaged flask produced much more AE, and that rate of this AE decreased rapidly towards the rate that was characteristic of the undamaged flask. The AE rate from the undamaged flask was relatively low and decreased much more slowly with time. This corresponded to the concentrated, very non-uniform nature of the stress field in the damaged region compared with the relatively uniform nature and lower magnitude of the stress field in undamaged material.
2. There is an indication that AE cascades occur more commonly in damaged material than in undamaged material. This is in accordance with the microscopically non-uniform nature of the stress field in the damaged material, which sets the stage for interactions between multiple closely-spaced "latent sites".
3. These discussions have touched on timescales ranging from thousands of seconds (the duration of the test on the air flasks), down through tens of milliseconds (the typical time between successive members of an AE cascade) to tens of microseconds (the durations of the typical AE signals). A common theme can be recognized across all these timescales: the material is always seeking equilibrium, and the elastic stress field (static or dynamic) is always being redistributed in pursuit of that goal.

## References

[1] ASTM Book of Standards, "Standard Terminology for Nondestructive Testing", E 1316, ASTM International, W. Conshohocken, PA, USA.
[2] A. A. Pollock, "Metals and Rocks: AE Physics and Technology in Common and in Contrast", Proceedings First Conference on Acoustic Emission/Microseismic Activity in Geologic Structures and Materials,

© 2008 Taylor & Francis Group, London, UK

Pennsylvania State University, June 9–11, 1975, pp. 384–401, Trans Tech Publications, ed. H. Reginald Hardy Jr., 1977.

[3] A. A. Pollock, "Observations on AE from Large Crack Jumps", Proceedings of the Sixth International Acoustic Emission Symposium, The Japanese Society for Nondestructive Testing, pp. 198–207, November 1982.

[4] A. S. Krausz and H. Eyring, "Deformation Kinetics", John Wiley & Sons, 1975.

[5] T.J. Fowler, "Acoustic Emission Testing of Fiber Reinforced Plastics", Preprint 3092, ASCE Fall Convention and Exhibit, San Francisco, California, American Society of Civil Engineers, Oct. 17–21, 1977.

[6] V. Godinez et al., "Acoustic Emission for Periodic Inspection of Composite Wrapped Pressure Vessels", 45th Acoustic Emission Working Group (AEWG) Meeting, Infrastructure Institute of Northwestern University, Evanston, Illinois, August 2002.

[7] A. A. Pollock, "Physical Interpretation of AE/MA Signal Processing", Proceedings Second Conference on Acoustic Emission/Microseismic Activity in Geologic Structures and Materials, Pennsylvania State University, November 13–15, 1978, pp. 399–422, Trans Tech Publications, ed. H. Reginald Hardy Jr., 1980.

[8] A. A. Pollock, "Acoustic Emission", Interaction Ondes Acoustiques-Matière, 16e Cours de Perfectionnement de l'Association Vaudoise des Chercheurs en Physique, March 1974 (Switzerland); also printed in Journées d'Etudes sur L'Emission Acoustique, Institute National des Sciences Appliquées de Lyon (INSA), France, March 1975.

© 2008 Taylor & Francis Group, London, UK

*Acoustic Emission and Critical Phenomena – Carpinteri & Lacidogna (eds)*
*© 2008 Taylor & Francis Group, London, ISBN 978-0-415-45082-9*

# LOCALIZATION AND MODE DETERMINATION OF FRACTURE EVENTS BY ACOUSTIC EMISSION

**Hans W. Reinhardt[1], Christian U. Grosse[2] and Jochen H. Kurz[3]**
[1]Dept. of Construction Materials, University of Stuttgart, Germany
[2] Dept. of NDT & Monitoring Techn., MPA Universität Stuttgart, Germany
[3] Fraunhofer Institute Nondestructive Testing IZFP, Saarbrücken, Germany

## ABSTRACT

The paper deals with modern quantitative or signal-based acoustic emission (AE) techniques. In order to localize AE events accurately one needs an exact onset-time determination method. These are the wavelet transformation for the filtering of signals and the autoregressive AIC picker for the automatic picking instead of the very time consuming picking by hand. Examples of localization results are given. The signal-based AE technique can also be used for the determination of the fracture mode when the moment tensor is being evaluated. An example demonstrates how the method can be used.

## 1 INTRODUCTION

Acoustic emission techniques allow passively the observation of crack growth or internal defects. However, there are fundamental differences between different ways to apply AE techniques due to historical developments in electronics and sensor technologies. *Quantitative* or *signal-based* acoustic emission techniques [1] differ generally from so-called *classical* or *parameter-based* AE techniques, where only parameters are recorded and not the signal itself is stored. Signal-based techniques allow detailed fracture mechanical evaluations of brittle materials like concrete, if a proper setup and adequate instruments are chosen. Since these differences between the traditional parameter-based and newer signal-based techniques are described earlier [2, 3] we will focus on recent results in the following.

There are four different steps of a modern AE analysis consisting of (1) the analysis of mechanical data and the acoustic emission rate, (2) the localization of acoustic emissions, (3) the evaluation of the topography of the fracture plane,

© 2008 Taylor & Francis Group, London, UK

and (4) fracture mechanical studies based on moment tensors. Here, advances of the techniques addressed under (2)–(4) are described in more detail along with some examples of measurements to study different failure modes in concrete.

## 2 AE-EVENTS AND LOCALIZATION OF FRACTURES

AE is defined as the spontaneous release of localized strain energy in a stressed material resulting, for example, from micro-cracking and can be recorded by transducers (sensors) on the surface in analogue to earthquake recording. One of the advantages compared to other NDE techniques is the possibility to observe the time-dependent damage process during the entire load history. To do so, the application of signal-based methods requires reliable localization, i.e. the determination of the source coordinates of the events. There are several different ways to localize AE events [3, 4, 5, 13, 40], whereas the algorithms, using the arrival times of the waves recorded at multiple sensors, are in use since many years. Picking a distinct onset time of a signal at different sensors according to the example shown in Fig. 1, one can calculate the minimum of the sum of squares of the deviations and calculate the source coordinates usually with proper accuracy [6, 7] or determine the source coordinates using a direct algebraic approach [40].

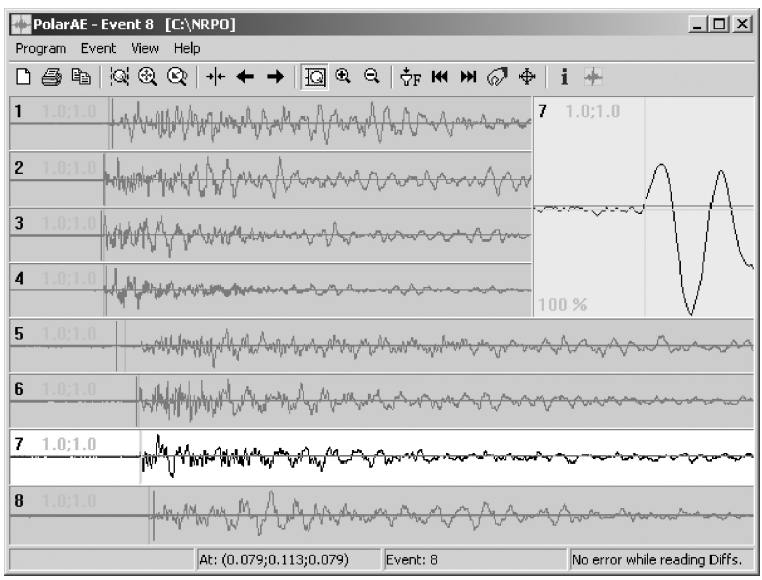



Figure 1: Example of the arrival time extraction for the 3D localization of acoustic emissions using the PolarAE software developed at the University of Stuttgart.

© 2008 Taylor & Francis Group, London, UK

Besides of these basic techniques two main issues had to be handled prior to the application of signal-based techniques – one concerning the data evaluation and the other concerning hardware requirements.

## 3 ONSET TIME DETERMINATION

Damage and failure processes often generate several thousand events from one damage zone within a very short time interval, revealing a huge amount of data. With *parameter-based* AE techniques a fast but only rudimentary analysis can be performed even on-line. Concerning the analysis of *signal-based* AE data usually needs the interpretation by an expert manually processing the data including a time consuming picking of the signal onsets by hand. For very large data sets this is not applicable. Therefore, the application of automatic analysis methods, including data conversion, denoising, and localization by the use of an automatic onset determination, moment tensor inversion and other features like b-value determination or the use of magnitude-squared coherence functions, is indispensable.

### 3.1 Threshold

The simplest form for onset picking is to use an amplitude threshold-picker. However, small amplitude signals and/or signals with a high noise level are not valuable for a pure threshold approach [8]. A widespread approach finally using a dynamic threshold, which is not applied to the raw signal, is the so called STA/LTA (STA Short Term Average, LTA Long Term Average) picker by Baer and Kradolfer [9]. A characteristic function based on the signal's envelope is defined. Here, the STA measures the instant amplitude of the signal and the LTA contains information about the current average seismic noise amplitude. The difference between STA and LTA function is further defined by multiplying the characteristic function with frequency dependent parameters. Earle and Shearer [10] chose a similar approach with a different envelope function. Due to the fact that signal and noise of acoustic emissions in concrete are often to be found in the same frequency range (20 kHz up to 300 kHz), the STA/LTA picker does not produce accurate enough results.

### 3.2 Hinkley criterion

A signal is evaluated with respect to its energy content. However, the energy content of the noise of the signal may blur the results and it is not easy to distinguish between noise and real meaningful signal. Therefore, a certain value

© 2008 Taylor & Francis Group, London, UK

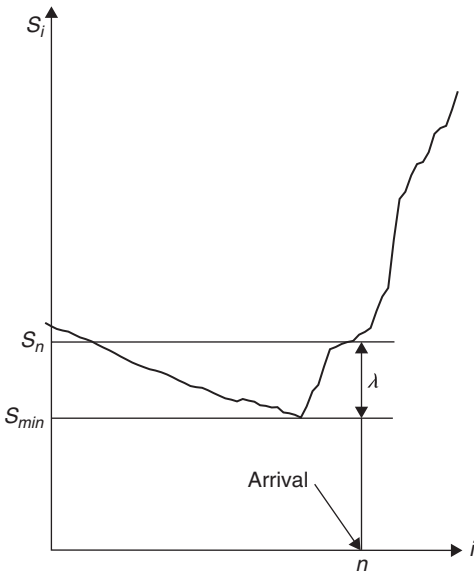



Figure 2: Energy of the signal and Hinkley criterion.

is subtracted from the energy and only if the subtraction reaches a certain value the procedure is stopped. Eq. (1) shows the energy of data points $0 < k < i$

$$S_i = \sum_{k=0}^{i} x_k^2 \tag{1}$$

The Hinkley criterion states

$$S_i - \min S_k > \lambda \quad \text{for} \quad i < k < n \tag{2}$$

Looking at Fig. 2 one can see the energy which has a certain value and which is decreased by $S_{min}$ until the threshold value $\lambda$ is reached. Then it is stated that the energy increase is due to the real signal whereas the previous energy is attributed to the noise. The time step $n$ indicates the onset of the arrival time. To apply the Hinkley criterion a negative trend $i\,\delta$ is subtracted

$$S_i^1 = S_i - i\delta = S_i - i\frac{S_n}{\alpha N} \tag{3}$$

It turned out that $\alpha$ has to be chosen between 5 and 20. A small $\alpha$ leads to a too late picking time whereas a large $\alpha$ may lead to a too early picking time. Figure 3 illustrates the situation. In the example the best evaluation would occur for $\alpha = 5$.

© 2008 Taylor & Francis Group, London, UK

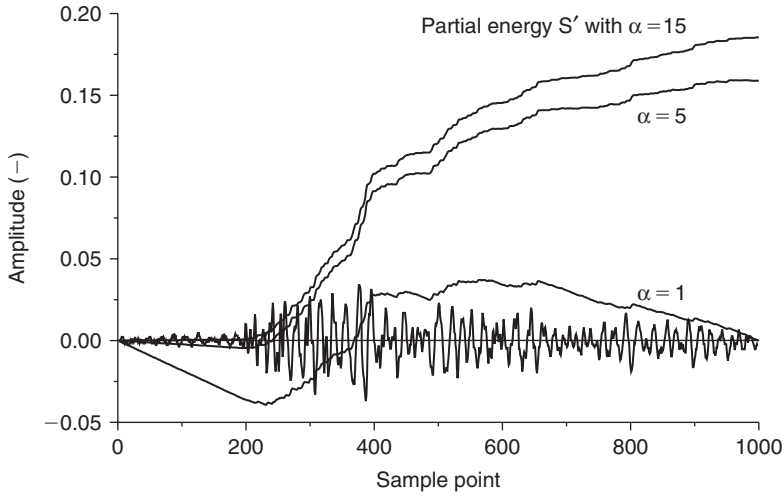



Figure 3: Signal and Hinkley criterion with adjusted value of λ.

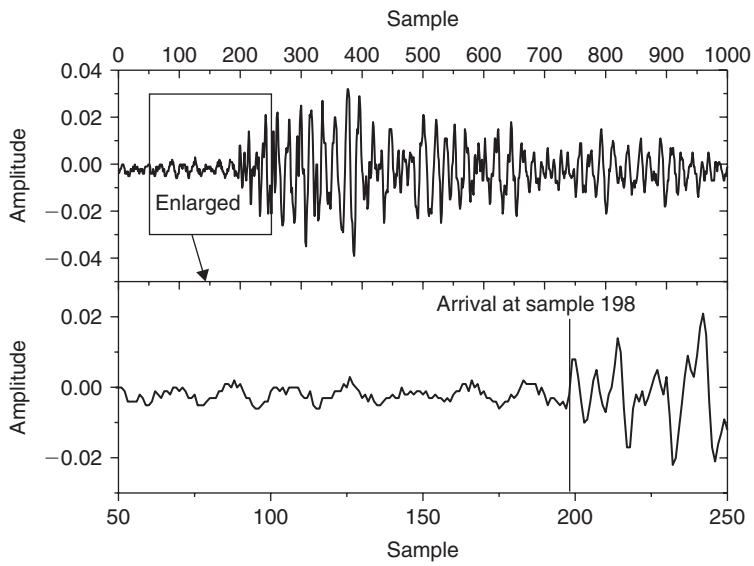



Figure 4: Recorded signal (top) and evaluated picking time (bottom).

To illustrate the quality of the evaluation procedure Fig. 4 (top) shows a recorded signal and Fig. 4 (bottom) the first 200 time steps enlarged with indication of the picking time.

This procedure has been emplemented in the software WinPecker [21] and can be used in an automated way.

© 2008 Taylor & Francis Group, London, UK

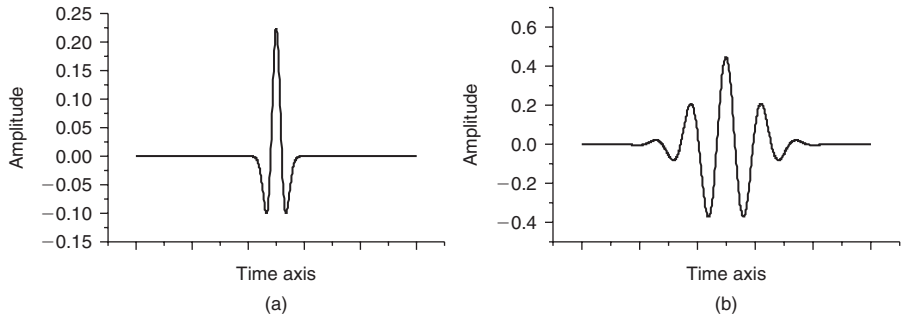



Figure 5: Wavelet function, (a) Mexican hat, (b) Morlet.

### 3.3 Wavelet transformation

The wavelet transformation is a mathematical procedure for the evaluation of signals [12]. Opposite to the well-known Fourier transform the wavelet transformed signal shows the frequency domain and the time domain. The continuous wavelet transformation is shown in Eq. (4)

$$f(a,b) = \frac{1}{\sqrt{a}} \int_{-\infty}^{\infty} f(t)\psi\left(\frac{t-b}{a}\right)\, dt \tag{4}$$

with $f(t) =$ signal, $\psi(t) =$ wavelet function, $a =$ scale variable, and $b =$ shift parameter. There are numerous wavelet functions in the literature and only two of them are shown in Fig. 5. These are widely used in technical applications.

A simple application is shown in Fig. 6 with a regular sine wave of four frequencies.

The application of a Fast Fourier Transform (FFT) to the time series in Fig. 6a (top) leads to the picture in Fig. 6a (bottom) which shows four distinct resonance frequencies but the time domain is lost. One cannot state from the figure which frequency appears first and which one last. Fig. 6b is the wavelet transformed signal which shows on the vertical axis the scale value which is proportional to the frequency and on the horizontal axis the time when these frequencies occur.

This procedure can even be improved if wavelet techniques in combination with a digital band-pass filter are used to enhance the signal-to-noise ratio [14]. Software can be designed to work automatically with large data sets of up to several thousand signals acting as a pre-processor followed by picking algorithms and an automatic onset time determination for reliable localization. Band-pass filtering alone is ineffective since signal energy is partly in the noise band. Usually, the raw data are transformed to the wavelet domain, where a threshold is automatically determined separating signal from noise [11]. A discrete or a

© 2008 Taylor & Francis Group, London, UK

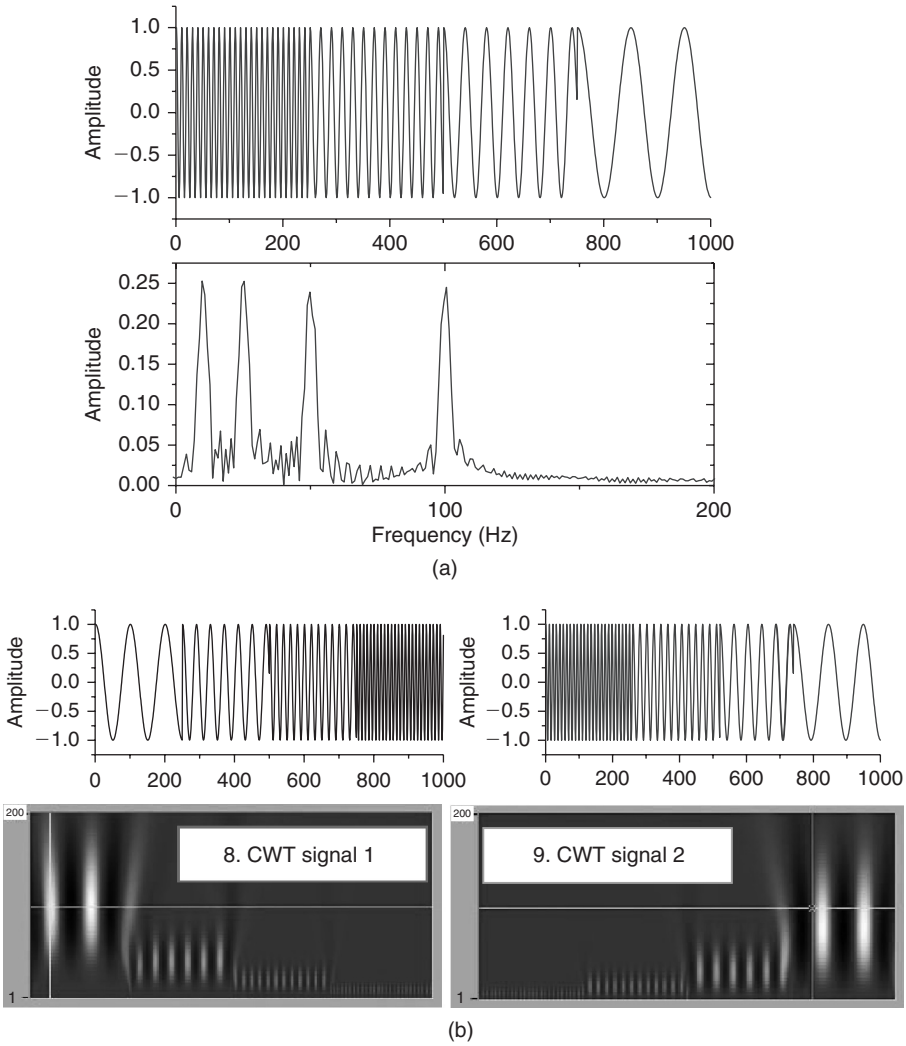



Figure 6: (a) Sine waves with Fourier transform and (b) wavelet transformation.

continuous wavelet transform is applied and after cutting off the noise the signal is transformed back to time domain using an inverse wavelet transform.

Fig. 7 is an example of a denoised AE signal. The upper signal is the original one with much noise and a low superimposed signal.

### 3.4 Autoregressive AIC-picker

Acoustic emissions and seismograms have many similarities, however, there also exist several differences which do not allow the application of exactly the

© 2008 Taylor & Francis Group, London, UK

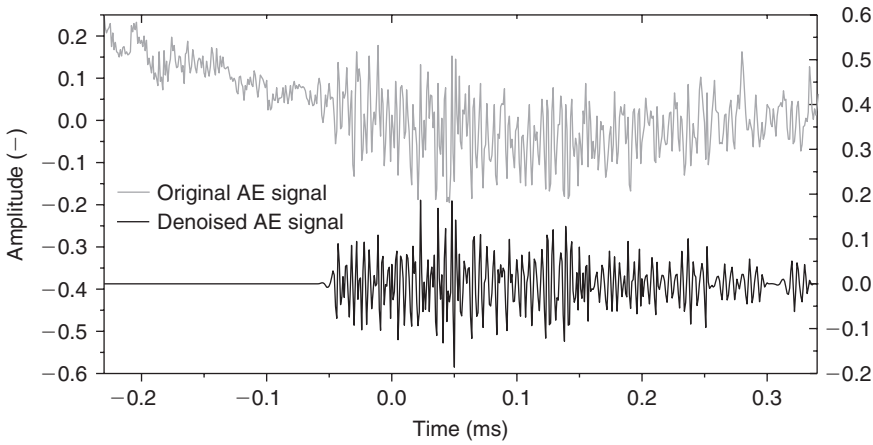



Figure 7: Original signal (above) and denoised signal (below) [11].

same picking algorithms in both fields. Concerning seismic events for instance, signal and noise are usually located in different frequency ranges. Therefore, we present an adapted automatic picker based on the AIC (Akaike Information Criterion) [35, 36]. It produces reliable results for acoustic emissions and for ultrasound signals with a relative high success rate. The problem concerning acoustic emissions and ultrasound signals in concrete is that signal and noise are often in the same frequency range. Furthermore, due to failure processes in the tested specimen, the signal to noise ratio of acoustic emissions is generally not constant during an experiment. Zang et al. [15] successfully applied an automatic onset determination algorithm similar to the STA/LTA picker to acoustic emissions from rock samples. However, acoustic emissions from rock samples are mostly to be found in a higher frequency range than acoustic emissions from concrete. Fig. 8 shows two examples of signals of concrete of one test with a different signal to noise ratio. The use of anti-causal, zero phase filters or the careful use of the wavelet transform can help to improve the signal to noise ratio. Nevertheless, a reliable automatic picker which can handle data of varying quality is needed.

An autoregressive AIC-picker gives picks (picks means determined onset times) of higher quality if the AIC is only applied to a part of the signal which contains the onset, of course [16]. Therefore, the onset is prearranged by using the complex wavelet transform or the Hilbert transform. Both transforms lead to a certain envelope of the signal (Fig. 9).

The Hilbert transform $\overline{R}(t)$ of a real time dependent function $R(t)$ is defined as [17]:

$$\overline{R}(t) = \frac{1}{\pi} \int_{-\infty}^{\infty} \frac{R(u)}{t-u} \mathrm{d}u = \mathscr{H}\{R(t)\} \tag{5}$$

© 2008 Taylor & Francis Group, London, UK

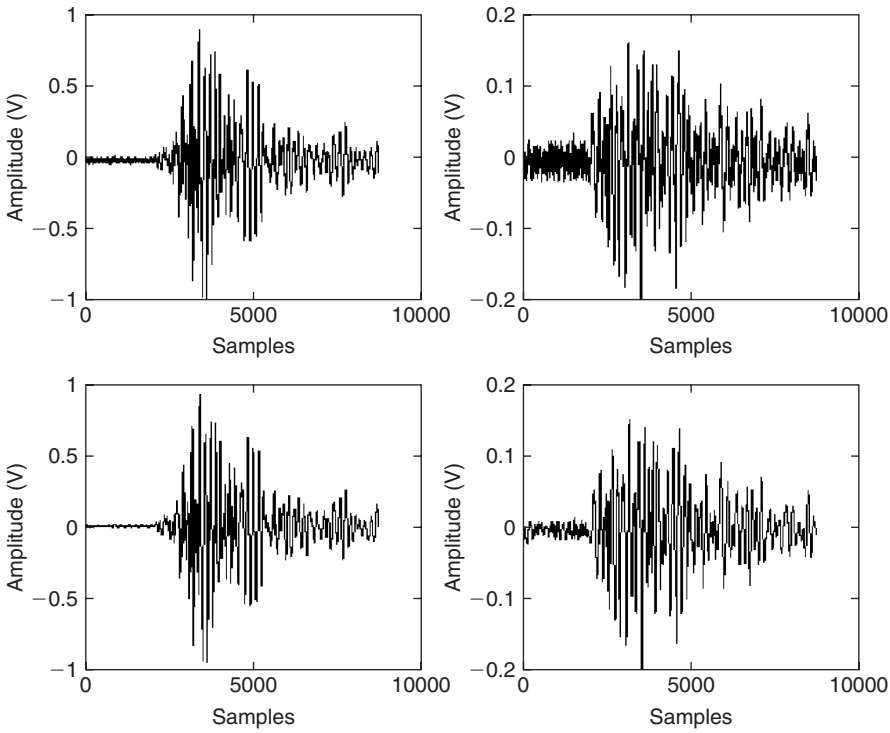



Figure 8: Raw acoustic emissions (top) and bandpass filtered acoustic emissions (bottom) from one test with a different signal to noise ratio. The bandpass filter was an anti-causal zero phase butterworth filter (3 kHz, 110 kHz) [37].

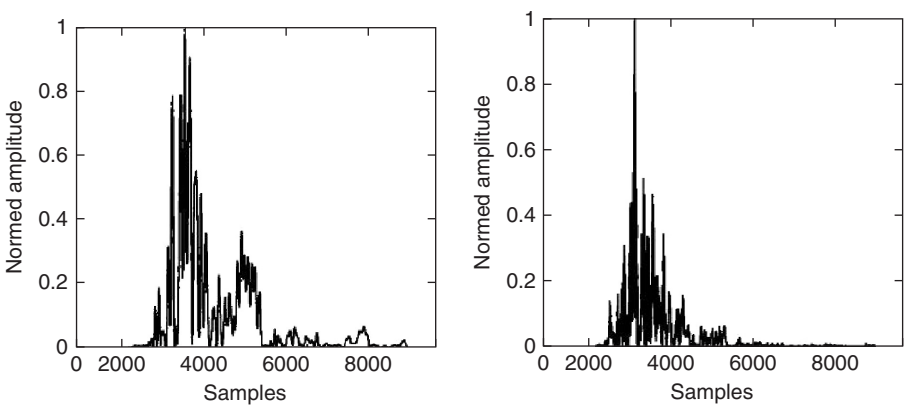



Figure 9: Envelope of the signal shown in Fig. 8 (bottom left) calculated by the Hilbert transform (left) and envelope of the signal shown in Fig. 8 (bottom left) calculated by the complex continuous wavelet transform (right) [37].

© 2008 Taylor & Francis Group, London, UK

where $t$ denotes the time and the singularity at $u = t$ is handled by taking the Cauchy principle value of the integral. The Hilbert transform is represented by a convolution integral, i.e. the Hilbert transform is a causal transfer function which behaves like a filter. Transforming a time series by the Hilbert transform, a phase shift of $\pi/2$ is generated. Thus, the envelope time function $E(t)$ can be calculated [17]:

$$E(t) = \sqrt{R(t)^2 + \overline{R}(t)^2} \tag{6}$$

The complex continuous wavelet transform $W$ of a discrete sequence $R(t)$ is defined as the convolution of $R(t)$ with a scaled and translated version of the wavelet function $\psi_{\lambda,\nu}$ [18]:

$$W(\lambda, \nu) = \int_{-\infty}^{\infty} \psi_{\lambda,\nu}(t)\, R(t)\, \mathrm{d}t, \quad \text{where } \psi_{\lambda,\nu}(t) = \frac{1}{\sqrt{\lambda}} \left( \frac{t - \nu}{\lambda} \right) \tag{7}$$

Continuous wavelet transform means continuously shifting a continuously scalable function $\psi_{\lambda,\nu}$ over the signal and calculating the correlation between the two. Thus, $\lambda$ denotes the scale (scale is proportional to frequency) and $\nu$ the translation. The discrete sequence $R(t)$ is decomposed into a set of basis functions with the new dimensions $\lambda$ and $\nu$.

Since the complex continuous wavelet transform is a complex valued orthonormal transform represented by a convolution integral, the modulus of one scale of the complex continuous wavelet transform represents the envelope of an signal at one certain frequency:

$$|W(\lambda, \nu)| = \sqrt{x^2 + y^2} \quad \text{where } W(\lambda, \nu) = x + \mathrm{i}y \tag{8}$$

The envelope is then used for prearranging the onset by a simple threshold. Each envelope is squared and normed, that a constant threshold value can be applied to all signals. A window of several hundred samples e.g. 400 before and 150 after this point is then cut off the signal. Within this signal the onset is determined exactly using the AIC.

The advantage of the envelope calculated by the wavelet transform is that even for noisy signals the prearrangement of the onset by a threshold works steady. The envelope is calculated only for one scale while most of the noise of the signals is found in different scales. However, if two or more signals of different amplitude and frequency superpose each other, i.e. if acoustic emissions occur in a very fast succession that more than one signal is recorded within the normal blocklength, the envelope calculated by the Hilbert transform should be used. Due to the automatic scaling, the wavelet transform can take the wrong signal

© 2008 Taylor & Francis Group, London, UK

for such a case. The exact onset is determined by calculating the AIC function direct from the signal according to Maeda [19]:

$$\begin{aligned}\mathrm{AIC}(t_w) = t_w \cdot \log(\mathrm{var}(R_w(t_w, 1))) + (T_w - t_w - 1) \\ \cdot \log(\mathrm{var}(R_w(1 + t_w, T_w)))\end{aligned} \tag{9}$$

The index $w$ e.g. from $R_w$ denotes that not the whole time series is taken but only the chosen window containing the onset (described above). $T_w$ is the last sample of the curtate time series, $t_w$ ranges through all samples of $R_w$ and var denotes the variance function. The term $R_w(t_w,1)$ means that the variance function is only calculated from the current value of $t_w$ while $R_w(1 + t_w, T_w)$ means that all samples ranging from $1 + t_w$ to $T_w$ are taken. The sample variance var or is $\sigma^2_{N-1}$ defined as [20]:

$$\sigma^2_{N-1} = \frac{1}{N-1}\sum_{i=1}^{N}(R_i - \overline{R})^2 \tag{10}$$

$N$ denotes the length of the signal, $R_i$ is sample $i$ of the time series $R$ and $\overline{R}$ is the mean value of the whole time series $R$. The global minimum of the AIC function defines the onset point of the signal (Fig. 10).

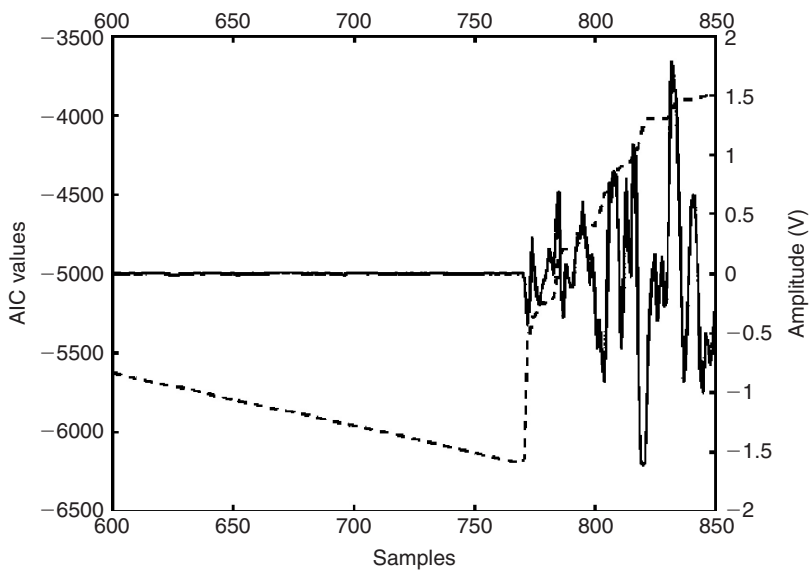



Figure 10: The AIC is used for onset determination only for the selected part of the signal containing the onset which is displayed by the solid line. The minimum of the AIC function which is represented by the dashed line denotes the onset time of the signal [37].

© 2008 Taylor & Francis Group, London, UK

## 4 EXAMPLES OF LOCALIZATION

### 4.1 Splitting test

For the localization of an acoustic emission with the focal coordinates $x_0$ and $t_0$, the positions $x_{Sn}$ of the sensors, the accurate onsets of the P-waves $t_{Sn}$ and the P-wave velocity $v_P$ must be determined to solve a linear system of equations based on

$$v_P(t_{Sn} - t_0) - (x_{Sn} - x_0) = 0 \tag{11}$$

Since the system of equations is overdetermined when data from eight sensors is available, the travel time residuals are minimized with the method of least squares. This leads to improved accuracy and yields error bounds for the estimated focal coordinates. From the 1800 acoustic emissions registered during the splitting test, the onset times of the first 900 events were picked with the WinPecker© software [21]. From these events, 378 could be localized with an accuracy better than 5 mm. In Fig. 11 results of the localization are illustrated.

The events are projected onto the main coordinate planes revealing a view from above, from the front and the right side of the specimen. The brightness of the data points provides information about the time when the events occurred. Light gray represents events from the beginning of the test, dark gray represents events from an advanced stage. The last localized event occurred at 4246 seconds after the start of loading.

The acoustic emissions are located along a well-defined zone of failure parallel to the steel edges applying compressive load. Local damage at the point of load application was minimized through the use of felt strips which evenly spread the applied compressive load. Consequently, only a small number of acoustic emissions were visible in the region where load was applied. It is possible,

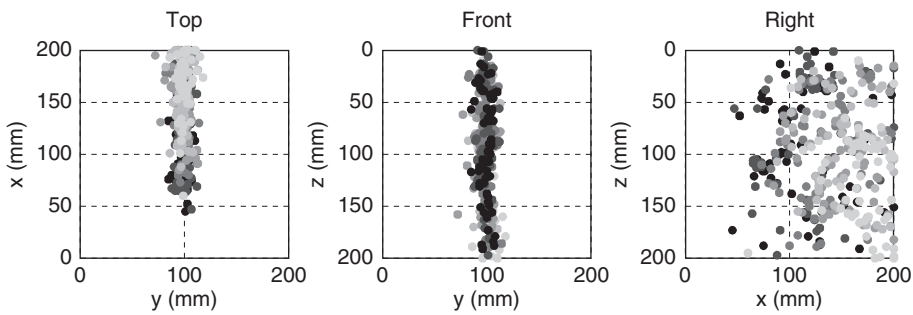



Figure 11: Projections of the localization of acoustic emissions onto the x/y, y/z and x/z planes. Events marked in light gray occurred at the beginning of the test, dark ones at an advanced stage of loading.

© 2008 Taylor & Francis Group, London, UK

however, that some of the acoustic emissions from this regions were ignored by the localization process due to a weak signal to noise ratio.

Considering the brightness of the data points, the growth of the crack from the back to the front is clearly visible. Even at an advanced stage of the test, where the crack front had progressed through the specimen, acoustic emissions occurred at the back side of the specimen, where the crack was already open. This can be explained by either an increasing accretion of micro cracks or a rubbing of the crack surfaces.

## 4.2 Pull-out test

The second test was a pull-out experiment. A detailed description of the failure analysis of pull-out experiments using acoustic emissions can be found in Köppel and Grosse [22]. A principle sketch of the specimen is shown in Fig. 12.

This was one test from a series of pull-out experiments which were conducted to study the bond between different steel bar reinforcements and concrete. At this stage, acoustic emission analysis is very helpful to investigate the debonding of steel in concrete and to survey the fracture initiation. From this experiment 44 events from the center region of the specimen, situated around the steel bar, were chosen for a comparative investigation. Since the chosen events occurred at different periods of the test, the chosen events are of varying signal to noise ratio. These 44 events were picked manually as well as automatically using the Hinkley-picker, the AIC-picker and a threshold-picker. The onset times were then used for a 3-dimensional localisation after Geiger [23]. The sound velocity was determined in preliminary ultrasound tests and was found to be isotropic for the whole specimen.

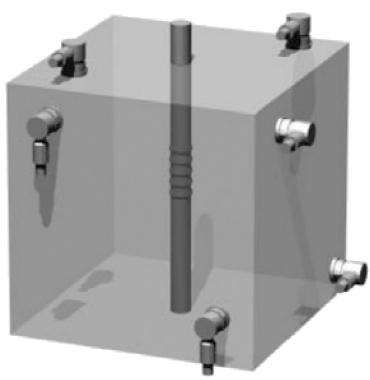


Figure 12: Principle sketch of a pull-out experiment. The steel bar was pulled out downwards. The acoustic emissions were recorded with the transducers mounted on the surface of the specimen [37].

© 2008 Taylor & Francis Group, London, UK

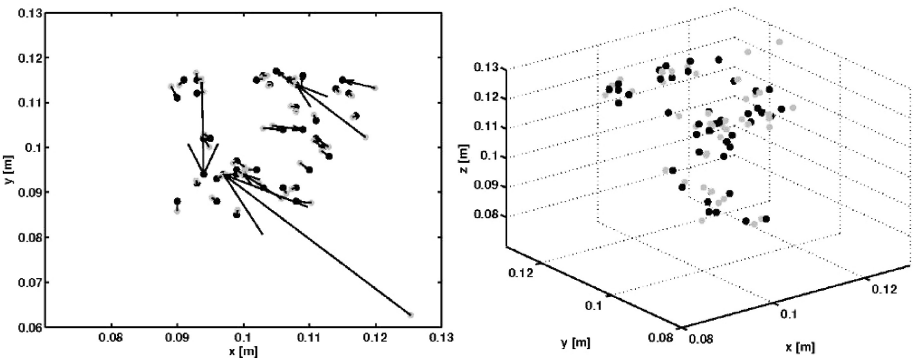



Figure 13: Comparison of the localisation results gained with the onset times (as reference values) determined manually (black) to the results gained with the onset times determined automatically by the AIC-picker (grey). On the left side only the x–y projection of the results is shown including mislocation vectors pointing from each automatic picked event to the corresponding manually picked event. The right hand side shows a 3-dimensional plot of the results [37].

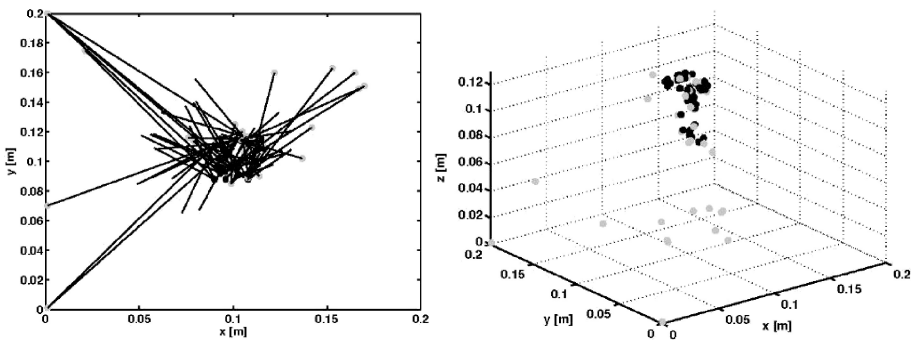



Figure 14: Comparison of the localisation results gained with the onset times (as reference values) determined manually (black) to the results gained with the onset times determined automatically by the Hinkley-picker (grey). On the left side only the x–y projection of the results is shown, including mislocation vectors pointing from each automatic picked event to the corresponding manually picked event. The right hand side shows a 3-dimensional plot of the results. Note the different scale of the graphs compared to Fig. 13 [37].

The localised events gained with the onset times of the AIC-picker are all situated close to the events localised with the onset times determined manually (Fig. 13).

The events localised with the results from the Hinkley-picker are not all located in close proximity to the manually picked events (Fig. 14).

© 2008 Taylor & Francis Group, London, UK

Table 1: Percentage of events with a deviation greater than 5 mm of each coordinate axis from the locations determined manually.

| Coordinate axis | AIC (%) | STA/LTA (%) | Hinkley (%) | Threshold (%) |
|---|---|---|---|---|
| $x$ | 9 | 27 | 59 | 64 |
| $y$ | 9 | 23 | 64 | 70 |
| $z$ | 11 | 30 | 68 | 73 |

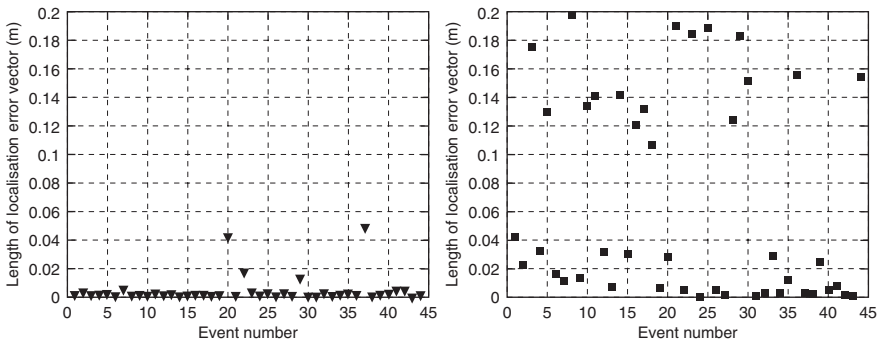



Figure 15: Length of the mislocation vectors of the comparison AIC-picker vs. manual picks (triangles, left side) and of the comparison Hinkley-picker vs. manual picks (squares, right side) [37].

Several events were localised on the side faces of the specimen. Therefore, the scaling of the graphs in Figs. 14 and 13 is different. The different results gained by the AIC-picker and the Hinkley-picker are also expressed through the mislocation vectors drawn from each automatic picked event to the corresponding manually picked event in Fig. 13 (left) and Fig. 14 (left). Furthermore, in Table 1 the deviation of all events localised with the onset times determined by the three auto-pickers as well as all events localised with the onset times determined manually is summarized. The order of the pickers in Table 1 represents their accuracy. The deviation of the locations created by the two auto-pickers from the locations created by manual picks is also shown in Fig. 15 which represents the length of the mislocation vectors.

## 5 FRACTURE MODES

Fundamental differences seem to exist between the application of source models (Fig. 16, top) to the two scientific disciplines *Seismology* and *Material Science*. The classical model used to interpret earthquake data is a shear crack without a moment along a planar rupture surface. This fracture model is sufficient to explain most earthquake mechanisms. However, this simple model of a

© 2008 Taylor & Francis Group, London, UK

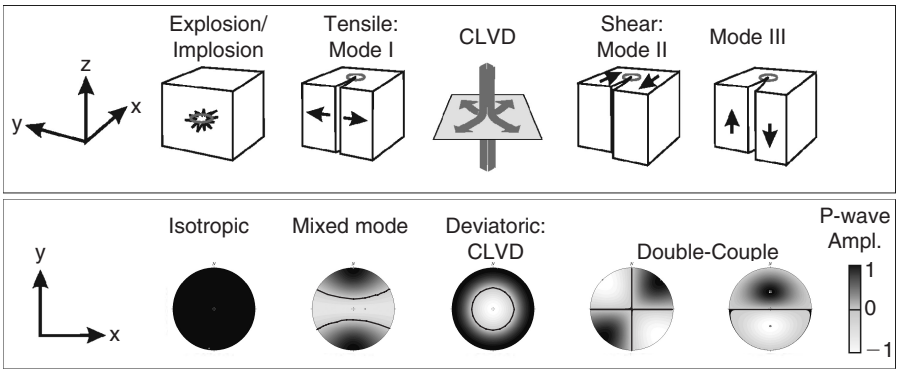



Figure 16: Various basic fracture mechanisms with appropriate radiation patterns of seismic amplitudes in a stereographic projection. CLVD = compensated linear vector dipole.

shear crack cannot describe more complex rupture phenomena, where opening of a crack and dilatational (or isotropic) components are present. The experimental work described in the following was done to study these effects more quantitatively.

For *mode 1* cracks, the incident particle motion is radial outwards, similar to an explosion. In the ideal (explosion) case the energy distribution is equal in all directions and the radiation pattern is not identical to that of a cleavage crack [25]. The collapse of a pore could be explained using an explosion model with negative sign, which means incident particle motion towards the hypocenter.

*Mode 2* and *mode 3* both are shear cracks with a progress of the tip of the crack parallel or perpendicular to the movement of sliding blocks, respectively. For *mode 2*, the rupture plane would be in the $x$-direction with the rear block moving to the right, which means an outwards particle motion on the right and inwards on the left. In material science most cracks cannot be described using only one of these fundamental mode types. Mixtures of the three mentioned models and other phenomena are necessary to explain the whole failure process.

## 6 MOMENT TENSOR INVERSION

Depending on material properties and the stress regime a variety of different and sometimes complex fracture mechanisms can occur. Usually, these can be explained by a combination of basic fracture models. Each basic model is characterized by a specific radiation pattern of seismic energy, which can be registered by suitable sensors. In Fig. 16 some basic fracture models are illustrated (upper row).

The relative motion in the damage zone is marked by an arrow. In the lower row the appropriate radiation patterns to the upper models are given. These plots are stereographic projections (Schmidt net, [26]) of the compressive wave onset

© 2008 Taylor & Francis Group, London, UK

amplitudes on a hemisphere around the source or tip of a crack viewed from above. The coordinate systems for these images are on the far left. Black represents positive amplitudes, white represents negative amplitudes. The zone with zero amplitude is marked by a black line. The first model is an ideal explosion, where the particle motion is outwards from the center, revealing positive onset amplitudes in all spatial directions. Negative amplitudes would describe an implosion. This model is pure isotropic and can be explained by a change of volume. The second model is a tensile crack (mode I). In the example, the mean principal tensile stress is parallel to the $y$-axis. Depending on the material properties little or no energy will be released parallel to $x$ and $z$. As long as there is a change in volume, isotropic and deviatoric components are inherent in this source type. Knopoff and Randall [27] suggested the compensated linear vector dipole (CLVD) as a possible component of deep earthquakes arising from mineralogical aspects. Its geometry is similar to that of the tensile crack, but usually with a compressive mean principal stress and tensile stresses in the two perpendicular directions, which leads to a zero isotropic component. The two models of a shear crack on the right are pure deviatoric sources as well. In the case of mode II, crack growth is parallel to the offset. Mode III is characterized by a crack growth perpendicular to the offset. A common physical model for these two source types is the seismological model of the double couple [28]. The majority of earthquakes can be described with this model. The radiation patterns of the double couple show an ambiguity. Two black lines mark the orientation of the two nodal planes. Which of these nodal planes is the active crack surface can not be resolved from the radiation pattern alone. Additional information from other investigations is needed for this purpose. A direct interpretation of the wave field is often complicated. As mentioned above, fracturing is usually more complex and has to be represented by a combination of different fracture models. Furthermore, material inhomogeneities and geometrical irregularities as well as technical aspects (e.g. sensitivity and coupling of the sensors) affect wave propagation and the registered amplitudes. Seismologists first estimated simple focal plane solutions for tectonic earthquakes from the polarities of the waves. The need for a better physical description of fracturing came with further investigations of fracture processes within the earth's crust and worldwide monitoring of nuclear tests.

A general elastodynamic source within a volume $V$ can be represented by a sum of single forces $f_k$ dependent on location $r$ and time $\bar{t}$. The observed displacement $u$ at a sensor position $x$ and time $t$ is then calculated from the integral of the source time function and the Greens's functions $G_k$ [28]:

$$u(x,t) = \int_{-\infty}^{\infty} \int_{V} G_k(x,t;r,\bar{t}) f_k(r,\bar{t})\, dV(r)\, d\bar{t} \tag{12}$$

The Green's functions represent all transfer functions of the medium and describe the propagation effects on elastic waves. The spatial integration in Eq. 12 is

© 2008 Taylor & Francis Group, London, UK

simplified on the assumption of only smooth variations of the Green's functions within the source region. Then, they can be expanded into a Taylor series around a reference point, the so called centroid $r = \xi$.

The physical source region is characterized by a set of equivalent forces. These forces arise due to differences between the model stress and the actual physical stress (stress glut). Using a temporal convolution of the Taylor expansion of the Green's functions and the introduction of the time dependent moment tensor, Eq. 12 can be expressed in the form [29]:

$$u(x,t) = \sum_{m=1}^{\infty} \frac{1}{m!} G_{k,j_1,\ldots j_m}(x,t;\xi,\bar{t}) \cdot M_{k,j_1,\ldots j_m}(\xi\bar{t}). \tag{13}$$

When the source volume is small compared to the distance between source and receiver and the duration of the source pulse is small compared to the period of the detected waveforms, the source can be depicted as a point source and the moment tensor is time invariant. Furthermore, external forces are neglected. The displacement field $u$ of an arbitrary source is then given as the convolution of the moment tensor $M$ with the Green's functions $G$

$$u = G \cdot M \tag{14}$$

The inverse problem

$$M^{calc} = G^{-1} \cdot u^{obs} \tag{15}$$

is the moment tensor inversion, where $M^{calc}$ is the calculated moment tensor from a convolution of the observed displacement data $u^{obs}$ and the inverse Green's functions (e.g. [28, 30]). Various methods for an inversion on the moment tensor are in use. Absolute inversion can be performed on single events, but require detailed knowledge of the Green's functions. Relative methods with or without a reference mechanism are applied on clusters of events where the Green's functions can be neglected by the assumption of common ray paths [31]. Problems occur when the signal to noise ratio is poor or the events within one cluster have similar mechanisms, which is often the case in acoustic emission analysis. Andersen [32] introduced a new approach, the hybrid moment tensor inversion, as a combination of the previous methods, where the effects of noise, low quality data, site effects, etc. are minimized and the solutions become more robust. The method is based on an iterative weighting scheme using the median of the distribution of residuals (for a particular geophone site, channel and wave phase), calculated using all events in the cluster.

The symmetric moment tensor $M = M_{ij}$ is a system of nine equivalent moments representing a source and is defined by six independent elements. The physical meaning of the tensor elements can be depicted by dipoles oriented parallel to the

© 2008 Taylor & Francis Group, London, UK

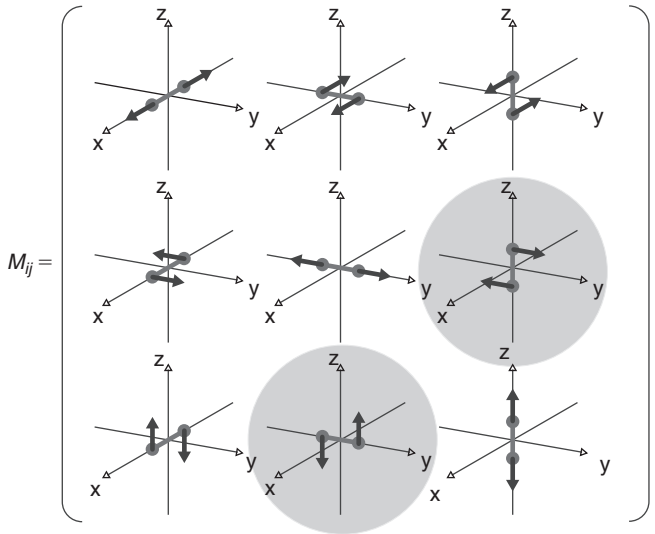



Figure 17: Schematic diagram of the moment tensor elements.

three coordinate axes and forces acting on the dipoles along the three coordinate axes (see Fig. 17).

The elements on the diagonal of the tensor define tension or compression and the trace of $M$ represents the isotropic component of the source. The symmetry of the matrix leads to three pairs of double couples (one pair is highlighted in Fig. 17) which sum to a zero net torsional moment. The concept of the moment tensor is very well-suited to describe even complex fracture mechanisms, as long as they can be approximated by a point source (e.g. [28, 33]). For a visualization of the results the P-wave radiation pattern in the far field of a source for a given, time invariant moment tensor can be calculated after [34]:

$$u_P = \frac{1}{4\pi\,\rho\upsilon_p^3}\frac{R}{R}(\gamma_i M_{ij}\gamma_j). \tag{16}$$

This calculation is similar to Eq. 14. The simplified Green's function contains the density $\rho$ and the P-wave velocity $v_P$. Geometrical spreading is realized by the term $1/R$. The second term accounts for the convolution of the time invariant moment tensor and the direction cosines $\gamma$. For the radiation pattern plots, the amplitudes are calculated for a sphere with constant radius. The Green's term can be neglected for an isotropic medium, since the radiation pattern is normalized to a maximum amplitude equal to 1.

The decomposition of the moment tensor into different sets of basic mechanisms and the interpretation is performed on the basis of an eigenvalue analysis:

$$M = AmA^T \tag{17}$$

© 2008 Taylor & Francis Group, London, UK

$m$ is the diagonalized moment tensor matrix containing the eigenvalues of $M$ and $A$ is the matrix of the corresponding eigenvectors, which denote the direction of the principal axes of the stress field. First, the moment tensor is decomposed into an isotropic and a deviatoric part:

$$m = m^{ISO} + m^{DEV}, \tag{18}$$

where the isotropic component is defined by

$$m^{ISO} = \begin{bmatrix} trace(m)/3 & 0 & 0 \\ 0 & trace(m)/3 & 0 \\ 0 & 0 & trace(m)/3 \end{bmatrix} \tag{19}$$

and the diagonalized deviatoric moment tensor can be calculated with:

$$m^{DEV} = m - m^{ISO}. \tag{20}$$

Assuming that the same principal stresses produce the radiation of the double couple and the CLVD, the most common decomposition of the deviatoric diagonalized moment tensor into a double couple and a CLVD can be performed [29]:

$$\begin{aligned} m^{DEV} &= m^{DC} + m^{CLVD} \\ &= \widetilde{m}_3(1-2F)\begin{bmatrix} 0 & 0 & 0 \\ 0 & -1 & 0 \\ 0 & 0 & 1 \end{bmatrix} + \widetilde{m}_3 F \begin{bmatrix} -1 & 0 & 0 \\ 0 & -1 & 0 \\ 0 & 0 & 2 \end{bmatrix} \end{aligned} \tag{21}$$

The deviatoric eigenvalues $\widetilde{m}_i$ are the elements of the deviatoric diagonalized moment tensor with $\left|\widetilde{m}_3\right| > \left|\widetilde{m}_2\right| > \left|\widetilde{m}_1\right|$ *and* $F = -\widetilde{m}_1/\widetilde{m}_3$.

The energy of the three components can as well be expressed in their relative percentile portions of the scalar moment of the event. Since the sensors used for our studies are not calibrated, the scalar moment is not an absolute measure. According to the procedure of decomposing the moment tensor, the sum of the three percentile portions is not 100%. A negative change of volume leads to negative values for % ISO. The deviatoric component is divided into a double couple and a CLVD portion, which sum to 100%.

## 7 EXAMPLE OF MODE DETERMINATION

Two clusters containing 5 and 9 events, respectively, were selected from the localized events in Fig. 11. Since the Green's functions, representing the transfer

© 2008 Taylor & Francis Group, London, UK

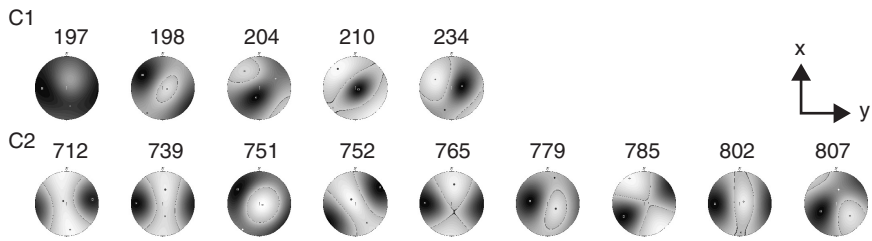



Figure 18: Radiation patterns of all moment tensors from clusters C1 and C2.

Table 2: Decomposition of the moment tensor solutions into isotropic, double couple and CLVD portions (in %).

| | evt ID | % ISO | % DC | % CLVD | |
|---|---|---|---|---|---|
| C1 | 197 | 47.07 | 61.97 | 38.03 | |
| | 198 | 41.10 | 95.17 | 4.83 | * |
| | 204 | 3.52 | 35.08 | 64.92 | |
| | 210 | −7.09 | 82.72 | 17.28 | |
| | 234 | 0.01 | 65.40 | 34.60 | |
| C2 | 712 | 0.84 | 75.69 | 24.31 | |
| | 739 | 6.00 | 86.92 | 13.08 | |
| | 751 | 13.71 | 71.28 | 28.72 | |
| | 752 | 7.88 | 90.63 | 9.37 | |
| | 765 | 3.75 | 75.99 | 24.01 | * |
| | 779 | 36.77 | 9.93 | 90.07 | * |
| | 785 | 0.50 | 46.30 | 53.70 | * |
| | 802 | 23.14 | 83.27 | 16.73 | |
| | 807 | 10.87 | 84.61 | 15.39 | |

functions of the medium are eliminated in the relative moment tensor inversion, the radii of these clusters have to be small enough and the events should originate in a relatively short temporal interval. Low frequency noise from the data was minimized by a suitable wavelet filter algorithm. The transient raw data, representing velocity over time, were then integrated to reveal the displacement. The first halfwave amplitudes of the longitudinal P-waves were picked from the data for input. An overview of the results of the moment tensor inversion is presented in the form of the radiation patterns in stereographic projections (Fig. 18). Furthermore, the decomposition of the moment tensors is revealing the percentile contributions of isotropic, double couple and CLVD mechanisms (Table 2). All events in cluster C2 show a similar behavior, with tension (dark) more or less parallel to the $y$-axis. A small compressive component almost parallel to the $z$-axis is indicated by negative amplitudes (light colored).

© 2008 Taylor & Francis Group, London, UK

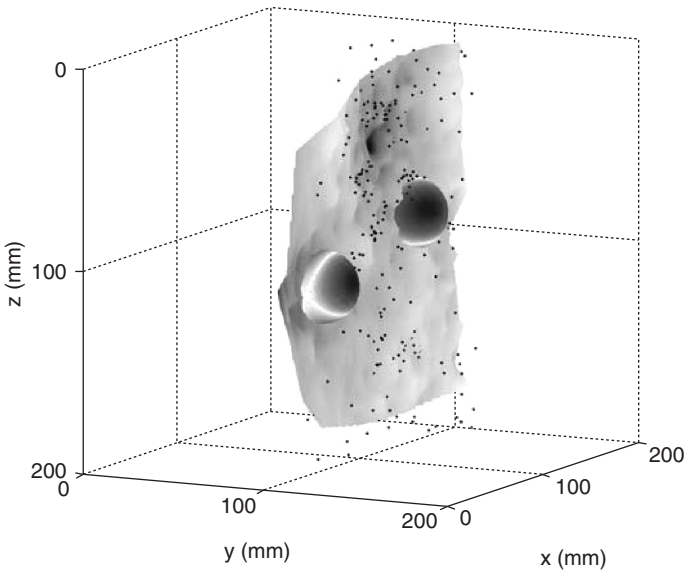



Figure 19: The topography of the crack surface and the radiation patterns of selected events from the two clusters. The radiation patterns were evaluated from the moment tensor solutions inverted with the hybrid method. Both radiation patterns reveal positive (red) amplitudes parallel to the mean tensile stress and some negative (blue) amplitudes parallel to the z-axis due to compressive stress.

The decomposition yields significant positive isotropic components and a mixture of double couple and CLVD mechanisms. The solutions for cluster C1 are not that consistent. The directions of positive amplitudes due to tensile stress vary more around the *y*-axis than in C2. The decomposition shows similar results as in cluster C1. Event 210 has a negative isotropic component, which could be explained by a pore collapse in combination with shear. The results corroborate the assumption of mode I failure with a major tensile crack parallel to the steel edges from which load was applied. The mean tensile stress axis is parallel to the *y*-axis, which is also the preferred direction of positive amplitudes. Since the solutions of the moment tensor inversion showed a similar behavior for most of the events, two examples were selected for a comprehensive, 3D presentation of all results (Fig. 19).

The radiation patterns are projected onto a sphere around the source. Positive amplitudes plotted in dark red colors are parallel to the mean tensile stress. A small compressive component parallel to the *z*-axis is indicated by negative amplitudes in light blue. Additionally, in this figure the surface of the digitized crack and the localized acoustic emissions (black dots) are plotted. To highlight the undulations of the crack surface around aggregates, the *y*coordinates of the crack surface are shaded in tones of grey. This 3-dimensional visualization of a damage zone, evaluated from a digitization of the visible crack, the localization

© 2008 Taylor & Francis Group, London, UK

of acoustic emissions and fracture investigations is a new approach as far as the authors are aware. The result can be observed from any arbitrary direction. This is an improvement compared to 2-dimensional, stereographic plots of the radiation patterns, which allow only a view from one direction.

## 8 OUTLOOK

The inspection of building structures is currently made by visual inspection or by wired sensor techniques, which are relatively expensive, vulnerable to damage, and time consuming to install. Wireless sensor networks instead are easy to deploy and flexible to adjust to the individual structure. Different types of sensing techniques can be used along with such a network, but acoustic emission techniques are a promising additional monitoring method to investigate the status of a bridge or some of its components. It has the potential to detect defects in terms of cracks propagating during the routine use of structures indicating a future failure.

However, acoustic emissions recording and analysis techniques need powerful algorithms to handle and reduce the immense amount of data generated. These algorithms are developed using a new concept called Acoustic Emission Array Processing.

## REMARK

This workshop contribution is mainly based on [37–41].

## References

[1] C. Ouyang, E. Landis, S.P. Shah, "Damage Assessment in Concrete using Quantitative AE," J. Engineering Mechanics, Vol. 117, No. 11, ASCE, 1991, 2681–2698.

[2] C.U. Grosse, H.W. Reinhardt, T. Dahm, Localization and classification of fracture types in concrete with quantitative acoustic emission measurement techniques. NDT&E Int. 1997; 30: 223–230.

[3] C.U. Grosse, H.W. Reinhardt, F. Finck, Signal-based acoustic emission techniques in civil engineering. J. of Mat. Civ. Eng. 2003; 15(3): 274–279.

[4] J.M. Berthelot, J.L. Robert, Modeling concrete damage by acoustic emission. J. of Ac. Emission 1987; 6 (1): 43–60.

[5] J.F. Labuz, H.S. Chang, C.H. Dowding, S.P. Shah, Parametric study of AE location using only four sensors. Rock mechanics and rock engineering 1988; 21: 139–148.

[6] C.U. Grosse, H.W. Reinhardt, Entwicklung eines Algorithmus zur automatischen Lokalisierung von Schallemissionsquellen. Die Materialprüfung 1999; 41: 342–347.

© 2008 Taylor & Francis Group, London, UK

[7] S. Köppel, C.U. Grosse, Advanced acoustic emission techniques for failure analysis in concrete. Proc. of 15.World Conf. on Non-Destructive Testing (WCNDT), Rome, 2000, on CD-ROM, <http://www.ndt.net/article/wcndt00/papers/idn231/idn231.htm>.
[8] A. Trnkoczy, Understanding and parameter settings of STA/LTA trigger algorithm, in: P. Bormann (Ed.), IASPEI New Manual of Seismological Observatory Practice, vol. 2, GeoForschungsZentrum Potsdam, Ch. IS 8.1, 2002, pp. 1–19.
[9] M. Baer, U. Kradolfer, An automatic phase picker for local and teleseismic events, Bulletin of the Seismological Society of America 77 (1987) 1437–1445.
[10] P. Earle, P. Shearer, Characterization of global seismograms using an automatic picking algorithm, Bulletin of the Seismological Society of America 84 (2) (1994) 366–376.
[11] C.U. Grosse, M. Motz, H.W. Reinhardt, H. Kröplin, Signal conditioning in acoustic emission analysis using wavelets. In: NDT.net 7 (2002), Nr. 9. –URL http://ndt.net/article/v07n09/09/09.htm.
[12] G. Kaiser, A friendly guide to wavelets. Birkhäuser 1994, 300 pp.
[13] C.U. Grosse, M. Ohtsu (Eds.), Basics and Applications of Acoustic Emission Testing in Civil Engineering. Springer, Heidelberg 2007, 420 pp (in preparation).
[14] C.U. Grosse, H.J. Ruck, G. Bahr, Analyse von Schallemissionssignalen unter Verwendung der Wavelet-Transformation. DGZfP Berichtsband No. 78, 13. Kolloquium Schallemission, Jena. Berlin: DGZfP, 2001, pp 41–50.
[15] A. Zang, F. Wagner, S. Stanchits, G. Dresen, R. Andersen, M. Haidekker, Source analysis of acoustic emissions in Aue granite cores under symmetric and asymmetric compressive load, Geophysical Journal International 135 (1998) 1113–1130.
[16] H. Zhang, C. Thurber, C. Rowe, Automatic P-wave arrival detection and picking with multiscale wavelet analysis for singlecomponent recordings, Bulletin of the Seismological Society of America 93 (5) (2003) 1904–1912.
[17] B. Buttkus, Spektralanalyse und Filtertheorie in der Angewandten Geophysik, Springer Verlag, Berlin, Heidelberg, 1991.
[18] C. Torrence, G. Compo, A practical guide to wavelet analysis, Bulletin of the American Meteorological Society 79 (1) (1998) 61–78.
[19] N. Maeda, A method for reading and checking phase times in autoprocessing system of seismic wave data, Zisin = Jishin 38 (1985) 365–379.
[20] E. Kreyszig, Advanced Engineering Mathematics, seventh ed., John Wiley & Sons Inc., New York, USA, 1993.
[21] C.U. Grosse, 2000, "WinPecker – Programm zur vollautomatischen dreidimensionalen Lokalisierung von Schallemissionsquellen". In: *12. Kolloquium Schallemission, DGZfP Berichtsband 72, Jena*, pp. 191–204.

© 2008 Taylor & Francis Group, London, UK

[22] S. Köppel, C.U. Grosse, Advanced acoustic emission techniques for failure analysis in concrete, in: WCNDT Proceedings 2000, October 2000, Italian Society for Non-Destructive Testing and Monitoring Diagnostics.
[23] L. Geiger, Herdbestimmung bei Erdbeben aus den Ankunftszeiten, Nachrichten von der Königlichen Gesellschaft der Wissenschaften zu Göttingen 4 (1910) 331–349.
[24] F. Finck, M. Yamanouchi, H.W. Reinhardt, C.U. Grosse, Evaluation of mode I failure of concrete in a splitting test using acoustic emission technique. International J. of Fracture 2003; 124: 139–152.
[25] H.N.G. Wadley, C.B. Scruby, Elastic wave radiation from cleavage crack extension. Int. J. Frac. 1983; 23: 111–128.
[26] C.M.R. Fowler, 1990, "The Solid Earth – An Introduction to Global Geophysics". Cambridge University Press.
[27] L. Knopoff, M.J. Randall, 1970, "The Compensated Linear Vector Dipole: A Possible Mechanism for Deep Earthquakes". *Journal of Geophysical Research* **75/26**, 4957–4963.
[28] K. Aki, P.G. Richards, 2002, "Quantitative Seismology, Vol. 1". University Science Books, CA Sausalito, 2nd edition.
[29] M.L. Jost, R.B. Hermann, 1989, "A students guide to and review of moment tensors". *Seism. Res. Letters* **60**, 37–57.
[30] A. Ben-Menahem, S.J. Singh, 1981, "Seismic Waves and Sources". Springer-Verlag, New York.
[31] T. Dahm, 1993, "Relativmethoden zur Bestimmung der Abstrahlcharakteristik von seismischen Quellen". Ph.D. thesis, Universität Karlsruhe.
[32] L.M. Andersen, 2001, "A relative moment tensor inversion technique applied to seismicity induced by mining". Ph.D. thesis, University of the Witwatersrand, Johannesburg, South Africa.
[33] C.U. Grosse, 1999, "Grundlagen der Inversion des Momententensors zur Analyse von Schallemissionsquellen". In: Werkstoffe und Werkstoffprüfung im Bauwesen. Festschrift zum 60. Geburtstag von Prof. Dr.-Ing. H.-W. Reinhardt. pp. 82–105, Libri BOD, Hamburg.
[34] J. Pujol, R.B. Herrmann, 1990, "A student's guide to point sources in homogeneous media". *Seismological Research Letters* **61**(3–4), 209–224.
[35] H. Akaike, Markovian representation of stochastic processes and its application to the analysis of autoregressive moving average process, Annals of the Institute of Statistical Mathematics 26, (1974) 363–387.
[36] R. Allen, Automatic phase pickers: their present use and future prospects, Bulletin of the Seismological Society of America 72 (1982) 225–242.
[37] J.H. Kurz, C.U. Grosse, H.W. Reinhardt, Strategies for reliable automatic onset time picking of acoustic emissions and of ultrasound signals in concrete. Ultrasonics 43 (2005), pp 538–546.

© 2008 Taylor & Francis Group, London, UK

[38] C.U. Grosse, F. Finck, Quantitative evaluation of fracture processes in concrete using signal-based acoustic emission techniques. Cement & Concrete Composites 28 (2006), pp 330–336.
[39] C.U. Grosse, F. Finck, J.H. Kurz, H.W. Reinhardt, Improvements of AE technique using wavelet algorithms, coherence functions and automatic data analysis. Construction and Building Materials 18 (2004), pp 203–213.
[40] J.H. Kurz, Verifikation von Bruchprozessen bei gleichzeitiger Automatisierung der Schallemissionsanalyse an Stahl-und Stahlfaserbeton. Dissertation, University of Stuttgart, 2006.
[41] F. Finck, Untersuchung von Bruchprozessen in Beton mit Hilfe der Schallemissionsanalyse. Dissertation, University of Stuttgart, 2005.

© 2008 Taylor & Francis Group, London, UK

*Acoustic Emission and Critical Phenomena – Carpinteri & Lacidogna (eds)*
*© 2008 Taylor & Francis Group, London, ISBN 978-0-415-45082-9*

# SOURCE CHARACTERIZATION OF FRACTURE IN QUASI-BRITTLE MATERIALS

**C.S. Kao[1], F.C.S. Carvalho[1], G. Rosati[2], S. Cattaneo[2] and J.F. Labuz[1]**
[1]Department of Civil Engineering, University of Minnesota, USA
[2] Department of Structural Engineering, Politecnico di Milano, Italy

## ABSTRACT

A common feature of fracture propagation in quasi-brittle materials is the development of microcracking, which releases energy in the form of elastic waves called acoustic emission (AE). The AE technique can be used to monitor the evolution, including location and mechanism, of damage at various stages of loading. For an idealized point source of displacement discontinuity, the localized stress release from AE can be represented by dipoles of forces called the moment tensor. To determine the characteristics of the AE, a simplified transducer calibration is suggested, where constant values of the amplitude sensitivities were taken to capture the response up to the first peak associated with the P-wave arrival. Calibration breaks on at least three different points were performed to obtain an amplitude sensitivity for each transducer, owing to the dependency on the coupling between the transducer and specimen. Components of the displacement discontinuity were retrieved by minimizing the error between measured displacements obtained from the AE signal and the displacements calculated from the moment tensor at the source, subjected to restrictions on the form of displacement discontinuity and the moment tensor. A separable time dependency for all components of the moment tensor was assumed. A three-point-bend fracture test conducted on a typical quasi-brittle material and the AE data were analyzed with the source model. Even though most AE events were characterized as shear predominant, the displacement behavior associated with macroscopic crack opening was observed. This anomalous behavior can be explained by examining a torturosity angle, which is a measure of microcrack orientation on the horizontal plane.

## 1 INTRODUCTION

Fracture propagation in quasi-brittle materials such as concrete and rock is associated with the linking of microcracks, which produce microseismic events called

© 2008 Taylor & Francis Group, London, UK

acoustic emission (AE). These transient elastic waves carry information about the AE source, including the location and mechanism (magnitude and mode). In order to characterize the microcracking process in terms of microcrack displacement and orientation, the analyses involve several simplifying assumptions: (i) a point-source representation of displacement discontinuity, (ii) propagation of elastic waves in an isotropic medium, and (iii) known transducer response, which must be determined by calibration. Some quantitative methods to separate these three effects from the AE signal have been developed (Scruby et al. 1985; Ohtsu et al. 1998; Shah & Labuz 1995).

The source model of displacement discontinuities can be represented by force dipoles that form the so-called moment tensor (Burridge & Knopoff 1964; Rice 1980). A linearly elastic, isotropic medium is assumed, and the solution of the radiation problem entails the analytic Green's function for a buried impulse in an infinite space. Because the source is much smaller than the wavelength of an AE signal, it is usually considered that the radiation patterns, as well as elastic properties of material, do not change with accumulation of microcracks.

The calibration problem is more involved. The objective of transducer calibration is to establish a direct correlation between the mechanical disturbance taking place at its location and the corresponding voltage output. A convolution model can be used (Michaels et al. 1981; Shah & Labuz 1995), but the determination of the transducer response function is computationally-expensive, and for practical applications, it can be replaced by a scalar sensitivity parameter (Scruby et al. 1985; Ohtsu 1991; Carvalho & Labuz 2002). Once the response of the recording system is established, source parameters can be recovered by minimizing the error between measured displacements obtained from the AE signal at each transducer position and the theoretical displacements calculated from the moments (force dipoles) at the source. In this sense, transducer calibration becomes an essential part of the problem.

The calibration method in this research considers the simulation of a point-step force at a known position (Breckenridge et al. 1975). A point-step unloading on the surface is generated by breaking a thin-walled glass capillary (outer diameter approximately 0.15 mm). On the basis of laboratory data, a consistent approach to the simplified transducer calibration is proposed that could be used to elevate the quantitative analysis of AE signals.

A three-point-bend fracture test was performed on a quasi-brittle material (Charcoal granite) with controlled crack opening displacement (COD). A closed-loop, servo-hydraulic testing system was used to capture the global response and the AE technique was used to observe the crack propagation. Moment tensors of selected AE events were estimated according to the sensitivities of the transducers, and the source mechanisms (normal and shear displacements) and orientations were determined.

© 2008 Taylor & Francis Group, London, UK

## 2 REVIEW OF ELASTICITY SOLUTION

The calibration procedure of breaking a glass capillary involves the elastodynamic solution for a point-step force on a uniform elastic half-space, as represented in Fig. 1 (Pekeris 1955). A point-step force of magnitude $Z$ is applied to the surface of a uniform elastic half-space characterized by the shear modulus $\mu$, Poisson's ratio $\nu$, and mass density $\rho$. The normal and tangential displacements, $u_n(\tau)$ and $u_t(\tau)$, are calculated at a surface point located at distance $r$ from the source. The dimensionless time parameter, $\tau$, is used to describe the surface motion:

$$\tau = \frac{c_s t}{r} \tag{1}$$

where $c_s = \sqrt{\mu/\rho}$ is the shear wave velocity of the material, and $t$ denotes time. The surface displacements are expressed as

$$u_n(\tau) = \frac{\delta^2 Z}{\pi^2 \mu r} G(\tau), \quad u_t(\tau) = \frac{\delta^2 Z}{\pi^2 \mu r} R(\tau), \quad \delta^2 = \left(\frac{c_p}{c_s}\right)^2 = \frac{2-2\nu}{1-2\nu} \tag{2}$$

where $G(\tau)$ and $R(\tau)$ are given by Mooney (1974), and $\delta$ is the ratio between the compressional and shear wave velocities.

Only the expressions for $u_n(\tau)$, for an arbitrary value of $\nu$, are of interest in this study, as it is commonly assumed that the AE transducers respond to displacements normal to the material surface (Simmons et al. 1987). This assumption is related only to the transducer response and does not imply that the tangential component of the displacement is negligible compared to the normal component. In fact, in the case of a surface source, the tangential displacement component can be significant.

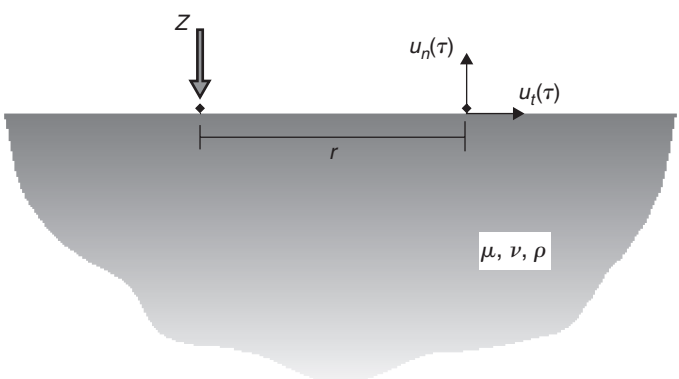



Figure 1: A point-step force Z at the surface of an elastic half-space.

© 2008 Taylor & Francis Group, London, UK

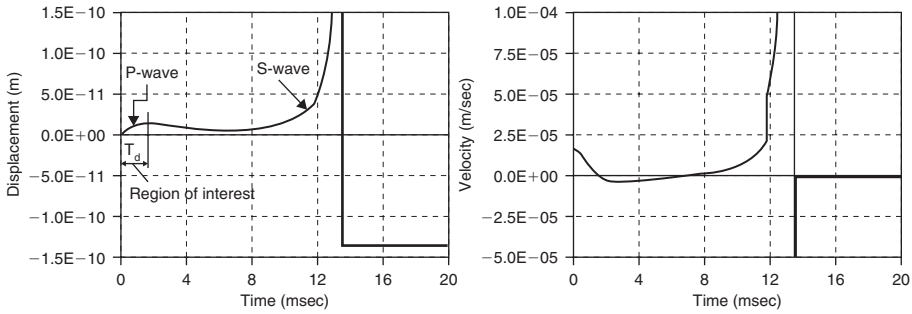



Figure 2: Displacement and velocity records from the elastic solution for a point-step force on a half-space.

Figure 2 shows the analytical solution for the vertical displacement and velocity as a function of time for a point at the surface of an elastic half-space due to a surface pulse. The magnitude of the break force is 2.5 N, and the distance between the source and receiver, $r$, is 0.075 m. The elastic constants used in the solution were those of aluminum: Young's modulus $E = 70$ GPa, Poisson's ratio $\nu = 0.33$, and mass density $\rho = 2707\ \text{kg/m}^3$, resulting in the P-wave velocity of 6.2 km/s and S-wave velocity of 3.1 km/s. The first peak of the displacement curve corresponds to the P-wave. The subsequent S-wave causes the displacement to go to infinity; finally, at the Rayleigh wave arrival, the displacement suddenly decreases, maintaining a steady-state value afterwards. The steady-state vertical displacement has the same direction as the applied force, generated by a step unloading at the specimen surface. The initial displacement corresponding to the P-wave, however, has an opposite direction. In other words, the break of a glass capillary initially produces an inward displacement at a point on the surface. It is the initial portion of the displacement record, leading to the first peak (Fig. 2) that is of primary interest in this study owing to its relevance to the simplified calibration of piezoelectric AE transducers.

## 3 TRANSDUCER RESPONSE AND CALIBRATION

The importance of transducer calibration is to connect the response of an AE sensor (voltage output) to mechanical disturbance (displacement). The motion obtained from the analytic solution is the free motion of an unloaded surface (i.e. no transducer attached). So the transducer's true response does not directly reflect the characteristics of the motion under the transducer, but rather includes information from the disturbance produced by the source and the loading effect due to the presence of the sensor.

In general, it is assumed that the wave modes are uncoupled and can be analyzed individually. Transducers are also need to be small compared to the

© 2008 Taylor & Francis Group, London, UK

predominant wavelength such that their physical dimensions can be ignored in the analysis. It is commonly assumed that the receiving system, including the piezoelectric transducer, is linear and to be principally sensitive to vertical motion (Hsu et al. 1977; Simmons et al. 1987). The output voltage V can be written as

$$V(t) = T * v_n \tag{3}$$

where $v_n$ is the normal velocity at the location of transducer, $T$ is the transfer function and * means convolution. The dependence on the displacement can be indirectly included in the velocity dependence (Michaels et al. 1981), such that the receiving system has only one characteristic transfer function $T(t)$.

Shah & Labuz (1995) performed several calibration tests to obtain the transfer function $T$, which was defined within a certain time-span, typically one microsecond. Such a signal curtailment was due to the practical limitation of the inapplicability of analytic solution after the arrival of reflections and the ringing of transducers. By considering the incident and reflected waves, the resultant transfer functions for all cases were almost identical. Nevertheless, performing the deconvolution with a curtailed, incomplete time history did not provide a transfer function representative of the AE sensor. In addition, the response was shown to be strongly dependent on the coupling between the transducer and the material surface (Shah & Labuz 1995). Thus, calibration is necessary prior to each individual experiment.

### 3.1 Sensitivity Parameter

In order to avoid the complicated and time consuming deconvolution process, several authors (e.g. Scruby et al. 1985) have directly related transducer output to normal displacement at the surface through a scalar sensitivity parameter. This is usually done by assuming that the first peak of the theoretical displacement record, which is associated with the P-wave, is directly proportional to the first peak of the recorded voltage signal:

$$S_A = \frac{V_p}{u_p} \tag{4}$$

where $u_p$ is the amplitude of the first displacement peak, $V_P$ is the amplitude of the first voltage peak, and $S_A$ is the amplitude sensitivity, estimated in V/μm. As examined in Ohtsu (1991), calibration of quantities associated with the first P-wave arrival is an important issue in moment tensor analysis. Furthermore, the initial rise time of the displacement curve, $T_d$ (Fig. 2) does not always correspond to the rise time of the recorded voltage signal, $T_s$, causing the sensitivity parameter $S_A$ to vary for different calibration distances and materials.

© 2008 Taylor & Francis Group, London, UK

In this study, a set of calibration tests were performed with the objective of determining how the amplitude sensitivity parameter, $S_A$, is influenced by different factors such as the source-receiver distance. The results obtained were used to recommend a consistent and simplified calibration procedure based on the sensitivity parameter estimation.

Figure 3 schematically shows the setup of the calibration tests that were performed on an aluminum ($E = 70\,\text{GPa}$, $\nu = 0.33$, $\rho = 2707\,\text{kg/m}^3$) block with dimensions of $20 \times 240 \times 78.5\,\text{mm}$. The break materials tested were glass capillaries, with thickness between 0.16 mm and 0.2 mm. The capillary was compressed by a sharp blade attached to a small load cell with a maximum capacity of 20 N and sensitivity of 0.4494 mV/N. The load was monitored by a digital voltmeter connected to the load cell. The glass capillary was slowly compressed by rotating a screw-driven rod until failure and the maximum voltmeter reading was recorded.

## 3.2 AE System

A high speed, CAMAC (Computer Automated Measurement And Control) based data acquisition equipment developed by LeCroy Corporation (Chestnut Ridge, New York) was used for data acquisition. This system is equipped with four two-channel modular transient recorders (model 6840) with 8-bit resolution and a sampling rate of 20 MHz (50 nanoseconds between points). A 486-processor microcomputer was interfaced with the LeCroy 6010 controller through National Instrument AT-GPIB card and cable. A Motorola 68020, 10 MHz microprocessor is built in the LeCroy 6010. A segmentation code, downloaded into 6010, permits

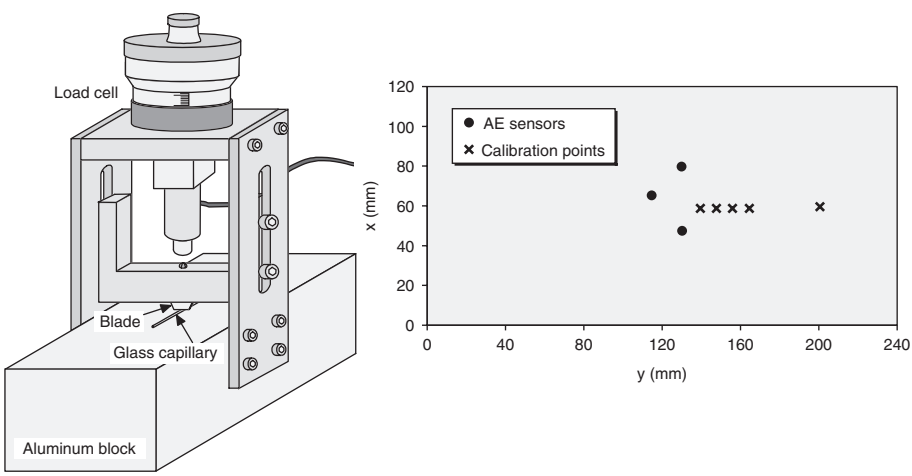



Figure 3: Calibration test configuration.

© 2008 Taylor & Francis Group, London, UK

data acquisition until 128 kbytes of digitizer memory are filled, before the data are transferred to the host computer.

The AE system accommodates eight piezoelectric transducers (Physical Acoustics model S9225). These sensors have a frequency response from 0.1–1 MHz and a sensor radius of approximately 3 mm. Preamplifiers (40 dB gain) and filters (bandpass 0.1–1.2 MHz) were chosen to maximize amplification, minimize noise, and assure matched frequency response. Typically, the noise at the output of the preamplifiers is around $\pm 2$ mV. In the calibration tests, the signal-to-noise ratios, considering the amplitude of the first arrival, were found to consistently exceed the value of ten. In order to capture events with high signal-to-noise ratios so that spurious events would not be included, the trigger level was set at $\pm 10$ mV, and a pretrigger of 50 $\mu$s allowed the entire wave form to be recorded.

### 3.3 Sensor Calibration

Figure 3 also illustrates the source-receiver configuration for one of the calibration tests performed with three piezoelectric transducers. To investigate the apparent variation of transducer sensitivity with source-receiver distance, three capillary breaks were performed at each of the source locations shown. The average break force for most capillary breaks was approximately 7 N, and a typical time history is shown in Fig. 4, which shows a qualitative resemblance between the voltage signal and the corresponding theoretical displacement signature associated with the P-wave arrival; this disappears shortly after the first peak due to resonant vibrations of the piezoelectric element.

Figure 5 shows the variation of the amplitude sensitivity parameter for two transducers. The results from different breaks performed at the same location

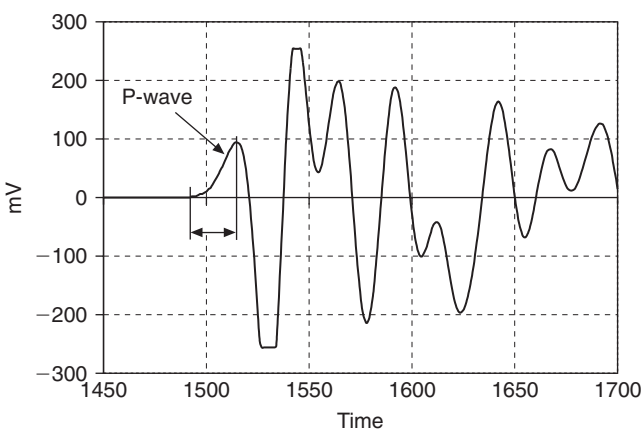



Figure 4: Typical time history from capillary calibration tests.

© 2008 Taylor & Francis Group, London, UK

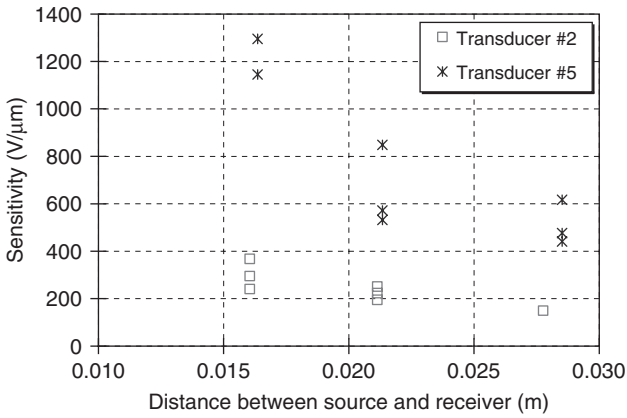



Figure 5: Amplitude sensitivities from glass capillary breaks as a function of the source-receiver distance.

were consistent, except where the break force varied due to the non-uniformity in capillary thickness. Overall, however, the sensitivity showed a linear decrease with the source-receiver distance. Although the two sensors were similar, the different sensitivities were due to the coupling condition, where a slight change in couplant thickness caused a considerable change in sensitivity. The results indicate that the amplitude sensitivity, for a specific coupling condition, is a function of both the rise time of the normal displacement (inherently governed by the distance) and its magnitude, which is also a function of the break force. The observed linear variation of $S_A$ with distance seems to be consistent with the underlying variation of theoretical displacement rise times. However, in this research, an average $S_A$ of each transducer was used in the source calculations.

## 4 SOURCE MODEL

For an idealized point source model of AE, the localized stress release can be simulated by an equivalent set of force dipoles or moments in specific directions, which can be written as the moment tensor $M$:

$$M_{kj} = C_{ijkl}(b_i n_j \Delta A) \tag{5}$$

where $C$ is the material's stiffness tensor, $b$ is the displacement vector, $n$ is the microcrack normal, and $\Delta A$ is the microcrack area (Rice 1980). Due to the symmetry of the moment tensor, the displacement vector $b$ and microcrack normal $n$ are not uniquely determined and other information is used to identify the orientation of the two vectors. Nevertheless, it is convenient to represent the

© 2008 Taylor & Francis Group, London, UK

AE source with the (symmetric) displacement discontinuity tensor $\psi$:

$$\psi_{ij} = sym[b_i n_j \Delta A] = \frac{1}{2}\left(b_i n_j + b_j n_i\right)\Delta A \tag{6}$$

For an isotropic material, the moment tensor under its eigenvector coordinate system can be written as

$$M_k = \lambda(\psi_1 + \psi_2 + \psi_3) + 2\mu\psi_k \tag{7}$$

where $\lambda$ and $\mu$ are the Lame constants, $M_k$ and $\psi_k$ are the eigenvalues of the tensors $M_{ij}$ and $\psi_{ij}$. When considering isotropic materials, the eigenvector coordinate systems of $M$ and $\psi$ coincide. The solution of the eigenvalue problem for $\psi_{ij}$ becomes

$$\begin{cases} \psi_1 = |b|\Delta A \cos^2\alpha \\ \psi_2 = 0 \\ \psi_3 = -|b|\Delta A \sin^2\alpha \end{cases} \quad \begin{cases} |b|\Delta A = \psi_1 - \psi_3 \\ \alpha = \pm\tan^{-1}\left(\sqrt{-\psi_3/\psi_1}\right) \end{cases} \tag{8}$$

where $\alpha$ is the crack mode angle, measured from the crack normal $n$ to the first eigenvector of $M$. The angle $2\alpha$ is the angle between the crack normal $n$ and the displacement discontinuity vector $b$, with normal $b_n$ and tangential $b_t$ components. If the crack mode angle $\alpha = 0°$ (crack normal $n$ is parallel to displacement vector $b$), then it is a pure opening mechanism; if $\alpha = 45°$, it is a pure sliding mode. Note that the intermediate value $\psi_2$ is zero, so the moment tensor must satisfy

$$M_2 = \frac{\lambda}{2(\lambda+\mu)}(M_1 + M_3) \tag{9}$$

In order to find the source mechanism from the recorded AE signals, the analytic solution of an abruptly generated displacement discontinuity in an infinite domain is used, and the displacement vector $u$ is conveniently given in terms of the moment tensor (Aki & Richards 1980). Considering only the first peak due to the P-wave, the displacement $u$ at any point $X$ and time $t$ is

$$u_i = \left(\frac{6\gamma_i\gamma_j\gamma_k - \gamma_i\delta_{jk} - \gamma_j\delta_{ik} - \gamma_k\delta_{ij}}{4\pi\rho c_p^2}\right)\frac{1}{r^2}M_{jk}\left(t - \frac{r}{c_p}\right) + \frac{\gamma_i\gamma_j\gamma_k}{4\pi\rho c_p^3}\frac{1}{r}\dot{M}_{jk}\left(t - \frac{r}{c_p}\right) \tag{10}$$

where $\gamma_i$ are the direction cosines of the vector connecting the source and sensor, $c_p$ is the P-wave velocity, $r$ is the distance between point $X$ where displacements

© 2008 Taylor & Francis Group, London, UK

are calculated and the source location $X_0$, $\rho$ is the density of the medium, and $\dot{M}_{jk}$ is the time derivative of the components of $M_{jk}$. By assuming that the time dependency of $M$ is separable and the same for all components, the solution problem is simplified:

$$M_{jk}(X_0, t) = M^0_{jk}(X_0)\, s(t) \tag{11}$$

where $s(t)$ is a scalar function of time. Thus, the source mechanism can be represented by a single constant matrix $M^0$, along with a space-time history $s(t)$, a reasonable approximation for a point source.

By looking at equation (10), the second term stands for the far-field behavior of the P-wave, which is the dominant term of the solution. The time dependency of the time derivative of the moment can similarly represent that of displacement at the locations of AE sensor, shifted by the signal travel time:

$$u_i(X, t) \propto \dot{M}_{jk}\left(X_0, t - \frac{r}{c_p}\right) = M^0_{jk}(X_0)\dot{s}(t) \tag{12}$$

The time dependency assumption of the moment tensor is that the maximum value $M^0$ is reached at time $T_u$, which is the rise time of the first peak of displacement at the transducer locations:

$$M_{ij}(X_0, T_u) = M^0_{ij}(X_0) \tag{13}$$

Therefore, the scalar function of time must satisfy

$$s(T_u) = \int_0^{T_u} \dot{s}(t)dt = 1 \tag{14}$$

By comparing the recorded AE signal, Carvalho & Labuz (2002) suggested a sine wave to approximate the time dependency of the displacement curve prior to first P-wave arrival (Fig. 6a):

$$\dot{s}(t) = \frac{\pi}{2T_u} \sin\left(\frac{2\pi t}{4T_u}\right) \tag{15}$$

where $T_u$ is the rise time of the first peak of displacement at the transducer locations. The coefficient $\pi/2T_u$ was selected so as to meet the condition in equation (14). However, although equation (14) is satisfied, this choice of scalar function cannot guarantee that the value $M^0$ is the maximum because the first derivative of $M$ is not zero (i.e. $\dot{s}(T_u) \neq 0$). In this paper, another type of scalar function is proposed (Fig 6b), which is

$$\dot{s}(t) = \frac{1}{T_u}, \quad \text{when } 0 < t < T_u; \;\; \dot{s}(t) = 0, \text{elsewhere} \tag{16}$$

© 2008 Taylor & Francis Group, London, UK

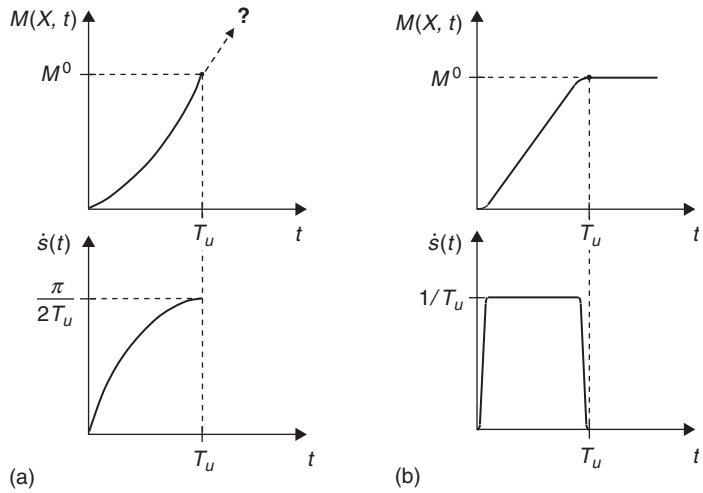



Figure 6: Time dependence of the moment tensor $M(X,t)$, and the time derivative of scalar function $s(t)$.

From this form of scalar function, the maximum value $M^0$ can be achieved at $t = T_u$. The time derivative of the moment can be written as

$$\dot{M}_{ij}(X_0, T_u) = \frac{1}{T_u} M^0_{ij}(X_0) \tag{17}$$

Since the measured displacements, taking into account mode conversion (Scruby et al. 1985), at each sensor are known, components in the moment tensor can be obtained by minimizing the sum of the error $E$:

$$E = \sum_{k=1}^{N} \left[ u^k - u_n \left( M_{pq}, X \right) \right]^2 + \gamma \left( I \cdot II + \frac{\kappa + 1}{\kappa} III + \frac{\kappa}{(\kappa + 1)^2} I^3 \right) \tag{18}$$

where $u^k$ is the mode-adjusted displacement measured at the k-th transducer, $u_n = u_i n_i$ is the displacement calculated from the moment tensor of the source, $n$ is the normal to the plane of the sensor, $\gamma$ is the Lagrange multiplier, and *I,II,III* are the invariants of the moment tensor. Now the number of unknowns in the problem is reduced to the six independent components of the constant matrix $M^0$, if equation (17) is substituted into equations (12) and (10) for the analytic solution of displacements calculated at real time $T_u + r/c_p$. Meanwhile, the restriction that second eigenvalue of displacement discontinuity tensor $\psi$ being zero must be satisfied so as to be compatible with the proposed displacement discontinuity source model. The problem is solved by using Levenberg-Marquardt algorithm to minimize the error.

© 2008 Taylor & Francis Group, London, UK

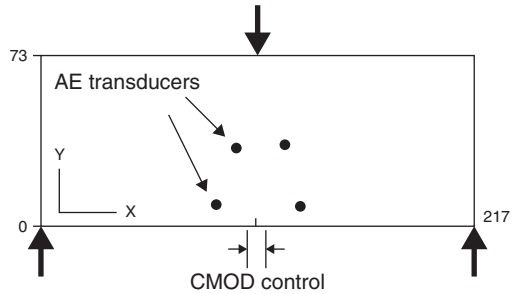



Figure 7: Three-point-bend fracture test.

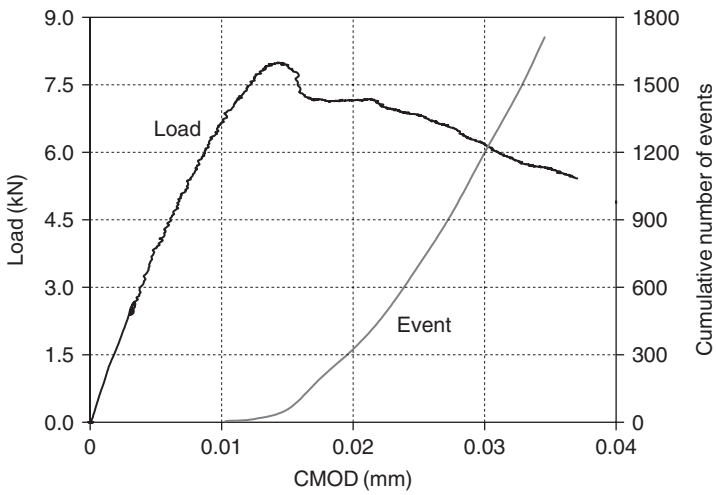



Figure 8: Load and cumulative number of AE events.

## 5 ANALYSES OF EXPERIMENTAL DATA

A closed-loop, servo-controlled fracture test with COD as the feedback signal was performed on a Charcoal granite specimen with dimensions of approximately $217 \times 73 \times 32.3$ mm and a 4 mm notch (Fig. 7). The rock has a density of 2700 kg/m$^3$, P- and S- wave velocities of 5.4 and 3.2 km/s, and a Young's modulus of 68 GPa. The beam was loaded at a crack mouth opening displacement (CMOD) rate of $5 \times 10^{-5}$ mm/s. A total of eight AE sensors were arranged on the front and back surfaces of the beam, surrounding a region adjacent to the notch at bottom surface of beam.

Figure 8 shows the load history with respect to CMOD. A total of 1711 AE events were recorded, with 692 events located with error $<2$ mm. Very few events ($<50$) were located before peak force was achieved, while most events were in the post-peak region (Fig. 8). From the cluster of AE hypocenters for different

© 2008 Taylor & Francis Group, London, UK

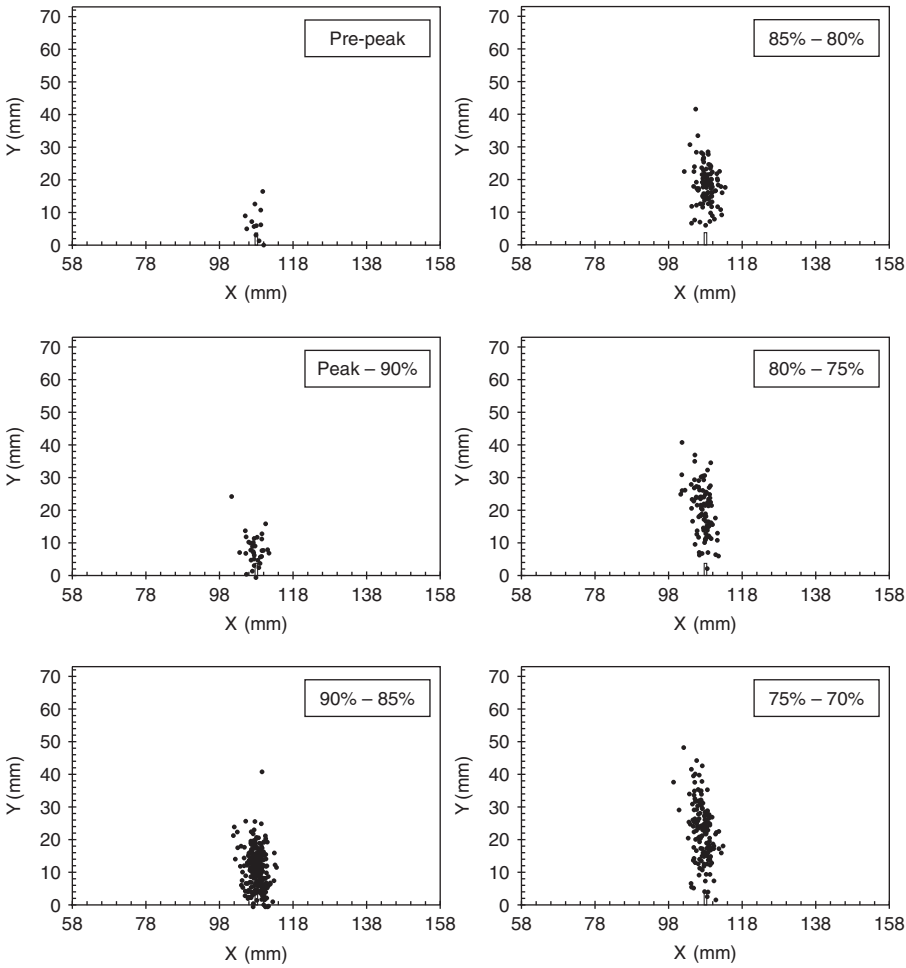



Figure 9: AE locations at separate loading stages for Charcoal granite beam.

stages of loading, crack propagation can be observed (Fig. 9). All AE locations closely coincided with the observed crack path.

Owing to the symmetry of the moment tensor, the source parameters are not uniquely determined. That is, except for the special case of $\alpha = 0°$ (opening) and 90° (closing), the displacement vector $b$ and crack normal $n$ can have two possible orientations to produce the identical moment tensor because they are interchangeable. Hence, it is necessary to introduce other information to identify the orientation of the two vectors.

The AE sources are on the order of the material's grain size, and inhomogeneities such as different crystals and the tortuousity of the fracture influence microcrack orientations. However, it is generally expected that mode I fracture

© 2008 Taylor & Francis Group, London, UK

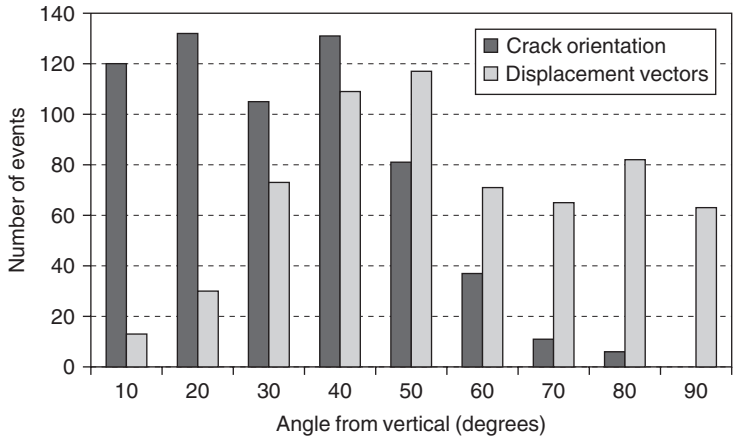



Figure 10: Orientations of microcracks and displacement vectors.

testing would involve microcracking perpendicular to maximum tension. In addition, when considering the global loading of the laboratory specimen, the kinematic motions from the microscopic scale are expected to be more or less compatible with that from the global scale. The mode I fracture test should involve opening in the X-direction (see Fig. 7). It is possible that normal components of displacement $b_n$ register closing, but when the tangential component $b_t$ and the orientation of the microcrack are considered, the global kinematics of opening in the X-direction should be followed.

Source characterization was completed for 623 events out of the possible 692, selected from events with sufficiently large first peaks to be recognized (signal-to-noise ratios $>5$) for eight channels of data and location error $<2$ mm. The amplitude sensitivity of each transducer was chosen from the average $S_A$ value obtained in the calibration tests. Figure 10 shows the distribution of microcrack orientations and displacement vectors. The average microcrack angle from vertical was about 26°, while for displacement vectors the average angle was approximately 50°. About 34% of characterized events were associated with a displacement vector within 30° of the horizontal direction, compatible with the global kinematic movement. Figure 11 shows the distribution of the crack mode angle $\alpha$, as defined in equation (8). Almost all of the events were characterized as predominantly shear, with $\alpha$ between 30° and 60°. The solid line shown is the moving average calculated with twenty points, indicating no significant change in the type of mechanism during crack propagation.

Moreover, the source mechanisms of mode I opening/closing and mode II sliding can be evaluated from equation (8) in terms of microcrack volume $b\Delta A$ (Fig. 12). It is observed that the tangential volume component $b_t \Delta A$ was dominant. The accumulated normal volume $b_n \Delta A$, which indicated a small amount

© 2008 Taylor & Francis Group, London, UK

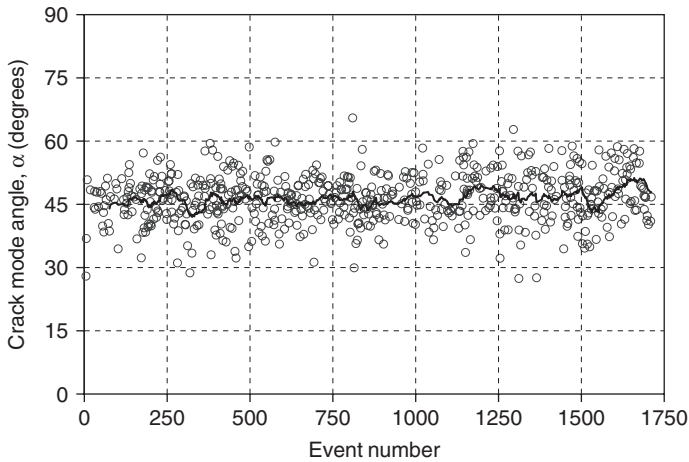



Figure 11: Moving average (20 points) of the crack mode angle.

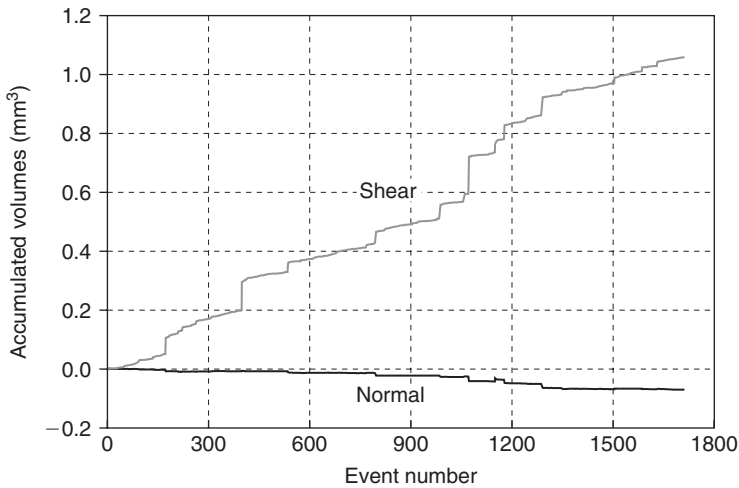



Figure 12: Cumulative microcrack volumes from the fracture test.

of closing at the end of test, was less than 10% of the accumulated shear volume component. However, displacement modes of each microcrack are locally based, while the opening displacement of the fracture involves a global view. The normal volumes generated from the AE events can be misleading, especially when most of the microcracks were not oriented perpendicular to the maximum tensile stress.

To capture the local effect, a torturosity angle is introduced to determine the orientation of microcracks on the horizontal plane (i.e. the X–Z plane for the fracture test). As shown in Figure 13, more than 50% of the microcracks

© 2008 Taylor & Francis Group, London, UK

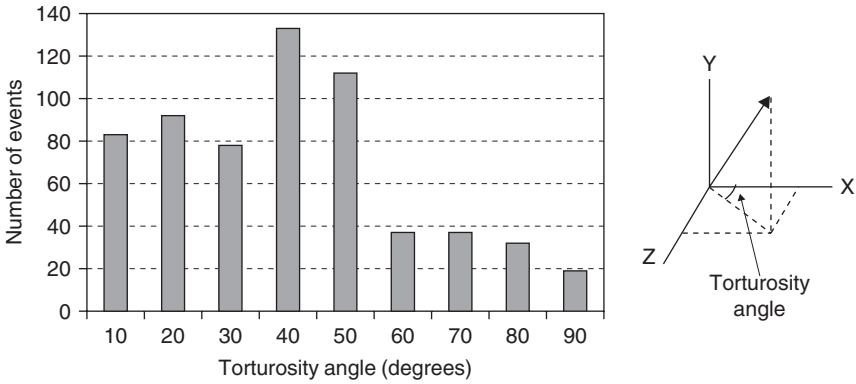



Figure 13: Torturosity angle of microcracks.

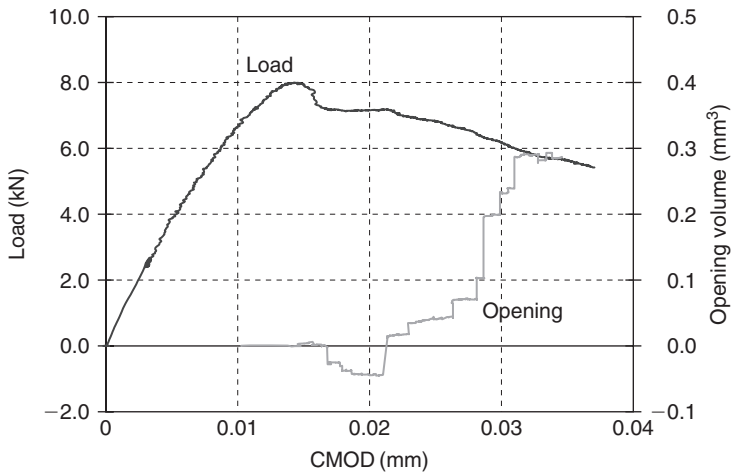



Figure 14: Comparison between the loading and opening volume.

were orientated at least 30° from the X-axis (i.e. the direction of maximum tensile stress). When decomposing the crack volume $b\Delta A$ into the X-direction, a pronounced amount of cumulative *positive* volume indicates overall fracture opening (Fig.14), which is consistent with the global behavior. Figure 14 shows the crack opening volume plotted against CMOD. Compared with the load history, it is interesting to note that from 0.017–0.021 mm of CMOD, crack closing was associated with the constant level of load after peak, which may indicate no crack growth. After this region, the crack volume started increasing with a decrease in load (the fracture was propagating).

© 2008 Taylor & Francis Group, London, UK

## 6 CONCLUSIONS

Part of the investigation focused on investigating the key features underlying a simplified AE transducer calibration, which utilizes the sensor response up to the first peak associated with the P-wave arrival. The amplitude sensitivity parameter is taken as constant for this class of problems. Amplitude sensitivities were also found to be strongly dependent on the coupling between the transducer and specimen surface. As a result, calibration is required for each specimen just before the actual experiment.

The AE source mechanism was described by a displacement discontinuity in the form of force dipoles called the moment tensor. The same type of separable time dependency for all components of the moment tensor was assumed. Components of the moment tensor were retrieved by minimizing the error between measured displacements obtained from the AE signal and the displacements calculated from moment tensor at the source. This optimization was also subjected to constraints that guarantee the form of a displacement discontinuity with the moment tensor. A three-point-bend fracture test was performed and the data were analyzed with the source model. Even though most AE events were characterized as shear, the displacement behavior associated with crack opening was observed, which was compatible with the global fracture mechanism.

## ACKNOWLEDGEMENT

Partial support was provided to Dr. F. Carvalho by the MTS Visiting Professorship in Geomechanics at the Department of Civil Engineering, University of Minnesota.

## References

[1] Aki, K. & Richards, P.G. (1980).*Quantitative Seismology: Theory and Methods*. W. H. Freeman and Company, San Francisco.

[2] Breckenridge, F.R., Tschiegg, C.E. & Greenspan, M. (1975). Acoustic emission: some applications of Lamb's problem. *J. Acoust. Soc. Am.*, 57(3), 626–631.

[3] Burridge, R. & Knopoff, L. (1964). Body force equivalents for seismic dislocations. *Bull. Seis. Soc. Am.*, 54, 1875–1888.

[4] Carvalho, F. & Labuz, J.F. (2002). Moment tensors of acoustic emissions in shear faulting under plane-strain compression. *Tectonophysics*, 356, 199–211.

[5] Hsu, N.N. & Breckenridge, F.R. (1979). Characterization and calibration of acoustic emission sensors. *Mater. Evaluation*, 39, 60–68.

© 2008 Taylor & Francis Group, London, UK

[6] Hsu, N.N. Simmons, J.A. & Hardy, S.C. (1977). An approach to acoustic emission signal analysis. *Mater. Evaluation*, 35, 100–106.
[7] Kim, Y.K. & Sachse, W. (1986). Characteristics of an acoustic emission source from a thermal crack in glass. *Int. J. Frac.*, 31, 211–231.
[8] Michaels, J.E., Michaels, T.E. & Sachse, W. (1981). Application of deconvolution to acoustic emission signal analysis. *Mater. Evaluation,* 3, 1032–1036.
[9] Mooney, H.M. (1974). Some numerical solutions for Lamb's problem. *Bull. Seismol. Soc. Am.*, 64, 473–491.
[10] Ohtsu, M. (1991). Simplified moment tensor analysis and unified decomposition of acoustic emission source. *J. Geophys. Res.*, 96(B4), 6211–6221.
[11] Ohtsu, M. & Ono, K. (1988). AE source location and orientation of tensile cracks from surface observation. *NDT International*, 21, 143–150.
[12] Ohtsu, M., Okamoto, T. & Yuyama, S. (1998). Moment tensor analysis of acoustic emission for cracking mechanisms in concrete. *ACI Struct. J.*, 95(2), 87–95.
[13] Pekeris, C.L. (1955). The seismic surface pulse. *Proc. Nat. Acad. Sci.*, 41, 469–480.
[14] Pekeris, C.L. & Lifson, H. (1957). Motion of the surface of a uniform elastic half-space produced by a buried pulse. *J. Acoust. Soc. Am.*, 29(11), 1233–1238.
[15] Rice, J.R. (1980). Elastic wave emission from damage processes. *J. Nondestruc. Eval.*, 1(4), 215–224.
[16] Scruby, C.B., Baldwin, G.R. & Stacey, K.A. (1985). Characterization of fatigue crack extension by quantitative acoustic emission. *Int. J. Frac.*, 28, 201–222.
[17] Shah, K.R. & Labuz, J.F. (1995). Damage mechanisms in stressed rock from acoustic emission. *J. Geophys. Res.*, 100(B8), 15, 527–15, 539.
[18] Simmons, J.A., Turner, C.D. & Wadley, H.N.G. (1987). Vector calibration of ultrasonic and acoustic emission transducers. *J. Acoust. Soc. Am.*, 82, 1122–1130.

© 2008 Taylor & Francis Group, London, UK

# *1.2 AE detection of failure processes in concrete structures*

© 2008 Taylor & Francis Group, London, UK

*Acoustic Emission and Critical Phenomena – Carpinteri & Lacidogna (eds)*
*© 2008 Taylor & Francis Group, London, ISBN 978-0-415-45082-9*

# ACOUSTIC EMISSION ANALYSIS OF CONCRETE FOR CORROSION, DAMAGE AND CRACKING MECHANISM

**M. Ohtsu[1], Y. Tomoda[2] and T. Suzuki[3]**
[1]Graduate School of Science & Tech., Kumamoto Univ., Kumamoto, Japan
[2]Faculty of Engineering, Kumamoto University, Kumamoto, Japan
[3]Department of Bio-resource Science, Nihon University, Kanagawa, Japan

## ABSTRACT

Acoustic emission (AE) techniques have been extensively studied in concrete engineering. As the state of the art, corrosion activity in reinforced concrete, damage of concrete members in service, and cracking mechanisms inside concrete are able to be quantitatively evaluated. Continuous AE monitoring is useful for earlier warning of corrosion in reinforcement. Onset of corrosion in reinforcement and nucleation of corrosion cracking in concrete are readily identified. In order to assess the damage levels of the structures, one criterion based on the Kaiser effect of AE is proposed as the recommended practice. AE parameters of the load ratio and the calm ratio are applied to qualify the damage. The applicability is examined by testing asbestos-cement pipes under incremental-cyclic loading. Crack kinematics can be identified by the SiGMA procedure based on the moment tensor analysis. Because kinematical information is obtained as three-dimensional (3-D) locations and vectors, 3-D visualization has been developed. These updated results are discussed and summarized.

## 1 INTRODUCTION

Concrete structures in service could deteriorate due to heavy traffic loads, fatigue, chemical reactions, and other disasters. It is recently recognized in concrete engineering that concrete structures are no longer maintenance-free, and a number of the structures are going to reach their service-life limit. Prior to maintenance and repair in damaged structures, diagnostic inspections on the current state of the deterioration are necessary. However, assessment of the damage or of the structural integrity in existing structures is generally neither an easy task nor readily standardized. In this regard, acoustic emission (AE) techniques are considered to be promising for estimation of the deteriorations in concrete structures.

© 2008 Taylor & Francis Group, London, UK

According to the standard specification for the maintenance of concrete structures (*JSCE* [1]), six deterioration mechanisms to be identified are specified for the maintenance. These are deteriorations due to salt attack, neutralization, chemical attack, freezing and thawing, alkali-aggregate reaction, and fatigue. The corrosion due to salt (chloride) attack has been referred to as the most critical deterioration of RC structures. Based on a result of the exposure test (*Ohtsu et al.* [2]), onset of corrosion in reinforcement and nucleation of cracking in concrete are attempted to be identified by AE monitoring.

One recommended practice by acoustic emission (AE) is currently published (*JSNDI* [3]), prescribing one new criterion to assess the damage of reinforced concrete (RC) beams in service. Based on the load ratio and the calm ratio defined from the Kaiser effect of AE, the damage levels of the structures are qualified. An applicability of the criterion is examined in bending tests of asbestos-cement pipes.

In order to perform the moment tensor analysis, one powerful technique for AE waveform analysis has been developed as SiGMA (Simplified Green's functions for Moment tensor Analysis) (*Ohtsu* [4]). Crack kinematics on locations, types and orientations are quantitatively determined. Because these kinematical outcomes are obtained as three-dimensional (3-D) locations and vectors, 3-D visualization of results is desirable. To this end, the visualization procedure has been developed by using VRML (Virtual Reality Modeling Language) (*Ohtsu and Shigeishi* [5]).

## 2 AE TECHNIQUES

### 2.1 Corrosion monitoring by AE

By applying AE monitoring, it has been reported that concrete cracking due to rebar corrosion is effectively detected (*Yoon et al.* [6]; *Uddin et al*. [7]).

According to a phenomenological model of reinforcement corrosion in marine environments (*Melchers and Li* [8]), a typical corrosion loss is illustrated in Figure 1. At phase 1, the corrosion is initiated. The rate of the corrosion process is controlled by the rate of transport of oxygen. As the corrosion products build up on the corroding surface of rebar, the flow of oxygen is eventually inhibited and the rate of the corrosion loss decreases at phase 2 as aerobic corrosion. The corrosion process involves further corrosion loss at phases 3 and 4 due to anaerobic corrosion. Thus, two-step corrosion losses are modeled. It is realized that physical phenomena at phase 1 and phase 3 could correspond to the onset of corrosion in reinforcement and the nucleation of cracking in concrete, respectively. Here, continuous AE measurement by a high-sensitivity system is conducted to monitor the corrosion process and locate sources in reinforced concrete specimens in a laboratory.

© 2008 Taylor & Francis Group, London, UK

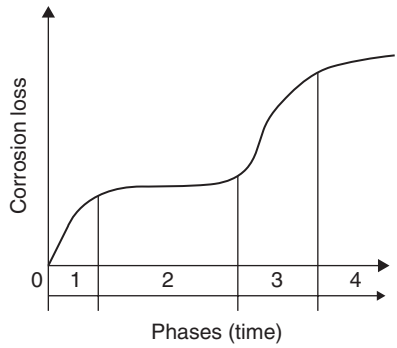



Figure 1: Typical corrosion loss for steel in seawater immersion [8].

## 2.2 Damage qualification by AE

Concrete structures undamaged are statically stable with high redundancy, as AE activity is very low because of the Kaiser effect. Ratios of AE activity to estimate the Kaiser effect are redefined in the recommended practice (*JSNDI* [3]), as follows:

(a) Ratio of **l**oad at the **o**nset of **A**E activity to previous loa**d**:
**Load ratio** = load at the onset of AE activity in the subsequent loading/the previous load.
(b) Ratio of **c**umulative **A**E activity during the un**l**oading process to that of the **l**ast **m**aximum loading cycle:
**Calm ratio** = the number of cumulative AE activity during the unloading process/total AE activity during the last loading cycle.

The load ratio could become larger than 1.0 in a very sound structure. Due to damage accumulation, the ratio decreases lower than 1.0, generating AE events even at lower loading levels than before. AE activity during unloading is another indication of structural integrity. In the case that the structure is statically stable, AE activity is seldom observed in the unloading process. In the recommendation, the damage assessment is proposed to qualify the damage levels as prescribed in Figure 2.

An applicability of the damage assessment is experimentally examined in fracture tests of acbestos-cement pipes.

## 2.3 SiGMA-AE analysis

For the moment tensor analysis, a simplified procedure has been developed, which is suitable for a PC-based processor and robust in computation (*Ohtsu* [4]). The procedure is now implemented as a SiGMA (Simplified Green's functions

© 2008 Taylor & Francis Group, London, UK

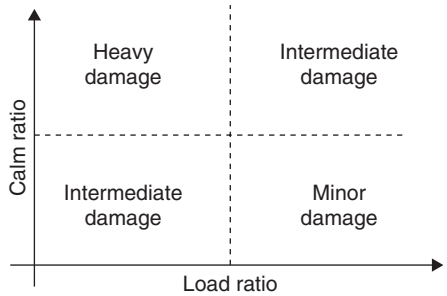



Figure 2: Qualification of damage levels by AE ratios.

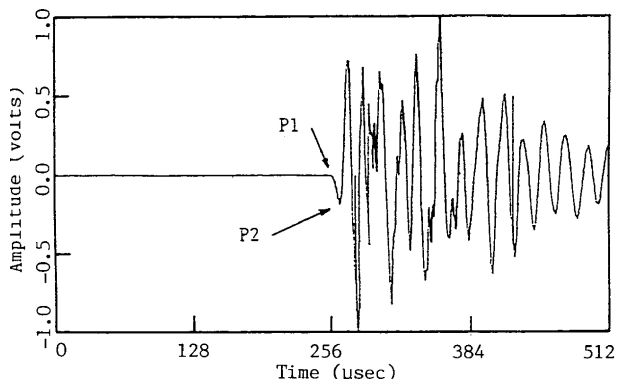



Figure 3: Detected AE wave and two parameters P1 and P2.

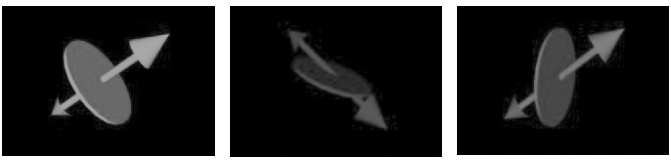
for Moment tensor Analysis) code. Considering the effect of reflection at the surface and neglecting the source-time function, the amplitude A(**x**) of the first motion is represented as,

$$A(\mathbf{x}) = [C_s \, \mathrm{Ref}(\mathbf{t}, \mathbf{r})/R] \, r_i M_{ij} r_j \tag{1}$$

where $C_s$ is the calibration coefficient including material constants. **t** is the direction of the sensor sensitivity. Ref(**t**,**r**) is the reflection coefficient at the observation location **x**. Since the moment tensor is symmetric, the number of independent unknowns $M_{ij}$ to be solved is six. Thus, multi-channel observation of the first motions at more than six channels is required to determine the moment tensor components.

Displaying AE waveform on CRT screen, two parameters of the arrival time (P1) and the amplitude of the first motion (P2) in Figure 3 are determined. In the location procedure, source location **y** is determined from the arrival time differences. Then, distance R and its direction vector **r** or $r_i$ are estimated and the amplitudes of the first motions at more than 6 channels are substituted

© 2008 Taylor & Francis Group, London, UK



(a) Tensile crack (b) Shear crack (c) Mixed-mode

Figure 4: 3-D display models for tensile, shear, and mixed-mode cracks.

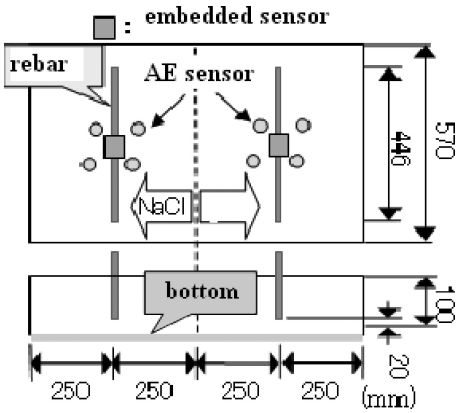



Figure 5: Sketch of reinforced concrete slab tested.

into Equation (1). Thus, the components of the moment tensor $M_{ij}$ are determined. Classification of a crack and the determination of crack orientations are performed by the eigenvalue analysis of the moment tensor.

Visualization procedure has been developed by using VRML (Virtual Reality Modeling Language) (*Ohtsu and Shigeishi* [5]). Crack modes of tensile, mixed-mode and shear are given in Figure 4. Here, an arrow vector indicates the crack motion vector, and a circular plate corresponds to the crack surface, which is perpendicular to the crack normal vector.

## 3 RESULTS AND DISCUSSION

### 3.1 AE activity during corrosion process

(1) Experiment

A reinforced concrete specimen of dimensions 1000 mm × 570 mm × 100 mm was tested. Two deformed steel-bars (rebars) of 13 mm nominal diameter were embedded with 20 mm cover-thickness. Configuration of the specimen is illustrated in Figure 5.

© 2008 Taylor & Francis Group, London, UK

When making the specimen, a half portion of concrete was mixed with NaCl solution as shown. In order to investigate the threshold limit of chloride concentration for the corrosion, the lower-bound threshold value (chloride amount 0.3 kg/m$^3$ of concrete volume; 0.093% mass of cement) prescribed in the code (*JSCE*, [1]) was taken into account. After the standard curing for 28 days in 20°C water, chloride content of the NaCl portion was measured by employing a standard cylindrical sample of 10 cm diameter and 20 cm height and found to be 0.197 kg/m$^3$ (0.039% mass of cement) in concrete as lower than 0.3 kg/m$^3$ in volume.

Concerning mixture proportion of concrete, the maximum size of gravel was 10 mm, and the slump value (6 cm) and air content (5%) were controlled by using air-entrained admixture. A compressive strength at 28 days of the standard curing was 35.0 MPa. Following the standard curing, all surfaces of the specimen were coated by epoxy, except the bottom surface for chloride diffusion as illustrated in the figure.

A cyclic wet-dry test were conducted. The specimen was cyclically put into the container filled with 3% NaCl solution for a week and subsequently dried under ambient temperature for another week. AE measurement was continuously conducted, by using AE analyzer (LOCAN 320, PAC). Eight AE sensors (R15, PAC) of 150 kHz resonance were attached to the upper surface of the specimen, surrounding two rebars by both 4-channel systems as shown. Frequency range of the measurement was 10 kHz–300 kHz and total amplification was 60 dB gain. For AE counting, the dead-time was set to 2 msec and the threshold level was 40 dB gain.

Half-cell potentials at the surface of the specimen were measured by a portable corrosion-meter (SRI-CM-II, Shikoku-Soken) weekly, until the average potentials in dry condition reached to −350 mV (C.S.E.). Internal potentials were also continuously measured by employing embedded sensors. During the half-cell potential measurement, AE measurement was discontinued.

Chloride concentrations were measured at several periods. From concrete of the both portions, the initial concentration was measured by using a standard cylinder sample after 28-day moisture-curing as an initial value. At other periods, two core samples of 5 cm diameter were taken from the accompanied specimens of dimensions 250 mm × 300 mm × 100. Slicing the core into 5 mm-thick disks and crushing them, concentrations of total chloride ions were determined by the titration method.

(2) Results

Total number of AE hits and the half-cell potentials during the test are shown in Figure 6. In the graphs, the total number of AE hits per 1 hrs. at all channels is plotted by a solid curve. The 1st AE activity around at 14 days elapsed is clearly observed, while the 2nd activity is found at 60 day around in the NaCl portion.

© 2008 Taylor & Francis Group, London, UK

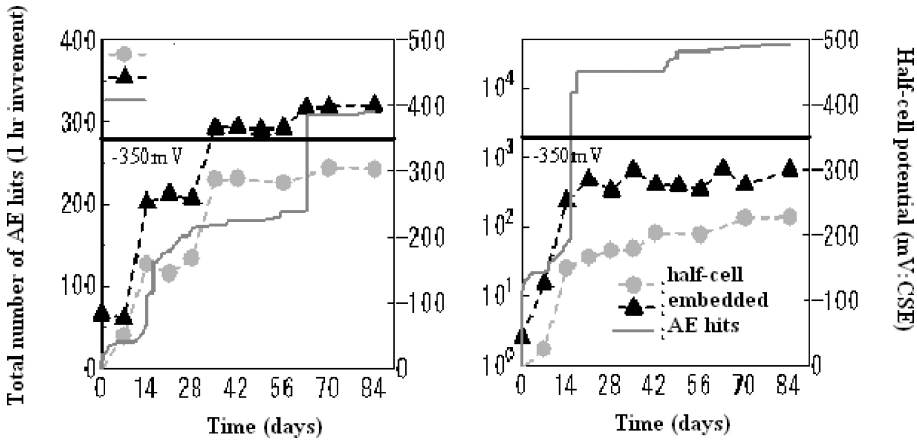



Figure 6: Total AE hits and half-cell potentials in the NaCl portion (left) and water portion (right).

It is interesting that the curve of AE activity in the NaCl portion is in remarkable agreement with the typical corrosion loss of the phenomenological model in Figure 1. Although a previous research reported that AE activity could be generated by concrete cracking due to expansion of corrosion products (*Zongjin, et al.* [9]). This result suggests that AE activity can be observed in the concrete specimen, starting with the onset of corrosion in reinforcement. Comparing AE activity with half-cell potentials, it is found that with the increase in the number of AE hits, the potentials shift to more negative values. Here, two kinds of potentials are plotted. One is the potentials measured at the surface and the other is those by the embedded sensor. As expected, the embedded sensor shows more negative potentials. The decreasing trends are similar.

In the NaCl portion, at the 2nd period of high AE activity around 60 days elapsed, the potentials reach to more negative than −350 mV. In the water portion, the decreasing manner of the potentials is in reasonable agreement with that of AE activity. In this case, the 1st high AE activity is only observed, and the potentials did not reach more negative than −350 mV.

Relations between chloride concentrations at the cover thickness and AE activities are shown in Figure 7. It is found that chloride concentration becomes higher than 0.3 kg/m$^3$ around at the 1st high AE activity, and it reaches higher than 1.2 kg/m$^3$, resulting in the 2nd high AE activity in the NaCl portion. In the water portion, the 1st high AE activity is observed prior to the stage, where chloride concentration becomes over 0.3 kg/m$^3$.

Comparing AE activities in Figures 6 and 7 with Figure 1, it could be summarized that two high AE activities reasonably correspond to two periods of the onset of corrosion and the nucleation of cracking.

© 2008 Taylor & Francis Group, London, UK

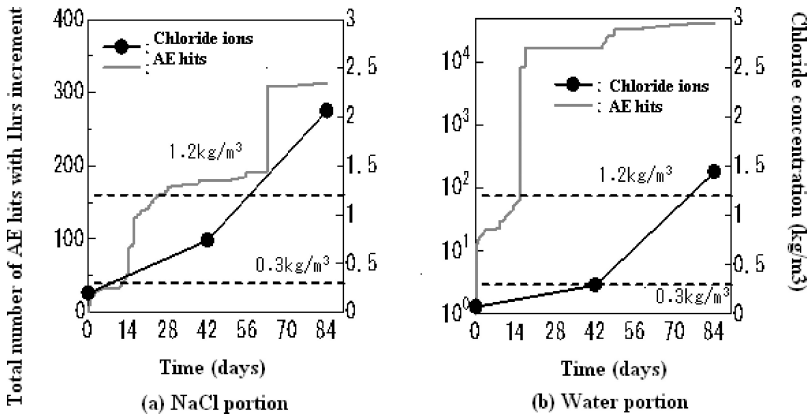



Figure 7: Total number of AE hits and chloride concentration.

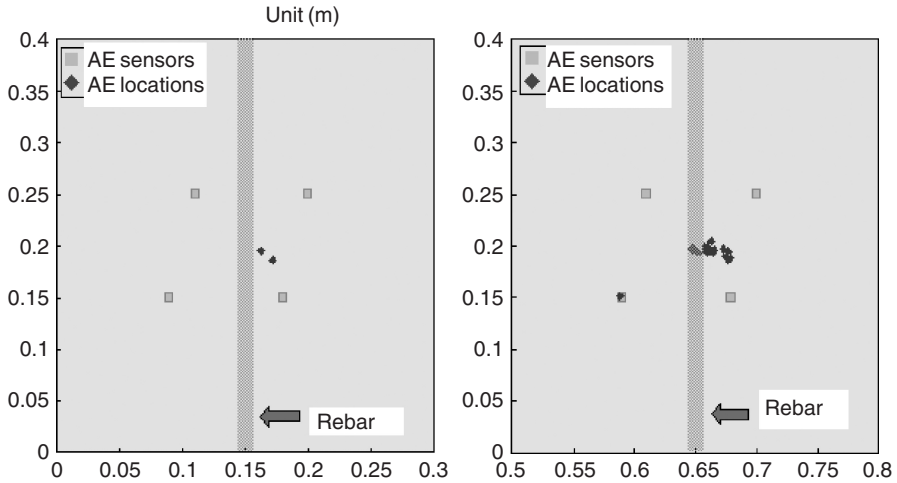
AE phenomena detected at all channels are named AE hits, while those located by 4 channel system are defined as AE events. Consequently, a relation between AE hits and AE events is investigated. The number of AE events located was just 10% of total AE hits. Corresponding to high AE activities twice, two active periods of AE events are observed in the NaCl portion. In contrast, only activity at the 2nd period is emphasized in the water portion. By employing the flaw location procedure, AE events were located. Then, it was found AE events located at the 1st period in the NaCl portion were only found around locations of AE sensors. So, AE waveforms were examined. AE events detected at the 1st period were of so small amplitudes that AE sources could be mistakenly located at the location of the nearest sensor, where AE waveform was detected of the biggest amplitude. AE source locations at the 2nd period of high AE activity are shown in Figure 8. It is realized that AE sources are reasonably located around rebar locations. This implies that corrosion activity due to concrete cracking, which is generated by expansion of corrosion products in rebar, is readily detected and located by AE technique. It is also noted that after removing rebars from one accompanied specimen made of NaCl solution at 84-day elapsed, it was demonstrated that embedded rebar was actually corroded.

## 3.2 Damage qualification in asbestos-cement pipes

### (1) Experiment

An asbestos-cement pipe of 600 mm diameter, which had been used for 32 years, was tested. The pipe had been buried underground 1.10 meters below the road and connected 73 meters long. Each 4.0 meter pipe was cut into two samples as two 1.0 meter samples for a compression test in Figure 9, and one 2.0 meter sample for a bending test in Figure 10.

© 2008 Taylor & Francis Group, London, UK




(a) Located AE sources in the NaCl portion during 63–70 days

(b) Located AE sources in the water portion during 63–70 days

Figure 8: AE sources located at the 2nd high AE activities in the test.

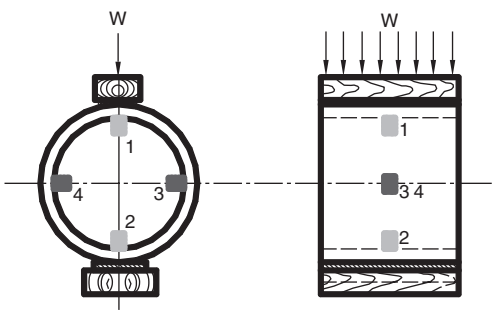



Figure 9: AE sensor arrangement in the compression test.

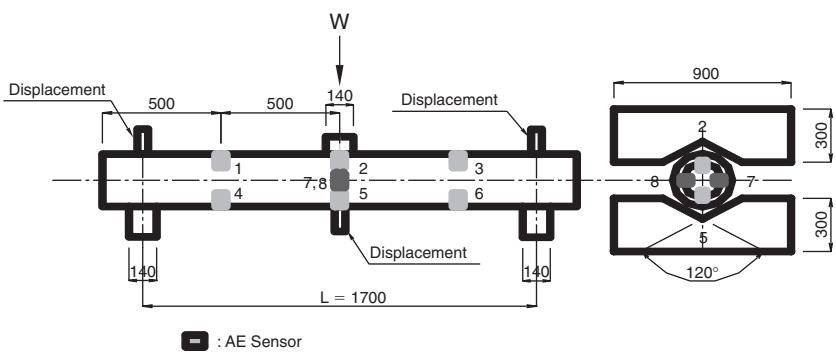



Figure 10: AE sensor arrangement in the bending test.

© 2008 Taylor & Francis Group, London, UK

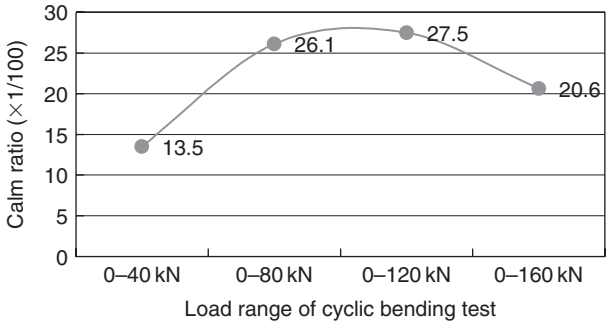



Figure 11: Calm ratios in the cyclic bending test.

For AE measurement, R15 sensors (manufactured by PAC) were installed on the inner surface of the asbestos cement pipes at four locations for the compression tests and eight locations for the bending tests. DISP-AE system (PAC) was used as a measuring device. AE hits were amplified with 40 dB gain in a pre-amplifier and 20dB gain in a main amplifier.

(2) Results

In the compression tests, the strengths of the pipes varied from 25.6 kN to 72.2 kN, with the mean value of 55.4 kN. Results of the bending tests show a relatively small variation from 201 kN to 227 kN. Different AE generating behaviors were observed in the compression test and the bending test. In the former, the displacement varied almost linearly with stress. As the load increased, the number of AE hits increased and the hits were observed frequently near the ultimate load. In the latter tests, diagonal shear fracture was observed as active AE generation at 44.5 kN under monotonous loading. This load might be equivalent to the most frequent previous load recorded, which is related to the Kaiser effect. In the cyclic loading tests, frequent AE generation was again observed at about 40 kN. From these results, the test pipe is considered to have received 40 to 50 kN external pressure constantly, which is estimated from the Kaiser effect and corresponds from 19 to 23% of the failure load, which was estimated as 214 kN in the bending test.

Then, damage of this pipe was qualified from the relationships between the load ratio and the calm ratio, as a previous report (*Ohtsu et al.* [10]). Because the traffic load worked on the pipe from the transverse direction, the bending tests were conducted. A relation between the load and the calm ratio is shown in Figure 11. The high calm ratio implies accumulation of damages. The calm ratios slightly increase with the increase in the cyclic load levels. The maximum value is observed around 100 kN, which actually corresponds to the traffic load (T-25 rear wheel load).

© 2008 Taylor & Francis Group, London, UK

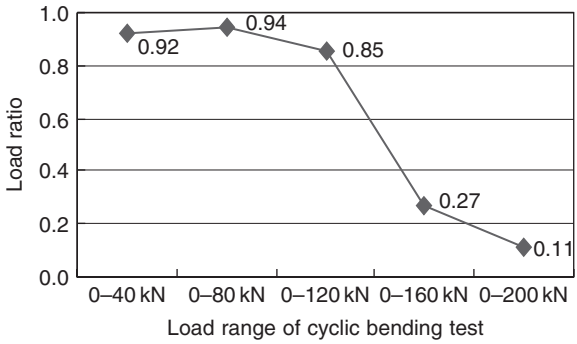



Figure 12: Load ratios in the cyclic bending test.

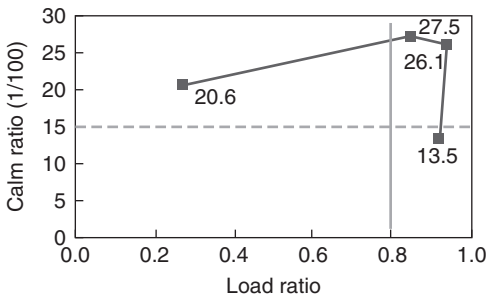



Figure 13: Relationships between the calm ratios and the load ratios during the cyclic tests.

Figure 12 shows the relation between the load and the load ratio. It is known that the load ratios less than 1.0 could result from accumulation of damages. The load ratio decreases sharply over 100 kN, as the deterioration is suggested.

The damage levels of tested pipes were qualified from the relationship between the load ratio and the calm ratio. As can be seen in Figure 13, it is clearly observed that the damage increases from the minor level to the heavy level, through the intermediate level illustrated in Figure 2.

### 3.3 Crack kinematics in the bending test of reinforced concrete beam

(1) Experiment

Reinforced concrete beams of dimensions 10 cm × 10 cm × 40 cm were tested. One rebar of 10 mm diameter was arranged at 30 mm cover-thickness. Compressive strength of concrete was 33.4 MPa at 28 days. Modulus of elasticity and the velocity of P wave were 24 GPa and 3140 m/s, respectively. Six AE sensors were

© 2008 Taylor & Francis Group, London, UK

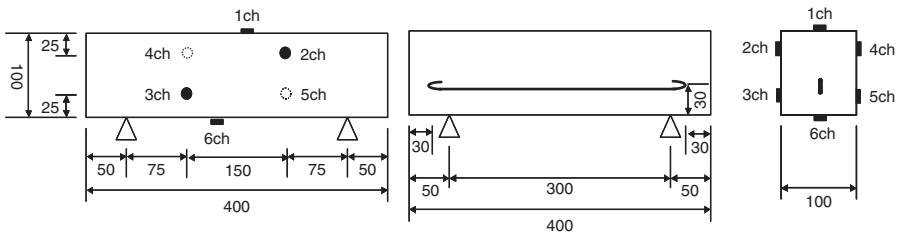



Figure 14: Specimen and sensor array.

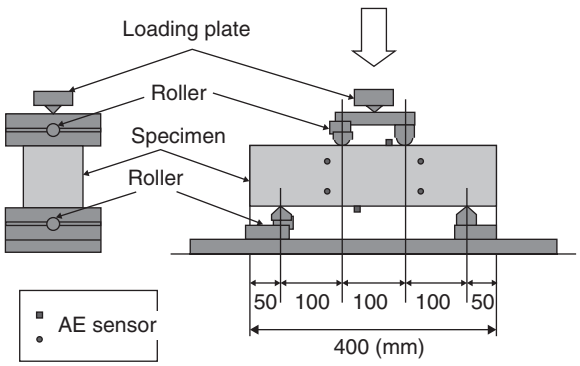



Figure 15: Experimental set-up.

attached to the specimen. The locations of sensors and the configuration of a reinforced concrete beam are shown in Figure 14.

The specimen was loaded as shown in Figure 15. Bending failure of the reinforced concrete beam was generated. Without reinforcement, concrete beams suddenly break into two pieces when the stress at the bottom side reaches the tensile strength. Sudden crack propagation from the bottom to the top is prevented with reinforcement. As a result, failure process is visually divided into several stages.

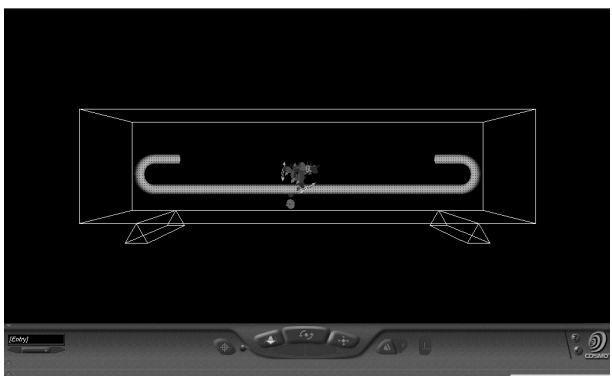
Tensile cracks are generated first at the bottom region as bending cracks. Then, delamination between the concrete and the reinforcement occurs. Along with this failure, bending cracks grow further. The tips of cracks extend upward, penetrating into the compressive zone of the upper half. The cracks may stop at this stage due to compression, and the beam reaches final failure of diagonal-shear failure or concrete crashing at the upper half.

3-D visualization of SiGMA analysis on the beginning three stages is given in Figure 16. At the first stage, a few tensile cracks (green) and mixed-mode cracks (red) are mostly observed near reinforcement at the central region. Activity of cracking increases at the second stage as the increase of mixed-mode cracks. At this stage, bending cracks are visually observed. At the third stage, AE cluster expands upward, increasing the number of shear cracks (blue).

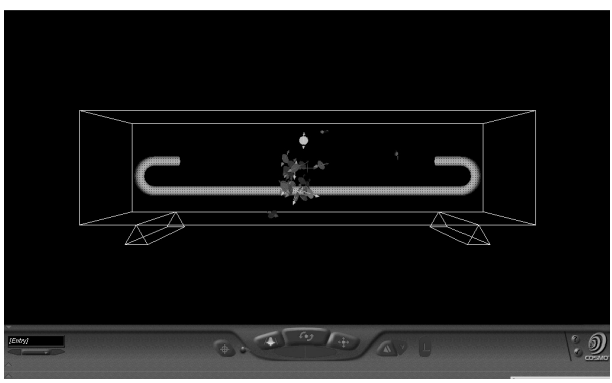
© 2008 Taylor & Francis Group, London, UK



(a) First stage



(b) Second stage



(c) Third stage

Figure 16: Results of SiGMA analysis on the beginning three stages.

The latter stage is shown in Figure 17. Cluster of AE sources further expands and the nucleation of cracks is really mixed up of tensile, mixed-mode, and shear cracks. It is noted that tensile and mixed-mode cracks are intensely observed around reinforcement, while shear cracks are particularly observed

© 2008 Taylor & Francis Group, London, UK

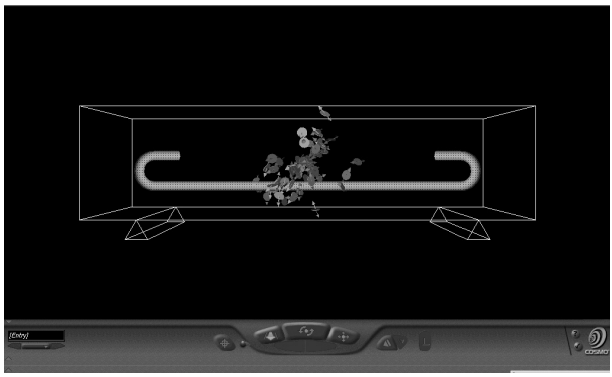


Figure 17: Results of SiGMA analysis on the last two stages.

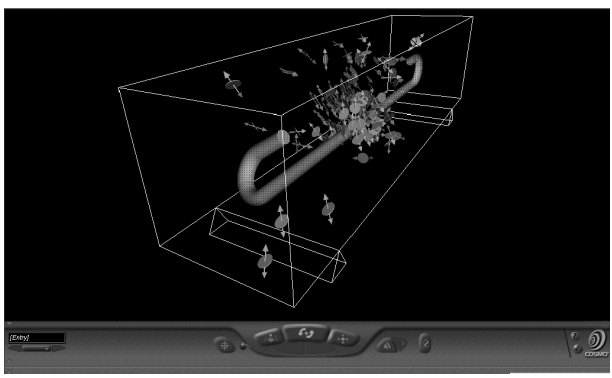


Figure 18: Results of all the data analyzed.

at the compressive zone. At the fifth stage, cracks distribute widely, probably corresponding to the nucleation of diagonal shear cracks between the loading point and the support.

Combining all results analyzed, Figure 18 is obtained. All figures are actually movable and rotatable. Therefore, locations and orientations of the source can be visually identified.

## 4 CONCLUSION

(1) Because corrosion of reinforcing steel is modeled phenomenologically as corrosion losses of three phases, AE activities in the corrosion process are compared with the model. At phase 1, corrosion is initiated in reinforcement. Then the rate of the corrosion loss decreases at phase 2 under aerobic conditions. The corrosion activity at phase 1 can be detected by AE monitoring as the 1st period of high AE activity. At the next phase of anaerobic corrosion, the expansion

© 2008 Taylor & Francis Group, London, UK

of reinforcing steel due to corrosion product nucleates concrete cracking. The period is readily observed as the 2nd high AE activity. Although AE events were not accurately located at the 1st high AE activity because of small events, it is demonstrated that AE events can be located at the period of the 2nd high AE activity.

(2) Loading tests (compression tests, bending tests) were carried out on the existing asbestos-cement pipe and the fracture process was monitored by AE. The maximum previous load and the damage accumulation of the pipe were evaluated. The damage evolution in the pipes under cyclic bending is resonably qualified by the relation between the load ratio and the calm ratio.

(3) Nucleation of cracks can be quantitatively analyzed from AE waveforms, by applying SiGMA code. Crack kinematics on locations, types and orientations are determined three-dimensionally. Visualization procedure for SiGMA analysis is developed by using VRML (Virtual Reality Modeling Language). As a case study, failure process of a reinforced concrete beam is successfully visualized.

## References

[1] Standard Specifications for Concrete and Concrete Structures on Maintenance, Japan Society for Civil Engineers (JSCE), 2001.

[2] M. Ohtsu, Y. Tomoda, Y. Sakata, M. Murata and H. Matsushita, "In Situ Monitoring and Diagnosis of RC Members in an Exposure Test against Salt Attack," *Proc. 10th Int. Conf. Structural Faults & Repair*, CD-ROM, 2003.

[3] NDIS 2421, Recommended Practice for In-Situ Monitoring of Concrete Structures by AE, Japanese Society for Nondestructive Inspection (JNSDI), 2000.

[4] M. Ohtsu, "Simplified Moment Tensor Analysis and Unified Decomposition of Acoustic Emission Source: Application to In Situ Hydrofracturing Test", *Journal of Geophysical Research*, 96(B4), pp. 6211–6221, 1991.

[5] M. Ohtsu and M. Shigeihsi, "Virtual Reality Presentation of Moment Tensor Analysis by SiGMA," *J. Korean Soc. for NDT*, Vol. 23, No. 3, pp. 189–1999, 2003.

[6] D. J. Yoon, W. J. Weiss and S. P. Shah, "Assessing Damage in Corroded Reinforced Concrete using Acoustic Emission," *J. Engineering Mechanics*, ASCE, Vol. 126, No. 3, pp. 273–283, 2000.

[7] A. K. M. F. Uddin, M. Shigeishi and M. Ohtsu, "Fracture Mechanics of Corrosion Cracking in Concrete by Acoustic Emission," *Meccanica*, No. 41, pp. 425–442, 2006.

[8] R. E. Melchers and C. Q. Li, "Phenomenological Modeling of Reinforcement Corrosion in Marine Environments, *ACI Materials Journal*, Vol. 103, No. 1, pp. 25–32, 2006.

© 2008 Taylor & Francis Group, London, UK

[9] L. Zongjin, L. Faming, A. Zdunek, E. Landis and S. P. Shah, "Application of Acoustic Emission Technique to Detection of Reinforcing Steel Corrosion in Concrete," ACI Materials Journal, Vol. 95, No. 1, pp. 68–76, 1998.

[10] M. Ohtsu, M. Uchida, T. Okamoto and S. Yuyama, "Damage Assessment of Reinforced Concrete Beams qualified by AE," ACI Structural Journal, Vol. 99, No. 4, pp. 411–417, 2002.

© 2008 Taylor & Francis Group, London, UK

*Acoustic Emission and Critical Phenomena – Carpinteri & Lacidogna (eds)*
*© 2008 Taylor & Francis Group, London, ISBN 978-0-415-45082-9*

# LOCALIZATION ACCURACY OF MICROCRACKS IN DAMAGED CONCRETE STRUCTURES

**A. Carpinteri, G. Lacidogna and A. Manuello**
Department of Structural Engineering & Geotechnics, Politecnico di Torino, Torino, Italy

## ABSTRACT

In order to investigate fracture mechanisms in concrete, quantitative acoustic emission (AE) techniques can be applied. In this context, a 3D localization of the recorded AE events is required. In a first step of this work, laboratory tests were carried out to evaluate the accuracy of localization results. In addition, to the triangulation process an interesting method for the automatic picking of the AE signals is shown. This method, which analyses the variation in the fractal dimension along the signal trace, allows a 3D localization using a reduced number of AE sensors applied to the external surface of the specimen. A change in the fractal dimension is found to occur close to the transition from noise to signal pulse at the first *P*-wave arrival time and at the first *S*-wave arrival time. In order to set this procedure, AE sources were artificially generated on the surface of the specimens. A six channel acquisition array was used to record AE parameters and waveforms. In a second step the AE technique is applied to evaluate the damage evolution of fiber reinforced beams. These beams, retrofitted by FRP sheets, were tested up to failure under three point bending. During the loading tests, AE source characteristics are determined. In this connection, the authors have tuned an original procedure using advanced techniques that are usually applied for the analysis of seismic events, such as moment tensor and *b*-value analysis.

## 1 INTRODUCTION

Acoustic emission is defined as the spontaneous release of localized strain energy in a stressed material resulting, for example, from micro-cracking and can be recorded by sensors (piezoeletric transducers) applied on the surface of the specimen. AE analysis is a useful method for the investigation of local damage in materials (*Shah and Li* [1], *Carpinteri et al.*[2], *Köppel and Grosse* [3]).

© 2008 Taylor & Francis Group, London, UK

To obtain informations on the damage evolution in materials and structures the cumulative and differential counts of AE events are considered (*Carpinteri and Lacidogna* [4]). Nevertheless to investigate the failure mechanisms of AE sources it is also possible to apply more sophisticated procedures, such as the moment tensor analysis. The use of five or more transducers is required to determine the radiation pattern of a general AE source. Fracture type, size and orientation can be deduced using at least six sensors. The basis for these quantitative methods are the localization techniques to be used in order to extract the source coordinates of the AE events as accurately as possible (*Shigeishi and Ohtsu* [5], *Grosse et al.* [6], *Carpinteri et al.* [2]).

With the localization of AE sources, damage or material flaws can be detected. If AE source characteristics are to be analysed quantitatively in order to investigate damage mechanisms, the knowledge of the source locations is a requirement (*Shigeishi and Ohtsu* [5]). Traditionally source locations are calculated by the differences in arrival times of *P*-waves at different transducers (*Shah and Li* [1], *Carpinteri et al.* [2]). A minimum number of five transducers have to be employed to determine uniquely the three source coordinates and the *P*-wave propagation velocity. The corresponding system of nonlinear equations is solved by an iterative algorithm. Applying a least squares approach, time residuals at the different transducers are calculated and random measurement errors can be recognized. Mean residuals correspond to the theoretical accuracy of the localization result (*Carpinteri et al.*[2]).

This paper proposes a method to identify not only the arrival time of the *P*-waves, but also the arrival time of the *S*-wave. The transversal wave propagation (*S*-waves) together with longitudinal waves (*P*-waves) represent the body waves generated in a medium in which a source of damage is occurring.

The quality of the arrival time determination (picking) is the most crucial factor for the accuracy of localization results (*Köppel and Grosse* [3]). In order to obtain reliable source locations, it is necessary to ensure the correct picking of arrival times. The proposed method allows a 3D localization considering that a change in fractal dimension is found to occur close to the transition from noise to signal pulse at the first *P*-wave arrival time and at the first *S*-wave arrival time. This procedure is automated allowing to improve the results significantly and quickly. A manual determination of arrival times is time-consuming and not reasonable in most cases in view of very large amounts of data (*Boschetti et al.*[7]).

Afterwards, AE technique is applied to evaluate the damage evolution of fiber reinforced beams retrofitted by FRP sheets tested up to failure under three point bending. During the loading tests, AE source characteristics are determined. In this connection, the authors have tuned an original procedure using advanced techniques that are usually applied for the analysis of seismic events, such as moment tensor and *b*-value analysis, (*Carpinteri et al.*[8],[11], *Anzani et al.*[9], *Colombo et al.* [10]).

© 2008 Taylor & Francis Group, London, UK

## 2 LOCALIZATION OF AE SOURCES

Source localization concepts originated in seismology where the aim is to localize the hypocenter or epicentre of an earthquake from seismograms obtained at stations distributed over the Earth's surface (*Geiger* [12]). If the hypocenter is confined into a region of the Earth's interior whose linear dimensions do not exceed a few kilometres, seismologists find it possible (using an array of seismometers and arrival-time data for seismic waves) to determine within reasonable accuracy its location provided wave propagation characteristics are known.

Similar problems are posed when attempting to locate sources of acoustic emission. Again, knowledge of the wave propagation characteristics between source and receiver is necessary. For the most general case, these characteristics depend on the mode of propagation, the elastic moduli, the existence of attenuation due to heterogeneities and the anisotropy of material.

The equations used for source location in concrete are based on the assumptions of homogeneous and isotropic medium and point-like sources, implying spherical wave propagation. Generally speaking, for single point-like sources in geometries having continuous straight line paths between the source and each receiver, the location technique is called "triangulation prucedure" (*Shah and Li* [1], *Carpinteri et al.* [2]). If the observed wavelengths are usually larger than the maximum aggregate size in concrete, a more or less homogeneous and isotropic distribution of the $P$-wave velocity can be assumed. During the first stage, the groups of signals, recorded by the various sensors, that fall into time intervals compatible with the formation of microcracks in the volume analysed, are identified. These time intervals, of the order of micro-seconds, are defined on the basis of the presumed speed ($v_p$) of transmission of the waves ($P$) and the mutual distance of the sensors applied to the surface of the material.

In the second stage, when the formation of microcraks in a three-dimensional space is analysed, the triangulation technique can be applied if signals recorded by at least five sensors fall into the time intervals. Thus, with this procedure it is possible to define both the position of the microcracks in the volume and the speed of transmission of $P$-waves. Having denoted with $t_i$ the time of arrival at a sensor $S_i$ of an AE event generated at point $S$ at time $t_0$, $|S - S_i| = [(x - x_i)^2 + (y - y_i)^2 + (z - z_i)^2]^{1/2}$, the distance between $S_i$ and source $S$, in Cartesian coordinates, and assuming the material to be homogenous, the path of the signal is given by: $|S - S_i| = v_p(t_i - t_0)$. If the same event is observed from another sensor $S_j$ at time $t_j$, it is possible to eliminate $t_0$ from the equation:

$$\left|S - S_j\right| - |S - S_i| = v_p(t_j - t_i) \equiv v_p \Delta t_{ji}. \tag{1}$$

Assuming the arrival times of the signals and the positions of the two sensors to be known, eq. (1) is an equation with four unknowns, $x$, $y$, $z$ and $v$. Hence,

© 2008 Taylor & Francis Group, London, UK

the localisation of $S$ is a problem that can be solved in an exact manner if it is possible to write a sufficient number of equations such as eq. (1), i.e., when an AE event is identified by at least five sensors.

If this did not occur, it would be necessary to adopt simplifying assumptions to reduce the degrees of freedom of the problem.

In the case in which the wave propagation velocity is imposed, and its value is assumed as a characteristic constant of the material, the localization problem is reduced to three unknowns: i.e. the Cartesian position of the source $(x, y, z)$. Other simplifications can be taken when the medium analysed has one or two geometrical dimensions negligible. The localisation procedure can also be performed through numerical techniques using optimisation methods such as the Least Squares Method (LSM) (*Shah and Li* [1], *Carpinteri et al.*[2]). LSM seeks to determine the source location-estimate which minimizes the sum of all squared time-residuals. The non-linear system involved during LSM method is usually solved using iterative techniques with algorithms based on Gauss-Newton's method usually adopted in Seismology (*Shah and Li*[1], *Carpinteri et al.*[2], *Aki and Richards* [13]).

It is clear how the procedure of localization is essential to define the process of damage in the structural elements. A limit of the method is undoubtedly due to the number of AE sensors necessary for the identification of AE point source.

We have observed that, when special conditions allowing to simplify the problem aren't available (speed of wave propagation known a priori or testing geometries in which one or more dimensions can be neglected), the number of AE sensors that have to receive the signal must be equal to five.

It seems favourable to develop a procedure able to locate the point sources with a smaller number of sensors that receive the signal. Very often, some of the key applications of the AE technique are related to monitoring structures in the laboratory or on site, where a large number of sensors represent a serious difficulty because of different geometries and sizes that may occur.

To this purpose, a triangulation method is presented for the automatic picking of first arrivals of a signal by analysing the variation in time of the signal trace fractal dimension (*Boschetti et al.*[7]). A change in the fractal dimension is found to occur close to the transition from noise to signal pulse at the first $P$-wave arrival time and at the first $S$-wave arrival time. The nature of this change varies from trace to trace, but a detectable change is always found to occur (*Boschetti et al.*[7]).

This fact makes it possible to identify both the arrival times of the $P$-wave and $S$-wave for all the applied sensors.

In seismology, the accurate determination of the travel-time of seismic energy from source to receiver allows to determine the hypocentre position. Fundamentally, detection of first arriving seismic data reduces to determining the time when the seismic trace ceases to be composed entirely of noise and also starts to include seismic signal (*Boschetti et al.*[7]).

© 2008 Taylor & Francis Group, London, UK

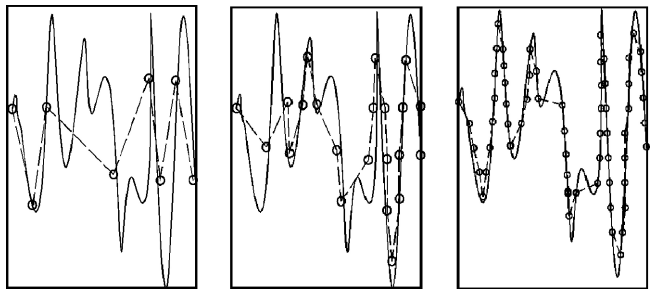



Figure 1: The curve is approximated with a number of steps. With a long step, only the main structures of the curve are approximated (a), while with a shorter step, the segments can follow the line more closely (b, and c).

## 3 FRACTAL DIMENSION ALONG THE SIGNAL TRACE

The AE signal trace can be considered as a digitised curve, along which the relative variation of geometrical and statistics characteristics are analysed independently of the absolute scaling of $x$- and $y$-axis (time and amplitude axis) (*Boschetti et al.*[7]).

In order to calculate the fractal dimension of the trace the "divider method" is used in this work. The basis of the divider method is to measure the length of the curve by approximating it with a number of straight-line segments, which are called "steps" (Fig.1a–c). The calculated length of the curve is the product of the number of steps by the length of the steps. As the step size is decreased, the straight-line segments can follow the curve more closely. Smaller-scale structure becomes more significant, and the calculated length of the curve increases (see Fig.1a–c).

If the data follow a fractal model, it can be written (*D.L. Turcotte* [14]):

$$N(r) \propto r^{-D}, \tag{2}$$

where $N$ is the number of steps necessary to cover the trace, $r$ is the step length, and $D$ is the fractal dimension. To assess the value of the fractal dimension $D$, a series of time windows are considered. These subsequent time windows are positioned along the trace as shown in Fig. 2a. Each of them corresponds to a time interval of about $10^{-4}$ seconds.

For the length $r$, different values, equal to 1/2, 1/4, and 1/8 of the time window size ($\tau$) are considered. In particular in Fig. 2b,the value assumed by the fractal dimension is shown and it corresponds to a time window positioned along the trace where only noise and no signal is detected (part I in Fig. 2a). In this case, plotting the logarithmic number of steps vs. the logarithm of the different values

© 2008 Taylor & Francis Group, London, UK

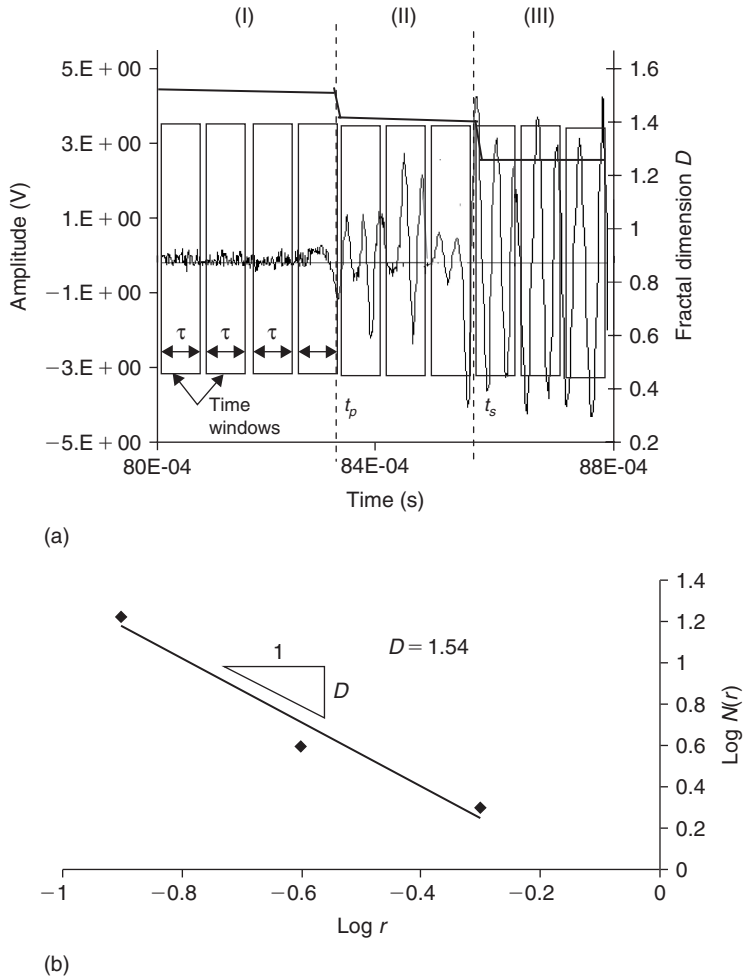



Figure 2: Change in fractal dimension, calculated along the trace of the AE signal. The fractal dimension denotes an abrupt change of its value between phase (I)–(II), and (II)–(III) (a). Fractal dimension corresponds to a time window positioned along the trace where only noise and no signal is detected (b).

of $r$, the graph in Fig. 2b is obtained. The slope of the fitting line is the fractal dimension of the trace and it represents the degree of complexity of the curve being analysed.

Using this procedure, the variation in fractal dimension along the trace can be computed (see Fig. 2a). Considering the values assumed by the fractal dimension, the graph in Fig. 2a can be subdivided into three distinct parts: the first one (I) indicates the fractal dimension of the noise, the second one (II) shows a change in fractal dimension in correspondence of the first $P$-wave arrival time and

© 2008 Taylor & Francis Group, London, UK

the third (III) denotes a further change in $D$, in correspondence of the first $S$-wave arrival time. The change in fractal dimension between phases (I)–(II), and (II)–(III) occurs a few steps after the first arrival time of $P$- and $S$-waves. This happens because the algorithm –implemented by the authors– useful to calculate the fractal dimension $D$, needs a few points to detect the presence of change in the signal trace.

The change in the value of fractal dimension of the signal trace allows to detect on time axis the instants $t_p$ and $t_s$, that can be considered the arrival times of the $P$- and $S$-wave respectively at the sensor position. Therefore, the localization procedure can be done through the following system of equations (*Aki and Richards* [13]):

$$|S - S_i| = (t_{pi} - t_{si}) \left( \frac{v_p v_s}{v_s - v_p} \right), \tag{3}$$

where $S$ is the position of the AE source, $S_i$ is the position of the ith sensor, $t_{pi}$ and $t_{si}$ represent the arrival times at the sensor of $P$-and $S$-waves respectively. It is noted that, considering the propagation speeds of the $P$-waves ($v_p$) and $S$-waves ($v_s$) related by a constant $k$, the problem in four unknowns (described in Section 2) can be solved with the use of only four sensors instead of five. Furthermore, assuming $v_p$ as a characteristic constant of the material, the problem in three unknowns using eq.(3) can be solved employing only three sensors instead of four. The advantages are clear for the localization procedure, where the application of a small number of sensors is usually required.

## 4 LOCALIZATION ACCURACY IN EXPERIMENT

Adopting the localization methods described above, the influences on the accuracy of localization results in concrete were analysed. Experiments were carried out with artificial sources (pencil breaks) at defined positions on the surfaces of a concrete specimen (*Köppel and Grosse* [3]).

Specific tests were designed to produce AE due to pencil breaks in small and predictable regions. A concrete cube with a 300 mm side was cast at the Fracture Mechanics Laboratory of the Politecnico di Torino. Subsequently, an array of six AE sensors was applied to the external surfaces of the concrete element (Fig. 3).

In particular, a grid corresponding to 16 points (stations) was drawn on one face of the concrete cube (Fig. 3b and 4). The tip of a pencil was broken 5 times in correspondence to each station, for a total of 80 measurements. The localization results, which are obtained using 4 sensors and the arrival times of both $P$- and $S$-waves, are shown in Fig. 4a. Figure 4b shows the localization results with 5 sensors and using exclusively the $P$-wave arrival times. In both cases it is possible to locate the AE sources corresponding to the pencil breaks with sufficient accuracy.

© 2008 Taylor & Francis Group, London, UK

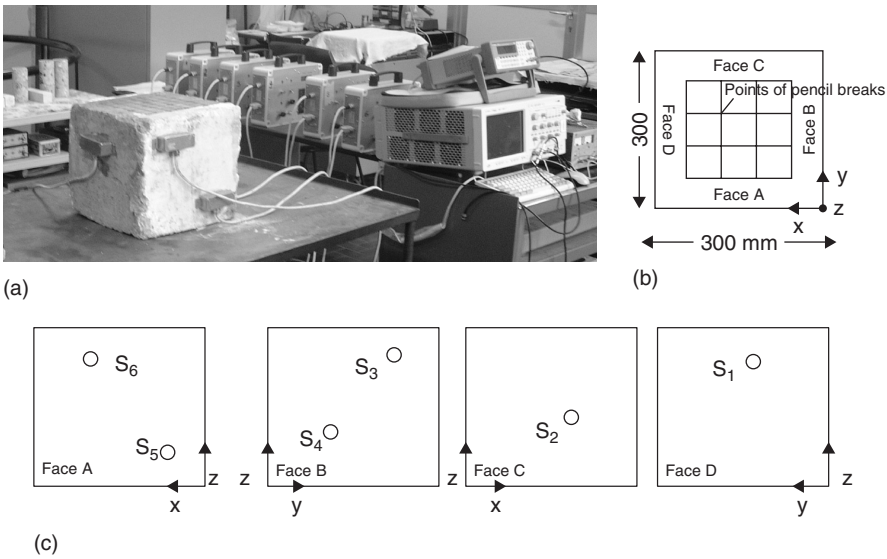



Figure 3: Concrete cube with AE sensors applied on lateral faces (a). the concrete element measures $300 \times 300 \times 300\,\text{mm}^3$ (b). Arrangement of the AE sensors positioned on external surfaces (c).

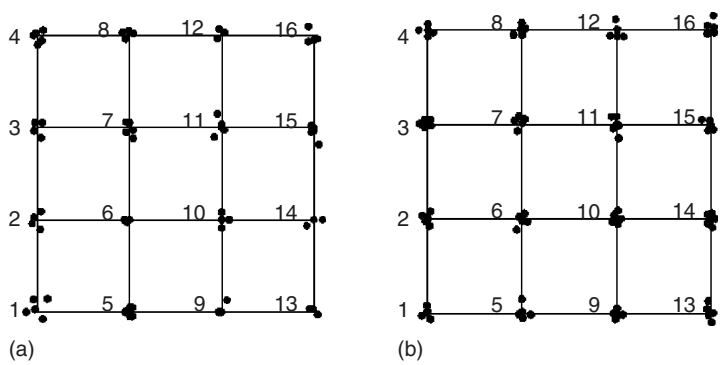



Figure 4: Localization results in the upper face of the concrete element using both *P*-and *S* wave arrival times (a) and using only *P*-wave arrival times and a greater number of sensors (b).

Considering the surface of the cube where the grid is drawn, the maximum errors occurred in both localization methods are c.a. 11 mm. In Figs.5a and 5b the maximum and minimum errors observed in the measurements for each of the grid point are shown. In Figs 5c and 5d the distances measured between the localized points and the grid points are shown for the two localization methods. The line corresponds to the points of pencil breaks (grid points). The graphs

© 2008 Taylor & Francis Group, London, UK

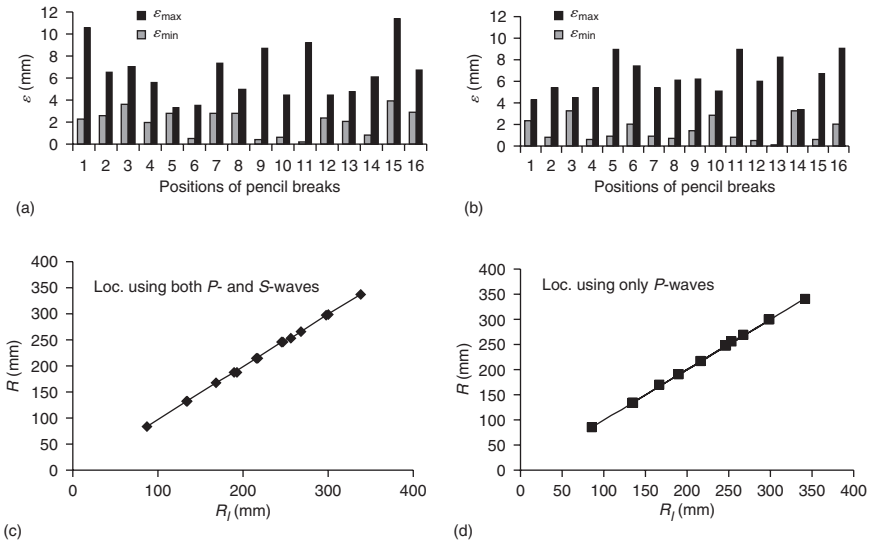



Figure 5: Comparison between the max ($\varepsilon_{max}$) and minimum ($\varepsilon_{min}$) error at each position of pencil break (grid station) using the first arrival times of *P*-waves (a) and using *P* and *S*-wave arrival times (b). Distances measured between localized points and the position of each station of the grid are shown ($R_l$) for the two localization methods (c) and (d). The line corresponds to the points of pencil breaks (grid stations) ($R$).

show that the two localization methods are in good agreement and they are both sufficiently accurate.

In addition, distances ($r_e$) between the barycentre of the sensor array (shown in Fig. 6a) and the localized points corresponding to the maximum error occurred at each station, are computed (Fig. 6a). In this way, it is possible to consider the accuracy of the two localization methods, varying the distance $r_e$. In Fig. 6b, the maximum errors at each station of the grid vs. the distances between each station and the barycentre of the sensor array are shown for the two localization methods.

It is possible to conclude that both localization methods are sufficiently accurate for the tests that require localization of AE sources. In particular, the method using *P*- and *S*-waves arrival times can be used as a valid alternative in the tests in which a small number of sensors represents a necessity.

## 5 CHARACTERIZATION OF AE SOURCES

In the next Sections, the application of the AE technique is proposed for the evaluation of steel fiber reinforced concrete specimens retrofitted by FRP sheets.

© 2008 Taylor & Francis Group, London, UK

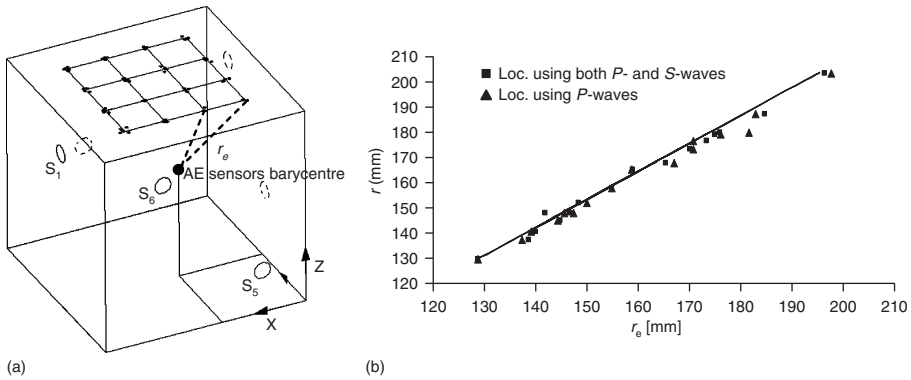



Figure 6: Barycentre of the sensor array (a). $r_e$ is the distance between the barycentre of the sensor array and each point of the grid drawn on the surface of the specimen. $r$ is the distance between each localized point and the barycentre of the sensor array. The graph shows the results for both localization methods (b).

In these tests, the AE activity is analysed using techniques similar to those employed for detection and interpretation of earthquake phenomena (*Carpinteri and Lacidogna* [4], [15]).

In particular, the position of emission sources were carried out in accordance with the indications given in the preceding Sections. Because no special geometric restrictions are present in these tests an array of six sensors and only the P-waves arrival times are used during the localization procedure. Furthermore using the results of triangulation it is possible to assess the type and direction of each crack through the moment tensor procedure. At the end the *b*-value analysis is performed in order to evaluate the statistical distribution of AE activity during damage phenomenon.

A set of steel fiber reinforced (SFRC) beams measuring $1000 \times 150 \times 150\,\text{mm}^3$ were cast and subsequently retrofitted with FRP sheets at the Fracture Mechanics Laboratory of the Politecnico di Torino (Fig. 7). These elements had different fibre contents. For TR 1-2 specimens with a lower fibre content ($40\,\text{kg/m}^3$), Young Modulus ($E_\text{a}$) and average compressive stress ($\sigma_c$) were 35 GPa and 90 MPa respectively. The mechanical parameters for TR 3-4 beams with a higher fibre content ($80\,\text{kg/m}^3$) were $E_a = 41$ GPa and $\sigma_\text{c} = 105$ MPa. The reinforcement, applied externally along the lower side of the elements, consisted of unidirectional carbon fibre laminates in the form 700 mm long and 100 mm wide flat plates, 1.4 mm thick, with Young modulus, $E_r = 165$ GPa. The sheets were bonded on the concrete surface (Fig. 7) by interposing a layer of epoxy adhesive (0.5 mm thick). The elastic modulus, Poisson's ratio, the average compressive stress, the fibre contents in the SFRC beams as well as the mechanical parameters of the FRP sheets are summarized in Table 1.

© 2008 Taylor & Francis Group, London, UK

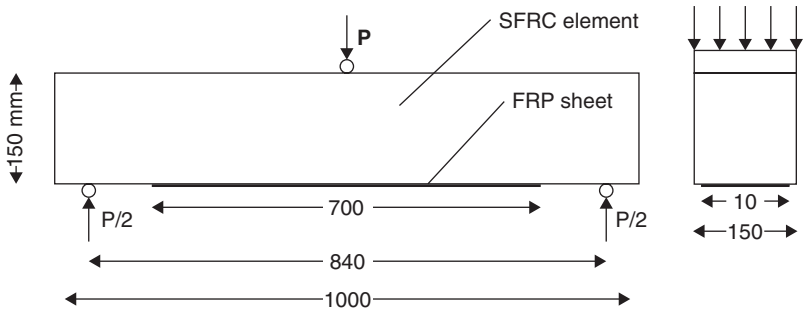



Figure 7: Retrofitted fibre reinforced beam under three point bending.

Table 1: Mechanical parameters of the SFRC beams and FRP sheets.

| SFRC | TR 1-2 | TR 3-4 | FRP | |
|---|---|---|---|---|
| Young's Modulus ($E_a$) | 35 GPa | 41 GPa | FRP Young's * Modulus ($E_r$) | 165 GPa |
| Poisson's Ratio ($\nu_a$) | 0.18 | 0.18 | FRP Max. Tensile Strain | 1.8% |
| Medium Comp. Stress ($\sigma_c$) | 90 MPa | 115 MPa | FRP Tensile Strength** | 2300 MPa |
| Steel Fibre Content | 40 Kg/m$^3$ | 80 Kg/m$^3$ | Adhesive Shear Modulus | 20 GPa |

*ASTM D303 , **ASTM D3039

The beams were tested to failure under three-point bending (*RILEM FMC1* [16]) using a servo-controlled machine (MTS) with a closed-loop control (Fig. 8). In particular, four specimens with the same nominal geometric characteristics (TR1 – TR4) were considered and analysed.

Moreover, the equipment adopted by the authors consisted of six USAM® units for AE measurements, and six pre-amplified piezoelectric (PZT) AE sensors applied to the external surfaces of the specimens (Fig. 8). Such sensors were calibrated on frequencies from 50 through 800 kHz. PZT sensors were used, thereby exploiting the capacity of certain crystals to produce electric signals whenever they are subjected to a mechanical stress.

The USAM® units were synchronized for multi-channel data processing (*Carpinteri et al.* [2],[8]). The most relevant parameters acquired from the signals were stored in the memory of the USAM units and then downloaded to a PC for multi-channel data processing for micro-crack localisation. The signal parameters recorded by each USAM unit include: the first up-threshold crossing

© 2008 Taylor & Francis Group, London, UK

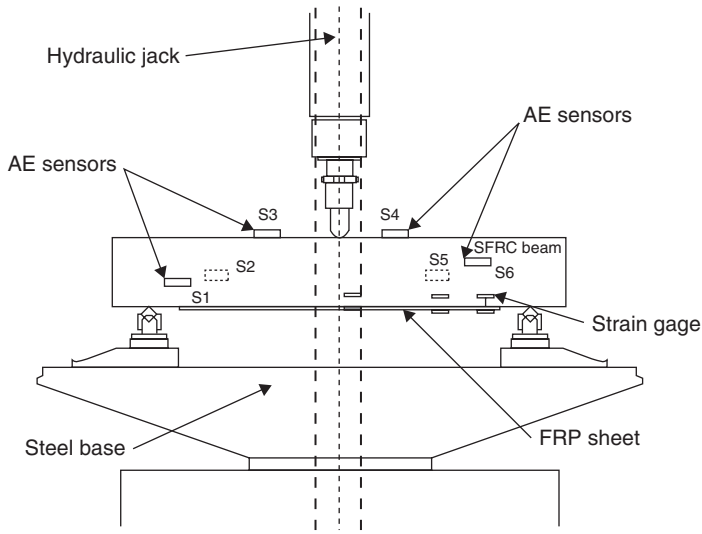



Figure 8: Three point bending experimental setup and positions of AE sensors.

time ($t_0$) for *P*-waves, the last down-threshold time ($t_1$), and the number of threshold crossings.

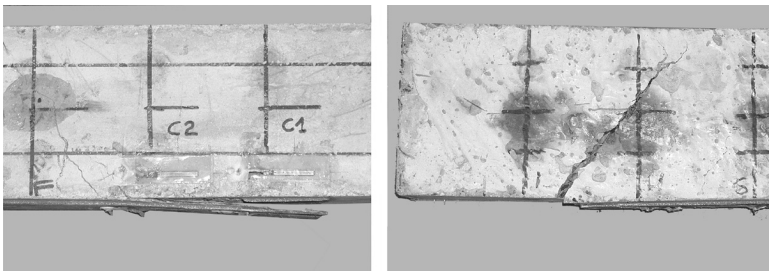
## 6 FAILURE MODES OBSERVED IN FRP RETROFITTED BEAMS

The two conditions requiring rehabilitation most commonly observed in SFRC beams are exceedingly high deformations in service conditions and inadequate load carrying capacity.

In retrofitted structures the most frequently observed failure modes are (*Arduini et al* [17], A*laee and Karihaloo* [18], *Leung* [19], *Taljiesten* [20]): (i) FRP debonding or concrete detachment at the ends of the beam (concrete cover separation), coupled with critical diagonal cracks (CDC); (ii) FRP debonding in the proximity of intermediate flexural cracks (IC); (iii) shear crack propagation in a concrete beam at the end of the FRP plate bonded to it.The presence of an FRP sheet causes two principal failure modes: (i) delamination between the FRP sheet and the concrete surface; (ii) shear failure starting at the cut-off edge of the FRP sheet and spreading through the beam (Fig. 9).

The two failures modes mentioned above were assessed through tests on SFRC beams retrofitted with FRP sheets. In particular, specimens TR1 and TR3 displayed a shear rupture near one of the two lower supports (Fig. 9b). The resulting shear crack propagated across the entire cross-section, with a peak load, after the application of FRP sheet, of approx. 86 kN for specimen TR1 and 65 kN for specimen TR3. For specimens TR2 and TR4, the failure mode was delamination with a peak load of about 65 kN and 85 kN, respectively (Fig. 9a).

© 2008 Taylor & Francis Group, London, UK




(a) (b)

Figure 9: Delamination failure for specimen TR2 (a). Shear crack at the FRP edge for specimen TR1 (b).

## 7 MOMENT TENSOR ANALYSIS

From the theoretical standpoint this study relies on the procedure defined by Shigeishi and Ohtsu (*Shigeishi and Ohtsu* [5]). This procedure characterizes the AE signal by taking into account only the first arrival time of the *P*-waves. The elastic crack displacements **u**(**x**,t), at points **x,** which are the sources of the AE signals, are given by:

$$\mathbf{u}_i(\mathbf{x},t) = G_{ip,q}\,(\mathbf{x},\mathbf{y},t)\,m_{pq} * S(t), \tag{4}$$

where $G_{ip,q}(\mathbf{x},\mathbf{y},t)$ is the space derivative of Green's function, $m_{pq}$ are the moment tensor components, $S(t)$ is the function describing the displacement time-dependence and the asterisk denotes the convolution operator (*Shigeishi and Ohtsu* [5], *Aki and Richards* [13]). Green's functions describe the elastic displacements, $\mathbf{u}(\mathbf{x},t)$, due to a unit displacement applied at **y** at time $t$. In the SiGMA procedure, the magnitude of the elastic displacements, proportional to the amplitude, $A(\mathbf{x})$, of the first *P*-waves reaching the transducers, is given by a modified version of Eq. (4):

$$A(\mathbf{x}) = \frac{C_s\ REF(\mathbf{t},\mathbf{r})}{R}(r_1\ r_2\ r_3)\begin{pmatrix} m_{11} & m_{12} & m_{13} \\ m_{21} & m_{22} & m_{23} \\ m_{31} & m_{32} & m_{33} \end{pmatrix}\begin{pmatrix} r_1 \\ r_2 \\ r_3 \end{pmatrix}, \tag{5}$$

where $C_s$ is a calibration coefficient of the acoustic emission sensors, and $R$ is the distance between the AE source at point **y** and the sensor located at point **x**; vector **r** represents the components of the distance between the source and the sensor; $REF(\mathbf{t},\mathbf{r})$ is the reflection coefficient of the sensitivity of the sensor depending on the angle between the directions of the two unit vectors **r** and **t**; these vectors are the unit vector along the $R$ distance and the unit vector along the sensitivity sensor direction respectively.

© 2008 Taylor & Francis Group, London, UK

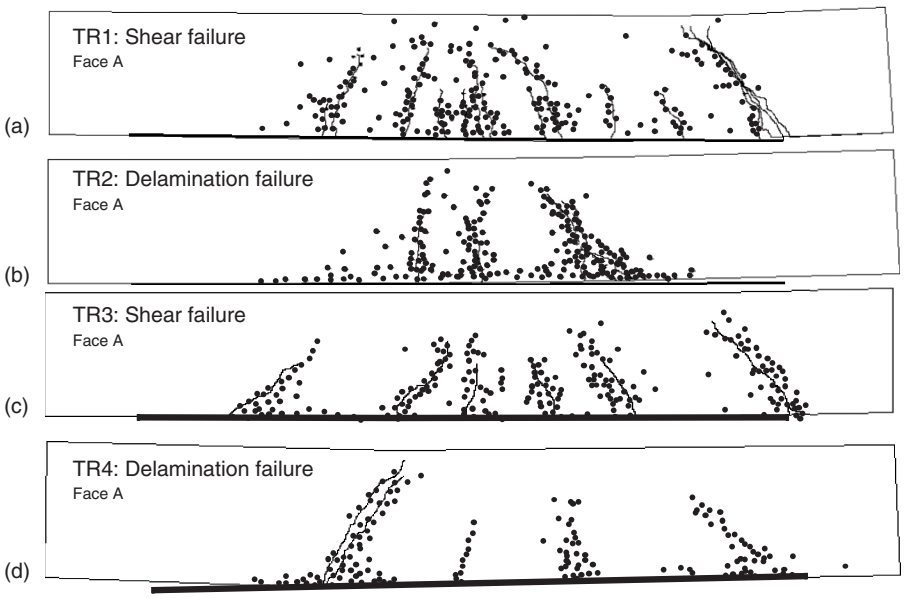



Figure 10: AE sources localization in specimens: TR1 (shear failure) (a), TR2 (delamination) (b), TR3 (shear failure) (c), TR4 (delamination) (d).

To represent the moment tensor, it is necessary to determine the six independent unknowns, $m_{pq}$. The amplitude of the signal, $A(\mathbf{x})$, must be received by at least six AE sensors. Through an eigenvalue analysis of the moment tensor, it is possible to determine the type of crack localised. Using the ratios between the individual eigenvalues and the maximum one, we can write:

$$\frac{\lambda_1}{\lambda_1} = X + Y + Z, \quad \frac{\lambda_2}{\lambda_1} = 0 - \frac{Y}{2} + Z, \quad \frac{\lambda_3}{\lambda_1} = -X - \frac{Y}{2} + Z, \qquad (6)$$

where, $\lambda_1, \lambda_2, \lambda_3$ are the maximum, medium and minimum eigenvalues respectively, $X$ is the component due to shear, $Y$ is the deviatoric tensile component, $Z$ is the isotropic tensile component. Ohtsu classified an AE source with $X > 60\%$ as a shear crack (Mode II), a source with $X < 40\%$ and $Y + Z > 60\%$ as a tensile crack (Mode I), and a source with $40\% < X < 60\%$ as a Mixed Mode crack (*Shigeishi and Ohtsu* [5]). Moreover, from an eigenvector analysis it is possible to determine the unit vectors, **l** and **n**, which determine the directions of the displacement and the orientations of the crack surface.

Using the USAM® equipment the authors have fine-tuned a computer-based procedure including the AE source location and the moment tensor analysis. The 3D AE source positions obtained are overlapped to the 3D crack patterns obtained from the observation of the cracking map (Fig. 10). Damage localization, typology and direction vector of the crack for specimens TR1 and TR2 are

© 2008 Taylor & Francis Group, London, UK

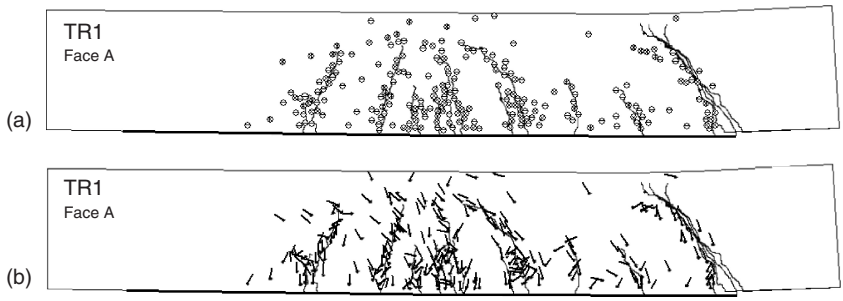



Figure 11: AE sources in TR1: (a) crack type for Mode I, Mode II and Mixed Mode, (b) crack direction for Mode I and Mode II.

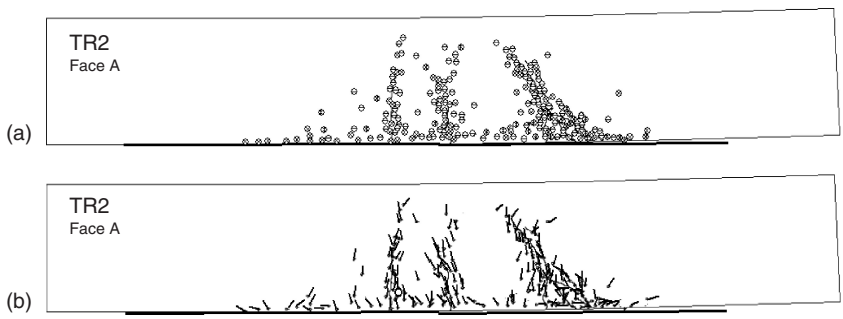



Figure 12: AE sources in TR2: (a) crack type for Mode I, Mode II and Mixed Mode, (b) crack direction for Mode I and Mode II.

shown in Figs. 11, and 12. The position of each emission source, the typologies for Mode I, Mode II and Mixed Mode and the crack directions for Mode I and Mode II are represented according to the notation listed in Table 2.

The crack types identified under three point bending tests were analysed as shown in Figs. 13 and 14. As for specimens TR1 and TR3 (shear rupture), we observe that the percentage of shear cracks (Mode II) becomes progressively comparable with the percentage of tensile cracks (Mode I) in the course of the test (Figs. 13a and b). Beyond a certain distance from the midpoint of the beam, in fact, the cracking maps shown in Figs. 11 and 12 denote that the micro-cracks propagate along oblique crack planes. On the other hand, in the TR2 and TR4 specimens that failed by delamination, Mode I cracks were prevalent. At the end of the test, they consisted of more than 50% of the total number of the events localized (Figs. 13c and d). This behaviour can be interpreted by considering that, during the progress of damage, the specimens experienced flexural cracks near the mid-span position, which are typically classified as Mode I cracks.

The effect of delamination was also quantified by analysing a set of events located in a portion corresponding to a volume of $25 \times 1000 \times 150\,\text{mm}^3$ along

© 2008 Taylor & Francis Group, London, UK

Table 2: Markers of AE sources and labels identifying crack typology and direction.

| Crack Mode | |
|---|---|
| Mode I | ⊖ |
| Mode II | ⊗ |
| Mixed Mode | ⊛ |
| Crack Direction | / |

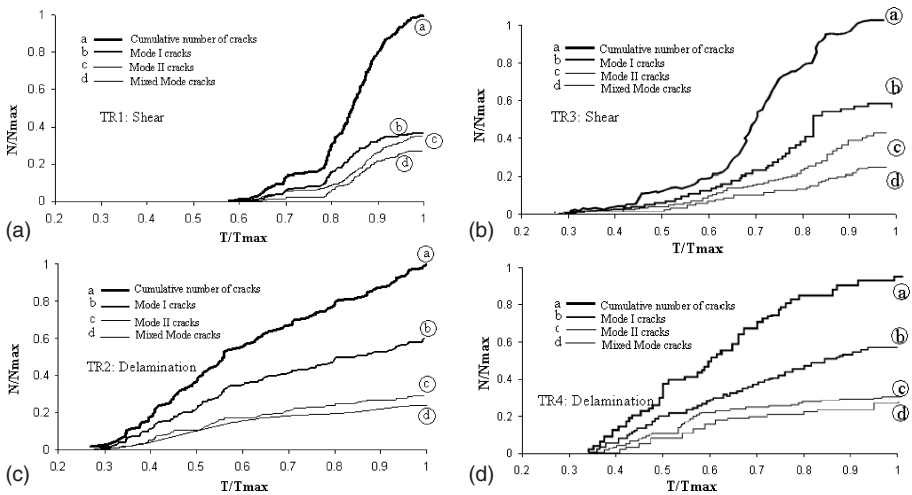



Figure 13: Cumulative number of cracks of different types and total number of cracks for specimens TR1–TR4.

the lower surface of the specimens. This volume was taken to be the damage zone involved in the delamination process between concrete and FRP. As far as the TR1 and TR3 specimens are concerned, the events localized in this representative zone account for less than 20% the total number of events at the end of the tests (see Figs. 14a and b). On the other hand, for TR2 and TR4 specimens (see Figs. 14c and d) the percentage of events coming from this zone is significantly higher (50%) than is observed for TR1 and TR3 specimens. Considering the total amount of events localized during the tests, it should be noted that the delamination process in the TR4 specimen started earlier than in the TR2 specimen, as confirmed by the comparison between the percentages of localized events falling in the delamination process zone. The difference in failure modes is due to the effectiveness of the bonding between the FRP sheet and the concrete surface for the two specimens.

© 2008 Taylor & Francis Group, London, UK

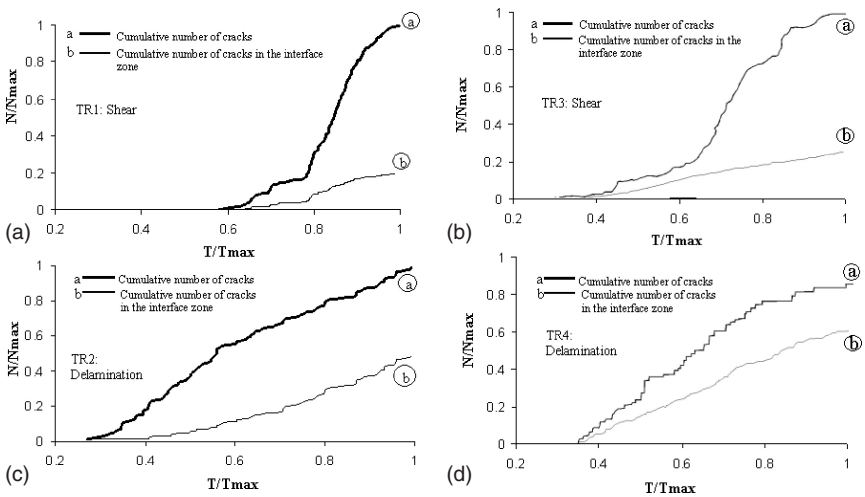



Figure 14: Cumulative number of cracks in the delamination process zone and total cumulative number of cracks for specimens TR1–TR4.

## 8 STATISTICAL DISTRIBUTION OF AE EVENTS

By analogy with seismic phenomena, in the AE technique the magnitude may be defined as follows:

$$m = Log_{10}A_{\max} + f(r), \tag{7}$$

where $A_{\max}$ is the amplitude of the signal expressed in $\mu$V, and $f(r)$ is a correction coefficient whereby the signal amplitude is taken to be a decreasing function of the distance $r$ between the source and the AE sensor. In seismology the Gutenberg-Richter's empirical law(*Richter* [21]):

$$Log_{10}N(\geq m) = a - bm \quad \text{or} \quad N(\geq m) = 10^{a-bm}, \tag{8}$$

expresses the relationship between the magnitude and total number of earthquakes in any given region and time period, and it is one of the most widely used statistical relation to describe the scaling properties of seismicity. In eq. (8) $N$ is the cumulative number of earthquakes with magnitude $\geq m$ in a given area and a within specific time range, whilst $a$ and $b$ are positive constants varying from a region to another and from a time interval to another. Equation (8) is used successfully in the AE field to study the scaling laws of AE wave amplitude distribution. This approach evidences the similarity between structural damage phenomena and seismic activities in a given region of the earth, extending the applicability of the Gutenberg-Richter law to Structural Engineering. According to eq. (8), the "$b$-value" stands for the slope of the regression line in the "log-linear" diagram of AE signal amplitude distribution. This parameter changes systematically at different times in the course of the damage process

© 2008 Taylor & Francis Group, London, UK

and therefore can be used to estimate damage evolution modalities. Scale effects on the size of the cracks identified by the AE technique entail, by analogy with earthquakes (*Carpinteri et al.* [2] *Richter* [21]), the validity of the following relationship:

$$N(\geq L) = cL^{-2b}, \tag{9}$$

where $N$ is the cumulative number of AE events generated by cracks having a characteristic size $\geq L$, $c$ is the total number of AE events and $D = 2b$ is the noninteger (or fractal) exponent of the distribution. It is pointed out that this interpretation rests on the assumption of a dislocation model for the seismic source and requires that $2 \leq D \leq 3$, i.e., the cracks are distributed in a fractal domain comprised between a surface and the volume of the analysed region (*Rundle et al.* [22]).

The cumulative distribution (9) is substantially identical to the one proposed by Carpinteri (*Carpinteri* [23], [24]), according to which the number of cracks with size $\geq L$ contained in a body is given by:

$$N^*(\geq L) = N_{tot}\, L^{-\gamma}. \tag{10}$$

In equation (10), $\gamma$ is an exponent reflecting the disorder, i.e., crack size scatter, and $N_{tot}$ is the total number of cracks contained in a body. By equating distributions (9) and (10), we find that $2b = \gamma$. When the final propagation occurs, defects concentrate along preferential paths, in a narrow band around the final fracture surface. In this case, as shown by Carpinteri et al. (2008) (*Carpinteri* [11], [25]), the self-similarity condition entails $\gamma = 2$. This exponent corresponds to value $b = 1$, which is experimentally approached in structural members during the final crack propagation.

By a subdivision of the loading process into consecutive stages, it is possible to explain the evolution of damage in terms of increasing microcrack density on preferential surfaces. The trends of the $b$-value during the tests conducted on specimens TR1 and TR2 are shown in Fig. 15. In the diagram only the AE signals detected by sensor 3 are considered. This sensor-always located on the middle area of the beams during the two tests (see Fig. 8) – can be considered to give a global representation of the full beams.

In Fig. 15, $b$-value trends are computed for sliding windows of 100 consecutive AE events. In other words, the $b$-values are determined in course of the various testing stages by taking into account current values only and discarding the earlier ones. With this method, already adopted in other works on the analysis of damage in structural concrete elements (*Colombo* [10], *Shiotani* [26], *Raghu* [27]), the testing time was subdivided into 14 and 21 intervals (1400 and 2100 events) for TR1 and TR2 specimens, respectively. In Fig. 15 we observe that the $b$-values related to shear failure become smaller than the $b$-values of delamination specimens after $10 \times 10^3$ seconds, and the final $b$-value is $<1$. In this

© 2008 Taylor & Francis Group, London, UK

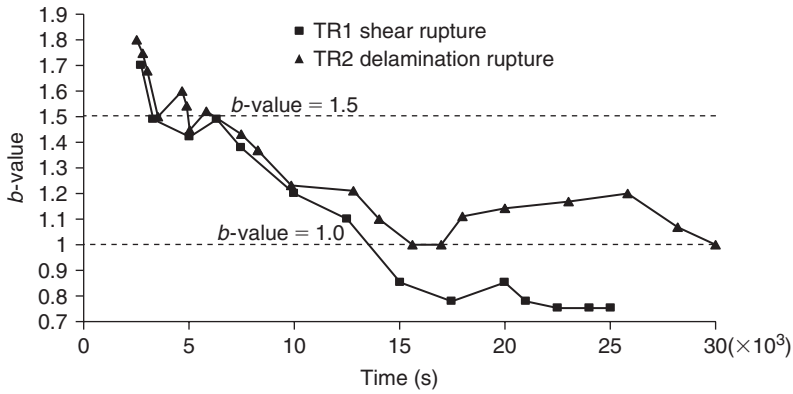



Figure 15: Trends of the *b*-value computed for specimens TR1 and TR2.

case, a complete separation of the specimen has occurred close to the support (*Carpinteri* [11], [25]). Similar trends are observed for specimens TR3 and TR4.

The previous analysis, and particularly the result given by eq. (10), can provide insight into the evolution of the crack size population during the development of cracking and damage, making it possible to interpret the experimentally observed variations in the *b*-value, expressed as already stated as $D/2$.

From Fig. 15, by restricting the analysis to the interval $1 \leq b\text{-value} \leq 1.5$, which entails $2 \leq D \leq 3$, it can be seen that, in the early phases of the loading process, when crack nucleation is the main mechanism, cracks are likely to be evenly spread throughout the volume of the structure ($b$-value $\cong 1.5$ and $D \cong 3$). During the subsequent loading stages, microcracks coalesce into larger cracks and hence the *b*-value begins to decrease below 1.5. Immediately before final collapse, the damaging process concentrates at the cracks near the final failure surface, along the oblique cracks in specimens that failed due to shear, and at the interface between the FRP sheet and the concrete surface in specimens damaged by delamination. At this point, microcrack coalescence is the main damage mechanisms and strong localisation occurs. The number of cracks being proportional to the size of the element analysed, the *b*-value approaches 1 and the fractal dimension of damage $D$ approaches 2. Moreover, the fact that during the final loading stages the *b*-value might drop below 1 does not only signify an increase in damage, but also implies an increase in crack size (*Carpinteri et al.* [11]).

## 9 CONCLUSIONS

Quantitative Acoustic Emission (AE) techniques are applied in order to investigate fracture mechanisms in concrete. In this context, an interesting method for the automatic picking of the AE signals is shown. This method allows a

© 2008 Taylor & Francis Group, London, UK

3D localization using a reduced number of AE sensors applied to the external surface of the specimens. In the second part of this work, loading tests are presented to analyse crack propagation in retrofitted fibre reinforced beams by AE monitoring. In this connection, an original procedure is tuned using advanced techniques that are usually applied for the analysis of seismic events, such as moment tensor and *b*-value analysis. The experimental results demonstrated the effectiveness of the AE technique for the interpretation and prediction of failure modes in these composite structures.

## ACKNOWLEDGMENTS

The authors wish to express their gratitude to Mr. V. Di Vasto for the technical support provided and to Eng. R. Gottardo, Technical Manager of the D.L. Building System DEGUSSA Construction Chemicals Italia, for providing the FRP sheets used in the testing campaign. The financial support granted by the European Union (EU) Leonardo da Vinci Programme –ILTOF Project is gratefully acknowledged.

## References

[1] S P. Shah and Z. Li, "Localisation of Microcracking in Concrete Under Uniaxial Tension," *ACI Materials Journal,* vol. 91, pp. 372–381, 1994.

[2] A. Carpinteri, G. Lacidogna, and G. Niccolini, "Critical Behaviour in Concrete Structures and Damage Localization by Acoustic Emission," *Key Engineering Materials*, vol. 312, pp. 305–310, 2006.

[3] S. Köppel and C.U. Grosse, "Advanced Acoustic Emission Techniques for Failure Analysis in Concrete", *Proceedings of 15th World Conference on Nondestructive Testing,* Roma, 2000.

[4] A. Carpinteri, and G. Lacidogna, "Damage Monitoring of an Historical Masonry Building by the Acoustic Emission Technique" *Materials and Structures,* vol. 20, pp. 143–149, 2006.

[5] M. Shigeishi, and M. Ohtsu, "Acoustic Emission Moment Tensor Analysis: Development for Crack Identification in Concrete Materials," *Construction and Buildings Materials,* vol. 15, No. 5–6, pp. 311–319. 2001.

[6] C.U. Grosse, H.W Reinhardt, and F. Finck, "Signal Based Acoustic Emission Techniques in Civil Engineering," *ASCE Journal of Materials in Civil Engineering*. , vol. 15, No. 3, , pp. 274–279, 2003.

[7] F. Boschetti, M Dentith and R. D. List, "A fractal based algorithm for detecting first arrivals on seismic traces", *Geophysics*, vol. 61, pp. 1095–1102, 1996.

© 2008 Taylor & Francis Group, London, UK

[8] A. Carpinteri, Lacidogna, G. and Manuello, A. "An Experimental Study on Retrofitted Fiber-Reinforced Concrete Beams using Acoustic Emission", in *Fracture Mechanics of Concrete Structures, Proceedings of the 6th International FraMCoS Conference, Catania, Italy*, vol. 2, pp.1061–1068, 2007.

[9] A. Anzani, L. Binda, A. Carpinteri, G. Lacidogna, and A. Manuello, "Evaluation of the Repair on Multiple Leaf Stone Masonry by Acoustic Emission" *Materials and Structures (RILEM)*, accepted: September 2007, DOI 10.1617/s11527-007-9316-z.

[10] S. Colombo, I.G. Main, and M.C. Forde, "Assessing Damage of Reinforced Concrete Beam Using *b*-Value Analysis of Acoustic Emission Signals," *ASCE Journal of Materials in Civil Engineering*, vol. 15, No. 3, pp. 280–286, 2003.

[11] A., Carpinteri, G., Lacidogna, G., Niccolini, and S., Puzzi, "Morphological Fractal Dimension Versus Power-Law Exponent in the Scaling of Damaged Media," *International Journal of Damage Mechanics*, in print, 2007.

[12] L. Geiger, "Probability Method for the Determination of Earthquake Epicentres from the Arrival Time Only", *Nachrichten von der Koniglichen Gesellschaft der Wissenschaften zu Gottingen,* vol. 4 pp. 331–349, 1910.

[13] K. Aki, P.G. Richards "Quantitative Seismology, Theory and Method", *2nd ed. University Science Books*, Sausalito CA, 1980.

[14] D.L. Turcotte, "Fractals and Chaos in Geology and Geophysics" *Cambridge University Press,* 1997.

[15] Carpinteri, A. Lacidogna, G., "Structural Monitoring and Integrity Assessment of Medieval Towers", *Journal of Structural Engineering (ASCE)*, vol.132, pp. 1681–1690, 2006.

[16] RILEM FMC1, "Determination of the Fracture Energy of Mortar and Concrete by Means of Three-Point Bend Tests on Notched Beams," *Materials and Structures (RILEM)*. vol. 18, No. 106, pp.285–290, 1985.

[17] M. Arduini, A. Di Tommaso, and A. Nanni, "Brittle Failure in FRP Plate and Sheet Bonded Beams," ACI *Structural Journal*, vol. 94, No.4, pp.363–370, 1997.

[18] F.J. Alaee, and B.L. Karihaloo, "Fracture Model for Flexural Failure of Beams Retrofitted with CARDIFRC," *ASCE Journal of Engineering Mechanics,* V. 129, No. 9, pp.1028–1038, 2003.

[19] C.K.Y. Leung, "Delamination Failure in Concrete Beams Retrofitted with a Bonded Plate, "*ASCE Journal of Materials in Civil Engineering*, vol.13, No. 2, pp. 106–113, 2001.

[20] B. Taljiesten, "Strengthening of Beams by Plate Bonding," *ASCE Journal of Materials in Civil Engineering,* vol. 9, No. 4, pp.206–212, 1997.

[21] C. F. Richter, "Elementary Seismology," W.H. Freeman, San Francisco and London, 1958.

© 2008 Taylor & Francis Group, London, UK

[22] J. B. Rundle, D. L. Turcotte, R. Shcherbakov, W. Klein, and C. Sammis, "Statistical Physics Approach to Understanding the Multiscale Dynamics of Earthquake Fault Systems," *Reviews of Geophysics*, V. 41, No. 4, pp. 1–30, 2003.

[23] A. Carpinteri, "Mechanical Damage and Crack Growth in Concrete: Plastic Collapse to Brittle Fracture", Martinus Nijhoff Publishers, Dordrecht, 1986.

[24] A. Carpinteri, "Scaling Laws and Renormalization Groups for Strength and Toughness of Disordered Materials," *International Journal of Solids and Structures,* vol. 31, No. 3, pp. 291–302, 1994.

[25] A. Carpinteri, G. Lacidogna, G. Niccolini, and Puzzi, S., "Critical Defect Size Distributions in Concrete Structures Detected by the Acoustic Emission Technique," *Meccanica,* 2007, in print. DOI: 10.1007/s11012-007-9101-7.

[26] T. Shiotani, S. Yuyama, Z. W. Li, and M. Othsu, "Quantitative Evaluation of Fracture Process in Concrete by the Use of Improved *b*-value," *5th Int. Symposium Non-Destructive Testing in Civil Engineering*, Eds. Elsevier Science, Amsterdam, pp. 293–302, 2000.

[27] B. K. P. Raghu, and Sagar, R. V., "An Experimental Study on the Development of Fracture Process in Plain Concrete Beams Using *b*-value Analysis of AE signals," *Fracture Mechanics of Concrete and Concrete Structures, Proceedings of the 6th International FraMCoS Conference, Catania, Italy*, Eds. Carpinteri et al., V. 1, pp. 233–242, 2004.

© 2008 Taylor & Francis Group, London, UK

## *1.3 AE damage quantification in civil structures*

© 2008 Taylor & Francis Group, London, UK

*Acoustic Emission and Critical Phenomena – Carpinteri & Lacidogna (eds)*
*© 2008 Taylor & Francis Group, London, ISBN 978-0-415-45082-9*

# CONTRIBUTION OF AE MONITORING TO THE NEW ERA OF SUSTAINABLE CIVIL STRUCTURES

**T. Shiotani**
Research Institute of Technology, Tobishima Corporation, Chiba, Japan

## ABSTRACT

To sustain on going social activity, such infra-structures as bridges, dams, tunnels as well as natural civil structures shall be maintained with a proper manner. Recent lowering of infra-investments due to rapid aging of the human population resulting from the decline in the birth rate dwindling tax revenues, makes it an un-trivial task. Accordingly an appropriate allocation program of the budget over the structures to be repaired would be necessarily conducted. Additionally, there are two cases: civil structures are repaired along with monitoring; and those preserve in-service together with monitoring until repair. Acoustic emission monitoring could be applicable for both cases. Real time criticality/stability of structures can be assessed by continuous AE monitoring, while the current damage/integrity of structures can be estimated by short-term AE monitoring. In the present paper, such two applications of AE monitoring are described showing in-situ monitoring of rock and concrete materials.

## 1 INTRODUCTION

In Japan many infra-structures enthusiastically built since 1950s are approaching to their safe life age. Correspondingly, maintenance works are expected to rise dramatically. However, recent lowering of infra-investment makes it difficult to repair all the structures requiring attention. In order to allocate a limited budget to the structures really needed to be repaired, it is crucial to rank the severity of damage in structures on the basis of assessment of health status. On the other hand, since more than 70% of Japanese land is covered with mountainous areas social activity must somehow cope with surrounding steep slopes since slope failure or landslides are a constant threat to people and infrastructures. Acoustic emission technique has potential to contribute to the aforementioned two crucial issues i.e., AE activity from existent defects is used to quantify the damage of structures, and real-time AE activity provides precursor of eventual failure in slopes. In the present paper, basics of AE testing are introduced and

© 2008 Taylor & Francis Group, London, UK

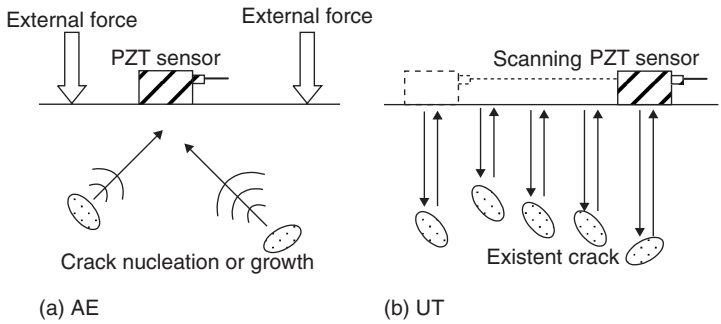



Figure 1: Configuration of AE and UT.

actual rock monitoring, followed by damage diagnosis of concrete structures, are discussed.

## 2 ACOUSTIC EMISSION

### 2.1 Piezoelectric signals

AE (acoustic emission) and UT (ultrasonic testing) both utilize the similar piezoelectric sensors against external stress input; however, in the case of AE the wave released from the defects/cracks under external load, while in the case of UT the waves detected by a sensor was originally excited by another or the same sensor (see Fig. 1). Accordingly AE is referred to as passive monitoring, and UT is referred to as active monitoring. As mentioned AE is defect/crack related emissions from materials. Specifically there are two types of AE activities: one is primary AE activity due to crack nucleation, coalescence and formation; and the other is secondary AE activity resulted from the friction between the interfaces of existent cracks. AE has thus been used broadly not only to characterize processes of materials fracture that detect primary AE activity but also applying for the damage assessment of structures in which the secondary AE activity is utilized. To enhance the weak signals to detected ones, resonant frequency characteristics of piezoelectric element is utilized to AE sensors that is different from accelerometers. Thus the AE sensor should be selected as to consider the scale of fracture and kinds of materials. Then the care should be taken that the detectable range and frequency is a trade-off relation i.e., as shown in Fig. 2 the higher the frequency is employed, the larger the attenuation rate of elastic wave becomes. The frequency response of sensor employed should thus be considered to correspond to the objective fracture scale (e.g., microscopic failure happens transiently while macroscopic failure is generated rather slowly, correspondingly high frequency and low frequency, respectively).

© 2008 Taylor & Francis Group, London, UK

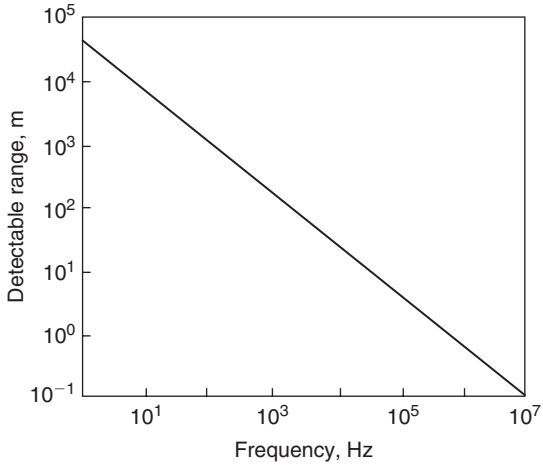



Figure 2: Relations between detectable ranges and frequency components.

## 2.2 AE parametric features

Differed to continuous waves, AE signals emerge rapidly and randomly. The discrimination of AE signal waves from the running waveform is carried out by means of "threshold," namely a voltage level on an electronic comparator. Only signal waveforms exceeded the threshold are identified as AE signals. Conventionally used AE parametric features are: hit, count, amplitude, duration and energy (see Fig. 3) with reference to ISO 12716 2000. It is noted that the aforementioned protocol for identifying AE signals is developed for extracting AE parametric features only i.e., the recording condition of signal waveform is individually given by a sampling rate and the number of samples (e.g., 1 μs and 1024 samples, respectively).

## 2.3 AE based damage/fracture indices

Under incremental cyclic loads in concrete, AE activity can be represented with damage progress as shown in Fig. 4, provided that damage progress is classified into four different levels: intact; almost intact; slightly damaged; and heavily damaged. Due to crack occurrence, AE activity starts to be observed in a loading stage in the first cycle, and in subsequent second load cycle, the AE activity starts at the load level of maximum prior load. This coincidence between pre-stress and applying stress is referred to as Kaiser effect and have been studied to evaluate initial rock stress (e.g., Seto et al [1]). During the third load cycle in which the material shows slightly damaged, the onset of AE appearance is observed at a smaller level than previously. Decrease of effective areas against external force or accumulation of microcracks within materials appear to play a significant role in

© 2008 Taylor & Francis Group, London, UK

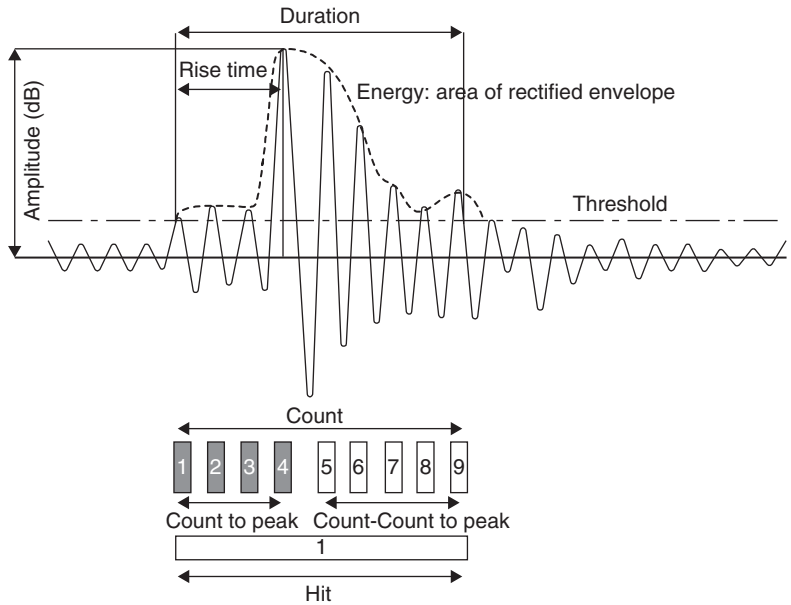



Figure 3: Convenctional AE parametric features.

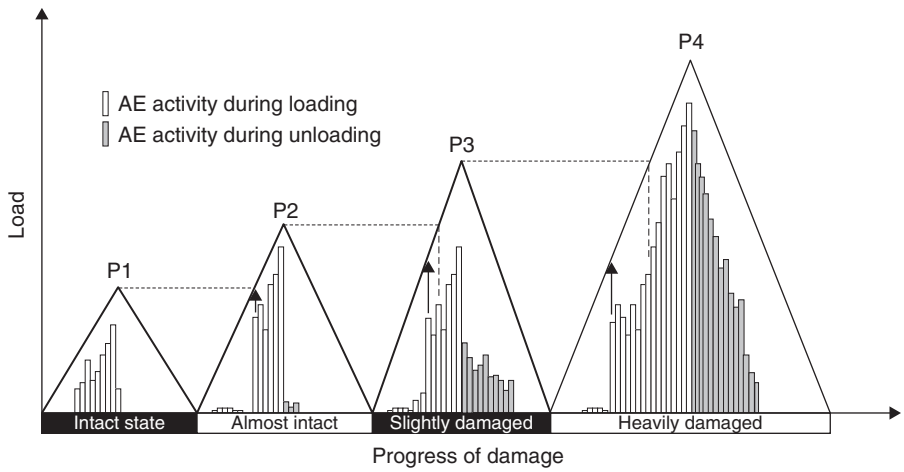



Figure 4: Representation of AE activity due to damage progress in concrete.

this. Considering the relation of AE activity to the stress level experienced, such damage-indices as Felicity ratio (Fowler [2]), CBI ratio (Yuyama et al [3]), and Load ratio (JSNDI [4]) have already been proposed. With damage evolution, not only the AE activity during uploading, but that during unloading becomes more

© 2008 Taylor & Francis Group, London, UK

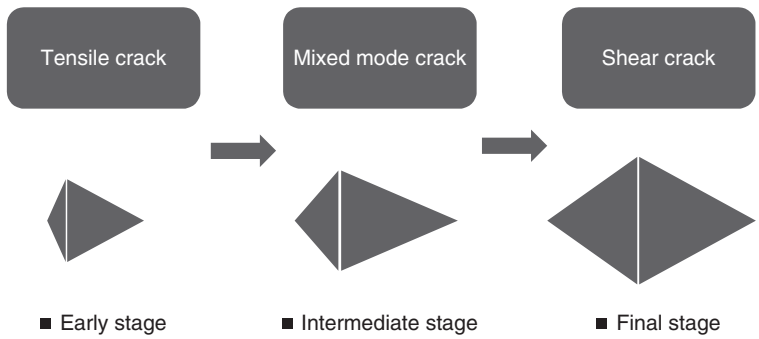



Figure 5: Expecting variations of waveform with progress of fracture.

intense. Therefore, it is also important to focus attention on unloading processes (Shiotani et al [5]). Accumulation of shear type of cracks seems to be attributed to this phenomenon. The ratio of accumulated number of AE activity during uploading to that during a whole loading cycle is refereed to as Calm ratio (JSNDI, [4]).

For the ratios mentioned previously, they may be difficult to apply for in-situ monitoring since evaluation of the maximum stress in which materials have experienced is not an easy task. Thus, a RTRI ratio has been proposed instead (Luo et al [6]). The RTRI ratio can be defined with regard to any measured mechanical parameters, such as stress/load, strain/deformation. Specifically it is the ratio of the value of the parameter when AE is initiated divided by the maximum value of this parameter during the inspection period, regardless of the maximum load in the whole loading history of structures.

Figure 5 illustrates the variation of waveforms with fracture processes. In the process of progressing fracture within materials, tensile type of cracks would be mostly obtained in early stage, then mixed mode of tensile and shear type, followed by shear type of cracks (Yuyama et al [7]). It is known that tensile fracture velocity ranges from P-wave to 60–70% of S-wave velocity and shear fracture velocity would be 60–70% of S-wave velocity (Kanamori [8]). Hence corresponding to the variation of crack types, it is expected that fracture velocity becomes smaller with progress of fracture although dislocation-scale becomes larger. This implies two important aspects in AE waveforms. One is that gradients of ascending parts of waveforms become smaller with the progress of fracture. The other suggests that low-frequency components would be dominant with progressing fracture. Therefore '*grade*' is introduced, which is defined as the peak amplitude divided by the rise time. The large values of *grade* suggest the early stage of fracture where cracks of tensile type are dominantly generated, while smaller ones correspond to the final stage where cracks of shear type primarily occur (see Fig. 5). Indeed as shown in Fig. 6, the *grade* due to tensile type of failure exhibits the largest value followed by mixed type and the shear

© 2008 Taylor & Francis Group, London, UK

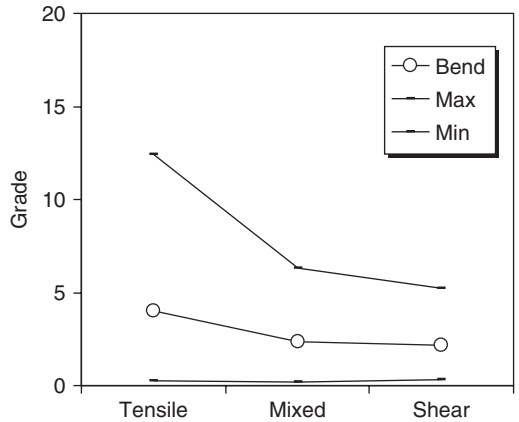



Figure 6: Variation of grade (dB/μs) due to different type of fracture in four point bending test of RC. Fracture type characterization was implemented by SiGMA procedure (Ohtsu et al. [13]).

type of fracture. It is noted that applicability of the gradient has also been studied on the process of concrete materials (Iwanami et al [9]) or classification of types of cracks in combination with average frequency (JCMS-III B5706-2003 code).

Because AE peak amplitude is associated with the scale of fracture, the *b*-value that is defined as a slope of the amplitude distribution is known as an effective index related to the states of fracture (Mogi [10], Scholz [11]). Larger *b*-values show the state of materials where microscopic fractures occur more predominantly than macroscopic fractures, whereas smaller *b*-values indicate that the occurrence of macro-fractures prevails. Since the *b*-value was originally defined in seismology i.e., obtained in a long time span and precise observation was possible with a lot of numbers of observatories, there existed issues to be addressed in case of AE applications. Thus, instead of the seismic *b*-value, an improved *b*-value (I*b*-value) has been proposed (Shiotani *et al*. [12]), which is suitable for AE applications ranging from concrete to rock materials.

In the improved *b*-value analysis, the number of AE data to be used should be first set. Roughly, two methods for determining the calculation number have conventionally been employed: (a) accumulated numbers from the beginning data; and (b) numbers per unit time. In the former case, the number of data used to determine the *b*-value is increasing with elapsed time. In the latter case, because the AE activity increases exponentially with approaching final failure, it is apparent that the number of AE data determining the *b*-value is differed in each unit time. Accordingly, it is important to use the constant number of AE data when determining the *b*-value. To improve the calculation of the *b*-value,

© 2008 Taylor & Francis Group, London, UK

the number of AE data: $\beta$, is introduced as in (1):

$$\int_0^\infty n(a)da = \beta \tag{1}$$

where $a$ is an amplitude, $n(a)$ is a number of AE at $da$ and $\beta$ is a number of AE data. Values of $\beta$ between 50 and 100 are considered appropriate as suggested by enormous studies (Shiotani et al [14]). In actual, in the improved $b$-value calculation, a fixed number of $\beta$ between 50 and 100 should be used throughout the whole experimental data.

The value of AE peak amplitude varies with monitoring conditions such as sensor installations, propagation media, and occurrence locations, resulting that the AE amplitude distribution is also dependent on these conditions. In order to obtain the $b$-value qualitatively, a method to determine the amplitude interval being independent on the distributed amplitude is necessary. In the improved $b$-value analysis, the range of AE amplitude is determined based on such statistical values as the mean $\mu$ and standard deviation $\sigma$, where the upper amplitude $w_2$ and lower $w_1$ are formulated as $\mu + \alpha_1\sigma$ and $\mu - \alpha_2\sigma$, respectively. Defining the accumulated numbers of amplitude over $w_1$ and $w_2$, as $N$ $(w_1)$ and $N$ $(w_2)$, which is obtained by,

$$N(w_1) = N(\mu - \alpha_2\sigma) = \int_{\mu-\alpha_2\sigma}^\infty n(a)da \tag{2}$$

$$N(w_2) = N(\mu + \alpha_1\sigma) = \int_{\mu+\alpha_1\sigma}^\infty n(a)da \tag{3}$$

where, the interval of amplitude analyzed would be $(\alpha_1 + \alpha_2)\sigma$. Then the I$b$-value is given by,

$$Ib = \frac{\log_{10} N(w_1) - \log_{10} N(w_2)}{(\alpha_1 + \alpha_2)\sigma} \tag{4}$$

where, $\alpha_1$ and $\alpha_2$ are empirical constants. It is noted that since I$b$-value is calculated on the basis of decibel unit. When comparing with seismic $b$-value, the I$b$-value shall be multiplied by a coefficient of 20. The I$b$-value has successfully been applied to evaluate the developing process of fracture in such fields as soil (Shiotani et al. [15]), rock (Shiotani et al. [16, 17]), and concrete (Shiotani et al. [14, 18, 19]).

© 2008 Taylor & Francis Group, London, UK

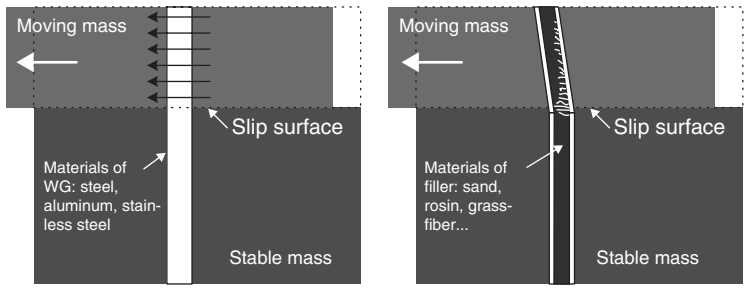



Figure 7: Two types of wave-guides devised to monitor geotechnical materials.

## 3 ROCK APPLICATION

### 3.1 Installation of AE sensors

In the case of AE monitoring for rock slope stability, effective detection of AE waves generated due to rock deformation is usually difficult because AE waves are strongly attenuated when they propagate through joints of rock. In geotechnical application of the AE technique, to avoid energy attenuation of AE waves and to drive weak AE signals to the sensors, wave-guides are conventionally employed (Hardy et al [20], Nakajima et al [21]). There are two types of the wave-guides. One is low-attenuation solid type, devised as to lead weak AE signals to AE sensors. Metal is generally adopted in this case as shown in Fig. 7(a). In this type, AE waves due to friction between the wave-guide and deforming soil are generated. Another type is the deformation-related wave-guide, designed as to generate self-emissions due to deformation of the guide corresponding to the soil motion as shown in Fig. 7(b). Pipes are used for this type of wave-guides filled with sand rosin or fiberglass. In this hollow type, AE waves are generated due to fracture of the filler. It is noted that the detected AE signals by those types of wave-guides are not emissions that are directly generated from soil but indirectly produced due to interaction between the wave-guides and soil mass or self-breakage. Since strong attenuation of soil does not allow AE signals to reach the sensors sufficiently, this indirect monitoring of AE activity has been commonly used in slope stability measurements.

With regard to rock monitoring these wave-guides are difficult to apply since they are devised for relatively ductile materials like soil. Unlike soil, rock materials exhibit brittle nature and deformation is expected quite smaller than of soil. Moreover since they include macroscopic joints, high attenuation rate could not avoid. Therefore it is not easy to detect AE signals especially after passing through the joints. Desirable conditions to detect AE signals in rock stability

© 2008 Taylor & Francis Group, London, UK

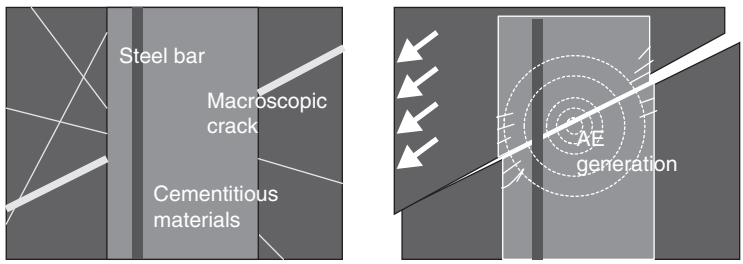



Figure 8: Behavior of the borehole by WEAD under deformation of rock.

monitoring are as follows: AE waves can propagate up to the AE sensor as to avoid strong attenuation influenced by the existent joints, characteristics of AE waves detected should reflect actually caused fracture mechanisms, and stability of the rock can be reasonably evaluated by the AE signals acquired.

In order to meet the above conditions specifically on rock AE monitoring, a prospective way of sensor installation, namely WEAD (wave-guide for AE waves due to rock-deformation) has been developed (Shiotani et al [22]). The WEAD consists of cementitious materials and reinforcement with AE sensors. In order to know the mechanical properties of rock as well as to determine the effective monitoring areas, core sampling is performed for some representative locations before installing AE sensors. In the WEAD the cementitious material is designed with reference to the mecanical properties of the retrieved core samples. In this way, as shown in Fig. 8, the WEAD would deform corresponding to the deformation of surrounding rock, leading generation of AE waves within the cementitious material. Thus fracture of the WEAD occurs similarly to those of the deformed rock. As a result, characteristics of the AE waves are compatible to those due to actual rock-deformation. Because the initial state of the WEAD is intact, AE waves generated can efficiently propagate to the AE sensors. The WEAD has another advantage. Since the filler is made of known materials, it can be reproduced in laboratory and AE characteristics of the filler with evolving steps of fracture can be obtained experimentally. Then, comparing field data with empirical ones, a fracture condition of actual rock can be readily evaluated. It is noted, when the WEAD contains many cracks due to the deformation progress in the surrounding rock, it may be difficult to detect AE signals effectively. To resolve this issue, reinforcement of steel bar is installed into the borehole along with AE sensors. This enables to detect AE signals until the final failure. It should be mentioned that these AE waves are indirectly obtained through reinforcement similarly to the wave-gude for geotechnical materials (see Fig. 7), and therefore actual fracture mechanism cannot be examined with those; however, AE counting or scale of AE energy-parameters can provide crucial information on the final stage of fracture.

© 2008 Taylor & Francis Group, London, UK

Table 1: Empirically obtained fracture evaluation criteria.

| AE parameters | | | | Fracture levels estimated | Fracture conditions & patterns expected |
|---|---|---|---|---|---|
| Count | Energy | I*b*-value | *Grade* | | |
| –40 | –50 | increase up to 0.15 | 10– | I | Early stage in bending |
| | 50–100 | decrease down to 0.04 | | II | Intermediate stage in bending |
| | | Repetition between I & II | 5–10 | III | Final stage in bending |
| 40– | 100–200 | | –5 | IV | Final stage in bending & early stage in shear |
| | 200–300 | Vibration between 0.02 to 0.06 | | V | Intermediate stage in shear |
| | 300– | | | VI | Final stage in shear |

Other condition requirements for rock monitoring of AE are the elimination of ambient noises such as mechanical impact due to raindrops and electric noise. These can be found in the literature (Shiotani [23]).

## 3.2 Example of rock slope monitoring

### 3.2.1 Monitoring condition

Geologically, a monitoring site is made of hornfels dipping with slope angle 80°. In the slope, it was observed that many diagonal joints are lying perpendicular to the slope surface. AE monitoring was carried out with the WEAD as shown earlier. Making reference to the mechanical properties of rock the composition of grouting material was determined, and criteria of fracture stages was established empirically as shown in Table 1. Figure 9 shows the sensor arrangement and joint condition. Five AE sensors (60 kHz) equally spaced along reinforcement (nominal diameter of 13 mm) by 1.50 m were installed into the slope and additional one AE sensor (60 kHz) was placed in the control room to monitor background noise. To eliminate raindrop-induced AE activity, a surface portion of the borehole was filled with sand down to 1.0 m (Shiotani [22]). AE signals generated from the slope were amplified by 40 dB at sensor-integrated preamplifiers, and the signals over the threshold 40 dB were acquired for their parametric features as well as waveforms by a Mistras AE system (Physical Acoustics Corporation).

© 2008 Taylor & Francis Group, London, UK

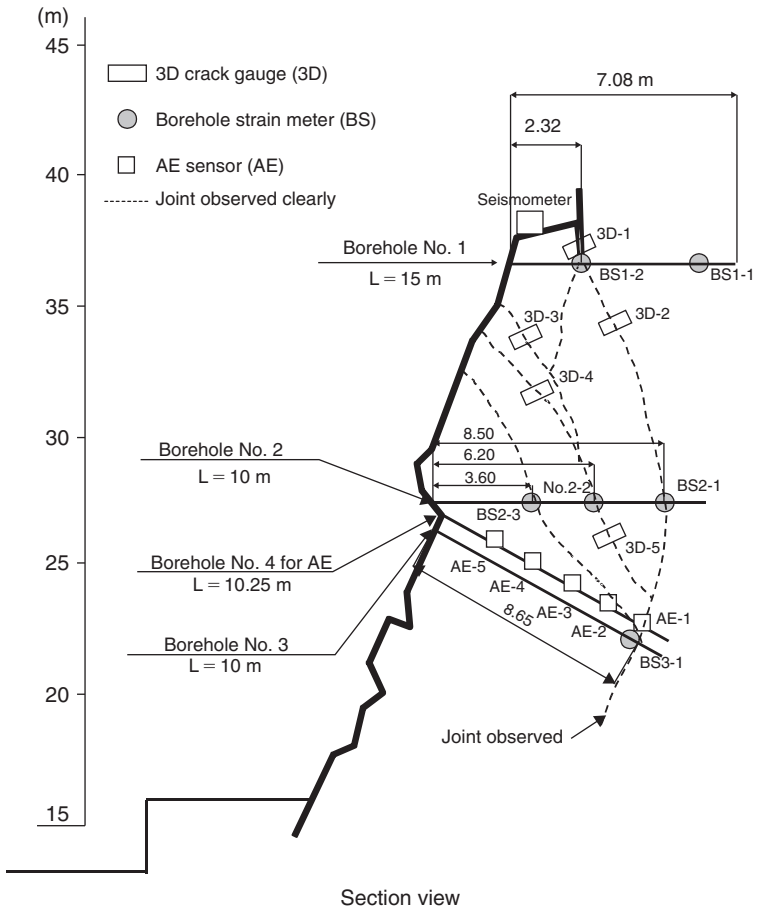



Figure 9: Sensor configuration of rock slope.

In this site, a seismometer, crack gauges in three dimensions and borehole strain gauges were also placed.

### 3.2.2 Data interpretation

Since AE sensors are linearly placed along the borehole in the WEAD, one-dimensional sources can be identified as shown in Fig. 10 based on the wave velocity within the filler. The diameter of circle reflects the scale of averaged ring-down counts of a set of AE hits attributed to the AE event.

Through three-year monitoring, remarkably large scale of AE sources were not observed excluding the end of 1999. Specifically at the beginning of December 1999, AE sources are intensively observed between 4 m and 5 m (around the location of Ch-3) along the borehole. Figure 11a shows the *grade* for Ch-3 during the period. Between November and December, two drops can be found including one

© 2008 Taylor & Francis Group, London, UK

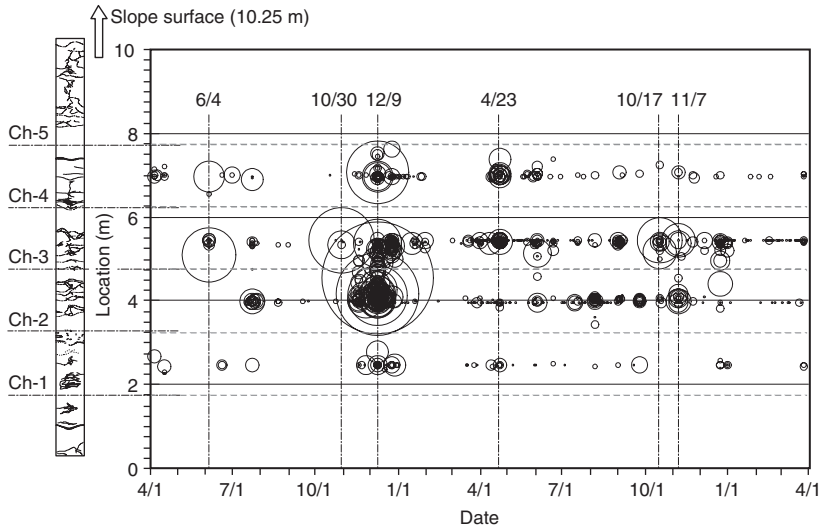



Figure 10: AE sources located during April 1999 and April 2000.

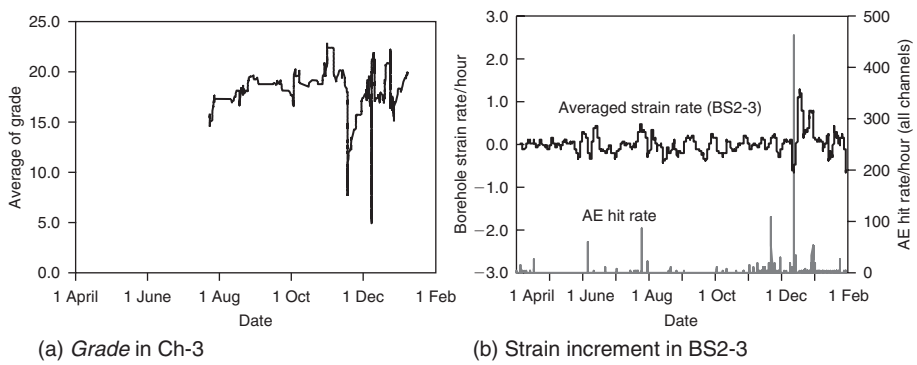



Figure 11: *Grade* and strain variation along date.

drop below 5, suggesting the generation of shear type of fracture (see Table 1). In the borehole No.2, three borehole strain-meters denoted as BS2-1, BS2-2 and BS2-3 are installed. The strain increment of BS2-3 is depicted in Fig. 11b. As seen, large scale of strain increment was obtained when higher AE activity was observed (see the beginning of December). From the detail observations of rock conditions with a CCD camera, the borehole of AE monitoring No. 4 was assumed to be connected to the borehole No. 2 with several cracks. Hence, the strong correlation between borehole strains BS2-3 and AE activity in Ch-3 is thought to be reasonable. From all of the findings, it was cocluded that the slope had transiently experienced the local failure in the beginning of December 1999.

© 2008 Taylor & Francis Group, London, UK

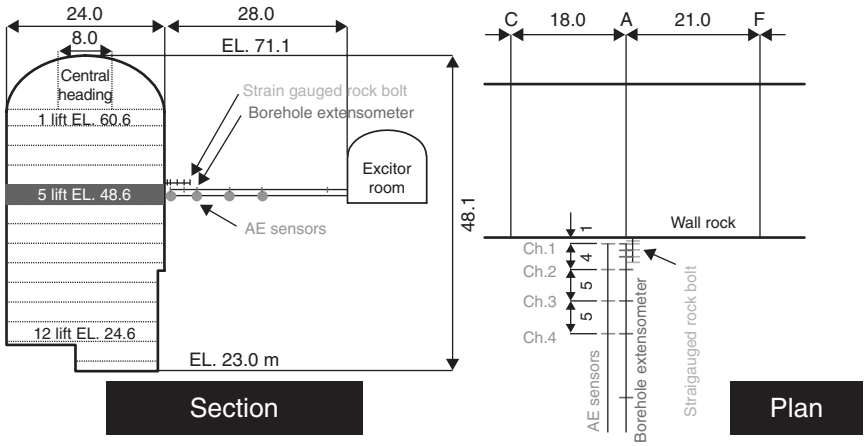



Figure 12: Sensor configurations at the excavation site.

## 3.3 Excavation-induced failure monitoring (Shiotani et al [17])

### 3.3.1 Site and measurements

AE monitoring was performed at a construction site of an underground power plant, located in a southern part of Japan. The power plant was constructed 400 m below ground, consisting of granodiorite. Figure 12 shows the section and plan view to be concerned. The bullet shaped section features: a height of 48.1 m; a width of 24 m; and a length of 188.0 m, resulting in excavation volume of 160,000 $m^3$. Excavation by means of blasting was first conducted from the central heading of the arch followed by enlargement of both sides, and spread from the 1st bench down to the 13th bench (lift).

Acoustic emission, rock displacement and axial load of rock bolt, all are measured for the 5th lift as shown in Fig. 12. Four AE sensors of 60 kHz resonance were installed at 1 m, 5 m, 10 m and 15 m from the wall along with reinforcement (nominal diameter of 13 mm). The void in the borehole was filled with cement-based material that was specially designed with reference to the surrounding rock property. The rock displacements between 25–15, 10–5, 5–3, and 3–1 m are measured with borehole extensometer. A strain gauged rock bolt was installed in the vicinity of the borehole extensometer, in which the loads were measured at 0.5, 1, 2, 3, 4 and 5 m. It is noted that with the extensometer the whole deformation can be measured between each span, whereas pinpoint measurements can be only conducted with the strain gauged rock bolt.

### 3.3.2 AE activity due to excavation

Figure 13a shows 1D AE sources. Arrows in the chart show the blasting time, and the scale of circle denotes the AE energy. With each blasting a large scale

© 2008 Taylor & Francis Group, London, UK

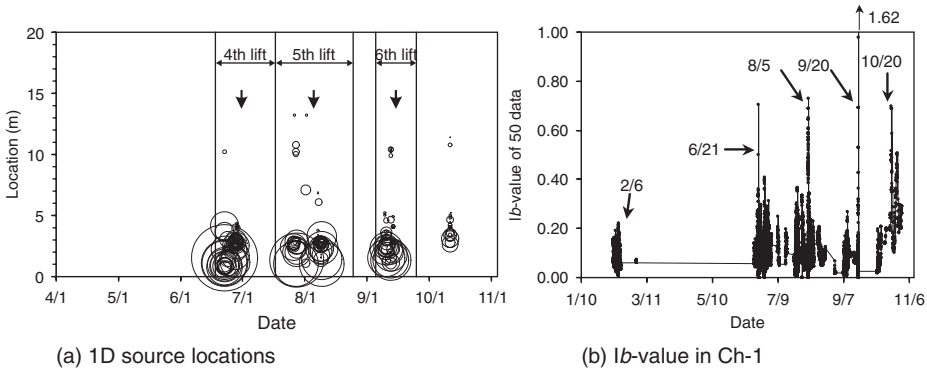



Figure 13: AE activity due to excavation.

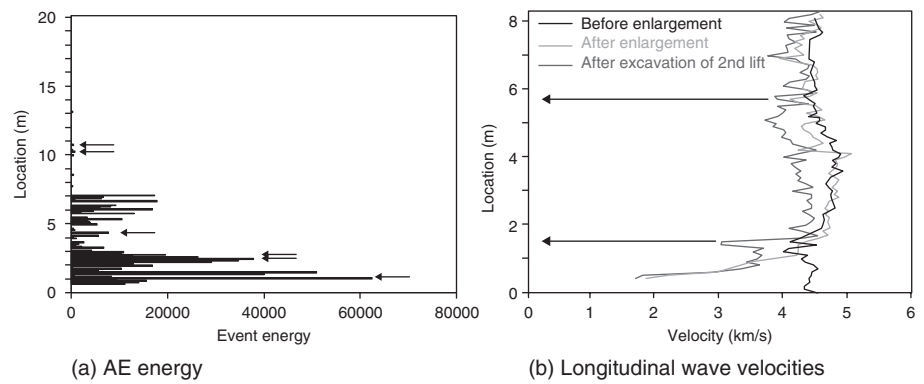



Figure 14: AE energy and longitudinal wave velocities along the depth.

of AE sources are remarkably obtained around the wall (see 0 m in location) to about 3 m. Deepest AE sources are found at 13 m before 5th blasting.

Figure 13b shows the result of I*b*-value analysis in Ch-1 with elapsed time. When discussing the I*b*-value trends, it is important to focus on the I*b*-value appearing below 0.05 (Shiotani et al [22]). As shown in the chart, many drops to values smaller than 0.05 were observed during excavation: on June 21st; August 5th; September 20th; and October 20th, for example, implying the onset of large scale of fracture. Thus the I*b*-value in combination with source locations leads to the temporal and spatial evolution of fracture that can not be inferred by other techniques.

Figure 14a shows frequency histogram of AE energy along the depth. Large scale of AE energy were only obtained up to the depth of 7 m, and specifically the frequency distribution can be separated into two clusters at about 4 m. Presumably the cluster ranging up to 4 m suggests the range of loosen zone directly induced by blasting, and the cluster ranging above 4 m is due to excavation.

© 2008 Taylor & Francis Group, London, UK

Figure 14b shows velocities of elastic wave obtained by seismic prospecting. The seismic prospecting was carried out three times in 'the uppermost lift': before enlargement; after enlargement; and after excavation of the 2nd lift. It can be found that after the enlargement, the velocity decreased by more than 20% around the wall (see up to 1 m). This implies that the influenced range due to enlargement reached about 1 m. After the excavation of 2nd lift, the velocity curve can be represented with two parts: the range up to 1.5 m and that from 1.5 to 5.5 m. The former appeared to be affected by the blasting, and the latter seemed to be caused by the excavation. Since the seismic prospecting was performed on the different elevation from that of AE monitoring, the one to one comparison could not be made; however, damaged or loosen area due to excavation would be about 6 m. Further examination with borehole camera concluded that pre-existing joints (marked by arrows in Fig. 14a) in the AE monitoring borehole were attributed to these excavation-induced microcracks, resulting in AE activity (see the reference 17).

## 4 CONCRETE STRUCTURES

### 4.1 Cyclic fatigue test of a full-scale concrete pier (Shiotani et al [24])

For substructures, the upper part can be investigated with visual observation, while for lower part including foundations of piers, accurate or precise diagnosis, which is necessarily performed for designing repair or reinforcement, is difficult to conduct with naked eyes. In order to obtain the damage characteristic of the lower part, AE technique is applied with utilizing train-induced mobile loads. In this technique existent defects/damages contribute to the AE generation by secondary AE activity. Herein, AE related damage indices as Calm ratio and RTRI are studied in association with fracture progress. Additionally in this specific investigation, identification of AE source is essential to extract only defect-related emissions from acquired AE data including undesirable emissions due to mechanical impact of mobile loads (Shiotani et al [25]). Therefore two source location procedures, namely 1D and 3D, are conducted to examine their compatibility with regard to damage indices.

#### 4.1.1 Testing condition

To characterize the AE activity corresponding to damage evolution, a railway RC pier (5.87 m high) was subjected to incremental cyclic loads, controlled by the lateral displacement applying from the north direction with step-wise increments: 1, 2, 4, 8, 16, 32, 64, and 128 mm. The tested pier and the sensor configuration are shown in Fig. 15. AE measurement system was similar to the cases mentioned previously. Four strain gauges were attached to the lower four

© 2008 Taylor & Francis Group, London, UK

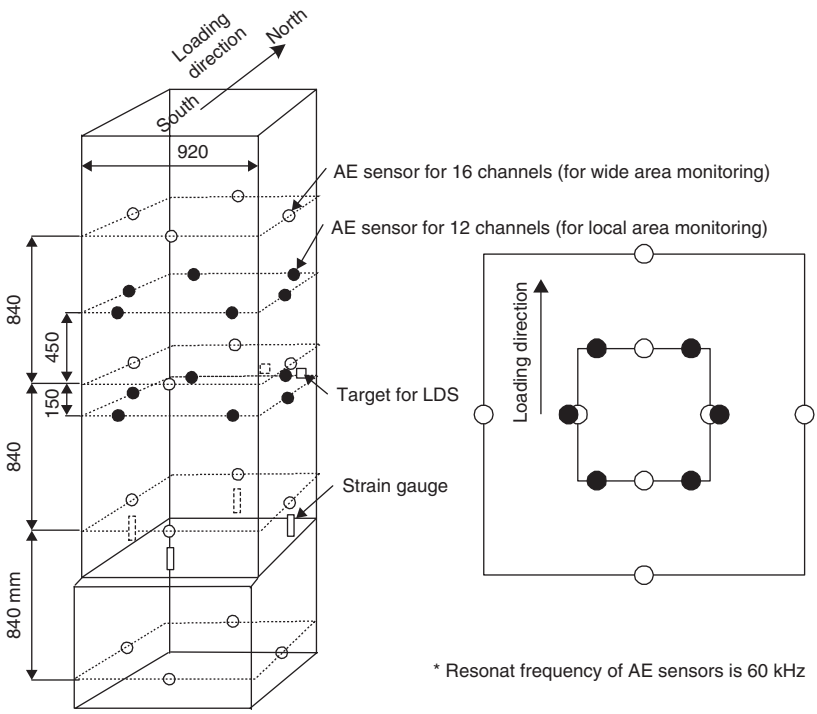



Figure 15: Tested pier and sensor configuration.

sides, and displacements on two sides: the north and the east side, are measured with laser displacement meter. To obtain the internal stress distribution, strain gauges were also attached to rebars located in the four corners. The sets of four strain gauges were each placed at three different heights: 400, 1800 and 3200 mm from the ground surface.

### 4.1.2 Results and discussion

Figure 16 shows measured strains in the rebar at height of 400 mm, where the strains named 1 and 2 were installed in the south and those named 3 and 4 were in the north. Again the displacement was given from the north. As shown, both strains of 3 and 4 showed negative values suggesting compression status, while the strains of 1 and 2 appeared positive values implying tensile status. These trends agreed well to the expected stress condition. Especially for strain 2 showing the value in the right vertical axis, a sudden jump is found at 16350s indicated by a chain line. Additionally conducted strength tests of rebar showed the yield point at 1500–1600 μ and 2200–2300 μ in the tensile strength. The strain at 16350s stood at 2274 μ already, suggesting that the rebar had yielded during the previous step of 64 mm in the displacement, and the sudden jump emerged at

© 2008 Taylor & Francis Group, London, UK

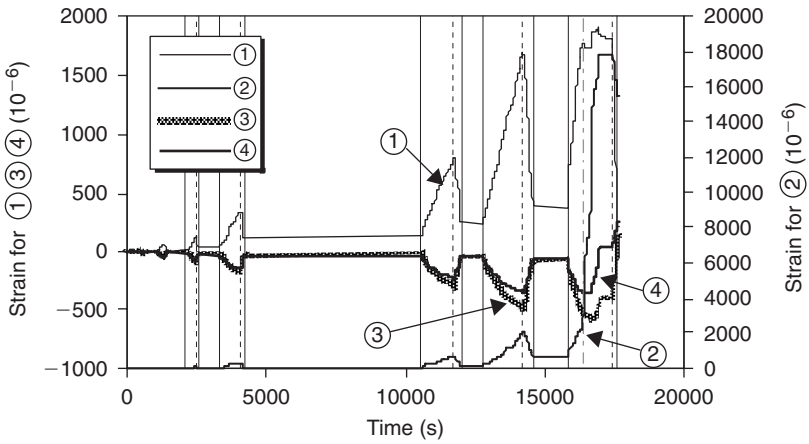



Figure 16: Rebar strains at 400 mm high.

16350s demonstrated the time when the stress had reached the maximum tensile strength. From these findings, the internal damage of the pier appeared to be developed intensively from the lateral displacement of 64 mm. Considering concrete surface strain monitoring (see [24]), the damage of pier was constantly progressing until 64 mm and accelerated during 64 mm application, while no remarkable development of strains (damage) was introduced into the pier during the further displacement applied.

Figure 17 shows Calm ratio with regard to displacement in which Calm ratios during 128 mm were calculated from such three different behaviors as lateral displacement, applied load, and rebar strain. As shown, the Calm ratio became active from 32 mm lateral displacement and remarkable increase was found in 64 mm. However for 128 mm displacement, the Calm ratio obtained from different parameters, showed intrinsic values i.e., a considerably large value was found based on rebar strain, while a small value both from load and displacement. In comparison with actual damage progress of pier as discussed above, the Calm ratio from rebar strain was resulted in over-evaluation of actual damage, whereas load or displacement, demonstrating the general behavior of pier seemed more reliable in relation with AE activity. The compatibility of 3D and 1D results is also depicted in Fig. 17. As observed, even from 1D results obtained individually from each surface, the similar variation of Calm ratio to that of 3D was derived. Consequently for practical investigations although the source location algorithm is necessarily implemented, 1D AE sources, derived from the simplest AE sensors array, suffice the monitoring condition.

Figure 18 shows the chart consisting of Calm ratio and RTRI as well as reported criteria (Ohtsu et al [26]) overlaid with broken lines. As seen, the plot moves from bottom right, bottom left and top left window with increase of displacement,

© 2008 Taylor & Francis Group, London, UK

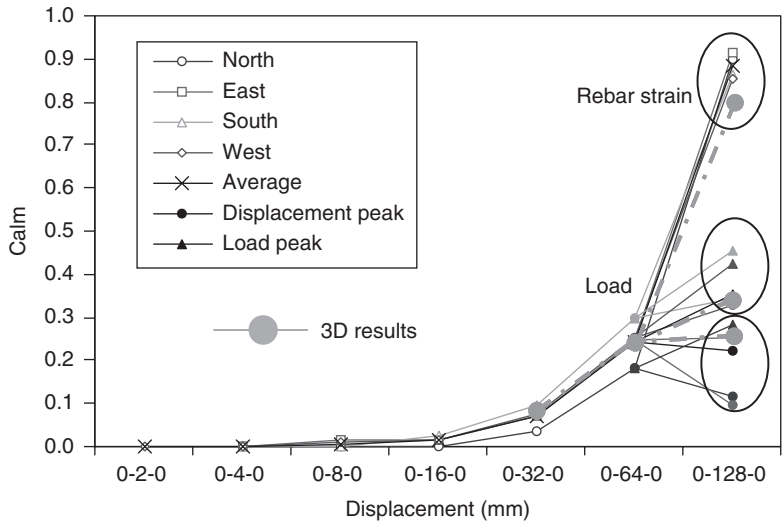



Figure 17: Calm ratio with applied displacements.

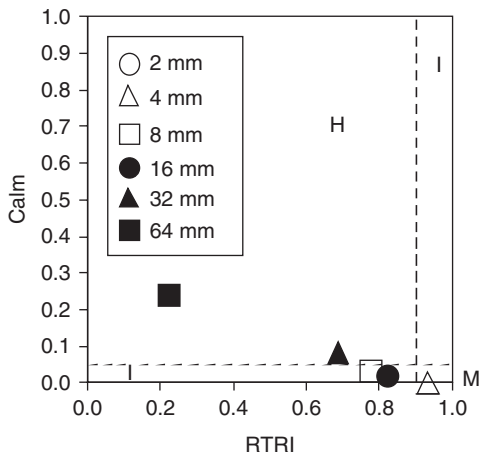



Figure 18: Calm ratio and RTRI with evolution of damage.

suggesting the damage progresses from M: minor, I: intermediately and H: heavily. These evaluations were thus in good accordance with the actual process of damage. Due to page limitation only experimental application was described herein. With regard to in-situ applications of railway sub-structures, several can be found in literature (e.g., Shiotani et al [6], [19],[24], [25], [27]).

© 2008 Taylor & Francis Group, London, UK

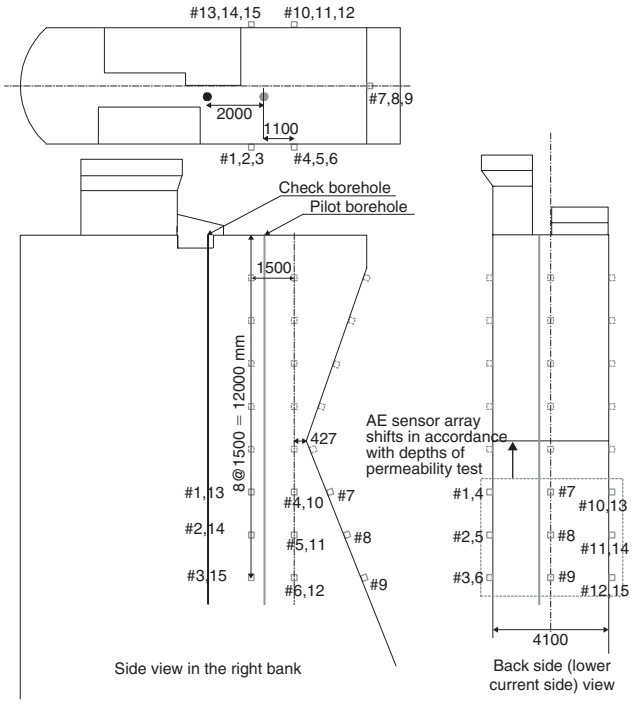



Figure 19: Configuration of AE sensor arrays at a large concrete pier.

## 4.2 Evaluation of repair effect for deteriorated concrete structures (Shiotani et al [28])

A water intake diversion facility was constructed 70 years ago in a cold region of Japan. Concrete piers supporting the rolling gate, the most crucial part of the facility, showed deterioration. Specifically, the surface layer was damaged due to freezing and thawing, and internal area was composed of poor quality's materials i.e., there include large amount of voids, pieces of wood and cobblestone, supposed to be filled when construction was made. Grouting with injection cement was used for repair and to confirm the repair work NDT was conducted. Herein only results of AE monitoring are described.

### 4.2.1 Monitoring condition

To study if the grouting successfully filled the cracked or void areas, permeability tests were carried out by means of water-pump. AE monitoring was conducted during the application of water pressure. As shown in Fig. 19, 6 sensors on one side, totally 12 sensors on both sides, and 3 sensors on back current side were set up with 1.5 m spacing. The permeability of concrete was monitored in intervals

© 2008 Taylor & Francis Group, London, UK

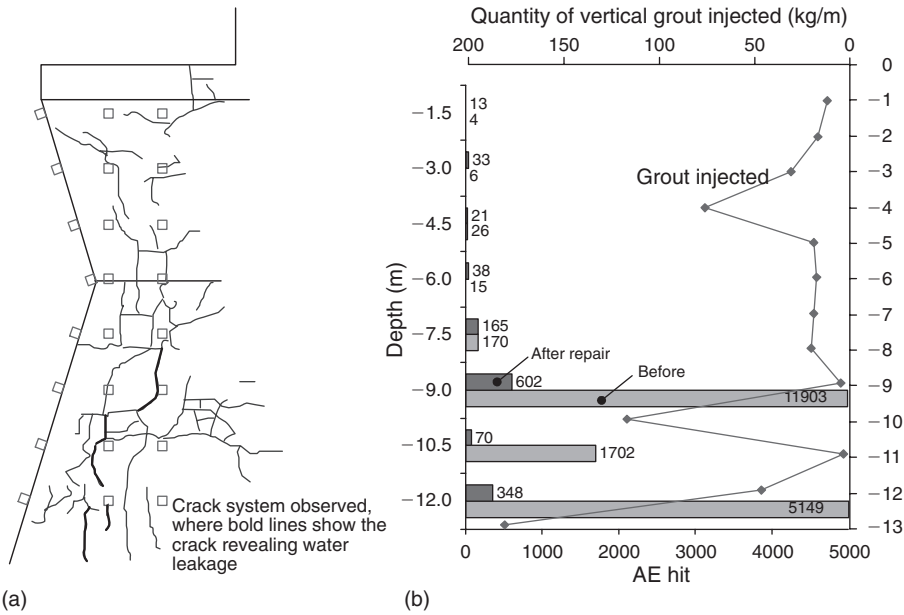



Figure 20: Arrangment of AE sensors (a) and hit activity along depth on left bank side of pier (b).

of one meter in depth. The AE signals detected with AE sensors (R6I, PAC) were amplified by 40 dB and the signals over 40 dB were acquired for their AE parameters as well as waveforms by DISP AE system (PAC).

### 4.2.2 Results and discussion

Figure 20 shows the arrangement of AE sensors (a), and accumulated AE hits for each depth for the left bank side (b). Total AE hits of two allocated sensors at the same height are depicted with horizontal bars. In the chart the injected quantity of vertical grout is drawn as well. Before repair high AE hit activity was observed particularly below −9.0 m. In these depths a complicated and well-evolved surface crack system was observed, leading water leakage from some macroscopic cracks (see bold lines in Fig. 20a). As a large quantity of grout was injected in those depths, a large volume of macroscopic cracks were filled. AE activity after repair revealed decrease e.g., from 5149 hits to 348 at −12 m and from 11903 to 602 at −9.0 m. Thus AE hit activity confirmed the success of repair by the recorded number of hits.

Based on the derived AE activity, Calm and Load ratios are shown in Fig. 21. After repair, decrease of Calm ratio and increase of Load ratio were obtained, suggesting the improvement due to the repair work. With reference to other

© 2008 Taylor & Francis Group, London, UK

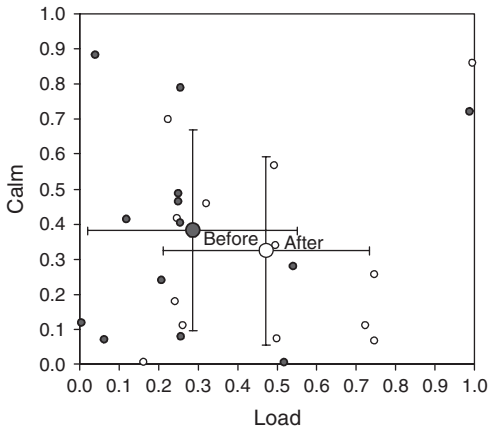



Figure 21: Calm ratio and Load ratio based on AE ringdown counts.

piers repaired, it can be concluded that these damage indices showed rational interpretation of the repair effect.

### 4.3 Early detection of damage in a PC bridge (Shiotani et al. [29])

As mentioned in the introduction, it is crucial to rank the severity of damage in structures on the basis of assessment of health status. AE testing has potential for this issue since the investigation of whole structures can be implemented with less numbers of AE sensors than conventionally used other techniques. Herein, a PC bridge, for which other investigations implied no remarkable deterioration, was monitored by AE monitoring.

#### 4.3.1 Experimental procedure

For the AE monitoring, totally 28 AE sensors (R6, PAC) were attached to the bottom surface of the bridge. They were placed on the longitudinal axis of the bridge with separation of 1.5 m. The approximate locations are shown in Fig. 22. The detected AE signals were pre-amplified by 40 dB and acquired in two synchronized data acquisition systems, namely a 16-channel DiSP and a 12-channel Mistras of PAC. Strain gauges were also placed in three locations of the top surface of the bridge, as shown in Fig. 22.

The active load for AE monitoring was supplied by a 20-ton crane vehicle, which passed three times over the bridge with a constant speed of about 0.5 m/s. As shown, the crane moved over the bridge, and the strain and stress field changed. The compressive strain measured on the top surface of the bridge at the mid-span can be seen in Fig. 23.

© 2008 Taylor & Francis Group, London, UK

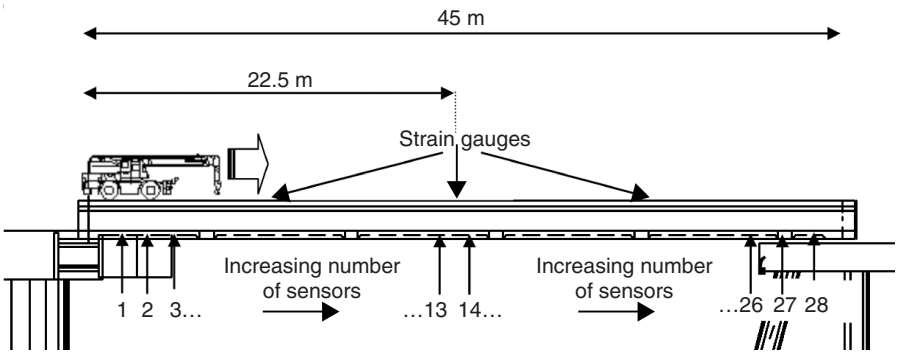



Figure 22: Representation of the vehicle passing over the PC bridge with sensor array.

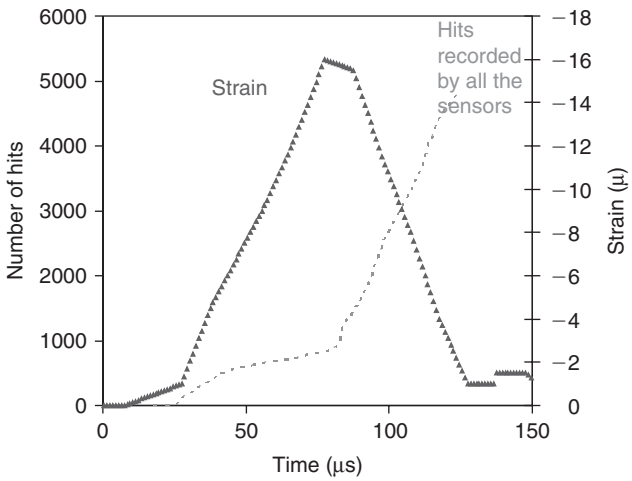



Figure 23: Strain at the center and AE hits activity during crane passage.

### 4.3.2 Results and discussion

The maximum strain was recorded at 88 s when the truck was in the middle of the span as shown in Fig. 23, suggesting the highest tensile stress due to bending at the bottom layer of the structure. In the figure, the cumulative number of AE hits recorded by all the sensors is drawn for one passage. It can be seen that the rate of AE hits was more intensive after the crane passed the center of the bridge at 88s. After that moment, more than 80% of the total number of AE hits was recorded, implying that more active sources were located in the second half of the bridge.

Since three cycles of crane passage exhibited the similar trend, the result of one dimensional source location along the longitudinal direction only for the first cycle is shown in Fig. 24. As seen, the second half area, namely above about

© 2008 Taylor & Francis Group, London, UK

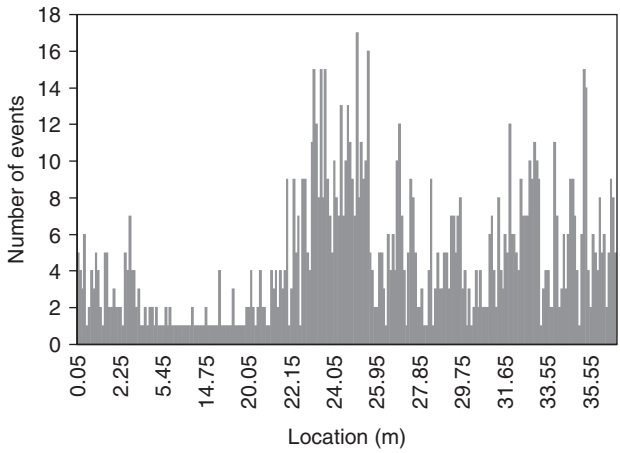



Figure 24: One dimentional AE sources along longitudinal axis of bridge.

20 m, exhibited more intensive AE activity than the first half area. Accordingly, the second half area was the most likely to have sustained more serious damage than the other area of the structure examined, and therefore this area was selected for more detailed 2D AE monitoring as well as tomography as described below.

For the detail measurement, nine AE sensors were used in an arrangement of three parallel arrays of three at around 25 m from starting point. The separation distance was 1.5 m, resulting in an examined area of 3 m by 3 m. AE measurement were performed in the same way as in previously. For ultrasonic tomography (Kobayashi et al [30]), the excitation was conducted by pencil lead break near the location of each transducer. This way the visualization of the velocity structure was obtained. As seen in Fig. 25, it is found that within the area of 9 $m^2$, considerable discrepancies of wave velocity emerge. These discrepancies correspond to different degree of deterioration since as reported (Naik et al [31]) velocities below 3000 m/s indicate low quality of concrete. Specifically, a zone approximately in the center of the selected area exhibited velocity of less than 2500 m/s, while other areas had velocity up to 4500 m/s. As for the AE activity, AE sources were emerged along the lines of crane tires' trace. Exact source of AE activity has not yet been clarified, but concrete cracks, delaminations of different layers (e.g. asphalt on concrete) or friction between the tendon ducts and matrix concrete, all those may contribute to the AE activity. Consequently, AE testing can thus been applied for global monitoring of large concrete structures. It is reminded that the general condition of the structure was considered satisfactory by the conventional inspections. However, even if the damage was in an early stage, it was identified and located by the AE activity, giving the engineers at site valuable information to decide the proper action program.

© 2008 Taylor & Francis Group, London, UK

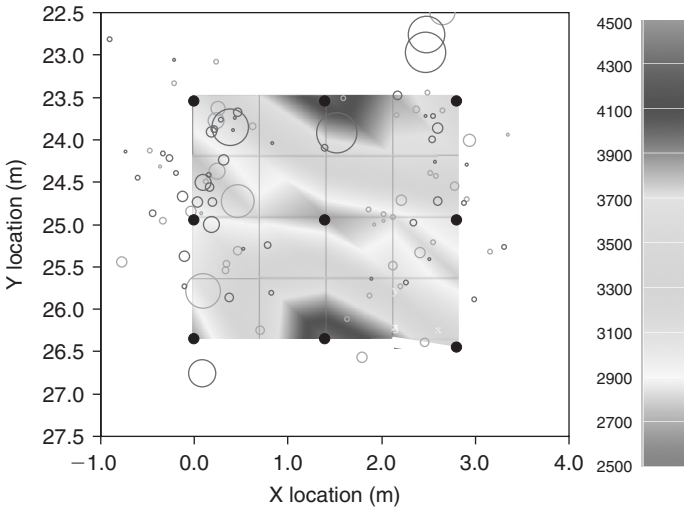



Figure 25: Two dimentional AE sources with ultrasonic tomogram.

## 5 CONCLUSIONS

In the paper, basics of AE testing and actual rock monitoring were introduced, followed by actual damage diagnosis of concrete structures. Through the study the followings are obtained: rock slope stability can be reasonably evaluated with the proposed WEAD procedure; excavation-induced loosen zones at a construction site of an underground power plant were identified with temporal and spatial behavior of AE events; current damage status as well as repair effectiveness of concrete structures can be inferred by damage indices obtained from AE activity; and additionally even in the case that structural integrity was considered satisfactory by conventional inspections, an early stage of damage can be identified and located by AE activity.

Consequently, current health status of civil structures, which should be necessarily conducted with an appropriate NDT, can be rationally evaluated with AE testing. AE monitoring has great potential for global monitoring of large civil structures in the new era of sustainable civil structures.

## References

[1] M. Seto, M. Utagawa and K. Katsuyama, “The estimation of pre-stress from AE in cyclic loading of pre-stressed rock.” *Progress in AE VII*, pp. 159–166, 1992.

© 2008 Taylor & Francis Group, London, UK

[2] T. J. Fowler, "Experience with acoustic emission monitoring of chemical process industry vessels," *Progress in AE III*, pp. 150–162, 1986.

[3] S. Yuyama, T. Okamoto, M. Shigeishi, M. Ohtsu and T. Kishi, "A proposed standard for evaluating structural integrity of reinforced concrete beams by AE, Acoustic Emission," *ASTM Standards and Technology Update*, ASTM STP1353, pp. 25–40, 1998.

[4] The Japanese Society for Non-Destuctive Inspection, "Recommended practice for in situ monitoring of concrete structures by acoustic emission," *NDIS2421*, p. 24, 2000.

[5] T. Shiotani, M. Shigeishi and M. Ohtsu, "Acoustic emission characteristics of concrete-piles." *Construction and Buildings Materials* Vol. 13, pp. 73–85, 1999.

[6] X. Luo, H. Haya, T. Inaba, T. Shiotani and Y. Nakanishi, "Experimental study on evaluation of breakage in foundations using train-induced acoustic emission," *Proc., Structural Engineering World Congress 2002*, Paper No. T9-1-e-3, 2002.

[7] S. Yuyama, T. Okamoto, M. Shigeishi and M. Ohtsu, "Quantitative evaluation and visualization of cracking process in reinforced concrete specimen by moment tensor analysis of acoustic emission," *Progress in AE VII*, pp. 347–354, 1994.

[8] H. Kanamori, *Physics of Earthquake*, Iwanami Shoten Publishers, 1994 (in Japanese).

[9] M. Iwanami, T. Kamada and S. Nagataki, "Application of AE technique for crack monitoring in RC beams," *JCI Proceedings of Cement and Concrete*, 51, 1997.

[10] K. Mogi, "Magnitude frequency relation for elastic shocks accompanying fractures of various materials and some related problems in earthquakes," *Bull. Earthq. Res. Inst*., 40, pp. 831–853, 1962.

[11] H. Scholz, "The frequency-magnitude relation of microfracturing in rock and its relation to earthquakes," *Bull. Seismo. So. America*, 58(1), pp.399–415, 1968.

[12] T. Shiotani, K. Fujii, T. Aoki and K. Amou, "Evaluation of progressive failure using AE sources and improved *b*-value on slope model tests," *Progress in AE VII*, pp 529–534, 1994.

[13] M. Ohtsu, "Simplified moment tensor analysis and unified decomposition of acoustic emission source: Application to in situ hydrofracturing test," *Journal of Geophysical Research*, Vol. 96, No. B4, pp. 4211–4221, 1991.

[14] T. Shiotani, Z. Li, S. Yuyama and M. Ohtsu, "Application of the AE improved *b*-value to quantitative evaluation of fracture process in concrete materials," *Journal of AE*, 19, pp. 118–133, 2001.

© 2008 Taylor & Francis Group, London, UK

[15] T. Shiotani and M. Ohtsu, "Prediction of slope failure based on AE activity," *ASTM Acoustic Emission: Standards and Technology Update*, ASTM STP 1353, pp.156–172, 1999.
[16] T. Shiotani, M. Ohtsu and K. Monma, "Rock failure evaluation by AE improved *b*-value," JSNDI & ASNT, *Proc. 2nd Japan-US Sym. on Advances in NDT*, pp 421–426, 1998.
[17] T. Shiotani, K. Kumagai, K. Matsumoto, K. Kobayashi and H. Chikahisa, "Evaluation of excavation-induced microcracks during construction of an under-ground power plant using acoustic emission," *Contribution of Rock Mechanics to the New Century*, pp. 573–57, 2004.
[18] T. Shiotani, J. Bisschop and JGM van Mier, "Temporal and spatial development of drying shrinkage cracking in cement-based materials," *Engineering Fracture Mechanics*, pp. 1509–1525, 2003.
[19] T. Shiotani, Y. Nakanishi, K. Iwaki, X. Luo and H. Haya, "Evaluation of reinforcement in damaged railway concrete piers by means of acoustic emission," *Journal of AE*, 23, pp. 260–271, 2006.
[20] H.R. Hardy and F. Taioli, "Mechanical waveguides for use in AE/MS geotechnical applications," *Progress in AE IV*, pp. 293–301, 1988.
[21] I. Nakajima, J. Sato, N. Taira and N. Kubota, "The observation of landslide by the acoustic emission monitoring rod," *Progress in AE IV*, pp. 273–281, 1988.
[22] T. Shiotani, M. Ohtsu and K. Ikeda, "Detection and evaluation of AE waves due to rock deformation," *Construction and Building Materials*, 15, pp. 235–246, 2001.
[23] T. Shiotani, "Evaluation of long-term stability for rock slope by means of acoustic emission technique," *NDT&E International* 39, pp. 217–228, 2006.
[24] T. Shiotani, X. Luo and H. Haya, "Damage diagnosis of railway concrete structures by means of one-dimensional AE sources," *Progress in AE XIII*, pp. 153–159, 2006.
[25] T. Shiotani, Y. Nakanishi, X. Luo, H. Haya and T. Inaba, "Damage evaluation for railway structures by means of acoustic emission," *Key Engineering Materials* Vols. 270–273, pp. 1622–1630, 2004.
[26] M. Ohtsu, M. Uchida, T. Okamoto and S. Yuyama, "Damage assessment of reinforced concrete beams quantified by acoustic emission," *ACI Structural Journal* Vol. 99, No. 4, 411–417, 2002.
[27] T. Shiotani, X. Luo, H. Haya and M. Ohtsu, "Damage quantification for concrete structures by improved *b*-value analysis of AE," *11th International Conference on Fracture*, No. 3390, CD-ROM, 2005.
[28] T. Shiotani, "Evaluation of repair effect for deteriorated concrete piers of intake dam using AE activity," *Advanced Materials Research* Vols. 13–14, pp. 175–180, 2006.

© 2008 Taylor & Francis Group, London, UK

[29] T. Shiotani, D.G. Aggelis and O. Makishima, "Global monitoring of large concrete structures using acoustic emissino and ultrasonic techqniques," *Journal of JSCE*, submitted.

[30] Y. Kobayashi, H. Shiojiri and T. Shiotani, "Damage identification using seismic travel time tomography on the basis of evolutional wave velocity distribution model," *Proc. Structural Faults and Repair-2006*, CD-ROM, 2006.

[31] T.R. Naik and V.M. Malhotr, "The ultrasonic pulse velocity method," *Nondestructive Testing of Concrete*, CRC Press, pp. 169–188, 1991.

© 2008 Taylor & Francis Group, London, UK

*Acoustic Emission and Critical Phenomena – Carpinteri & Lacidogna (eds)*
*© 2008 Taylor & Francis Group, London, ISBN 978-0-415-45082-9*

# ACOUSTIC EMISSION ANALYSIS DURING TEST LOADING OF EXISTING STRUCTURES

**G. Kapphahn[1] and V. Slowik[1]**
[1]Leipzig University of Applied Sciences, Leipzig, Germany

## ABSTRACT

Test loading of existing structures appears to be an alternative way of proving structural safety in case computational methods fail. During such loading tests, the behaviour of the structure needs to be continuously monitored in order to avoid damages. For the identification of the critical load level which marks the beginning of damage processes acoustic emission analysis has proved to be an appropriate tool. This method allows efficient and sensitive crack detection and complements the deformation measurements. Taking into consideration the characteristic load-carrying behaviour of the tested structure, on the basis of the acoustic emission results, conclusions concerning failure mode and location can be drawn. As far as source localization is concerned simple methods like regional or linear localization have proved to give reliable results, whereas strict 2D or 3D localization appears to be difficult in existing and especially pre-damaged structures.

## 1 INTRODUCTION TO EXPERIMENTAL SAFETY EVALUATION

Conventional safety evaluation by computational means requires exact input data concerning the current geometrical and material properties of the structure as well as the mechanical boundary conditions. For existing structures, however, these preconditions cannot always be met. This may be due to unknown effects of structural faults or due to uncertainties in the mechanical model with the corresponding boundary conditions. In such cases, additional data may be acquired by material testing or by measuring the exact structural geometry. If the structural safety still cannot be proved by computational means, it is in certain cases possible to evaluate the structural safety experimentally by performing an in situ loading test. Nowadays, such loading tests may be performed without causing any damage to the structure. Methods and equipment have

© 2008 Taylor & Francis Group, London, UK

been significantly improved throughout the last two decades and in Germany, a technical recommendation for loading tests (*DAfStb* [1]) has been issued. This national guideline contains the safety concept and technical rules for loading tests as well as criteria for critical load levels. Acoustic emission analysis is proposed in this guideline as one of the methods for monitoring the structural behaviour under test loads and, thereby, its practical application has become state-of-the-art.

By loading tests, in numerous cases additional resistance reserves were revealed which could not be shown by structural analyses, especially in the case of concrete and masonry structures. Such structures are often characterized by spatially varying mechanical material properties as well as by boundary conditions which are difficult to model.

If an experimental safety evaluation yields positive results, a costly and time consuming replacement of the structure can be avoided or at least postponed. However, loading tests should be limited to cases

1. where computational methods fail to prove structural safety and
2. where a reasonable chance of experimentally proofing an acceptable safety level exists.

The concept of experimental safety evaluation includes imposing test loads on the structure and, simultaneously, the monitoring of the load-carrying behaviour, especially of the deformations and of acoustic emission. On the basis of the measured structural response, a critical load level characterizing the beginning of damage process is identified. This critical load level must not be exceeded in the loading test in order to avoid damage to the structure. Subsequently, the maximum test load level reached in the experiment is converted into the allowable service load for the corresponding structure by taking into account a certain safety margin. This concept is illustrated in Figure 1 which shows the applied test load versus a characteristic structural reaction, usually the deflection in the case of bending members. Prior to the loading test, an experimental target load ext $F_{targ}$ is calculated which corresponds to the design load level including live loads $Q_d$ and additional permanent loads $G_{d,j}$. Partial safety factors are included according to the concept of load and resistance factor design. A portion of the permanent loads $G_1$ resulting from the self-weight of the structure is already present before the test load is applied. While the test load is increasing, the load-carrying behaviour is monitored in order to identify the critical load ext $F_{lim}$, the so-called experimental limit load, characterizing the beginning of irreversible damage processes. If this load is equal or higher than the experimental target load sufficient structural safety has been proved.

According to the German guideline (*DAfStb* [1]), the following technical requirements have to be met in order to preserve the structure and to ensure

© 2008 Taylor & Francis Group, London, UK

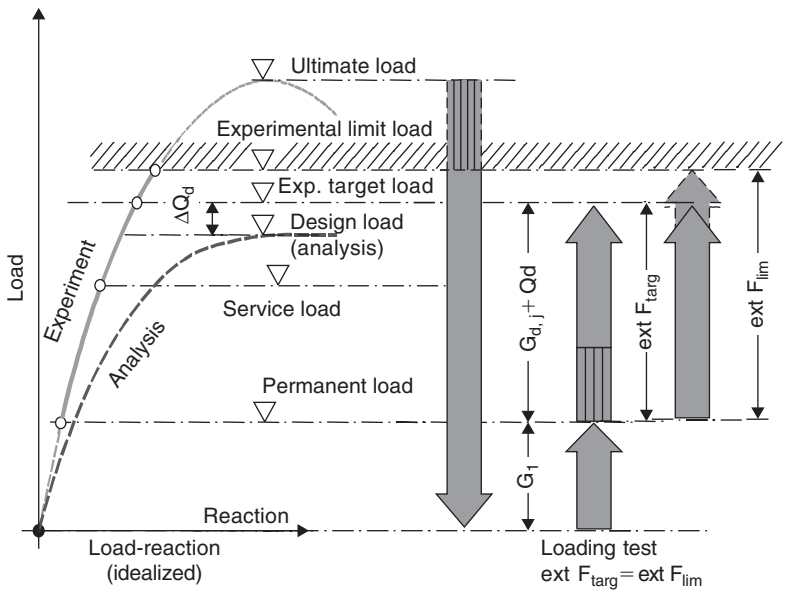



Figure 1: Safety concept of loading tests (*Gutermann et al.* [2]).

safety of crew and equipment:

1. The application of the test loads has to be undertaken in a way that sudden failure of the structure is avoided even in the case of unexpected fracture processes.
2. The behaviour of the structure has to be continuously monitored and evaluated in real time during the test.

Consequently, gravitational loads are not applicable for generating the test loads and, therefore, alternative technical solutions have been proposed (*Gutermann et al.* [2], *Steffens* [3]).

## 2 ACOUSTIC EMISSION ANALYSIS DURING LOADING TESTS

Under monotonically increasing load, acoustic emission may be detected before the structure experiences damages of significance for its mechanical behaviour. This effect and the spatially integral character of the sensing are the major attributes of acoustic emission analysis, making it a valuable tool for monitoring the structural behaviour during loading tests. The method allows very sensitive crack detection as compared to deformation measurements.

According to the concept of experimental safety evaluation, the acoustic emission results have to be evaluated and interpreted at least partially already during

© 2008 Taylor & Francis Group, London, UK

the loading test. This is possible by recording wave form parameters only and displaying some of them in real time. The original wave signal is reduced into data sets of relevant wave form parameters. From the practical point of view, acoustic emission analysis may easily be incorporated in the procedure for in situ loading tests because of the easy sensor application, the comparably large number of individual sensors and because of the robustness and long-term stability of the method. The possibility of long distances between sensors and data acquisition system is another technical advantage.

Usually, about 8 to 16 acoustic emission sensors are attached to the structure at certain critical positions where acoustic emission is expected to originate from. Appropriate sensor positioning is of great importance and depends on the anticipated failure mechanisms. The high signal damping in concrete and masonry allows a separation of distant acoustic emission sources. This type of regional localization has proved to give reliable results. In some cases, a linear localization is possible. However, conventional 2D or 3D acoustic emission localization algorithms usually appear to be not applicable in existing and especially pre-damaged structures. This is mainly attributed to material induced spatial velocity variations and the influence of cracks.

By using acoustic emission analysis during loading tests the following objectives may be achieved:

- reliable experimental determination of the cracking load in reinforced concrete bending members,
- avoidance of unwanted cracking during the loading test,
- additional protection against brittle failure,
- getting information on the behaviour of hidden joints, for instance about debonding between different concrete layers.

The method should always be applied complementary to deformation measurements. An exclusive application is not recommendable.

## 3 INTERPRETATION OF THE RESULTS

A simple three-phase model is adopted in order to attribute acoustic emission events to cracking in quasi-brittle materials like concrete. In the first phase, the crack *initiation phase*, microcracks are formed in the interfacial transition zones. The resulting acoustic emission events are characterized by small energy contents and medium amplitudes. In the following phase, the *active phase* of cracking, the microcracks coalesce, larger cracks are formed and friction between crack surfaces as well as local crack closing occurs. Accordingly, a high acoustic emission activity is observed with high hit rates and wide spectra of the recorded wave form parameters. In the subsequent *inactive phase*, the cracks are widely opened ($>0.2$ mm) and the crack surfaces have lost contact. Consequently, nearly

© 2008 Taylor & Francis Group, London, UK

no acoustic emission is detectable. However, in case of reinforced concrete, debonding causes further acoustic emission. Cracks in bending members might be assignable to all three phases at the same time due to their non-uniform crack opening.

In the following, the model will be applied to three different situations encountered when testing reinforced bending members. In the first situation, the structure is in its uncracked state. As long as the test load is lower than the cracking load, nearly no acoustic emission is detected. If cracking starts in the tensile zone, the initiation phase is reached followed by the active phase of cracking. The cracking load may reliably be identified when reaching the active phase. If cracking is to be avoided the test loading may be interrupted in the initiation phase.

In the second situation considered here, the bending member is only at certain locations in the cracked state. Only isolated cracks are visible. Due to the Felicity effect, acoustic emission is detected above the cracking load, but already below the previously highest load level. By multi-channel data acquisition the cracked regions may easily be localized, see section 2.

The third situation is characterized by a fully developed crack pattern in the tensile zone. Most of the cracks are in their inactive phase. Acoustic emission is detected only at high load levels compared to the cracking load. The wave propagation between source and sensors is significantly influenced by the cracks. This is another reason for the observed low acoustic emission activity. A strong increase of the latter might already indicate an ultimate limit state of the structure.

In addition to the three characteristic situations described above, unexpected brittle failure might be an additional scenario which is accompanied by acoustic emission. Shear cracks in reinforced bending members are an example for such a failure mode. In laboratory experiments, it has been shown that this failure mode may be predicted by acoustic emission analysis. However, the load increment between detection of the corresponding acoustic emission signals and brittle failure is comparably small. This fact points to the necessity of a real time evaluation of the acquired data. The formation of shear cracks is accompanied by a significant increase in hit and energy rates. In real structures, the distance between the regions of extensive bending cracking and of the expected shear cracks is quite large. If sensors are attached to both regions, acoustic emission sources may reliably be assigned to bending or shear cracks, respectively. In the case of increasing hit or energy rates in the shear region, the structure should be immediately unloaded. The loading test should not be continued before the reason for the extensive acoustic emission is known.

Under cyclic loading, acoustic emission is detected during reloading as well as during unloading. Usually, almost identical wave form parameters may be recorded for thousands of cycles. The signals predominantly originate from friction between the crack surfaces. For identifying structural changes the evaluation

© 2008 Taylor & Francis Group, London, UK

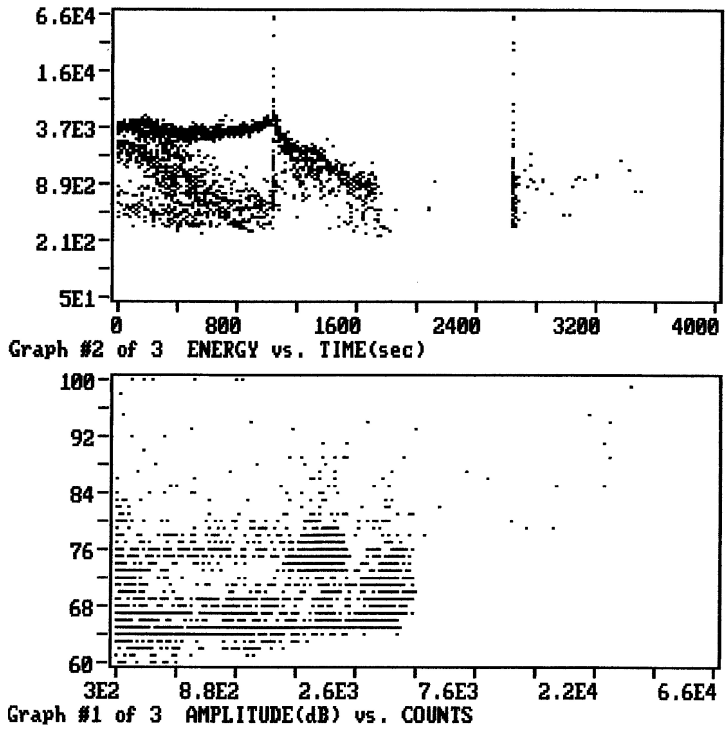



Figure 2: Acoustic emission results under cyclic loading of a prestressed concrete beam, rupture of tendons after about 1000s and 2600s.

of correlation plots, especially signal amplitude versus counts or signal amplitude versus energy, has proved to be a suitable method. During cyclic loading, the mentioned parameters intermittently increase or decrease depending on the physical processes taking place in the structure. Discrete events, like rupture of tendons, may be easily identified in energy versus time plots, see Figure 2.

## 4 EXAMPLES

Figure 3 shows a curved concrete bridge which had to be tested in order to evaluate the structural safety. For generating test loads, the loading vehicle BELFA was used (*Gutermann et al.* [2], *Steffens* [3]). It allows to simulate nearly arbitrary arrangements of quasi-static traffic loads by a hydraulic system. The vehicle self weight and additional ballast serve as reaction force. During the loading test, acoustic emission measurements with six channels have been undertaken. The sensors were attached to the prestressed edge girder which is subjected to the highest load under service conditions, see Figure 4.

© 2008 Taylor & Francis Group, London, UK




Figure 3: Test loading of a reinforced concrete bridge by using the loading vehicle BELFA.




Figure 4: Acoustic emission sensors attached to one of the longitudinal bridge girders.

This loading test is an example for a characteristic behaviour found in pre-stressed concrete structures. Under service load, the bending cracks in the tensile zone are closed or even not existent. However, if this load level is increased by a certain safety margin bending cracks are formed. Acoustic emission measurements clearly confirm this observation.

© 2008 Taylor & Francis Group, London, UK

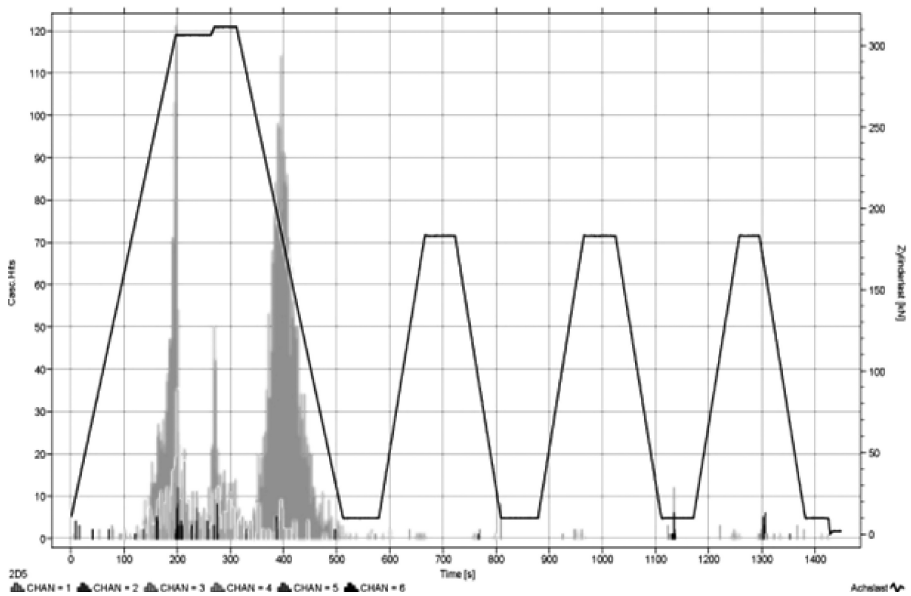



Figure 5: Number of hits (left axis) and applied load (solid line, right axis) versus time.

Figure 5 shows the number of hits versus time for the different acoustic emission channels. The solid line corresponds to the time dependent test load applied by one of the actuators. With the first load cycle, the experimental target load including safety factors was reached. The following load cycles end at the service load level. It may be seen that at the beginning of the loading, nearly no acoustic emission is detected. Above 180 kN, however, which corresponds to the service load level the hit rate starts increasing. Bending cracks are formed. When the constant maximum load level was reached the acoustic emission hit rate is going down to a significantly lower level. The cracks are arrested. Hence, this crack propagation is a stable one. Under decreasing load, there is a peak in the hit rate at about 200 kN. This may be attributed to closing of the bending cracks. During the following load cycles up to the service load level, nearly no acoustic emission is detected. The bending cracks in this prestressed member are closed under compression.

The acoustic emission results acquired by the six channels have been used for a linear localization. Figure 6 shows the hits versus the position along the bridge axis. In the background of this graph, the bridge geometry with the sensor positions is presented. The six acoustic emission sensors are marked with "S". It may be seen that most of the hits were allocated within a region having a length of less than one meter. This region is located approximately at midspan, as expected. During the loading test, cracks were formed in this region only. After the evaluation of all the deformation and acoustic emission measurements

© 2008 Taylor & Francis Group, London, UK

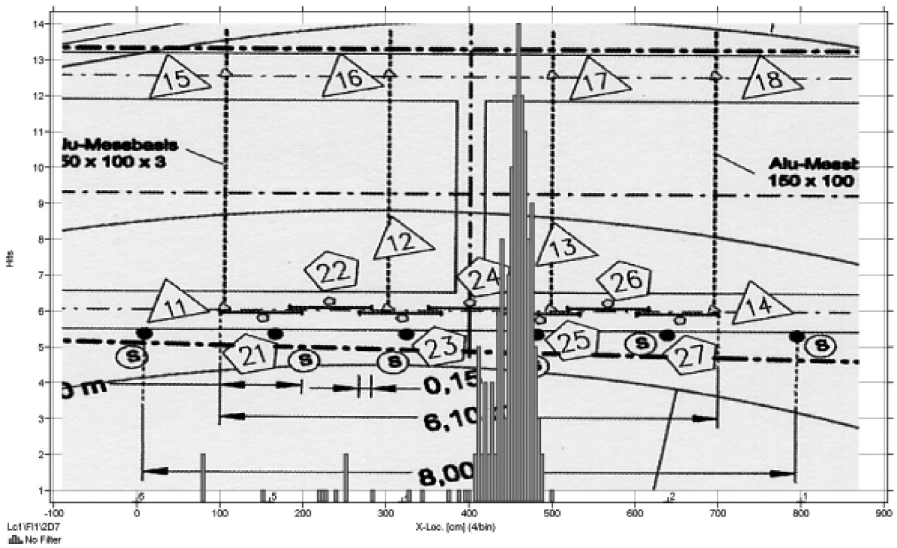



Figure 6: Hit rate versus position along the bridge axis.




Figure 7: Bottom side of a concrete staircase with LVDTs and acoustic emission sensors.

taken, it was recommended not to replace the bridge. The service life of the structure could be extended.

The second example to be presented here is a reinforced concrete staircase. In Figure 7, the structure may be seen from its bottom side. Acoustic emission sensors as well as LVDTs were applied. The results of the acoustic emission

© 2008 Taylor & Francis Group, London, UK

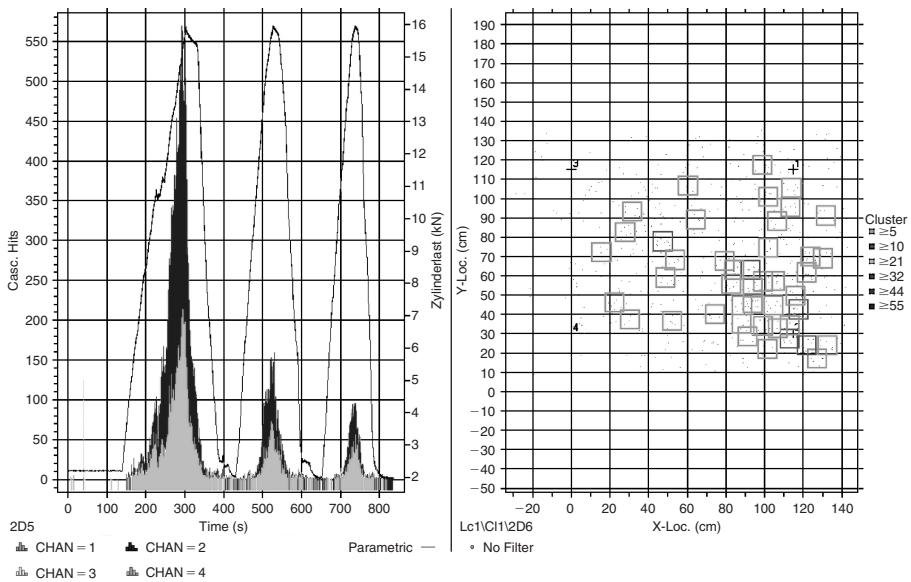



Figure 8: Left side: number of hits (left axis) and applied load (solid line, right axis) versus time; Right side: results of a 2D localization.

analysis clearly demonstrate that the structure has been in its cracked state already prior to the loading test. Figure 8 shows on the left side the number of hits versus time and, in addition, the load applied by one of the actuators (solid line). Acoustic emission starts immediately after the beginning of the loading. The existing cracks are opening and propagating. During the second and third load cycle, however, significantly lower hit rates were observed. This is due to the fact that the load dependent crack pattern was formed almost completely during the preceding (first) load cycle and, during the following load cycles, the cracks are to a large extent already in their inactive phase. This means, the cracks are opened wide resulting in comparably low hit rates, see section 3. The results of deformation measurements confirm the outlined interpretation of the results. During the first load cycle, a significant decrease of the bending stiffness was observed whereas the following load cycles yielded almost identical load-deflection curves. The crack pattern had stabilized.

At the example of the staircase, results of a 2D localization are presented, see Figure 8, right side. The graph shows the individual events with their position. Clusters of events are marked by surrounding squares. Although numerous events could be localized it has to be taken into account, however, that their number is comparably small when compared to the total hit rate. Hence, only a small percentage of the hits could be localized which leads to a reduced reliability of the results. The reasons for this phenomenon are discussed in section 2. A 2D or 3D localization during loading tests of concrete structures is not recommended.

© 2008 Taylor & Francis Group, London, UK

On the basis of the test results, sufficient structural safety of the investigated concrete staircase could be proved.

## 5 CONCLUDING REMARKS

Experimental safety evaluation of existing concrete or masonry structures by test loading should always include acoustic emission analysis. However, this method is applicable only complementary to conventional deformation measurements and the correct interpretation of the acoustic emission results requires a comprehensive evaluation of all experimental observations made during the loading test, including deformations and visible crack patterns. As far as the technical equipment is concerned, acoustic emission analysis during loading tests requires multi-channel sensing as well as real time evaluation of wave form parameters.

## References

[1] Deutscher Ausschuss für Stahlbeton (DAfStb), Belastungsversuche an Betonbauwerken. Richtlinie/Recommendation, Ausgabe/Edition September 2000.
[2] M. Gutermann, V. Slowik, K. Steffens, Experimental safety evaluation of concrete and masonry bridges. International Symposium Non-Destructive Testing in Civil Engineering (NDT-CE), Berlin, 16–19 September 2003.
[3] K. Steffens, Experimentelle Tragsicherheitsbewertung von Bauwerken. Berlin: Ernst & Sohn, 2002.

© 2008 Taylor & Francis Group, London, UK

*Acoustic Emission and Critical Phenomena – Carpinteri & Lacidogna (eds)*
*© 2008 Taylor & Francis Group, London, ISBN 978-0-415-45082-9*

# ACOUSTIC EMISSION MONITORING OF A CONCRETE HINGE JOINT BRIDGE STRUCTURE

**R. Pullin[1], K. M. Holford[1], R. J. Lark[1] and J. J. Hensman[2]**
[1]School of Engineering, Cardiff University, Queen's Buildings, The Parade, Cardiff, U.K.
[2]Dynamics Research Group, Department of Mechanical Engineering, University of Sheffield, Mappin Street, Sheffield, U.K.

## ABSTRACT

Inspections of bridges constructed using hinge joints have noted bridge deck waterproofing failure, which can cause steel reinforcement bar corrosion. Reinforcement is crucial to the integrity of the joint, and a loss of section can induce high stresses leading to possible fatigue fractures and eventually failure by yielding. Visual inspection of the steel reinforcement bars requires the removal of structural concrete, which can increase damage levels and cause further water ingress; therefore the use of acoustic emission (AE) inspection was investigated.

Two investigations were completed on a hinge joint over-bridge; three days of monitoring under normal traffic loading and a load proof test using a 41.55 tonne crane. Under normal traffic loading conditions it was observed that all vehicles resulted in AE hits being detected. Heavy vehicles caused a larger number of hits with high energy than cars but heavy vehicles moving quickly across the joint caused the largest energy emissions. Several regions of possible damage were located. The proof load test showed that the maximum emission energy detected is associated with the load vehicle spanning the joint. Sources previously identified during normal traffic loading were again located.

Three further, novel, data analysis techniques were utilised to analyse the recorded data; kernel probability density estimation (KPDE) function to visualise regions of high energy and hit densities, source location cluster analysis, which identifies regions of high activity and energy, and k-means analysis which is used to identify groups of similar signals in the collected data set. These three techniques and comparisons with previous laboratory experiments aided source characterisation. Three regions of damage were identified which are believed to relate to micro-cracking of concrete around the reinforcing bar. No active fatigue fractures in the steel reinforcement were detected.

© 2008 Taylor & Francis Group, London, UK

## 1 INTRODUCTION

Currently in the United Kingdom there are over 100 bridges containing hinge joint components. Hinge joints were first introduced into bridge construction as a method of simplifying and standardising designs. It is thought that the hinge joints transfer shear loads and accommodate small angular movements but restrict longtitudinal movements [1]. It was also assumed that hinges would enable the bridge to cope with any possible differential settlement. Hinge joints can either be intergrated into beams or slabs.

Visual inspections have noted bridge deck waterproofing failure, which can lead to chloride-rich seepage through the joint that can cause steel reinforcement bar corrosion. This may lead to fatigue fractures and to eventual failure by yielding. However, visual inspection of the steel reinforcement requires the removal of structural concrete which can be damaging to the overall bridge structure meaning new non-destructive testing methods need to be investigated.

Acoustic emission (AE) is a non-destructive testing technique that relies on the detection of transient elastic stress waves that are released as a material undergoes damage, such as cracking or yielding [2]. Surface-mounted sensors detect the stress waves and, by means of triangulation, can locate the origin of the source. Advantages of AE monitoring are that it detects many forms of active damage, is a passive system and that there is minimum disruption to the bridge structure as normal loading conditions are used to excite the bridge structure.

The monitoring of steel box girder structures is now well established [3, 4, 5, 6] but new applications in structural monitoring are constantly emerging particularly in concrete reinforced structures. Acoustic emission monitoring has been successfully applied to concrete structures, a summary and practical examples of some applications can be found in [7, 8, 9]. More detailed examples include the monitoring and determination of corrosion levels in steel encased reinforcement bar in a car park structure [10] and a concrete half joint structure [11] where the ranking of the condition of a number of joints was completed. Results correlated well with visual inspection and sources of damage were located in three dimensions. An investigation of the acoustic monitoring of a beam hinge joint has been previously reported, however no damage was detected in the reinforcing bar which was subsequently confirmed using x-ray monitoring [12].

The overall aim of this investigation was to conduct an experimental study into the use of acoustic emission as a non destructive technique to detect hinge joint deterioration including corrosion induced fatigue cracking of the steel reinforcement bars, on a slab hinge joint structure, using surface mounted sensors.

## 2 EXPERIMENTAL SETUP

16 Physical Acoustics R3I sensors (resonant frequency 30 kHz) were attached to the bridge (Figures 1, 2 and 3). Sensors were attached using aluminium clamps

© 2008 Taylor & Francis Group, London, UK

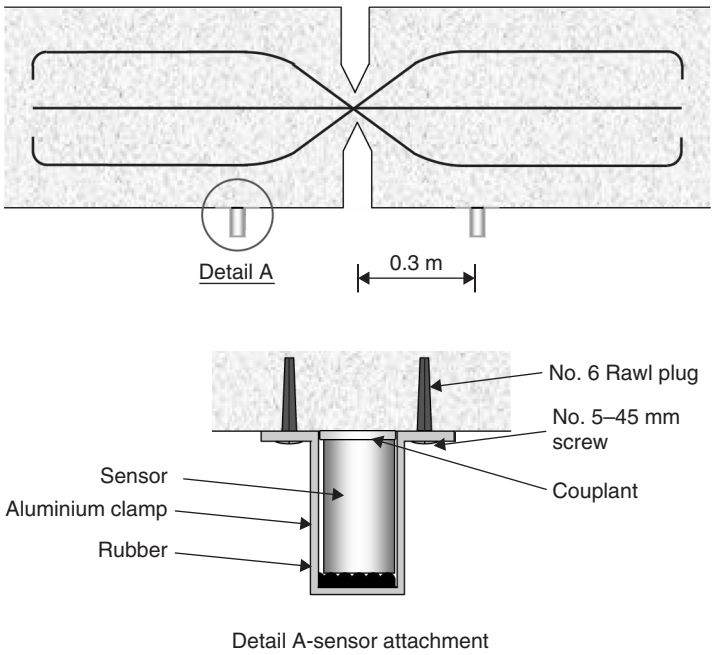



Figure 1: Section of a typical hinge joint assembly and sensor attachment.



Figure 2: Photographs of sensor installation and completed sensor attachment.

(Figure 1) at 1 m intervals along the length of the joint. The exact positioning of the internal reinforcement bars was unknown, however they were believed to be at 308 mm centres. Grease was used as an acoustic couplant. A photograph of sensor attachment and the completed test set-up is shown in Figure 2. The

© 2008 Taylor & Francis Group, London, UK

orientation of the structure (North, East, South and West) was used to reference source positions and groups of sensors as shown in Figure 3.

**Initial evaluation of AE properties.** Pencil lead fractures (PLFs) [13, 14] were used as a source to assess the sensitivity of the sensors. An automatic centre punch was used as a source to assess attenuation and the location of signals in the throat of the joint. The centre punch was initially activated at sensor 12 and at known positions (eastward) along the throat (Figure 3).

**Monitoring during normal traffic loading.** Monitoring was completed for a period of 12 hours (7am–7pm) for three days. Heavy vehicles crossing the joint were logged using time marks for a period of five hours during the initial day of monitoring. AE feature data (Figure 4) was recorded at a threshold of 35 dB.

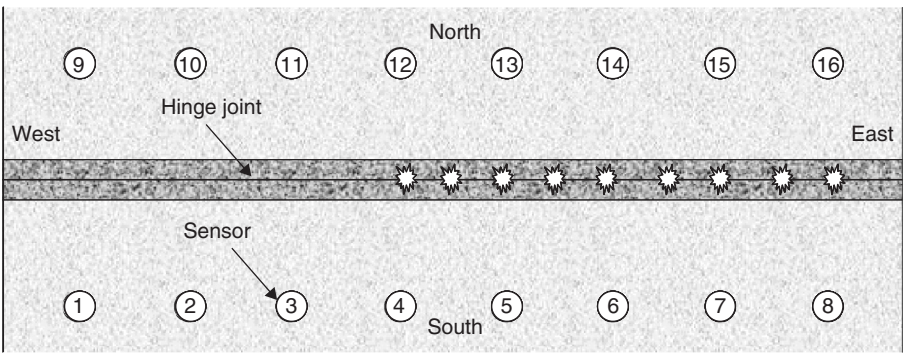



Figure 3: Bridge orientation and position of centre punches along hinge to assess location accuracy.

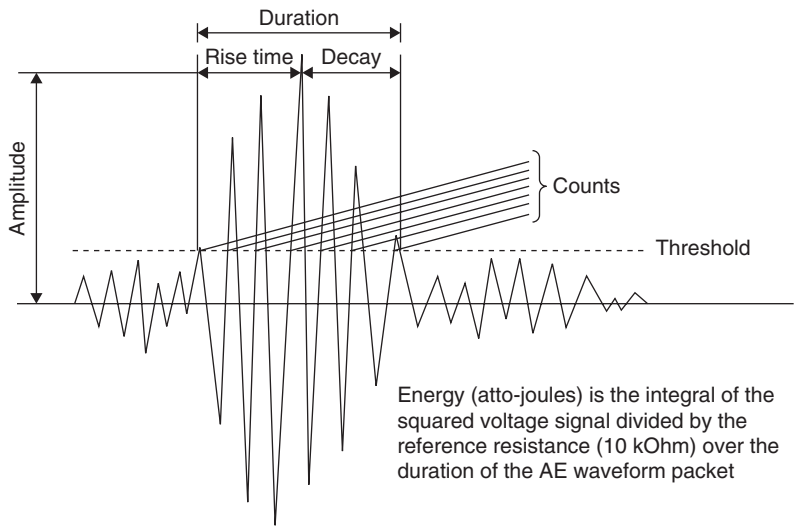



Figure 4: Acoustic emission wave parameters used to describe the recorded signal.

© 2008 Taylor & Francis Group, London, UK

**Load test.** A load test on the bridge was completed using a 41.55 tonne crane. The load travelled from off-span south of the joint to off-span north of the joint. The process was completed in both directions and over both lanes (east and west lanes). AE feature data was recorded at a threshold of 35 dB. Time marks were logged in the data as the front wheel of the load vehicle passed points marked at 5m intervals along the length of the bridge in the northerly direction, whilst the rear wheel was used in the southerly direction.

**Further data evaluation.** An initial analysis of the data was using commercially available software. However after the test data was collected three new methods of data interpretation were developed. A method utilising the kernel probability density estimation (KPDE) function [15] was created that enabled not only the density of signals, but the density of the energy of the signals to be visualised, this is currently not possible using commercial software.

A further technique was developed that expanded on the commercial technique of location cluster analysis and employed k-means analysis [16] to aid source characterisation, a summary of which is shown in Figure 5.

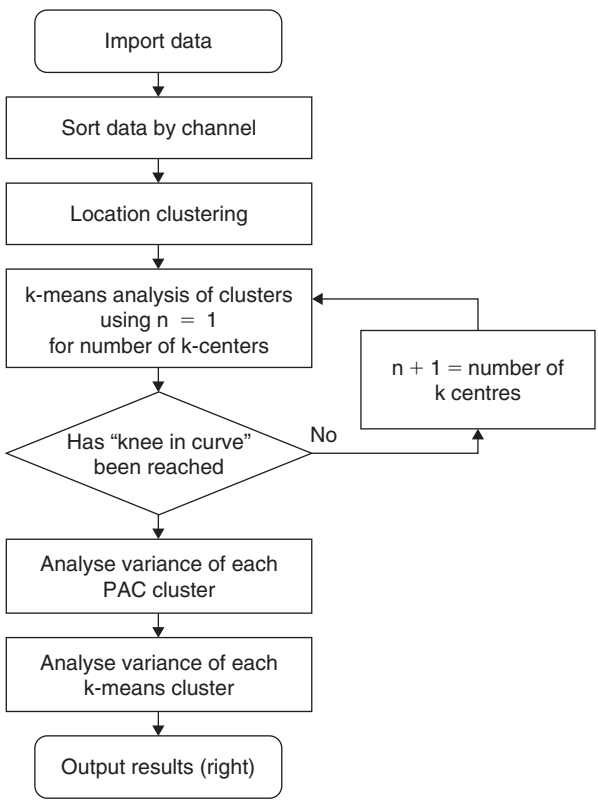



Figure 5: Flow chart of designed script used to further analyse the recorded data.

© 2008 Taylor & Francis Group, London, UK

The purpose of source location clustering is to automatically identify and associate groups of events, based on user controlled spatial criteria and a number of signal threshold. In commercial software clusters can be organised in terms of their total energy, however there is a limit imposed on the total number of clusters (100), which was removed in the developed script. A k-means analysis of the feature data from the location clusters can then be completed. A k-means analysis assigns a set of data points to k-centres, or means. The algorithm is popular due to its fast convergence and simplicity. The algorithm is initiated in a random state: each data point is assigned as a member of one of the k-groups. The set of centres is calculated by taking the mean of the members of each group, and then each data point is re-assigned to a new group according to its nearest center. The process is repeated until no points change groups. The algorithm works exceptionally well on well-spaced groups of Gaussian-distributed data points. In order to make the AE feature data resemble this, the data is normalised, such as to have unit variance in each feature. The variance of each group in the feature space, compared with the entire data set can then be calculated. In theory any regions of high activity that are identified via source location clustering and have very similar signals, as identified via the level of variance in the feature space, are likely to be from a repetitive damage mechanism such as fatigue fracture or concrete micro-cracking.

## 3 RESULTS AND DISCUSSION

**Initial Evaluation of AE Properties.** The response of all sensors to PLFs adjacent to the sensors was above 97 dB. This demonstrates that all sensors were attached correctly. Table 1 shows the results of the attenuation test. The response of all sensors to a centre punch at sensor 12 demonstrates that the signal travels along and across the joint suggesting that the location of signals from within the joint is possible.

Figure 6a shows the results of the centre punch test to establish the accuracy of the time of arrival location technique along the joint (the dashed line represents the location of the centre punches). The results indicate that the location of signals will be accurate within 250 mm using the linear location technique. The results assume that the centre punch was positioned and activated in the correct position along the throat; however there is no such problem across the joint due to the small width of the concrete throat. The location of signals across the joint from the centre punch between sensors 14 and 15 is shown in Figure 6b & c; the signals are located to within 100 mm of the centre of the hinge.

**Monitoring during normal traffic loading.** The numbers of hits within specific amplitude ranges from each day of monitoring are presented in Table 2. The results indicate that there is no significant difference between the numbers of

© 2008 Taylor & Francis Group, London, UK

Table 1: Sensor response to centre punch at sensor 12.

| Sensor number | Energy (aJ) | Amplitude (dB) |
|---|---|---|
| **12** | $8.8 \times 10^8$ | 100 |
| **11** | $4.1 \times 10^8$ | 100 |
| **13** | $1.9 \times 10^8$ | 100 |
| **4** | $1.7 \times 10^7$ | 92 |
| **5** | $7.1 \times 10^6$ | 87 |
| **3** | $6.7 \times 10^6$ | 89 |
| **10** | $2.4 \times 10^8$ | 100 |
| **14** | $1.3 \times 10^8$ | 99 |
| **6** | $1.2 \times 10^6$ | 79 |
| **2** | $3.0 \times 10^6$ | 81 |
| **7** | $9.0 \times 10^5$ | 79 |
| **15** | $6.6 \times 10^7$ | 99 |
| **9** | $1.5 \times 10^7$ | 94 |
| **1** | $9.8 \times 10^5$ | 79 |
| **16** | $3.6 \times 10^7$ | 96 |
| **8** | $1.6 \times 10^5$ | 69 |

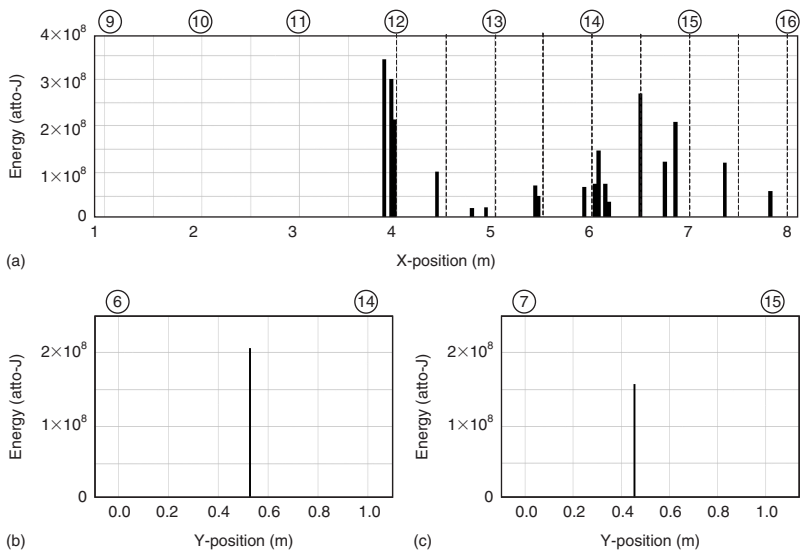



Figure 6: AE location of signals produced by (a) centre punch along the throat, (b) response of sensors 6 and 14 to centre punch at hinge between sensors 14 and 15 and (c) response of sensors 7 and 15 to centre punch at hinge between sensors 14 and 15.

© 2008 Taylor & Francis Group, London, UK

Table 2: Summary of monitoring results.

| Amplitude of hits (dB) | No. of hits Day 1 ($\times 10^3$) | No. of hits Day 2 ($\times 10^3$) | No. of hits Day 3 ($\times 10^3$) |
|---|---|---|---|
| **35–45** | 1500 | 1500 | 1200 |
| **45–55** | 226 | 187 | 152 |
| **55–65** | 58.8 | 40.2 | 37.3 |
| **65–75** | 12.9 | 8.4 | 7.3 |
| **75–85** | 2.09 | 1.28 | 1.09 |
| **85–100** | 0.23 | 0.16 | 0.15 |

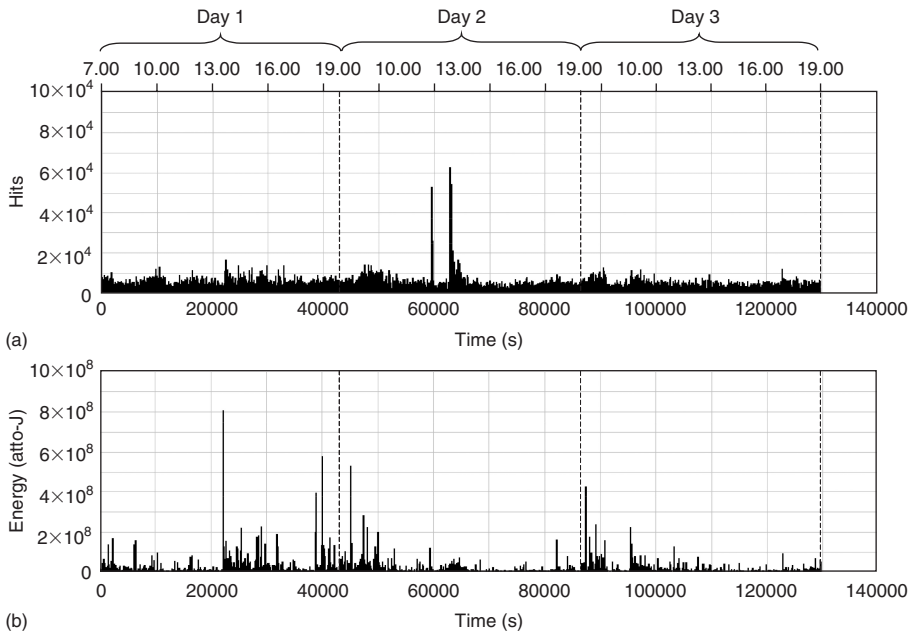



Figure 7: History of hits and energy recorded during the three days of monitoring.

hits on each day of monitoring suggesting that at this site one day of monitoring is sufficient to provide the necessary data.

Figure 7 shows the AE activity of the joint in terms of the number of hits and the amount of energy detected on all sensors, for the three days of monitoring. The plots show that there was higher energy activity associated with the initial day of monitoring (Fig 7b). It was visually observed during the monitoring period that there were a higher number of heavy vehicles travelling to and from a construction site on the north side of the bridge on the first day of the test. The

© 2008 Taylor & Francis Group, London, UK

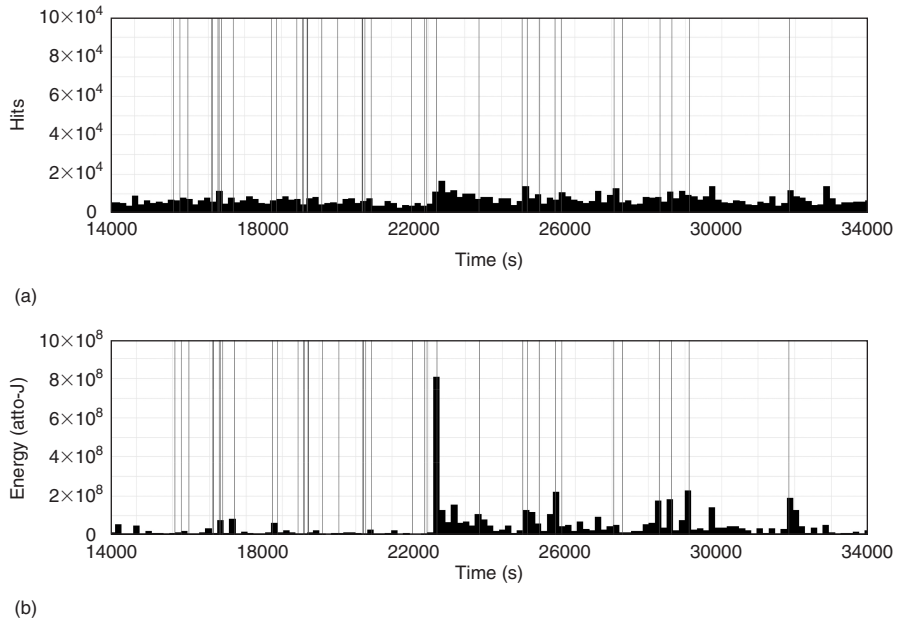



Figure 8: Activity of joint with logged vehicles in terms of (a) detected hits and (b) the energy of the detected hits.

high energy peaks detected through the three days of monitoring were associated with heavy vehicles crossing the joint.

Figure 8 shows the period of logging during which the activity of heavy vehicles (solid line on plot) was recorded. The highest energy emissions from the joint can be associated with heavy vehicles crossing the joint, however not all heavy vehicles produced large energy emissions. During monitoring it was visually observed that all vehicles caused some emissions, most may be associated with the normal stress loading of the joint and that vehicles travelling at higher speeds across the joint produced greater energy emissions.

The location of the detected energy along the joint for the three days of monitoring is shown in Figures 9 and 10 for sensors on the north and south sides of the joint. Detected energy across the joint is shown in Figure 11. Circled numbers at the top of each plot represent the location of the sensors.

There is only one dominant source of energy on the north and south side of the bridge but several peaks of hits. These peaks could be related to damage in or around the steel reinforcement bars. The energy of the emissions is between two and ten times greater on the north side and locations on this side are more defined. This suggests that there are sources on the north side and that the signals from these sources are detected at both sides but attenuated, as expected, across the joint.

© 2008 Taylor & Francis Group, London, UK

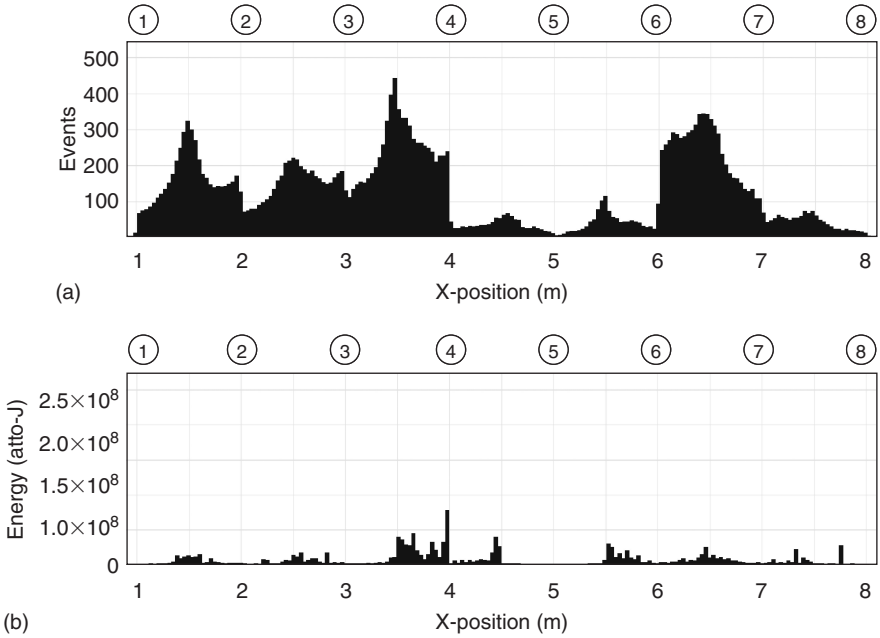



Figure 9: Location of signals along south side of joint (a) events and (b) the energy of the detected hits.

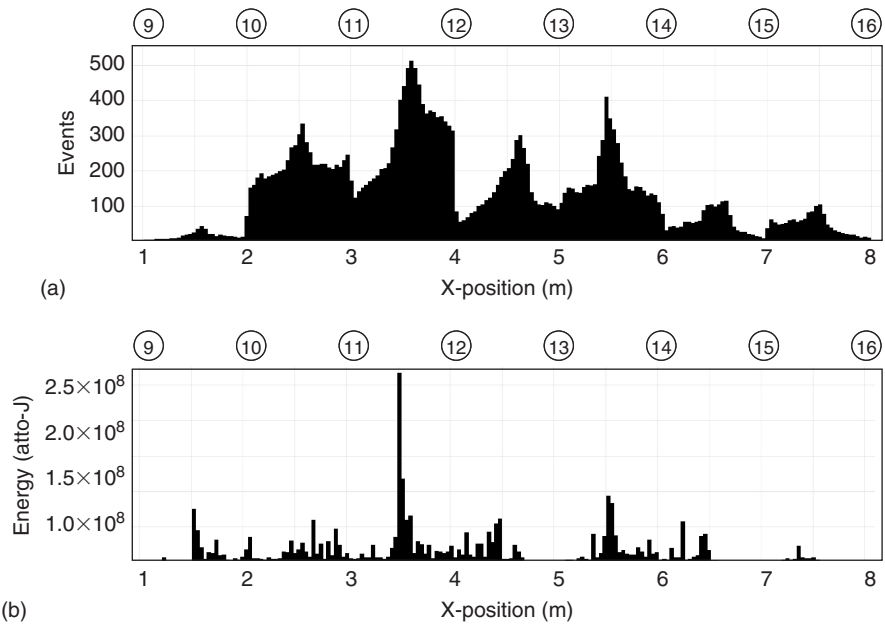



Figure 10: Location of signals along north side of joint (a) events and (b) the energy of the detected hits.

© 2008 Taylor & Francis Group, London, UK

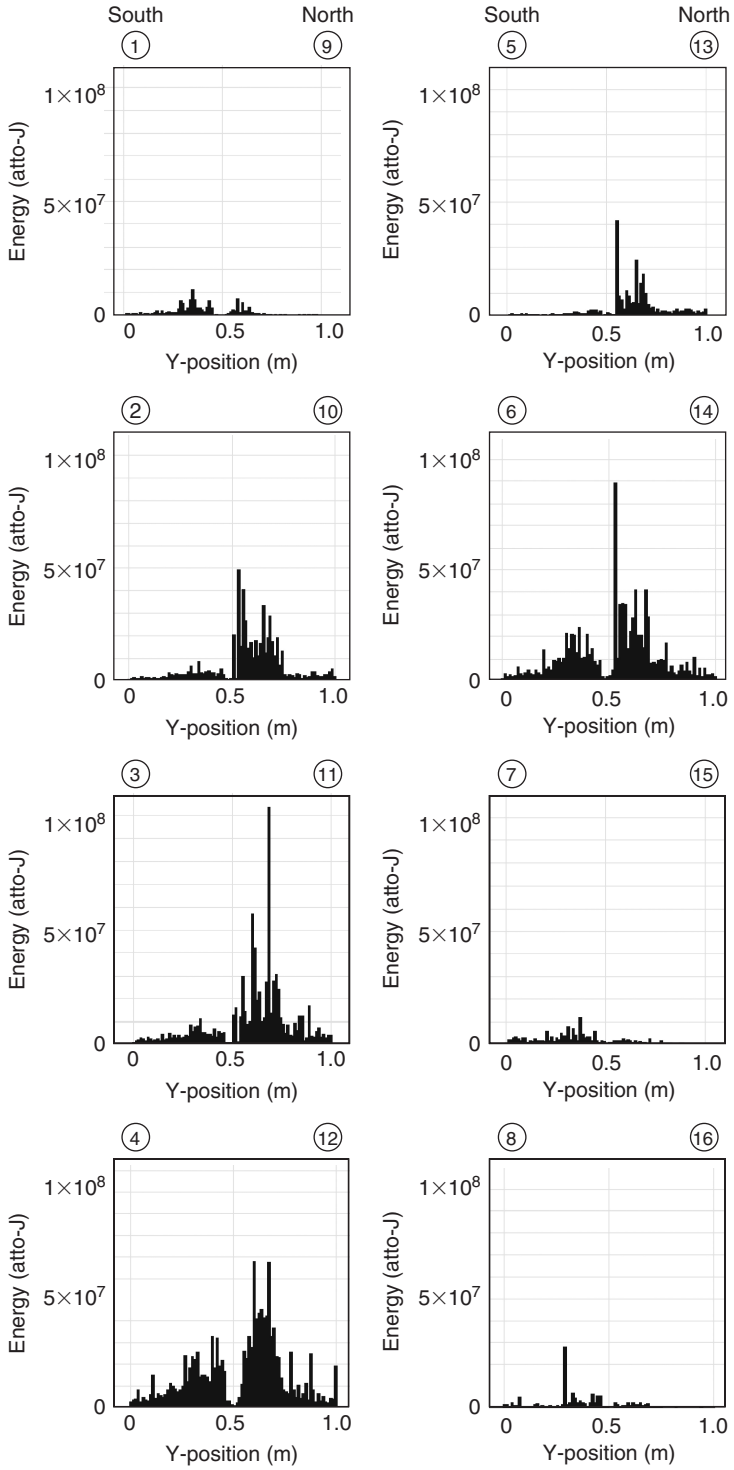



Figure 11: Energy of signals located of signals across the joint.

© 2008 Taylor & Francis Group, London, UK

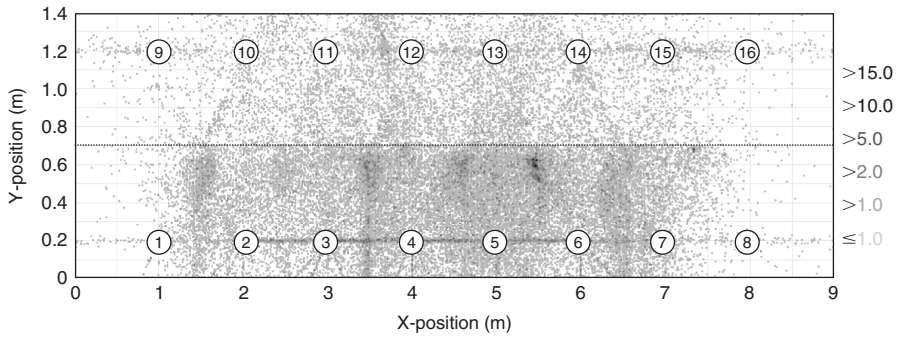



Figure 12: Location of signals recorded during the three days of monitoring.

This is confirmed in Figure 11, which shows the location of signals across the joint. Sensors 4 and 12, which oppose each other across the joint, show a large peak of energy approximately 200 mm north of the joint. Similarly a peak of energy between sensors 5 and 13 and 6 and 14 can be seen, which coincides with the peaks of energy located along the joint at approximately 5.5 m. This suggests that the detected signals are not due to noise at the construction joint but arise from sources away from the centre, possibly damage.

Figure 12 shows the planar location (two-dimensional) results for the three days of monitoring. One source of emission is evident and coincides with the peak in the linear location plots (Figures 9, 10 and 11) between sensors 5 and 6 and 13 and 14. On the planar plot, however, the source is shown to be on the south side of the joint. This may be due to a loss of sensitivity at channel 5, which would affect the amount of energy detected from a signal but not its time of arrival, therefore this source is on the south side of the joint. The source is away from the construction joint and again suggests a site of possible damage. In addition distinct bands of vertical emission can be seen and probably coincide with the position of the internal reinforcement hinge joint bars. These bands occur at larger intervals than the 308 mm reinforcement centres shown on the construction drawings and implies that the AE is detecting sources at some bars but not every bar.

**Load Test.** The activity of the joint during the load test is shown in Figures 13a, b, c & d for the forward and reverse directions. The largest energy in the forward direction occurs when the front wheel of the load vehicle is between 15–20 m onto the bridge and coincides with the vehicle spanning the joint. This is consistent with results obtained previously [10]. The result is confirmed in the south direction, however there is also energy detected as the load vehicle is just on the span of the bridge in the west lane.

The location of signals detected during the load test is presented in Figure 14. As the vehicle travels over the east lane, sources coinciding with the x-position of previously identified sources are located. The location of signals in the west

© 2008 Taylor & Francis Group, London, UK

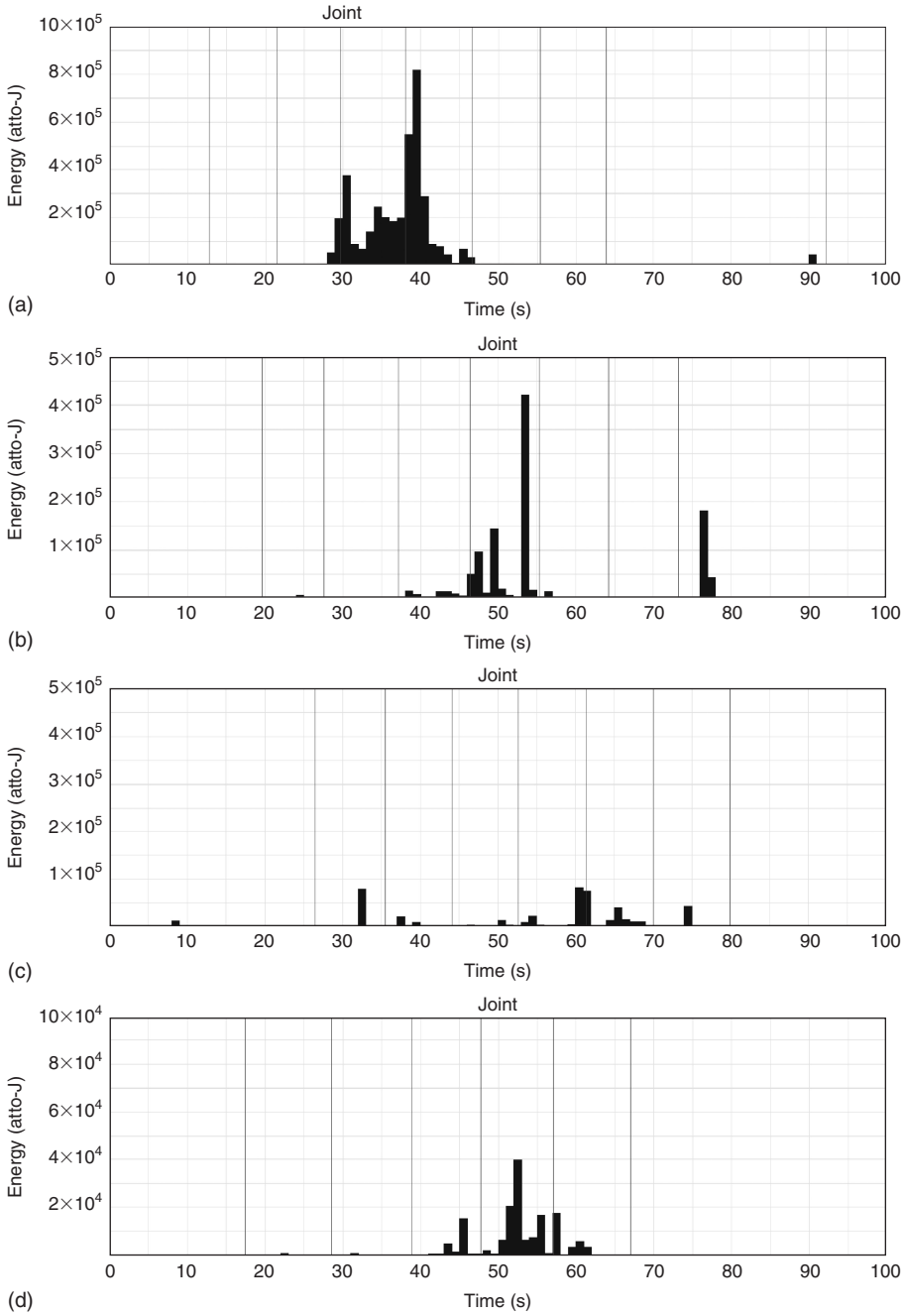



Figure 13: Energy detected during load tests (a) forward 1, (b) forward 2, (c) reverse 1 and (d) reverse 2.

© 2008 Taylor & Francis Group, London, UK

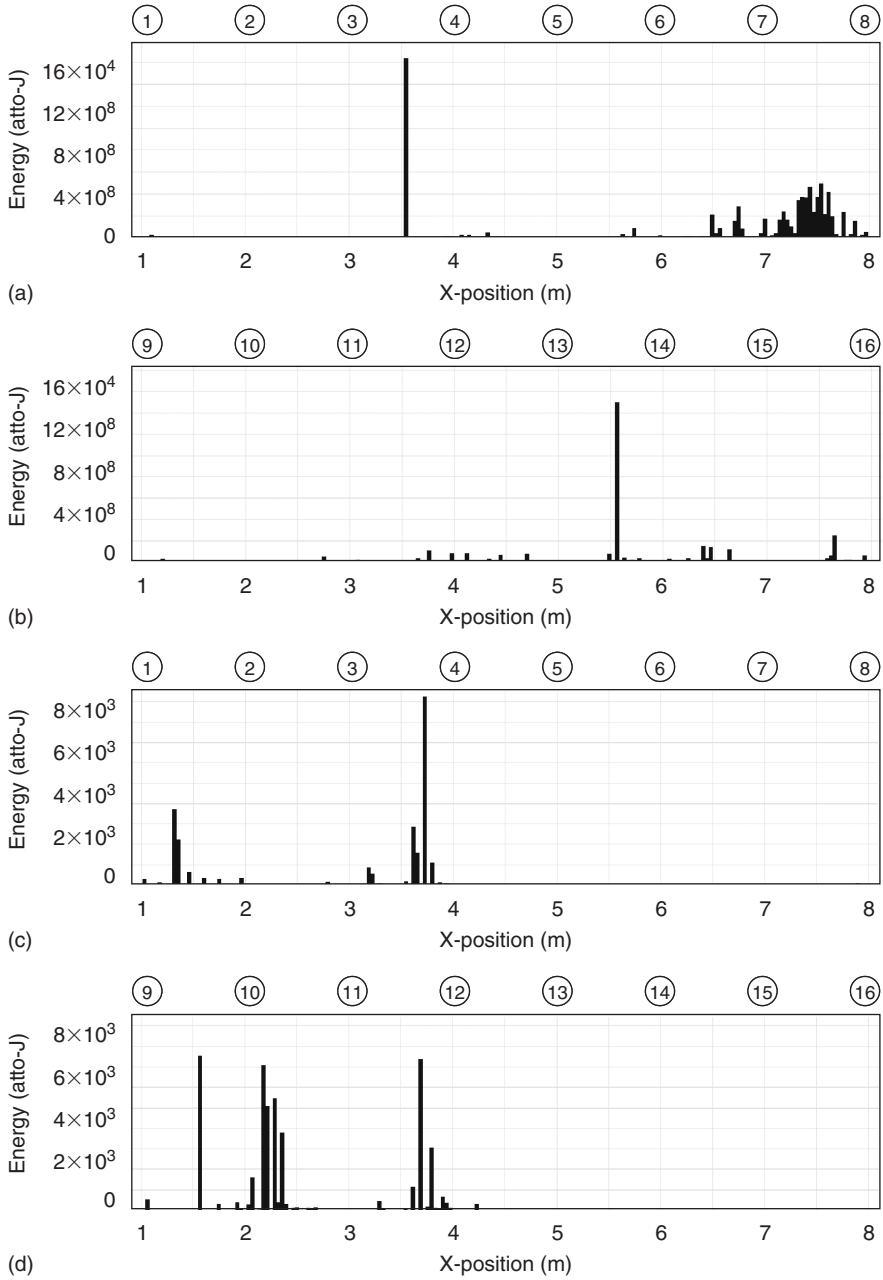



Figure 14: Location of energy released during forward load tests (a) east (b) east 2, (c) west and (d) west 2.

© 2008 Taylor & Francis Group, London, UK

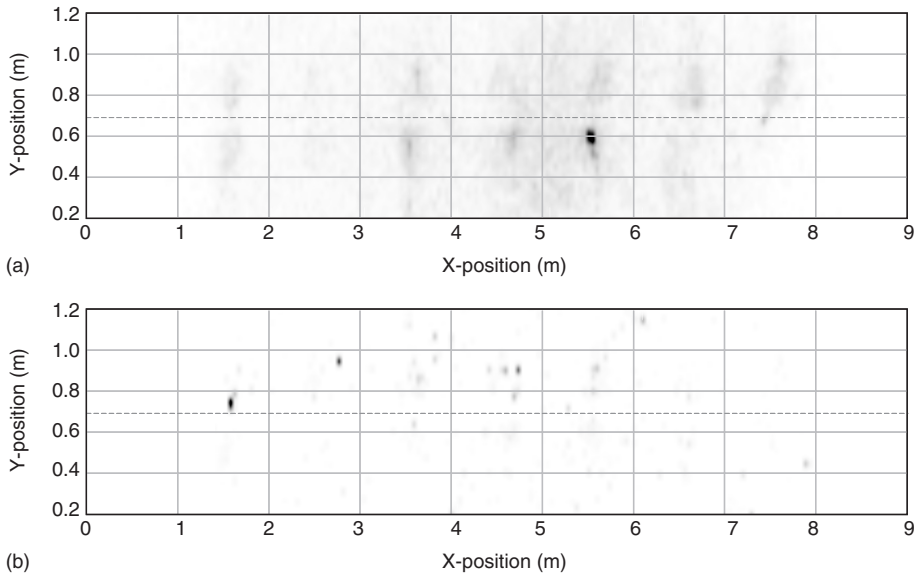



Figure 15: Kernel probability density estimation plot (a) hits (b) energy.

lane are confined to the west side of the bridge, and coincide with the bands of vertical emissions previously identified in Figure 12.

**Further Data Evaluation.** The resulting plots of the KPDE analysis are presented in Figures 15a and b. The region of high activity at approximately (5.5 m, 0.6 m) is clearly visible in Figure 15a, whilst the remaining bands that are associated with the internal reinforcing bar are clearly visible. However of more interest is the region of densely populated energy in Figure 15b, which using the commercial software could not be visualised. This is a region of low density in terms of events (Figure 12) but high energy and it is very close to the centre line of the hinge section. This suggests that this region is made up of a small number of high-energy events that could be attributed to concrete fractures. Fatigue fractures of the reinforcing bar would be likely to occur more frequently and with greater consistency in energy release under normal traffic loading therefore the region is attributed to concrete fractures near to the throat of the hinge.

To further analyse the regions of high event density on the south side of the joint in Figure 15, feature data, including location, from channels 3, 4, 5 and 6 was processed by the developed k-means analysis based script (Figure 5). A source cluster area, based on a circle with diameter 30 mm, and threshold of 30 events was used to analyse the data. A graphical representation of the script results is shown in Figure 16, together with a key to the level of variance of the feature data. Three regions of grouped, low variance clusters are clearly visible and are in close proximity to the joint. Although the definite position of the reinforcing bars is unknown, the distance between the bars is believed to be

© 2008 Taylor & Francis Group, London, UK

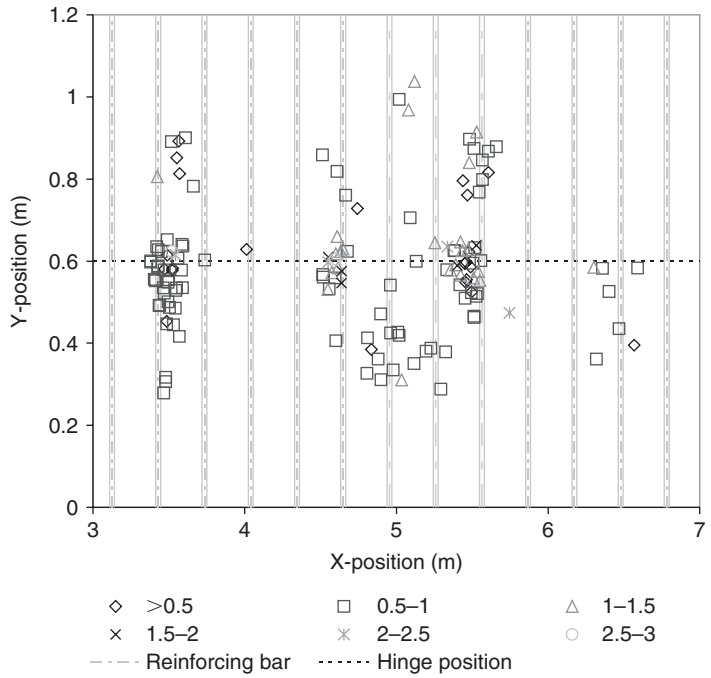



Figure 16: Graphical display of results from k-means analysis based script.

308 mm, and the possible positions of the bars based on the lowest variance clusters are superimposed. It can be seen that the other grouped regions would also appear to be in close proximity to reinforcing bars, whilst several bars appear to have no active damage in their vicinity.

Feature data of the cluster with the highest number of events (242) in the low variance group, which is centred on a reinforcing bar, were compared with that of regions at a similar distance from the same sensor, that were not associated with a reinforcing bar position; this revealed little difference in features. This suggests that the detected signals are associated with damage in the concrete structure rather than the steel reinforcing bar, which would have distinctly different features. This suggests that the regions detected are due to micro-cracking of the concrete.

The activity history of this cluster in terms of energy is presented in Figure 17. The plot shows sharp rises in the magnitude of energy during the monitoring period. From experience, the amplitude and energy of each detected hit increases [17] with increasing fracture length, until close to rupture when there is a rapid increase in energy associated with the increase in fracture length per cycle. This again suggests that the emissions are not due to steel fatigue and are due to fractures of variable intensity and magnitude in the concrete surrounding the

© 2008 Taylor & Francis Group, London, UK

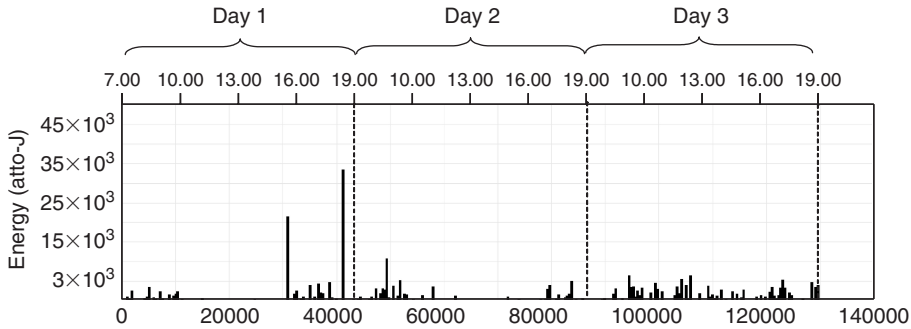



Figure 17: History of the energy of the detected hits in principal cluster.

steel reinforcing bar. However this cannot be verified without the removal of structural concrete.

## 4 CONCLUSIONS

System verification and assessment of location showed that the installed AE system was operating correctly. Attenuation trials across the joint showed a low loss of signal allowing the potential location of defects through the hinge joint. Under normal traffic loading conditions on this structure it was observed that all vehicles caused emissions. Heavy vehicles caused larger emissions than cars and heavy vehicles moving quickly across the joint caused the largest energy emissions.

Energy recorded during a load test showed that the maximum emission detected is associated with the load vehicle spanning the joint. Sources previously identified were again located, confirming the existence of damage. Linear location plots of energy recorded during the three days of monitoring under normal traffic loading showed several regions of activity. Using source location cluster analysis and k-means analysis three regions of activity were identified and it is believed that the activity is due to regions of concrete micro-cracking around the reinforcing steel. No regions of fatigue fracture of steel reinforcement were positively identified.

## References

[1] C. B. Wilson, Assessment of the reinforced concrete hinges on five M6 overbridges in Staffordshire, Proceedings Institution Civil Engineers, Vol. 110 (1995) pp 4–10

[2] R. K. Miller and P. McIntire, Acoustic Emission Testing- Non-destructive Testing Handbook Volume 5, American Society for Non-destructive Testing, (1987)

© 2008 Taylor & Francis Group, London, UK

[3] D. C. Carter, R. Pullin and K. M. Holford, Acoustic Emission Studies of a Steel Box Girder Bridge, 23rd European Conference on Acoustic Emission Testing, (1998) pp. 225–229
[4] K. M. Holford, D. C. Carter, R. Pullin and A. W. Davies, Bridge Integrity Assessment by Acoustic Emission – Global Monitoring, 2nd International Conference on Identification in Engineering Systems, (1999) pp 392–400
[5] R. Pullin, D. C. Carter, K. M. Holford and A. W. Davies, Bridge Integrity Assessment by Acoustic Emission – Local Monitoring, 2nd International Conference on Identification in Engineering Systems, (1999) pp 400–405
[6] A. W. Davies, K. M. Holford, R. Pullin, J. Watson, P. T. Cole and S. N. Gautney, Acoustic emission monitoring trial, Report for The Highways Agency: Maintenance Agency Area 12: Midlands Links Motorway Viaducts, Cardiff University and Physical Acoustics Ltd. (1999)
[7] J. R. Watson, S. Yuyama, R. Pullin and M. Ing, Acoustic Emission Monitoring Applications for Civil Structures Surrey University's International Bridge Management Conference (2005)
[8] M. Ohtsu, A review of AE in Civil Engineering with Emphasis on Concrete, Journal of Acoustic Emission, Vol. 8, No. 4, (1989) pp. 93–98
[9] M. Ohtsu, The History and Development of Acoustic Emission in Concrete Engineering, Magazine of Concrete Research, 48, No. 177 (1996) pp. 321–330
[10] M. J. Ing, R. Lyons and S. A. Austin, Risk-Based Investigation of Steel Reinforcement Corrosion Using the AeCorr Technique, Proceedings of 3rd International Conference on Emerging Technologies in Non Destructive Testing, Thessaloniki, Greece (2003), pp 410–418
[11] J. R. Watson, P. T. Cole, I. Kennedy-Reid and J. Halliday, Condition Assessment of Concrete Half Joints, First International Conference on Bridge Maintenance, Safety and Management, Barcelona, 14–17th (July 2002)
[12] R. Pullin, K. M. Holford, R. J. Lark and P. Beck, Acoustic Emission Assessment of Concrete Hinge Joints, Key Engineering Materials, Vols. 245–246 (2003) pp. 323–330
[13] ASTM, Standard guide for determining the reproducibility of acoustic emission sensor response, American Society for Testing and Materials, E 976 (1994)
[14] N.N. Hsu and F.R Breckenbridge, Characterization and Calibration of Acoustic Emission Sensors, Materials Evaluation 39, pp 60–68 (1979)
[15] B. W. Silverman and B. S. Silverman, Density Estimation for Statistics and Data Analysis, CRC Press (1986)
[16] C. M. Bishop, Pattern Recognition and Machine Learning, Springer, ISBN-10: 0387310738, (2006)
[17] P. Beck, Quantitative Damage Assessment of Concrete Structures Using Acoustic Emission, PhD Thesis, University of Wales Cardiff (2004)

© 2008 Taylor & Francis Group, London, UK

# 2 Seismic Mechanics and Critical Behaviours

## *2.1 Critical state transition in earthquake dynamics*

© 2008 Taylor & Francis Group, London, UK

*Acoustic Emission and Critical Phenomena – Carpinteri & Lacidogna (eds)*
*© 2008 Taylor & Francis Group, London, ISBN 978-0-415-45082-9*

# NUCLEATION AND CRITICAL PHENOMENA, DAMAGE, AND CHARACTERISTIC EARTHQUAKES

**D.L. Turcotte[1], J.B. Rundle[1,2], M. Yoder[2], S.G. Abaimov[1] and W. Klein[3]**
[1]Department of Geology, University of California, Davis, CA
[2]Department of Physics, University of California, Davis, CA
[3]Department of Physics, Boston University, Boston, MA

## ABSTRACT

We consider the sequence of earthquakes on the Parkfield segment of the San Andreas fault to be representative "characteristic" earthquakes. We consider the recurrence interval statistics of these earthquakes and the frequency-magnitude statistics of smaller earthquakes prior to the 2004 Parkfield earthquake. We give results for a "stiff" slider-block model and show strong similarities between the model and the Parkfield results. In both cases a power-law distribution of smaller events were observed. In both cases the Weibull fit to the distribution of interval times was quite good with similar values of the power-law exponent. We have also drawn an analogy between an earthquake rupture and a first-order phase change (nucleation). We consider this analogy both with and without damage. With damage the rupture is equivalent to an equilibrium phase change, without damage the rupture is equivalent to a spinodal phase change. We argue that the absence of a systematic precursory acceleration of seismicity prior to earthquakes is evidence that precursory damage does nor occur. Thus fault rupture can be associated with a spinodal phase change.

## 1 INTRODUCTION

The process of earthquake initiation and failure typically involves a large range of scales. In most cases well defined foreshocks do not occur and earthquake rupture occurs suddenly (Main and Al-Kindy, 2002, Rundle *et al.*, 2002, Turcotte, 1997). The physics of these processes are similar to the processes involved in damage mechanics in materials, which can be studied in the laboratory (Garcimartin *et al.*, 1997, Guarino *et al.*, 1999, Guarino *et al.*, 1998, Wawersik and Brace, 1970, Wawersik and Fairhurs C., 1970). Material damage occurs when microscopic processes of dislocation dynamics and microcrack formation

© 2008 Taylor & Francis Group, London, UK

are produced in association with strain and fracture mechanisms operating on the macroscopic scale. Here we discuss the physics of self-organization and damage at the "microscopic" scale, and how it relates to the "macroscopic" scale of the fracture. We consider a free energy functional that connects the microscale with the macroscale processes. Since damage represents a modification of a brittle elastic system, we expect to find that the interactions produce the mean field dynamics characteristic of elastic systems. Sudden transitions in the state of these systems can be understood in the context of first-order phase transitions, where the influence of the classical limit of stability, or spinodal, is felt. We can use ideas from thermodynamics and kinetics of phase transitions in order to better understand earthquake rupture (Klein *et al.*, 2002, Rundle and Klein, 1989).

We formulate our analysis in terms of characteristic earthquakes. As a specific example we consider the sequence of characteristic earthquakes that have occurred on the Parkfield section of the San Andreas fault. We consider the return times of these earthquakes and their relation to the background seismicity.

We next give results of a slider-block model and show strong similarities to the behavior of characteristic earthquakes. As a model for fault rupture we introduce damage mechanics. Using damage mechanics we argue that fault rupture can be considered to be a first-order phase change.

## 2 CHARACTERISTIC EARTHQUAKES

If a point on a fault experiences a sequence of earthquakes, we refer to the intervals between these earthquakes as recurrence times. Of particular interest are the recurrence times on major faults. These faults experience the quasi-periodic occurrence of large earthquakes. They are usually referred to as characteristic earthquakes. Available evidence is that there is considerable variability in both the recurrence times and in the magnitudes of characteristic earthquakes. This variability can be attributed to the interactions between faults and fault segments. It is the purpose of this paper to consider this variability in terms of concepts of statistical physics.

Various distributions have been used to fit observed earthquake recurrence time statistics. Ogata (1999) and Utsu (1984) have considered in some detail the Weibull, lognormal, gamma, exponential, and doubly exponential distributions. Matthews et al. (2002) has made a similar comparison of the above distributions as well as the Brownian passage-time distribution. Many authors have applied the Weibull distribution to distributions of recurrence times between earthquakes. Rikitake (1982) applied the Weibull distribution to the observed recurrence times of great earthquakes at six subduction zones. In general the number of data points in any sequence of recurrence times of characteristic earthquakes is too small to differentiate between alternative distributions (Savage, 1994, Sornette and Knopoff, 1997). In order to overcome this difficulty Yakovlev *et al*. (2006)

© 2008 Taylor & Francis Group, London, UK

utilized data from a one million year simulation of earthquakes on the northern San Andreas fault. This study showed conclusively that the Weibull distribution gives a better fit to the data than the lognormal and Brownian passage-time distributions. Abaimov et al. (2007a) determined the recurrence time statistics for creep events on the San Andreas fault in central California and also found that the Weibull distribution is preffered.

In this paper we will make comparisons only with the Weibull distribution. The cumulative distribution function (cdf) for the Weibull distribution is given by

$$P(t) = 1 - \exp\left[-\left(\frac{t}{\tau}\right)^{\beta}\right] \tag{1}$$

where $P(t)$ is the fraction of the recurrence times that are shorter than $t$ and $\beta$ and $\tau$ are fitting parameters.

If $\beta = 1$ the Weibull distribution becomes the exponential (Poisson) distribution with $\sigma = \mu$ and $C_V = 1$. In the limit $\beta \to +\infty$ the Weibull distribution becomes a $\delta$-function with $\sigma = C_V = 0$ and the occurrence of earthquakes is periodic.

## 3 PARKFIELD EARTHQUAKES

Probably the best studied sequence of characteristic earthquakes is the sequence that occurred on the Parkfield, California section of the San Andreas fault between 1857 and 2004 (Bakun *et al.*, 2005). This is because the slip rate is relatively high ($\approx$30 mm/year) and the earthquakes are relatively small ($m \approx 6.0$), thus the recurrence times are relatively short ($\approx$25 years). Also, this fault is subject to a near constant tectonic drive due to the relative motion between the Pacific and North American plates. Slip on the Parkfield section of the San Andreas fault occurred during $m \approx 6$ earthquakes that occurred in 1857, 1881, 1901, 1922, 1934, 1966, and 2004. The mean and coefficient of variation of these recurrence times are $\mu = 24.5$ years, and $C_V = 0.378$, respectively. The cumulative distribution of recurrence times $P(t)$ is given as a function of the recurrence time $t$ in Figure 1. Also included in Figure 1 is the best log likelihood ($-21.22$) fit of the Weibull distribution with $\tau = 27.4 \pm 3.7$ years and $\beta = 3.21 \pm 1.03$ (the error bars are 95% confidence limits).

We will consider in some detail the most recent Parkfield earthquake (28 September 2004; $m_{ms}$ 6.0; epicenter 35.818°N, $-120.366$°W). The high-quality seismic network in the vicinity of this mainshock provided a particularly well documented sequence of aftershocks (Bakun *et al.*, 2005).

In Figure 2 we show the spatial distribution of seismicity for 365 days following the Parkfield earthquake. The epicenter of the mainshock is shown as a star. The aftershocks are defined to be all earthquakes that occurred in an

© 2008 Taylor & Francis Group, London, UK

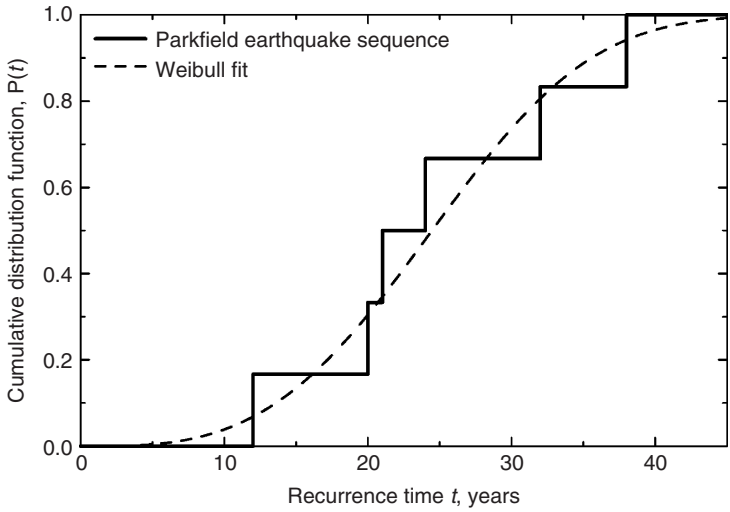



Figure 1: Cumulative distribution of recurrence times of Parkfield earthquakes. The continuous line is the distribution of six actual recurrence times. The discontinuous line is the best-fit Weibull distribution ($\mu = 24.5$ years, $\sigma = 9.25$ years, $C_V = 0.378$, $\tau = 27.4$ years, and $\beta = 3.21$).

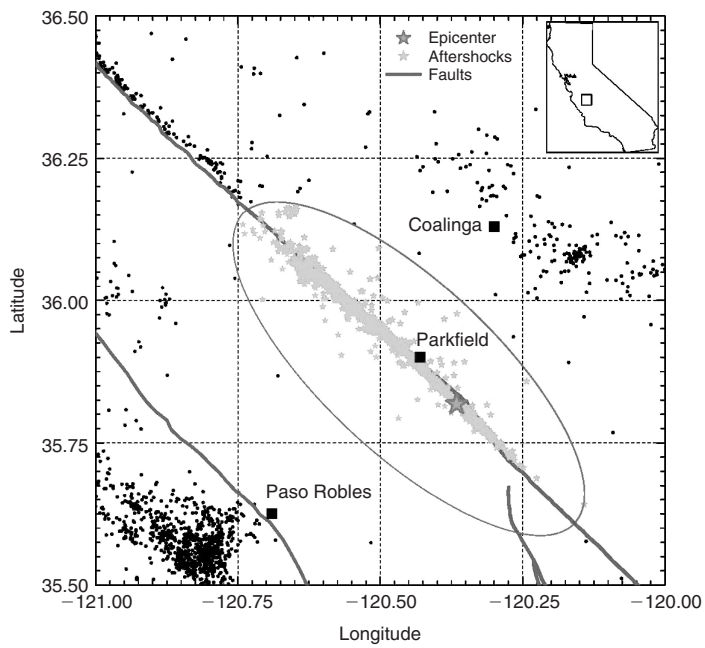



Figure 2: The spatial distribution of seismic activity for 365 days after the Parkfield earthquake (28 September 2004; $m_{ms}$ 6.0; epicenter 35.818°N, −120.366°W). The aftershocks are defined to be all earthquakes that occurred in the elliptical region.

© 2008 Taylor & Francis Group, London, UK

elliptical region centered at 35.9°N and −120.5°W with the radii of sizes 0.4° and 0.15° and oriented 137°NW during this time interval. We have 4583 events that we consider to be aftershocks. In our analysis we have used a catalog provided by the Northern California Earthquake Data Center (NCSN catalog, http://quake.geo.berkeley.edu/ncedc/).

We first consider the frequency–magnitude scaling for the Parkfield aftershock sequence for different time intervals after the mainshock. The cumulative numbers of aftershocks with magnitudes greater than $m$, $N(\geq m)$, are given as a function of $m$ in Figure 3 for different time intervals following the mainshock. We correlate this dependence with a modified form of Gutenberg–Richter scaling relation given by

$$\log_{10} N(\geq m) = b(m_{ms} - \Delta m^* - m) \tag{2}$$

where $m_{ms}$ is the magnitude of the mainshock and $m^* = m_{ms} - \Delta m^*$ is the magnitude of the largest inferred aftershock for this sequence. This is obtained by formally solving the equation $\log_{10} N(\geq m^*) = 0$ (Shcherbakov and Turcotte, 2004b). The fit of equation (1) to the Parkfield data for 365 days given in Figure 3 is obtained by a least-squares fit to the data in the magnitude range $m$ 1.2 to $m$ 4.0. For smaller magnitudes the observed rollover is clearly due to incomplete data, for larger magnitudes the small number of earthquakes leads to considerable scatter in the data. Our straightline fit of equation (1) requires

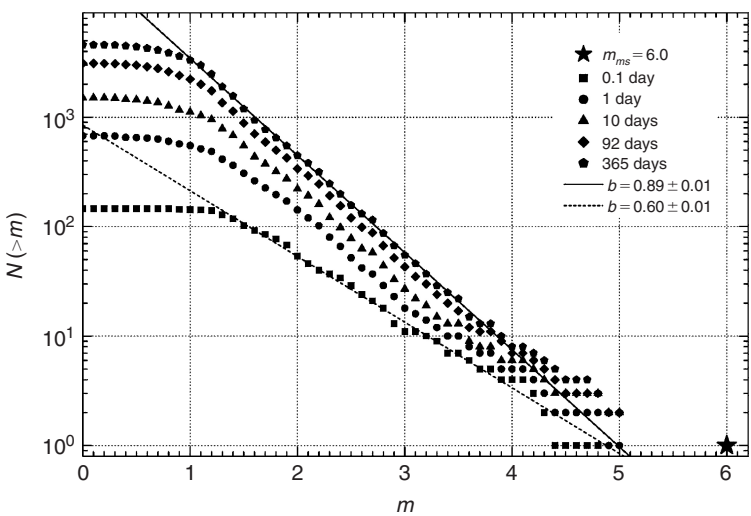



Figure 3: The cumulative frequency-magnitude distribution of aftershocks for several time intervals following the Parkfield mainshock. Straight-line fits of the Gutenberg-Richter scaling relation (equation 2) to yield b-values for 0.1 day ($b = 0.6 \pm 0.01$) and 365 days ($b = 0.89 \pm 0.01$) after the mainshock.

© 2008 Taylor & Francis Group, London, UK

$b = 0.89 \pm 0.01$. In Figure 3 we also give the fit of equation (1) to the data for 0.1 days after the mainshock; in this case we consider the magnitude range $m$ 1.5 to $m$ 4.0 and find the best least-squares fit gives $b = 0.6 \pm 0.01$. The $b$-value appears to systematically increase with time after the mainshock. In this analysis the $b$-values have been calculated over the whole aftershock zone.

The invariance of the observed difference between the magnitude of a mainshock and its largest aftershock is known as Bath's law (Bath, 1965). The intersection of the straight line given by equation (1) with $N(\geq m^*) = 1$ ($\log_{10} N(\geq m^*) = 0$) gives $m^* = 5.0$ and $\Delta m^* = 1.0$. The value of the inferred largest aftershock, $m^* = 5.0$, for the Parkfield earthquake has the same magnitude as the value of the largest detected aftershocks. Shcherbakov and Turcotte (2004b) proposed a modified version of Bath's law in which $\Delta m^*$ is nearly constant. For 10 California earthquakes they found $\Delta m^* = 1.11 \pm 0.09$ compared with the value $\Delta m^* = 1.0$ for the Parkfield earthquake as given previously.

We next consider the frequency-magnitude scaling for Parkfield seismicity prior to the earthquake. We consider earthquakes that occurred during the 365 days prior to 28 September 2004. There were no recognizable foreshocks, the rate of occurrence of small earthquakes during the period was stationary, the rates of occurrence of earthquake 1 with magnitudes greater than $m = 1.0$, 1.5, and 2.0 are given in Figure 4 as a function of magnitude. These rates of occurrence are extrapolated to higher magnitudes using Gutenberg-Richter frequency

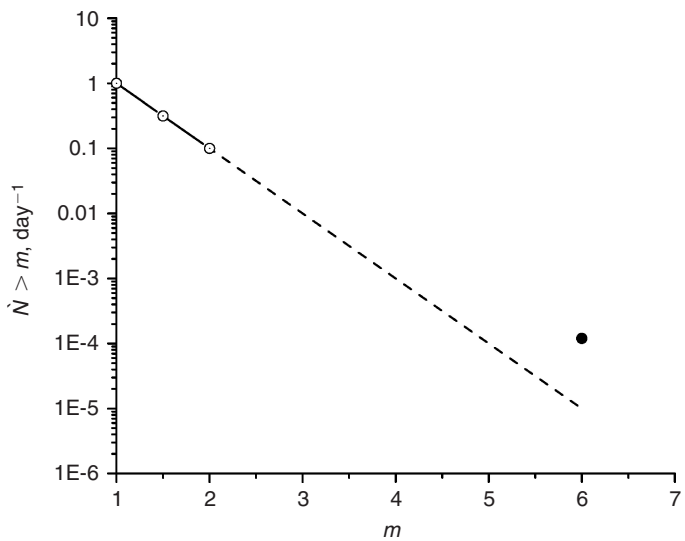



Figure 4: The open circles are the rates of earthquake occurrence $\acute{N}$ for magnitudes greater than $m$. The straight line is an extrapolation of this data using equation (2) with $b = 1$. The solid circle is the rate of occurrence of the Parkfield characteristic earthquakes.

© 2008 Taylor & Francis Group, London, UK

magnitude scaling, equation (2), with $b = 1$. Also shown in Figure 4 is the rate of occurrence of the $m = 6$ Parkfield earthquakes. It is seen that this rate is about one order of magnitude greater than the extrapolated value deduced from the rate of occurrence of small earthquakes.

## 4 SLIDER-BLOCK MODEL

Burridge and Knopoff (1967) proposed the multiple slider-block model as a simple model for earthquake occurrence. Carlson and Langer (1989) showed that the multiple slider-block model exhibits self-organized criticality. In this paper we show that the slider-block model can simulate important aspects of the behavior of characteristic earthquakes. Specifically, we show that there is a background of smaller slip events that satisfy Gutenberg-Richter frequency-magnitude scaling and that the recurrence statistics of the characteristic slip events is well approximated by a Weibull distribution.

In our analysis we utilize a variation of the linear slider-block model which Carlson and Langer (1989) used. We consider a linear chain of 100 slider blocks of mass $m$ pulled over a surface at a constant velocity $V_L$ by a loader plate as illustrated in Figure 5 (Abaimov *et al.*, 2007b). Each block is connected to the loader plate by a spring with spring constant $k_L$. Adjacent blocks are connected to each other by springs with spring constant $k_C$.

The blocks interact with the surface through a static-dynamic friction law. The static stability of each slider-block is given by

$$k_L y_i + k_C \left(2y_i - y_{i-1} - y_{i+1}\right) < F_{Si} \tag{3}$$

where $F_{Si}$ is the maximum static friction force on block $i$, and $y_i$ is the position of block $i$ relative to the loader plate.

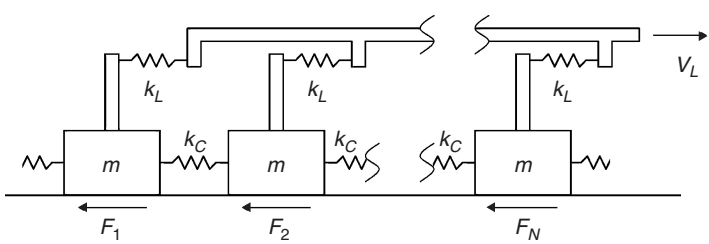



Figure 5: Illustration of the one-dimensional slider-block model. A linear array of $N$ blocks of mass $m$ are pulled along a surface by a constant velocity $V_L$ loader plate. The loader plate is connected to each block with a loader spring with spring constant $k_L$ and adjacent blocks are connected by springs with spring constant $k_C$. The frictional resisting forces are $F_1, F_2, \ldots, F_N$.

© 2008 Taylor & Francis Group, London, UK

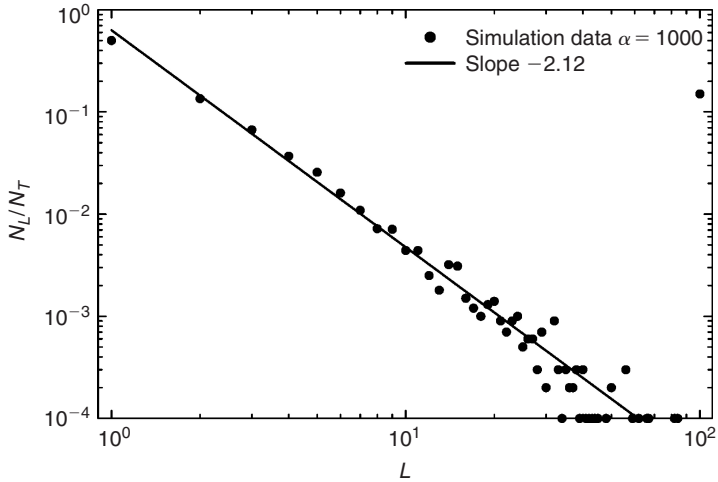



Figure 6: Frequency-size distribution of 10,000 slip events for a "stiff" system with $\alpha = 1000$. The ratio of the number of events $N_L$ of event size $L$ to the total number of events $N_T$ is given as a function of $L$.

When the cumulative force from the springs connected to block $i$ exceeds the maximum static friction $F_{Si}$, the block begins to slide. The dynamic slip of block $i$ is controlled by the equation

$$m\frac{d^2y_i}{dt^2} + k_L y_i + k_C\,(2y_i - y_{i-1} - y_{i+1}) = F_{Di} \tag{4}$$

where $F_{Di}$ is the dynamic (sliding) frictional force on block $i$. The loader plate velocity is assumed to be much smaller than the slip velocity so that the movement of the loader plate is neglected during a slip event. The sliding of one block can trigger the instability of the other blocks forming a multiple block event.

The behavior of the system is controlled by three parameters. The first is the stiffness of the system, $\alpha = k_C/k_L$, the second is the ratio of static to dynamic friction $\phi$ which is assumed to be the same for all blocks, and the third $\beta_i = F_{Si}/F_S^{ref}$ introduces a random variation of the friction from block to block with $F_S^{ref}$ as a reference value of the static frictional force.

Before obtaining solutions, it is necessary to prescribe the parameters $\phi$, $\alpha$, and $\beta_i$. The ratio $\phi$ of static friction to dynamic friction is taken to be $\phi = 1.5$, while the values of frictional parameters $\beta_i$ are assigned to blocks with a uniform random distribution in the range $1 < \beta_i < 3.5$. This random variability in the system is a "noise" required to generate event variability in stiff systems.

In order to simulate the occurrence of characteristic earthquake we give results for a stiff system with $\alpha = 1000$. The motion organizes itself into the recurrence of system-wide (100 block) events separated by sets of small size events. Frequency-size statistics for 10,000 events are given in Figure 6. The smaller

© 2008 Taylor & Francis Group, London, UK

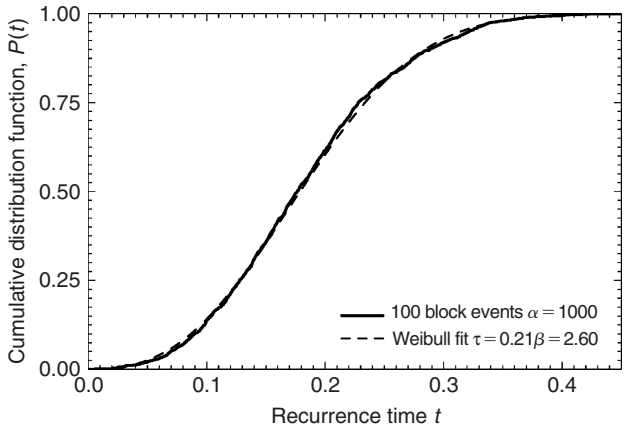



Figure 7: Cumulative distribution function $P(t)$ of recurrence times $t$ for the 1500 system-wide (100 block) events with $\alpha = 1000$. The continuous line is the distribution of observed recurrence times. The dashed line is the best-fit Weibull distribution with $\tau = 0.21$ and $\beta = 2.60$.

events are well approximated by a power-law relation with exponent $-2.12$. In this case there are about 1500 system-wide (100 block) events. We consider that these are equivalent to characteristic earthquakes. The results given in Figure 6 have a strong resemblance to those given in Figure 4 for the Parkfield earthquake. In both cases there are power-law distributions of small events associated with the quasi-periodic occurrences of larger events.

We next consider the recurrence time statistics for these events. The cumulative distribution of these recurrence times is given in Figure 7. Also included in this figure is the best log likelihood ($-1779.$) fit of the Weibull distribution (4) to this data obtained by taking $\tau = 0.206 \pm 0.002$ and $\beta = 60 \pm 0.05$. There is excellent agreement between the data and the Weibull distribution. It is of interest to compare the results given in Figure 7 with the distribution of recurrence times for the Parkfield earthquakes given in Figure 1. For that case we had $\beta = 3.21$ rather close to the $\beta = 2.60$ for the stiff slider-block model.

## 5 DAMAGE

The applications of continuum damage mechanics to fault rupture have been discussed in detail by Lyakhovsky *et al.* (2001, 2005, 1997), Ben-Zion and Lyakhovsky (2002, 2006), Turcotte *et al.* (2003), Shcherbakov and Turcotte (2003, 2004a), Turcotte and Shcherbakov (2006a), and Shcherbakov *et al.* (2005). For an elastic material Hooke's law is applicable and is written in the form

$$\sigma = E_0 \varepsilon \tag{5}$$

© 2008 Taylor & Francis Group, London, UK

where $\varepsilon$ is a strain and $E_0$ is the Young's modulus of the undamaged material.

In this paper we will consider a model of continuum damage mechanics as introduced by (Shcherbakov *et al.*, 2005). If the stress is less than the yield stress $\sigma \leq \sigma_y$, equation (5) is assumed to be valid. If the stress is greater than the yield stress, $\sigma > \sigma_y$, a damage variable $\alpha$ is introduced according to

$$\sigma - \sigma_y = E_0(1-\alpha)(\varepsilon - \varepsilon_y) \tag{6}$$

where $\sigma_y = E_0\varepsilon_y$. When $\alpha = 0$, equation (6) reduces to equation (5) and linear elasticity is applicable; as $\alpha \to 1$ ($\varepsilon \to \infty$) failure occurs. Increasing values of $\alpha$ in the range $0 \leq \alpha < 1$ quantify the weakening (decreasing E) associated with the increase in the number and size of microcracks in the material.

To complete the formulation of the damage problem it is necessary to specify the kinetic equation for the damage variable. In analogy to Lyakhovsky *et al.* (1997) we take

$$\frac{d\alpha(t)}{dt} = 0, \quad \text{if} \quad 0 \leq \sigma \leq \sigma y \tag{7}$$

$$\frac{d\alpha}{dt} = \frac{1}{t_d}\left[\frac{\sigma(t)}{\sigma_y} - 1\right]^{\rho}\left[\frac{\varepsilon(t)}{\varepsilon_y} - 1\right]^{2}, \quad \text{if} \quad \sigma > \sigma y, \tag{8}$$

where $t_d$ is a characteristic time scale for damage and $\rho$ is a constant to be determined from experiments. The power-law dependence of $d\alpha(t)/dt$ on stress (and strain) given above must be considered empirical in nature.

## 6 NUCLEATION

The concept of nucleation, which involves stability, metastability, and in our case leads to rupture on a fault, are illustrated in Figure 8. This figure gives the stress-strain histories for fault rupture in terms of the rate of application of stress. Path 1 applies if the rate of damage generation (small $t_d$ in equation (8)) is much faster than the rate of stress increase. Stress is increased slowly from 0 to a to c. From 0 to a there is no damage from equation (7) and equation (5) for linear elasticity is applicable. Damage occurs at $\sigma_c + \delta\sigma$ where $\delta\sigma << \sigma_c$. The critical stress $\sigma_c$ defines the lower boundary of the metastable region. Damage increases, $\alpha$ increases, from a to c and the strain increases. When $\alpha = 1$ fracture occurs. Path 1 corresponds to an equilibrium thermodynamic path and a first-order phase change. Path 2 applies if the rate of damage generation (large $t_d$ in equation) is much slower than the rate of stress increase. Stress is increased rapidly from 0 to *a* to *b*. From 0 to *b* there is no damage from equation (7) and equation (5) for linear elasticity is applicable. Point *b* is equivalent to a spinodal

© 2008 Taylor & Francis Group, London, UK

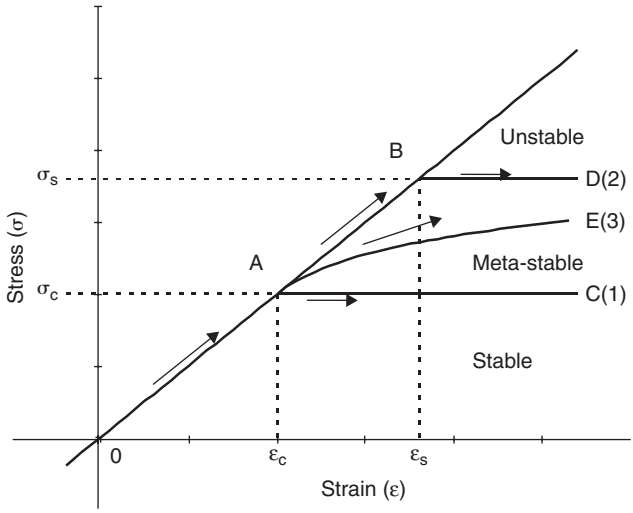



Figure 8: Stress-strain paths for fault rupture are given for three rates of stress application. Path 1 (0 to A to C) applies if the rate of damage generation is much faster than the rate of stress increase. Failure occurs at the critical stress $\sigma_c$ along the path A to C at the boundary between the stable region $\sigma < \sigma_c$, and the metastable region, $\sigma_c < \sigma < \sigma_s$. Path 2 (0 to A to B to D) applies if the rate of damage generation in much slower than the rate of stress increase. Failure occurs at the spinodal stress $\sigma_s$ along the path B to D between the metastable region $\sigma_c < \sigma < \sigma_s$ and the unstable region $\sigma > \sigma_s$. Path 3 is an intermediate case. Both damage and stress increase along the path A to E within the metastable region.

point in a phase change. Strain increases along path b to d and failure occurs at the spinodal stress $\sigma_s$. The spinodal stress defines the upper boundary of the metastable region.

Path 3 gives the intermediate case. When the applied stress $\sigma$ exceeds the critical stress $\sigma_c$ damage occurs and $\alpha$ increases according to equation (8). The increase in $\alpha$ results in an increase in the strain $\varepsilon$ along path a to e. When $\alpha = 1$ failure occurs. The analogy between Figure 8 and the water-steam phase change has been given in some detail by Shcherbakov and Turcotte (2003, 2004a).

We further illustrate these three paths of failure in Figures 9 to 11. In each case the barrier energy E is given as a function of position $\delta$ on a fault. Initially the stress on the fault $\sigma$ is less than the critical stress, $\sigma < \sigma_c$, and the minimum energy position (1) is stable. The stress builds up with time until an earthquake occurs with displacement $\delta_s$. After the rupture the displacement on the fault is at the energy minimum (2).

We first consider the near equilibrium Path 1 of Figure 8, this is illustrated in Figure 9. Initially we have $\sigma < \sigma_c$, and state (1) is stable relative to state (2) as illustrated in Figure 9a. The stress is increased until it is slightly above the

© 2008 Taylor & Francis Group, London, UK

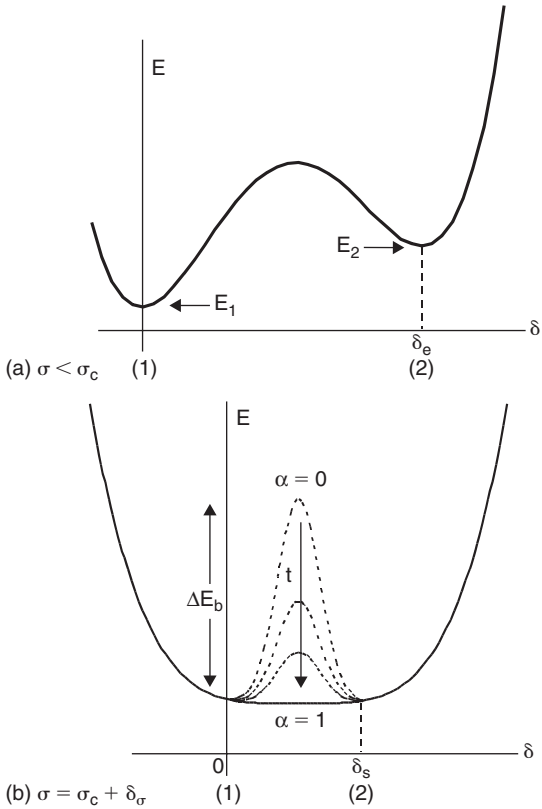



Figure 9: Illustration of the rupture process along path (1) in Figure 8. (a) Initially along path 0 to A in Figure 8 we have $\sigma < \sigma_c$ and the surface is stable at $\delta = 0$ (point 1), we have $E_2 > E_1$. (b) The stress has been increased so that it is slightly above the critical stress $\sigma_c$. Initially there is no damage, $\alpha = 0$, and there is an energy barrier to rupture $\Delta E_b$. With time, damage occurs, $\alpha$ increases, and the energy barrier erodes (decreases). When $\alpha = 1$ there is no energy barrier, rupture occurs with displacement $\delta_s$, a jump from stable position 1 to stable position 2. The rupture occurs at the nearly constant critical stress $\sigma_c$.

critical stress $\sigma = \sigma_c + \delta\sigma$, $\delta\sigma << \sigma_c$ as illustrated in Figure 9b. Initially there is an energy barrier $\Delta E$ and $\alpha = 0$. Damage occurs, $\alpha$ increases, and the energy barrier erodes with time $t$. This occurs along the path a to c in Figure 8. When $\alpha = 1$ there is no barrier and the earthquake rupture occurs with displacement $\delta_s$, from state (1) to state (2).

We next consider case of a very rapid stress increase corresponding to path 2 of Figure 8, this is illustrated in Figure 10. We have the same initial state with $\sigma < \sigma_c$ in Figure 10a as in Figure 9a. The stress is increased into the metastable region $\sigma_c < \sigma < \sigma_s$ between points a and b in Figure 8. This metastable state is

© 2008 Taylor & Francis Group, London, UK

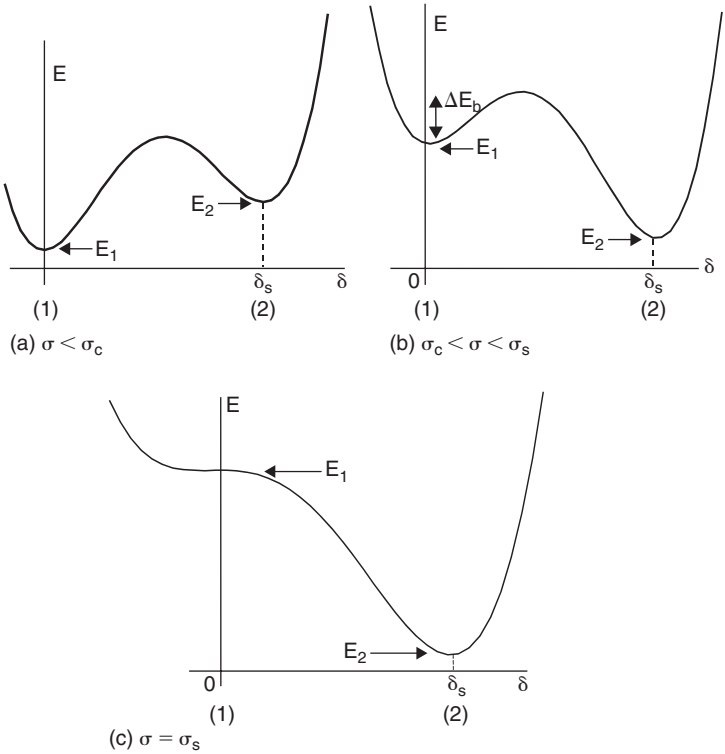



Figure 10: Illustration of the rupture process along path (2) in Figure 8. There is no damage. (a) Same as Figure 9a. (b) The stress has been increased so that it is intermediate between the critical stress $\sigma_c$ and the spinodal stress $\sigma_s$. This is in the metastable region with $E_2$ less than $E_1$ but the energy barrier $\Delta E_b$ prevents rupture. (c) The stress is increased to the spinodal stress $\sigma_s$. At this stress the energy barrier is zero, $\Delta E_b = 0$, and rupture occurs from state 1 to state 2 with displacement $\delta_s$. Because the stress is increased rapidly there is no damage, $\alpha = 0$, and the energy barrier is not eroded.

illustrated in Figure 10b. The energy at $\delta = \delta_s$, point 2, is less than the energy at $\delta = 0$, point 1. But the energy barrier $\Delta E_b$ prevents a rupture from state (1) to state (2). Because the stress is increased rapidly there is no damage, $\alpha = 0$, and the energy barrier does not erode. The stress is further increased to the spinodal stress $\sigma = \sigma_s$. At this stress the energy barrier is zero $\Delta E_b = 0$ as illustrated in Figure 10c and rupture occurs with displacement $\delta_s$ from state (1) to state (2). This rupture occurs along the path between points b and d in Figure 8.

Finally we consider the intermediate case corresponding to path 3 of Figure 8, this is illustrated in Figure 11. Both damage and stress increase along path a to e within the metastable region in Figure 8. Again we have the same initial

© 2008 Taylor & Francis Group, London, UK

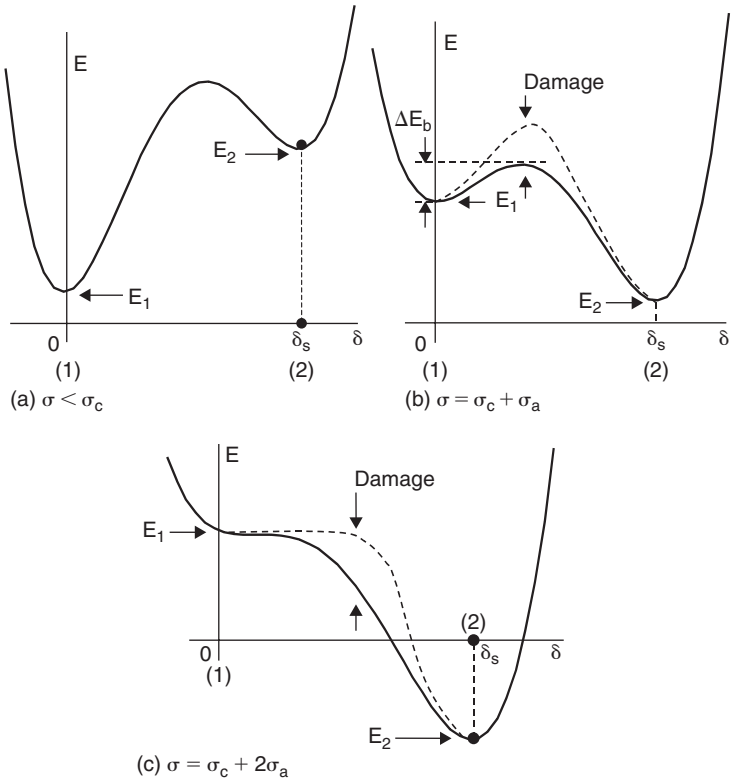



Figure 11: Illustration of the rupture process along path (3) in Figure 8. (a) Same as Figure 9a. (b) The stress has been increased into the metastable region $\sigma = \sigma_c + \sigma_a$. Damage has partially eroded the energy barrier so that the barrier $\Delta E_b$ prevents rupture. (c) The stress has been further increased into the metastable region with $\sigma = \sigma_2 + 2\sigma_a < \sigma_s$. Damage has completely eroded the energy barrier so that $\Delta E_b = 0$, and rupture occurs from state 1 to state 2 with displacement $\delta_s$.

state with $\sigma = \sigma_c$ in Figure 11a as in Figure 9a and 10a. The stress is increased in the metastable region with $\sigma = \sigma_c + \sigma_a$. This metastable state is illustrated in Figure 11b. Damage has eroded the energy barrier but the remaining energy barrier $\Delta E_b$ prevents a rupture from state (1) to state (2). The stress is further increased in Figute 11c with $\sigma = \sigma_c + 2\sigma_a$. Sufficient damage has now occurred to eliminate the energy barrier $\Delta E_b = 0$ and rupture occurs with displacement $\delta_s$ from state 1 to state 2. This rupture occurs in the metastable region the stress $\sigma = \sigma_c + 2\sigma_a$ less that the spinodal stress.

We now relate the results discussed above to observations made prior to the Parkfield earthquake in 2004. The high quality seismic network surrounding the site of this earthquake failed to note any anomalous seismic activity prior to the

© 2008 Taylor & Francis Group, London, UK

earthquake (Bakun *et al.*, 2005). Since damage prior to rupture is associated with acoustic emissions (Guarino *et al.*, 1999) we conclude that damage played a minor role in the rupture and spinodal rupture as illustrated in Figure 10 is applicable.

## 7 DISCUSSION

The objective of this paper has been to compare the behavior of characteristic earthquakes with the behavior of a slider-block model and to interpret the behavior in terms of damage mechanics and critical phenomena. We considered the sequence of seven $m \approx 6$ earthquakes that occurred on the Parkfield section of the San Andreas fault with emphasis on rates of background seismicity and recurrence intervals. We then presented the behavior of a "stiff" slider-block model. In both cases quasi-periodic "characteristic earthquakes" occurred with a power-law distribution of smaller events. In both cases the Weibull fit to the distribution of interval times was quite good with similar values of the power-law exponent $\beta$, $\beta = 3.21$ for the Parkfield earthquakes and $\beta = 2.60$ for the slip events.

We have also considered whether it is appropriate to associate characteristic earthquakes with first-order phase changes and the role of "damage" in earthquake rupture. The experimental studies of fiber-board rupture by Guarino *et al*. (1999) clearly illustrate the role of damage in this type of rupture. The rate of acoustic emissions systematically increased prior to rupture. The direct association of this increase in acoustic emissions with damage mechanics has been given by Turcotte and Shcherbakov (2006b). In general a systematic increase in seismicity prior to an earthquake is not observed. That is, precursory damage is not observed.

We have drawn an analogy between an earthquake rupture and a first-order phase transition. We have shown how the rupture occurs with and without damage. Rapid damage accumulation in the rupture is equivalent to an equilibrium phase change. The fault does not enter a metastable state. Without damage the rupture is equivalent to a spinodal phase change. The fault remains in a metastable state until the applied stress is sufficient to overcome the energy barrier to rupture.

## References

[1] Abaimov, S.G., Turcotte, D.L., and Rundle, J.B., 2007a. Recurrence-time and frequency-slip statistics of slip events on the creeping section of the San Andreas fault in central California, *Geophys. J. Int.,* 170**,** 1289–1299.

© 2008 Taylor & Francis Group, London, UK

[2] Abaimov, S.G., Turcotte, D.L., Shcherbakov, R., and Rundle, J.B., 2007b. Recurrence and interoccurrence behavior of self-organized complex phenomena, *Nonlinear Proc. Geophys.,* 24**,** 455–464.
[3] Bakun, W.H., Aagaard, B., Dost, B., Ellsworth, W.L., Hardebeck, J.L., Harris, R.A., Ji, C., Johnston, M.J.S., Langbein, J., Lienkaemper, J.J., *et al.*, 2005. Implications for prediction and hazard assessment from the 2004 Parkfield earthquake, *Nature,* 437**,** 969–974.
[4] Bath, M., 1965. Lateral inhomogeneities in the upper mantle, *Tectonophys.,* 2**,** 483–514.
[5] Ben-Zion, Y., and Lyakhovsky, V., 2002. Accelerated seismic release and related aspects of seismicity patterns on earthquake faults, *Pure Appl. Geophys.,* 159**,** 2385–2412.
[6] Ben-Zion, Y., and Lyakhovsky, V., 2006. Analysis of aftershocks in a lithospheric model with seismogenic zone governed by damage rheology, *Geophys. J. Int.,* 165**,** 197–210.
[7] Burridge, R., and Knopoff, L., 1967. Model and theoretical seismicity, *Bull. Seism. Soc. Am.,* 57**,** 341–371.
[8] Carlson, J.M., and Langer, J.S., 1989. Mechanical model of an earthquake fault, *Phys. Rev. A,* 40**,** 6470–6484.
[9] Garcimartin, A., Guarino, A., Bellon, L., and Ciliberto, S., 1997. Statistical properties of fracture precursors, *Phys. Rev. Lett.,* 79**,** 3202–3205.
[10] Guarino, A., Ciliberto, S., and Garcimartin, A., 1999. Failure time and microcrack nucleation, *Europhys. Lett.,* 47**,** 456–461.
[11] Guarino, A., Garcimartin, A., and Ciliberto, S., 1998. An experimental test of the critical behaviour of fracture precursors, *Eur. Phys. J. B,* 6**,** 13–24.
[12] Klein, W., Lookman, T., Saxena, A., and Hatch, D.M., 2002. Nucleation in systems with elastic forces, *Phys. Rev. Lett.,* 88.
[13] Lyakhovsky, V., Ben-Zion, Y., and Agnon, A., 2001. Earthquake cycle, fault zones, and seismicity patterns in a rheologically layered lithosphere, *J. Geophys. Res.,* 106**,** 4103–4120.
[14] Lyakhovsky, V., Ben-Zion, Y., and Agnon, A., 2005. A viscoelastic damage rheology and rate- and state-dependent friction, *Geophys. J. Int.,* 161**,** 179–190.
[15] Lyakhovsky, V., BenZion, Y., and Agnon, A., 1997. Distributed damage, faulting, and friction, *J. Geophys. Res.,* 102**,** 27635–27649.
[16] Main, I.G., and Al-Kindy, F.H., 2002. Entropy, energy, and proximity to criticality in global earthquake populations, *Geophys. Res. Lett.,* 29**,** 1121.
[17] Matthews, M.V., Ellsworth, W.L., and Reasenberg, P.A., 2002. A Brownian model for recurrent earthquakes, *Bull. Seism. Soc. Am.,* 92**,** 2233–2250.
[18] Ogata, Y., 1999. Estimating the hazard of rupture using uncertain occurrence times of paleoearthquakes, *J. Geophys. Res.,* 104**,** 17995–18014.

© 2008 Taylor & Francis Group, London, UK

[19] Rikitake, T., 1982. *Earthquake Forecasting and Warning,* edn, Vol., pp. 402, D. Reidel Publishing Co., Dordrecht.
[20] Rundle, J.B. and Klein, W., 1989. Nonclassical nucleation and growth of cohesive tensile cracks, *Phys. Rev. Lett.,* 63**,** 171–174.
[21] Rundle, J.B., Tiampo, K.F., Klein, W., and Martins, J.S.S., 2002. Self-organization in leaky threshold systems: The influence of near-mean field dynamics and its implications for earthquakes, neurobiology, and forecasting, *Proc. Natl. Acad. Sci. U. S. A.,* 99**,** 2514–2521.
[22] Savage, J.C., 1994. Empirical earthquake probabilities from observed recurrence intervals, *Bull. Seism. Soc. Am.,* 84**,** 219–221.
[23] Shcherbakov, R. and Turcotte, D.L., 2003. Damage and self-similarity in fracture, *Theor. Appl. Fract. Mech.,* 39**,** 245–258.
[24] Shcherbakov, R. and Turcotte, D.L., 2004a. A damage mechanics model for aftershocks, *Pure Appl. Geophys.,* 161**,** 2379–2391.
[25] Shcherbakov, R. and Turcotte, D.L., 2004b. A modified form of Bath's law, *Bull. Seism. Soc. Am.,* 94**,** 1968–1975.
[26] Shcherbakov, R., Turcotte, D.L., and Rundle, J.B., 2005. Aftershock statistics, *Pure Appl. Geophys.,* 162**,** 1051–1076.
[27] Sornette, D. and Knopoff, L., 1997. The paradox of the expected time until the next earthquake, *Bull. Seism. Soc. Am.,* 87**,** 789–798.
[28] Turcotte, D. and Shcherbakov, R., 2006a. Can Damage Mechanics Explain Temporal Scaling Laws in Brittle Fracture and Seismicity?, *Pure Appl. Geophys.,* 163**,** 1031–1045.
[29] Turcotte, D.L., 1997. *Fractals and Chaos in Geology and Geophysics,* 2nd edn, Vol., Cambridge Univ. Press, Cambridge.
[30] Turcotte, D.L., Newman, W.I., and Shcherbakov, R., 2003. Micro and macroscopic models of rock fracture, *Geophys. J. Int.,* 152**,** 718–728.
[31] Turcotte, D.L. and Shcherbakov, R., 2006b. Can damage mechanics explain temporal scaling laws in brittle fracture and seismicity?, *Pure Appl. Geophys.,* 163**,** 1031–1045.
[32] Utsu, T., 1984. Estimation of parameters for recurrence models of earthquakes, *Bull. Earthquake Res. Insti.-Univ. Tokyo,* 59**,** 53–66.
[33] Wawersik, W.R. and Brace, W.F., 1971. Post-failure behaviour of a granite and diabase, *Rock Mechanics and Rock Engineering*, 3**,** 61–85.
[34] Wawersik, W.R. and Fairhurs. C., 1970. A study of brittle rock fracture in laboratory compression experiments, *International Journal of Rock Mechanics and Mining Science,* 7**,** 561–575.
[35] Yakovlev, G., Turcotte, D.L., Rundle, J.B., and Rundle, P.B., 2006. Simulation based distributions of earthquake recurrence times on the San Andreas fault system, *Bull. Seism. Soc. Am.,* 96**,** 1995–2007.

© 2008 Taylor & Francis Group, London, UK

*Acoustic Emission and Critical Phenomena – Carpinteri & Lacidogna (eds)*
*© 2008 Taylor & Francis Group, London, ISBN 978-0-415-45082-9*

# ACCELERATING MOMENT RELEASE BEFORE LARGE EARTHQUAKES

**C. G. Sammis and A. Kositsky**
Dept. of Earth Sciences, Univ. of So. California, Los Angeles, CA

## ABSTRACT

Many large earthquakes have been preceded by an increase in the number of intermediate-sized events. In the seismological literature this phenomenon has been termed "accelerating moment release" (AMR), and it is currently being studied as a promising approach to earthquake forecasting. The AMR signal is observed over such a large area surrounding the impending mainshock that the intermediate events are generally viewed, not as triggers for the large event, but rather as indicators that the state of the fault network is such that a large event is possible. The size of the active area that optimizes the AMR signal has been shown to scale with the magnitude of the mainshock. We show here that the time over which the AMR signal develops also scales, but in this case with both the magnitude of the main shock and with the slip rate on the dominant fault in the network.

One proposed explanation for the AMR phenomenon, known as the "intermittent criticality model", is based on an analogy to critical point phenomena in statistical physics. In this model, a large earthquake is possible only when the fault network is in a critical state where patches of the crust that are at the failure level are connected at all length scales. An earthquake nucleated in this critical state can grow large by jumping geometrical barriers that would have arrested the rupture in a less connected non-critical stress field. This large event, and its aftershocks, lowers the stress over the network moving it away from the critical state. Tectonic loading and small events moves the system back toward the critical state and the possibility of the next network-wide large event.

The fault networks on which these spatial and temporal seismicity patterns develop have been shown to have a spatial fractal structure. Any discrete hierarchy in this structure can be shown to produce log-periodic fluctuation in the AMR signal. Mechanically heterogeneous systems in the laboratory show similar patterns of acoustic emissions prior to failure.

© 2008 Taylor & Francis Group, London, UK

## 1 INTRODUCTION

"Only fools and charlatans predict earthquakes." This quote from Charles Richter (*see Hough* [1]) fairly sums up the attitude of the geophysical community toward earthquake prediction research in the early 1960s, largely because there was no scientific framework upon which to base a prediction. This all changed with the emergence of plate tectonics in the mid 1960s. The plate tectonic model provided a simple and elegant explanation of where earthquakes occur (at plate boundaries), and why (to accommodate the relative motion of adjacent plates). More importantly, it gave a rate to the process. For example, the plate tectonics model gives a slip rate of about 5 cm/year on the southern San Andreas Fault. Since the slip during a large earthquake is about 6 meters, the recurrence interval between such events should be about 120 years. The last large earthquake on this segment of the San Andreas occurred in 1857, so the next is predicted to occur in 1977 – it has yet to occur.

Dating ancient earthquakes on this segment of the fault has revealed the problem with such predictions that are based on the recurrence interval. A trench across the San Andreas north of Los Angeles revealed evidence of 10 earthquakes in the period since 400 AD (*Sieh et al.* [2]). Although the average recurrence interval was 132 years, in approximate agreement with plate tectonics, the individual intervals ranged from 44 to 332 years, a variation too large to yield a useful prediction.

In the early 1970s, laboratory studies of rock failure suggested a different approach to earthquake prediction based on physical precursors that were observed to presage macroscopic sample failure. During laboratory experiments in which a rock was monotonically loaded to failure, microfracture activity was observed to begin at about half the failure stress and increase rapidly as the rock approached macroscopic failure. At the point of failure, so much crack porosity had opened that the sample volume exceeded its initial value before loading (*Brace et al.* [3]). Known as dilatancy, this phenomenon predicted many physical precursors that might be observed in the field before an earthquake. It explained, for example, temporal fluctuations in the ratio of compressional to shear wave velocities ($V_P/V_S$) observed to precede earthquakes near Garm in Tadjikistan, USSR (*Semenov* [4]). In these studies, the ratio $V_P/V_S$ was observed to first decrease and then increase just prior to the event (*see Scholz* [5], *for other examples*). The model proposed to explain these observations involves dilatancy of rock in and around the fault zone followed by the diffusion of ground water into the fault zone to fill the newly opened microcracks (*Nur* [6]). Ground water has a strong effect on the coefficient of friction that is described by the "effective friction law" $\tau = \mu(\sigma - P)$ where $\tau$ is the shear stress necessary to cause sliding on an interface subject to normal stress $\sigma$ and pore pressure $P$. The coefficient of friction $\mu$ is about 0.6 for rock on rock friction for nearly all rock types. By reducing fluid pressure in the fault zone, the initial phase of dilatancy

© 2008 Taylor & Francis Group, London, UK

increases the effective friction and delays failure. The rise in fault zone pressure as water diffuses in then reduces the effective friction and triggers the earthquake. The precursory anomaly in $V_P/V_S$ is explained by the fact that this ratio decreases as the density of dry cracks increases, and then increases as these new cracks become saturated. Known as the "dilatancy-diffusion model" for earthquakes, this scenario predicts many other physical precursors that should precede earthquakes including changes in the ground water level near faults, changes in ground water chemistry, and related changes in elevation, gravity and electrical resistivity (*Scholz et al.* [7]).

This approach looked particularly promising following the evacuation of the Chinese city of Haicheng in 1975 before a magnitude 7.3 earthquake that was predicted on the basis of physical precursors. However, this has proven to be an isolated success, and no other large earthquake has been predicted to date base on physical precursors predicted by the dilatancy diffusion model.

Beginning in the 1980s, the search for physical precursors in the United States has been focused at one location: Parkfield, California. This town on the San Andreas Fault in central California was the site of a sequence of 6 magnitude 6 earthquakes between 1857 and 1966 with recurrence intervals of 24, 20, 21, 12, and 32 years (*Bakun and McEvilly* [8]). Based on this record, the next event in the sequence was predicted to occur in $1988 \pm 5$ years so, in the early 1980s, this seemed like an ideal location to look for physical precursors without an excessive waiting period.

The next earthquake in the sequence didn't occur until 2004. The recurrence interval since 1966 was therefore 38 years, nearly double the average of the previous 5 intervals, which again emphasizes the futility of using recurrence intervals as a forecasting tool. This long recurrence interval was subsequently blamed on other magnitude 6 earthquakes in the general vicinity, which have been shown to have moved the stress state on the San Andreas fault at Parkfield further from Coulomb failure (*Miller* [9]). Prior to the 2004 earthquake, none of the experiments exhibited fluctuations that could be interpreted as a precursor (*Harris and Arrowsmith* [10]).

## 2 EARTHQUAKE FORECASTING BASED ON SPATIAL AND TEMPORAL PATTERNS IN REGIONAL SEISMICITY

The general failure to observe reliable physical precursors has produced a shift in research emphasis toward forecasting strategies that are based on spatial and temporal fluctuation in regional seismicity (*Turcotte* [11]). Seismicity-based strategies can be divided into two broad categories: statistical methods in which regional seismicity is used to continually modify the probability of a large event, and deterministic methods which search for precursory spatial and temporal patterns in the regional seismicity which presage large events.

© 2008 Taylor & Francis Group, London, UK

2.1 Statistical prediction strategies based on regional seismicity: the ETAS approach.

The most promising statistical strategies are based on the "epidemic type aftershock sequence" (ETAS) approach (*Helmstetter et al.* [12], *Kagan and Knopoff* [13], *Reasenberg and Jones* [14], *Ogata* [15]). ETAS is an extension of Omori's law for the rate of aftershocks, which is one of the most robust descriptors of regional seismicity (*Omori* [16]). Omori's law states that the rate of aftershocks following a mainshock decreases according to

$$\frac{dN}{dt} = \frac{\alpha}{(t+c)^{\beta}} \tag{1}$$

In this equation, $\alpha$ depends on the size of the mainshock and seismic characteristics of the region, $\beta$ is near 1, and $c$ regularizes the behavior near $t = 0$. The rate $dN/dt$ in Omori's law is for all events regardless of magnitude. The magnitudes of the events in an aftershock sequence are distributed according to the Gutenberg-Richter (G-R) magnitude-frequency relation (*Gutenberg and Richter* [17])

$$N_M = 10^{a-bM} \tag{2}$$

where $N_M$ is the number of events with magnitude greater than or equal to $M$. In this relation, the constant $a$ is adjusted such that, if $M^*$ is the magnitude of the mainshock, then $N_{M*-1} = 1$, an empirical observation known as Båth's law (*Richter* [18]) that most large events have one aftershock that is one magnitude unit less than the mainshock. The constant $b$ is usually near 1 reflecting the observation that the number of aftershocks increases by a factor of 10 for each unit decrease in M below $M^*-1$. The G-R relation gives a robust description of both aftershock sequences and also of regional seismicity. For regional seismicity, $a$ reflects the size and activity of the region and $b$ is again very near 1.

The ETAS method makes the simple assumption that aftershock sequences can also contain events that are larger than the mainshock. The probability that an aftershock is the same size or larger than the mainshock is then given by the G-R relation with a temporal probability that decreases with time according to Omori's law. Hence the probability of having an aftershock that is the same size as the mainshock is 0.1, of an aftershock one magnitude larger than the mainshock is 0.01, and so on. In statistical prediction algorithms based on ETAS, each event changes the probability of subsequent events in its neighborhood according to the generalized Omori's law and the G-R distribution.

© 2008 Taylor & Francis Group, London, UK

## 2.2 Prediction strategies based on precursory spatial and temporal patterns in regional seismicity: Accelerating moment release

The most promising precursory pattern is an increase in regional seismic activity over a wide area that has been observed to precede many large earthquakes. When first suggested by Keilis Borok and his colleagues (*Keilis-Borok and Malinovskaya* [19], *Keilis-Borok et al.* [20], *Keilis-Borok* [21]), the seismological community was skeptical because the active areas were far too large for the precursory events to trigger the large earthquake. The current view is that accelerating seismicity is not a triggering phenomenon, but rather an indication that the larger fault network is reaching a stress state that will support a large event. Keilis-Borok's observations were reinforced by *Sykes and Jaumé* [22] who documented large historical earthquakes in the San Francisco Bay area that were preceded by an increase in the frequency of intermediate-sized events on adjacent faults through the region. *Bufe and Varnes* [23] documented a similar increase in activity before the 1989 Loma Prieta earthquake which they fit to a "time-to-failure" equation of the form

$$\sum_{i=1}^{N} E_i^{1/2} = A - B(t_f - t)^m \tag{3}$$

In this equation $E_i$ is the energy of the ith earthquake, which can be found from its magnitude $M_i$ using the relation $\log E_i = 11.8 + 1.5M_i$. The time of the large event is $t_f$ and A, B, and $m$ are constants. A value of $m$ near 0.3 is typical of most accelerating earthquake sequences. The square root of the energy is called the Benioff strain. There is no theoretical reason for using Benioff strain as a measure other than that it is a compromise between the energy and the number of events. Benioff strain gives a smoother curve than either the energy, which is dominated by infrequent large events, or the number, which tends to be dominated by the myriad of smaller aftershocks.

*Bowman et al.* [24] fit equation (3) to seismicity preceding all 8 earthquakes with M > 6.5 in Southern California between 1950 and 1995. Figure 1 shows an example. For each event they found the radius of the circular region centered on the epicenter that minimized the variance of the data from equation (3). As shown in Figure 2, these optimal radii $R$ scale with magnitude as $\log R \propto M/2$ for large events above about magnitude $M = 6$ and $\log R \propto M/3$ for smaller events. This change in scaling reflects the fact that smaller events grow as a circular dislocation on the fault plane while larger events grow only laterally, having spanned the full depth of the brittle upper crust (about 15 km). These observed relations between R and M follow form the fact that the energy $E$ released by an earthquake is proportional to the area $A$ times the mean displacement $\langle d \rangle$. The mean displacement is observed to be proportional to fault length, $\langle d \rangle \propto R$. So, for a growing circular dislocation, $A \propto R^2$ and $E \propto R^3$ while for a large event $A \propto R$

© 2008 Taylor & Francis Group, London, UK

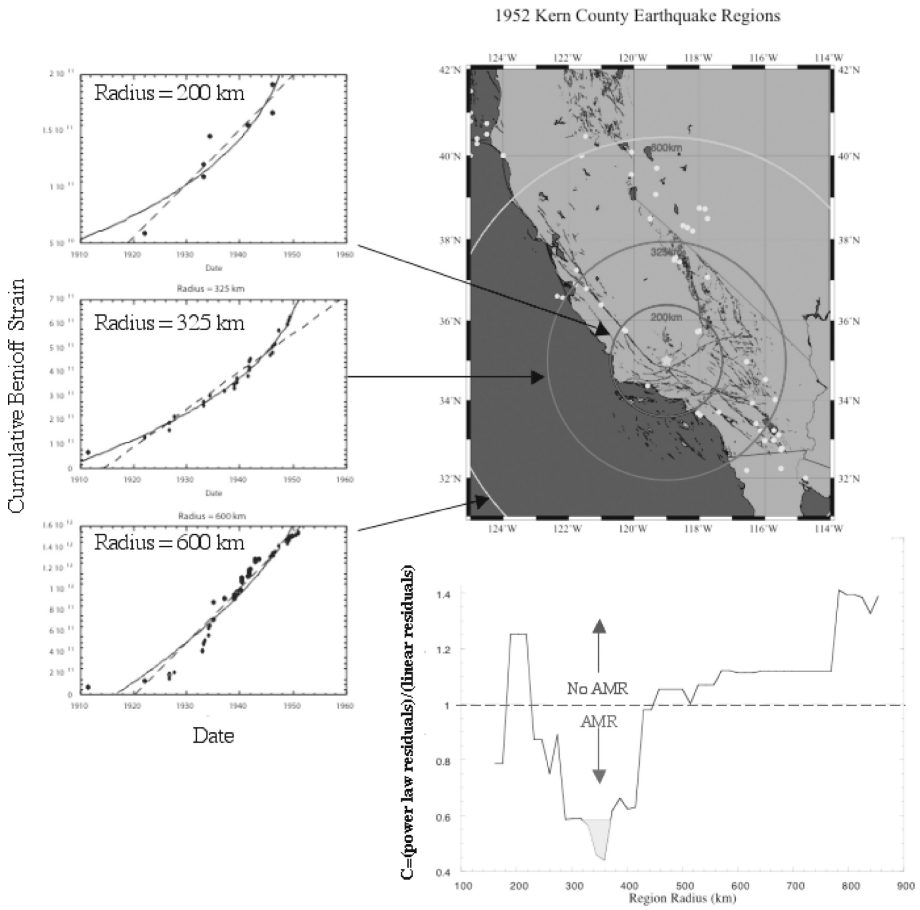



Figure 1: Optimization of the area of accelerating seismicity before the 1952 Kern County, California Mw = 7.5 earthquake. The cumulative Benioff strain in three circular regions on the map ($R = 200$, 325, and 600 km) is shown on the left. The fit parameter $C$, the ratio of the residuals of the power law fit (equation 3) to the residuals of the best linear fit, is plotted as a function of $R$ at the lower right. Note that $R$ near 350 km optimizes the fit to equation (3) relative to a linear fit. (*after Bowman et al.* [24]).

and $E \propto R^2$. Since $\log E = 11.8 + 1.5\,M$ or $\log E \propto M$, we have $\log R \propto M/3$ for small events and $\log R \propto M/2$ for large events as observed.

## 2.3 Mechanisms that produce Accelerating Moment Release

Several physical mechanisms have been proposed to explain the observations of accelerated moment release preceding macroscopic failure. All involve positive

© 2008 Taylor & Francis Group, London, UK

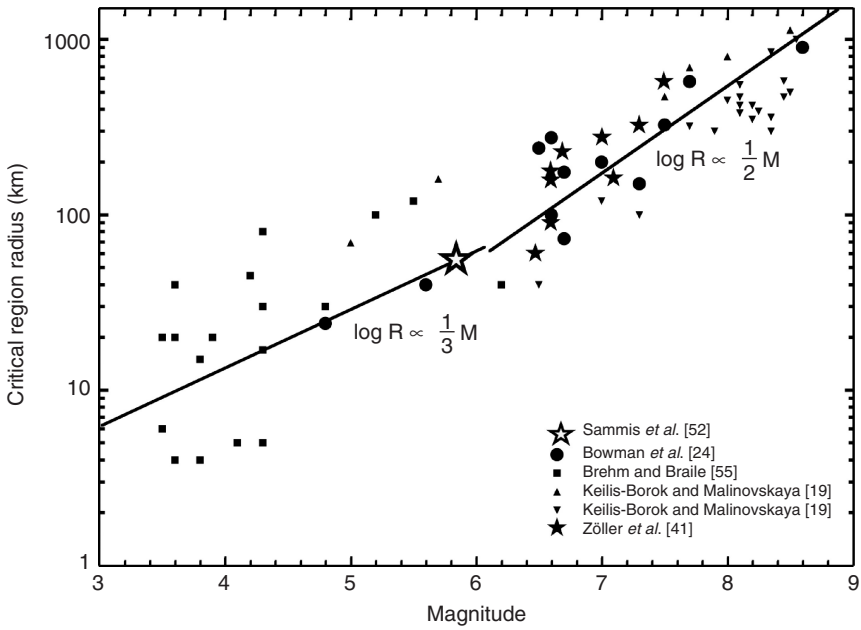



Figure 2: Radius of circular region that gives the best fit to equation (3) as a function of magnitude. Data from several studies are included as indicated. The points from *Keilis-Borok and Malinovskaya* [19] are the size of the fault network on which the earthquake occurred as a function of magnitude. The scaling relations logR = M/2 and logR = M/3 are discussed in the text.

feedback and a memory of past large events involving either healing or stress recovery (*Sammis and Sornette* [25]).

### 2.3.1 Cascading failure with feedback

It is easy to show that the time-to-failure equation (3) describes a cascade type failure under constant load in the laboratory where local failure feeds back to increase the average load on the remaining load-bearing cross-section (*Sammis et al.* [26]). More sophisticated versions of this idea such as the cable model (*Newman et al.* [27]), and a damage mechanics model with healing (*Ben-Zion and Lyahovsky* [28]) also lead to equation (3).

### 2.3.2 Approach to a critical point

*Sornette and Sammis* [29]pointed out that equation (3) is also the functional form that describes the approach of chemical and magnetic systems toward a critical point, and that ideas borrowed from statistical physics might offer new insights into the spatial and temporal evolution of regional seismicity (*see also*

© 2008 Taylor & Francis Group, London, UK

*Saleur et al.* [30]). Consider, for example, a phase transition in which islandls of a new phase A are growing at the expense of the old phase B. If this transition has a critical point, then near criticality the rate of transition is given by an equation like equation (3). In this case, $t_f$ is the time at which the system becomes critical. The critical state is defined by the point at which islands of phase A first become connected at all scale lengths (the percolation threshold). In the jargon of statistical physics, the correlation length of phase A increases, becoming infinite at the critical point. Beyond the critical point the transition rate slows as remaining islands of phase B shrink and become increasingly isolated.

How can an analogy be drawn between regional seismicity and a critical phase transition? Suppose we divide the heterogeneous regional stress field in the seismogenic upper crust into two "phases": phase A in which the stresses are at or above the Coulomb failure criterion for frictional slip on faults in the regional network, and phase B in which the stresses are below the Coulomb threshold. According to the plate tectonic model, most large earthquakes occur at plate boundaries where the relative motion of neighboring plates slowly and steadily loads the network of faults that accommodate the slip. In this environment, patches of high stress phase A are continually growing while patches of lower stress phase B are shrinking. One implication of this model is that the size of the largest earthquake should grow with time, reflecting the growing correlation length of high-stress A-phase patches. The idea is that large faults have many geometrical "barriers" to rupture propagation in the form of bends and jogs (*King* [31]), and that the size of an earthquake is limited by the area of the fault plane that is at or above the Coulomb slip level. If the connected patches of high-stress are small, then an earthquake rupture will arrest at a barrier. If the correlation length of the high-stress patches is large, then a growing rupture will jump geometrical barriers to become a large magnitude event. In this view, a great event is only possible when the crust is in the critical state such that a rupture, once nucleated, can jump all barriers to produce slip on the largest structure in the network.

This concept that the size of an event is determined by the correlation length of the stress field on the fault plane is captured by the cellular automaton (*Bak et al.* [32]). In this model, an array of cells is loaded by increasing the stress in a randomly chosen cell by some fixed increment. It this increase raises the stress level of the chosen cell above a preset threshold, then that cell transfers its stress to its neighboring cells. If this transfer causes the stress in one or more of the neighboring cells to exceed the threshold, then each spills into its neighboring cells (including the one that just spilled), and so on. Each such cascade is viewed as an earthquake, the size of which is determined by the number of cells that are involved. *Bak and Tang* [33] proposed the cellular automaton as a suitable model for earthquakes because it captures several important characteristics of regional seismicity. First, the regular sequential stress increments added to randomly chosen cells mimics the steady loading rate provided by plate tectonics. Second, the

© 2008 Taylor & Francis Group, London, UK

cascading process mimics the stress perturbations surrounding an earthquake, which are observed to produce aftershocks on real fault networks. Third, the cascades produced by the cellular automaton follow the G-R frequency-magnitude relation ubiquitously observed in regional seismicity.

If the cellular automaton model captures the statistical physics of regional seismicity, it has profound implications for the predictability of large earthquakes. This model belongs to a class of models that exhibit "self-organized criticality" (SOC). Beginning in any initial state, SOC models naturally evolve toward a critical state and, more importantly, remain in the critical state even after a large cascade. Since the correlation length is infinite in the critical state, a large event is equally likely at any time, and therefore inherently unpredictable (*although Pepke and Carlson* [34] *find some weak predictability in SOC systems*).

There are theoretical and observational reasons to doubt that the simple cellular automaton is a suitable model for regional seismicity, and, more generally, to doubt that seismicity is an SOC phenomenon. First, the elastic stress perturbations generated by an earthquake are long-range, and not well represented by the sequence of nearest neighbor transfers in the basic cellular automaton (*Anghel et al.* [35], *Weatherley et al.* [36]). Second, although an earthquake does increase the stress in certain locations, it lowers the stress in others. Globally, an earthquake and its aftershocks lower the regional stress in an area that scales with its size leaving a "stress shadow" in its wake (*Mignan et al.*, [37]). Such stress shadows have been observed to follow large earthquakes. *Harris and Simpson* [38] found that no earthquakes occurred in the stress shadow of the 1857 $M = 7.9$ Fort Tejon earthquake for 50 years following, while activity continued as normal in the unaffected regions. They observed a similar absence of seismicity in the shadow of the 1992 $M = 7.3$ Landers earthquake. *Jones and Hauksson* [39] and *Hauksson et al.* [40] documented a stress shadow for $M \geq 3$ earthquakes in southern California following the 1952 $M = 7.5$ Kern County earthquake and following the 1992 $M = 7.3$ Landers earthquake and the 1999 $M = 7.1$ Hector Mine event.

From a statistical physics point of view, by lowering the average regional stress these large events reduced the correlation length of the stress field thereby moving the fault network away from the critical point and reducing the size of the largest possible earthquake. Subsequent tectonic loading increases the correlation length, thereby moving the network back toward the critical state with an attendant increase in seismicity, which we identify as the precursory signal. *Zoller et al.* [41] report an increase in the correlation length of seismicity before large events.

This scenario has led to the "intermittent criticality model" for earthquake prediction, which is summarized by the following statements:

1) A large system-wide earthquake is possible only when the fault network is in a critical state. In the critical state, high-stress patches span the fault network

© 2008 Taylor & Francis Group, London, UK

so that an earthquake nucleated on a large fault will jump geometrical barriers to grow into a system-wide event.

2) This large event and its aftershocks lower stress across the fault network thereby reducing the correlation length of the high-stress patches and moving the network away from the critical point. The result is a sharp reduction in the number of intermediate-magnitude events, which were cited above as evidence for a stress shadow.
3) As tectonic loading raises the average stress level, the correlation length of high-stress patches increases which increase the number of intermediate events to produce the precursory accelerating seismicity, which forms the basis of a prediction.
4) When the stress field reaches the critical state a large earthquake is again possible and the cycle repeats.

Note that this scenario does not imply a strict periodicity. Recurrence times may vary because of variations in loading and stress transfer from intermediate events, or from variations in the nucleation process. Also, the large event need not occur when the stress field becomes critical, since this only means that a large event is possible. The exact time of the large event can depend on details of the nucleation process that can stretch over a long period of time (*Dieterich* [42]). The critical point mode for large earthquakes is reviewed by *Jaumé and Sykes* [43].

*Sammis and Smith* [44] modified the simple cellular automaton model to simulate the approach and retreat from criticality. In their model, when a cell reaches the threshold stress, it transfers only a fraction $q$ of its load to the neighboring cells. The result is a sequence of large events, each preceded by a period of accelerating seismicity and followed by a more quiescent shadow (Figure 3). They obtained the same results when they modified the automaton to have a fractal distribution of cell sizes. In this case, if the size of the largest cell in the fractal array was a significant fraction of the size of the entire array, then the redistribution of stress from the largest cell overwhelmed the grid to produce a stress shadow. In this case the stress shadow can be viewed as an edge-effect of a finite fault network.

*Sornette and Sammis* [29] showed that if the fault network is a discrete hierarchical fractal, then the accelerating seismicity before a large event should be decorated with log-periodic fluctuations. They presented evidence for such fluctuations in the regional seismicity that preceded the 1998 Loma Prieta earthquake in the California Bay Area (Figure 4). *Saleur et al.* [45] further discuss the source of such log-periodic fluctuations. *Hirata* [46] and *Robertson et al.* [47] present evidence that regional fault networks in Japan and southern California have a fractal structure while *Sammis et al.* [48] show that the spatial distribution of seismicity on the San Andreas fault near Parkfield has a hierarchical fractal structure.

© 2008 Taylor & Francis Group, London, UK

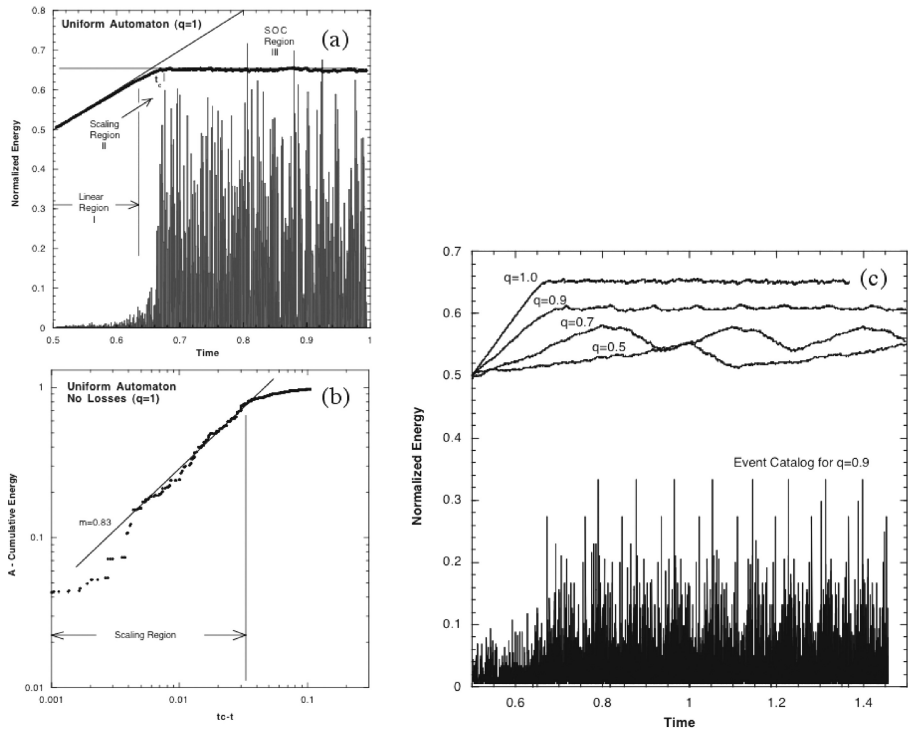



Figure 3: Cascades on a cellular automaton illustrating power law scaling during the approach to a critical point. Panel (a) shows the total energy on the grid during loading to the critical point and the individual events. Panel (b) illustrates the power-law scaling. Panel (c) shows that the effect of not transferring all the energy during a cascade is to produce a stress shadow following large events resulting in seismic cycles (*redrawn from Sammis and Smith,* [44]).

### 2.3.3 Stress Accumulation Model

*Bowman and King* [49] and *King and Bowman* [50] have developed a model that produces accelerating seismicity directly from the erosion of the stress shadow left by the previous large event without the direct assumption of a critical point. Their model considers a fault loaded by creep on its lower extension as illustrated in Figure 5. Because the AMR is a result of loading on the main fault, the precursory activity is predicted to be concentrated in the positive lobes of the far-field stresses calculated by a back-slip dislocation model of the mainshock. *Mignan et al.* [51] show that AMR occurs preferentially in the lobes of the backslip stress field test for all the Mw $\geq$ 6.5 earthquakes in central and southern California since 1950. By limiting the AMR signal to the expected lobes of the stress recovery pattern, it is possible to optimize the accelerating signal with respect to both spatial area and temporal duration (*see Sammis et al.* [52]).

© 2008 Taylor & Francis Group, London, UK

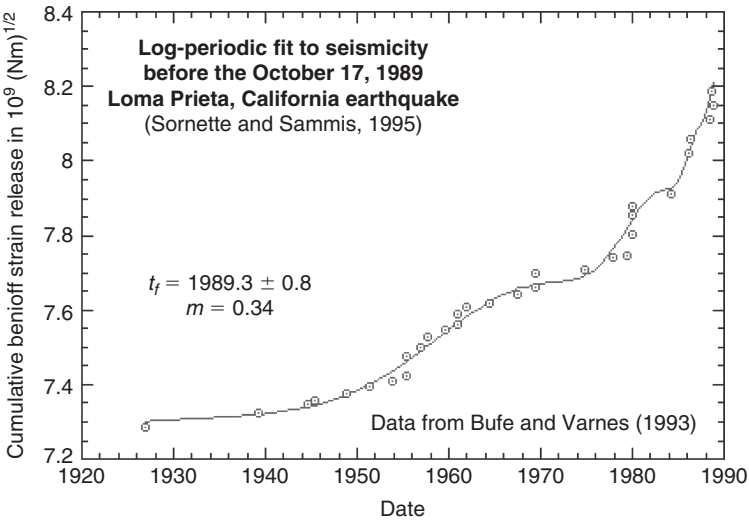



Figure 4: Log periodic fluctuations in seismicity before the 1989 Loma Prieta, California earthquake (*from Sornette and Sammis,* [28]).

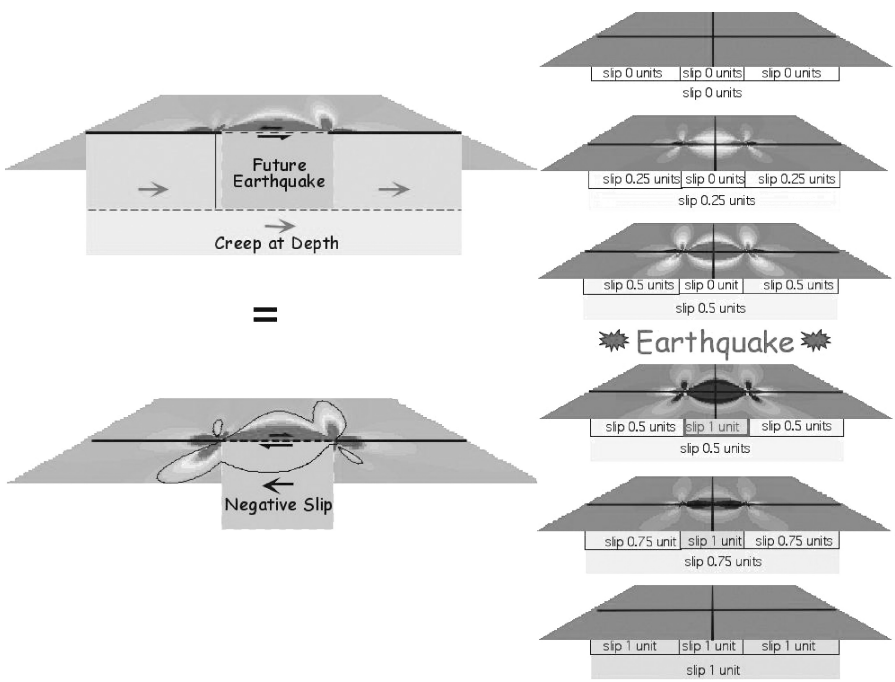



Figure 5: Stress accumulation model. The pair of illustrations on the left show that the loading of a locked patch of fault by creep below and adjacent earthquakes can be calculated by "back-slip" on the locked portion. The vertical series of illustrations show how this model evolves during a seismic cycle.

© 2008 Taylor & Francis Group, London, UK

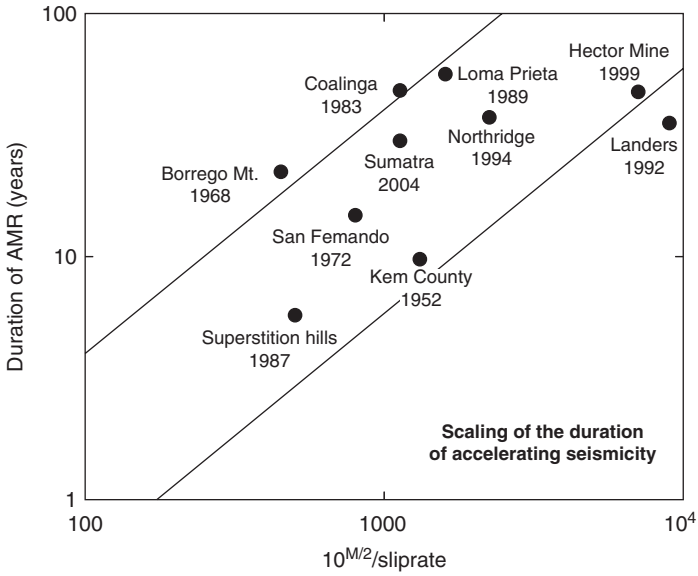



Figure 6: The duration of accelerating seismicity for California earthquakes. Durations were found by optimizing the fit of data to equation. (3) (*Mignan et al.* [51]). Lines show the expected scaling for large events where the energy is proportional to slip squared: Duration$\propto$ slip per event/slip rate$\propto 10^{M/2}$/sliprate where $M$ is the magnitude. The factor of ten scatter in the data are probably associated with variations in background seismicity (*see Mignan et al.* [37]).

The optimized durations of the signals for California earthquakes are plotted in Figure 6 as a function of magnitude and slip rate on the fault. Note that the durations scale as (total slip)/(slip-rate) as expected. As discussed above, the total slip for large events (M > 6) scale as the square root of the energy. The factor of ten scatter is most likely due to variations in background noise as discussed by *Mignan et al.* [37].

*Mignan et al.* [37] derive a variation of equation (3) by considering a threshold model for seismicity based on the G-R distribution. The accelerating moment release in their model is a consequence of the decrease, due to loading, of the size of the stress shadow due to a previous earthquake, and does not specifically require critical processes.

## 3 DISCUSSION

Earthquake prediction remains a controversial topic in the Earth Sciences. Some have expressed the view that earthquakes are inherently unpredictable (*Geller*

© 2008 Taylor & Francis Group, London, UK

*et al.* [53]). Others view earthquake prediction as the "holy grail" of geophysics that will demonstrate a new level of understanding of the tectonic processes that stress the crust, the local physics of nucleation, and the resultant stress transfers by which earthquakes talk to each other. If large earthquakes are predictable, then the most promising approach to prediction appears to lie in the spatial and temporal patterns of regional seismicity. ETAS methods that change the probability of future large events in time and space based on past seismicity by using Omori's law and the Gutenberg-Richter distribution have been shown to give better probabilistic predictions than those based on a random Poisson distribution. Whether precursory patterns of seismicity, such as AMR, can be developed to yield a robust deterministic predictor remains controversial (*Main* [54]).

## References

[1] S. E. Hough, *Richter's Scale: Measure of an Earthquake, Measure of a Man*, Princeton University Press, Princeton, N.J., 2007.

[2] K. Sieh, M. Stuiver and D. Brillinger, "A more precise chronology of earthquakes produced by the San Andreas Fault in Southern California," *J. Geophys. Res.,* vol. 94, pp. 603–623, 1989.

[3] W. F. Brace, B. W. Paulding and C. H. Scholz, "Dilatancy in the fracture of crystalline rocks," *J. Geophys. Res.*, vol. 71, pp. 3939–3953, 1966.

[4] A. N. Semenov, "Variations of the travel time of transverse and longitudinal waves before violent earthquakes," *Izv. Acad. Sci USSR, Phys. Solid Earth* (Eng. Trans.), vol. 13, pp. 245–258, 1969.

[5] C. H. Scholz, *The Mechanics of Earthquakes and Faulting*, 2nd editon, Cambridge University Press, 2002.

[6] A. Nur, "Dilatancy, pore fluids, and premonitory variations in $t_s/t_p$ travel times," *Bull. Seismol. Soc. Am.*, vol. 62, pp. 1217–1222, 1972.

[7] C.H. Scholz, L.R. Sykes and Y.P. Aggarwal, "Earthquake predicition: A physical basis," *Science*, vol. 181, pp. 803–809, 1973.

[8] W. H. Bakun and T.V. McEvilly, "Recurrence models and Parkfield, California Earthquakes," *J. Geophys. Res.,* vol. 89, pp. 3051–3058, 1984.

[9] S. A. Miller, "Fluid-mediated influence of adjacent thrusting on the seismic cycle at Parkfield," *Nature*, vol. 382, pp. 799–802, 1996.

[10] R. A. Harris and J. R. Arrowsmith, "Introduction to the Special Issue on the 2004 Parkfield Earthquake and the Parkfield Earthquake Prediction Experiment," *Bull. Seism. Soc. Amer.,* vol. 96, pp. S1–S10, 2006.

[11] D. L. Turcotte, "Earthquake Prediction," *An. Rev. Earth Planet Sci.*, vol. 19, pp. 263–281, 1991.

[12] A. Helmstetter, D. Sornette and J.-R. Grasso, "Mainshocks are Aftershocks of Conditional Foreshocks: How do foreshock statistical

© 2008 Taylor & Francis Group, London, UK

properties emerge from aftershock laws," *J. Geophys. Res*., vol. 108, no. (B1), pp. 2046, doi:10.1029/2002JB001991, 2003.

[13] Y. Y. Kagan and L. Knopoff, "Stochastic synthesis of earthquake catalogs," *J. Geophys. Res.,* vol. 86, pp. 2853–2862, 1981.

[14] P. A. Reasenberg and L. M. Jones, "Earthquake hazard after a mainshock in California," *Science,* vol. 243, pp. 1173–1176, 1989.

[15] Y. Ogata, "Statistical models for earthquake occurrences and residual analysis for point processes," *J. Am. Stat. Assoc.,* vol. 83, pp. 9–27, 1988.

[16] F. Omori, "On after-shocks," *Rep. Imp. Earthq. Inv. Com.,* vol. 2, pp. 103–138, 1894 (in Japanese).

[17] B. Gutenberg and C.F. Richter, "Magnitude and energy of earthquakes," *Ann. di. Geofis*, vol. 9, p. 1, 1956.

[18] C. F. Richter, *Elementary Seismology,* Freeman, San Francisco, 1958.

[19] V. I. Keilis-Borok, and L.N. Malinovskaya, "One regularity in the occurrence of strong earthquakes," *J. Geophys. Res*., vol. 69, pp. 3019–3024, 1964.

[20] V. I. Keilis-Borok, L. Knopoff, I.M. Rotwain and C.R. Allen, "Intermediate-term prediction of occurrence times of strong earthquakes," *Nature,* vol. 335, pp. 690–694, 1988.

[21] V. I. Keilis-Borok, "The lithosphere of the Earth as a large nonlinear system," in *Quo Vadimus: Geophysics for the Next Generation*, *Geophys. Monogr. Ser.*,60, edited by G.D. Garland, and J.R. Apel, pp. 81–84, AGU, Washington DC, 1990.

[22] L. R. Sykes and S. Jaumé, "Seismic activity on neighboring faults as a long-term precursor to large earthquakes in the San Francisco Bay Area," *Nature*, vol. 348, pp. 595–599, 1990.

[23] C. G. Bufe and D. J. Varnes, "Predictive modeling of the seismic cycle of the greater San Francisco bay region," *J. Geophys. Res*., vol. 98, pp. 9871–9883, 1993.

[24] D. D. Bowman, G. Ouillon, C. G. Sammis, A. Sornette and D. Sornette, "An observational test of the critical earthquake concept," *J. Geophys. Res*., vol. 103, pp. 24, 359–24,372, 1998.

[25] C. G. Sammis and D. Sornette "Postitive feedback, memory, and the predictability of earthquakes," *Proceedings of the National Academy of Sciences*, vol. 99, pp. 2501–2508, 2002.

[26] C. G. Sammis, D. Sornette and H. Saleur, "Complexity and earthquake forecasting", *Reduction and Predictability of Natural Disasters, SFI Studies in the Sciences of Complexity*, vol. XXV, edited by J.B. Rundle, W. Klein, and D.L. Turcotte, pp. 143–156, Addison-Wesley, Reading, Mass., 1996.

[27] W. I. Newman, D. L. Turcotte and A. M. Gabrielov, "Log-periodic behavior of a hierarchical failure model with applications to precursory seismic activation," *Phys. Rev. E.*, vol. 52, pp. 4827–4835, 1995.

© 2008 Taylor & Francis Group, London, UK

[28] Y. Ben-Zion and V. Lyakhovsky, "Accelerated seismic release and related aspects of seismicity patterns on earthquake faults," *Pure Appl. Geophys*, vol. 159, pp. 2385–2412, 2002.

[29] D. Sornette and C. G. Sammis, "Complex critical exponents from renormalization group theory of earthquakes : Implications for earthquake predictions," *J.Phys.I. France*, vol. 5, pp. 607–619, 1995.

[30] H. Saleur, C. G. Sammis and D. Sornette "Renormalization group theory of earthquakes," *Nonlinear Processes in Geophysics,* vol. 3, pp. 102–109, 1996.

[31] G. C. P. King, "The Accommodation of large strains in the upper lithosphere of the Earth and other solids by self-similar fault systems: the geometrical origin of b-value," *Pure Appl. Geophys.*, vol. 121, pp. 761–814, 1983.

[32] P. Bak, C. Tang and K. Wiesenfeld, "Self-organize criticality: an explanation of 1/f noise," *Phys. Rev. Lett.*, vol. 59, pp. 381–384, 1987.

[33] P. Bak and C. Tang, "Earthquakes as a self-organized critical phenomenon," *J. Geophys. Res.,* vol. 94, pp. 15, 635–15,637, 1989.

[34] S. L. Pepke and J. M. Carlson, "Predictability of self-organizing systems," *Phys. Rev. E* . Vol. 50, pp. 236–242, 1994.

[35] M. Anghel, W. Klein, J.B. Rundle and J.S. De Sa Martins, "Dynamics, scaling, and temporal patterns of stress-correlated clusters in a model of earthquake faults with long-range stress transfer" (abst), *EOS Trans. Am.Geophys. Union*, vol. 80, pp. F923–F924, 1999.

[36] D. Weatherley, P. Mora and M. Xia, "Long-range automaton models of earthquakes; power-law accelerations, correlation evolution, and mode-switching," *Pure and Applied Geophysics*, vol. 159, pp. 2469–2490, 2002.

[37] A. Mignan, G. C. P. King and D. Bowman, "A mathematical formulation of accelerating moment release based on the stress accumulation model," *J. Geophys. Res*., in press, 2007.

[38] R. A. Harris and R.W. Simpson, "In the shadow of 1857 – Effect of the great Ft. Tejon earthquake on the subsequent earthquakes in southern California," *Geophysical Res. Lett.,* vol. 23, pp. 229–232, 1996.

[39] L. M. Jones and E. Hauksson, "The seismic cycle in southern California: Precursor or response?", *Geophys. Res. Lett.*, vol. 24, pp. 469–472, 1997.

[40] E. Hauksson, L. M. Jones, S. Perry and K. Hutton, "Emerging from the stress shadow of the 1992 Mw 7.3 Landers southern California earthquake? A preliminary assessment," *Seism. Res. Lett.*, vol. 73, pp. 33–38, 2002.

[41] G. Zoller, S. Hainzl and J. Kurths, "Observation of growing correlation length as an indicator for critical point behavior prior to large earthquakes," *J. Geophys. Res.*, vol. 106, pp. 2167–2175, 2001.

© 2008 Taylor & Francis Group, London, UK

[42] J. H. Dieterich, "Nucleation and triggering of earthquake slip: effect of periodic stresses," *Tectonophysics*, vol. 144, pp. 127–139, 1987.

[43] S. C. Jaumé and L.R. Sykes, "Evolving toward a critical point: a review of accelerating seismic moment/energy release prior to large and great earthquakes," *Pure Appl. Geophys.,* vol. 155, pp. 279–306, 1999.

[44] C. G. Sammis and S.W. Smith, "Seismic cycles and the evolution of stress correlation in cellular automaton models of finite fault networks," *Pure Appl. Geophys.*, vol. 155, pp. 307–334, 1999.

[45] H. Saleur C. G. Sammis and D. Sornette, "Discrete scale invariance, complex fractal dimensions, and log-periodic fluctuations in seismicity," *J. Geophys. Res*., vol. 101, pp. 17, 661–17,677, 1996.

[46] T. Hirata, "Fractal dimension of fault systems in Japan: Fractal structure in rock fracture at various scales," *Pure Appl. Geophys*., vol. 131, pp. 157–170, 1989.

[47] M. C. Robertson, C. G. Sammis, M. Sahimi and A. J. Martin, "Fractal analysis of three-dimensional spatial distributions of earthquakes with a percolation interpretation," *J. Geophys. Res.,* vol. 100, pp. 609–620, 1995.

[48] C. G. Sammis, R.M. Nadeau and L.R. Johnson, "How strong is an asperity?", *J. Geophys Res*., vol. 104, pp. 10,609–10,619, 1999.

[49] D. D. Bowman and G. C. P. King, "Accelerating seismicity and stress accumulation before large earthquakes," *Geophy. Res. Lett.*, vol. 28, pp. 4039–4042, 2001.

[50] G.C.P. King and D. D. Bowman, "The evolution of regional seismicity between large earthquakes", *J. Geophys. Res.,* Vol. 108, doi: 10.1029/2001JB000783, 2003.

[51] A. D. Mignan, D. D. Bowman and G. C. P. King, "An Observational Test of the Origin of Accelerating Moment Release Before Large Earthquakes", *J. Geophys. Res.,* vol. 111, doi:10.1029/2006JB004374, 2006.

[52] C. G. Sammis, D. D. Bowman and G. C. P. King, "Anomalous Seismicity and Accelerating Moment Release Preceding the 2001 and 2002 Earthquakes in Northern Baja California, Mexico," *Pure Appl. Geophys.*, vol. 161, pp. 2369–2378, 2004.

[53] R. J. Geller, D. D. Jackson, Y. Y. Kagan and F. Mulargia, "Earthquakes cannot be predicted," *Science,* vol. 275, pp. 1616–1617, 1997.

[54] I. Main, "Long odds on prediction," *Nature*, vol. 385, pp. 19–20, 1997.

[55] D. J. Brehm and L. W. Braile,"Intermediate-term earthquake prediction using precursory events in the New Madrid Seismic Zone," *Bulletin of the Seismological Society of America*, vol. 88, pp. 564–580, 1998.

© 2008 Taylor & Francis Group, London, UK

## *2.2 Scale invariant behaviour in earthquake occurrence*

© 2008 Taylor & Francis Group, London, UK

*Acoustic Emission and Critical Phenomena – Carpinteri & Lacidogna (eds)*
*© 2008 Taylor & Francis Group, London, ISBN 978-0-415-45082-9*

# SCALING AND UNIVERSALITY IN THE DYNAMICS OF SEISMIC OCCURRENCE AND BEYOND

**Álvaro Corral**
Grup de Física Estadística, Departament de Física, Facultat de Ciències,
Universitat Autònoma de Barcelona, Bellaterra, Barcelona, Spain

## ABSTRACT

We present a very brief review of recent findings about scale-invariant behavior in the structure of earthquake occurrence in time and size, leading to the proposal of a striking universal scaling law that has also been shown to describe fracture phenomena. The range of validity of this law in space and energy is enormous. Previously, we discuss the concepts of self similarity and scale invariance and relate them with power laws and scaling laws, explaining the difference between them. The connections between critical phenomena, crackling noise, self-organized criticality, and the possible existence of universality and universality classes out-of-equilibrium are mentioned as well.

## 1 SELF-SIMILARITY, SCALE INVARIANCE, POWER LAWS, AND SCALING LAWS

In the last decades, the study of the natural world has witnessed the emergence of the *fractal revolution* for the description of many existing physical and biological entities [1–4]. A fractal can be informally defined as a geometrical object that shows the same structure independently on the scale of observation; i.e., it does not matter the magnification of the microscope we apply to the system, we will always see something *similar*.

This *self-similarity* has the implication that any property of the system $f(x)$ depending on the scale of observarion $x$ (for instance, the number of structures of size $x$ or the auto-correlation at a distance $x$) must be *scale invariant*, i.e., it does not change when the scale of observation is changed. A change of scale is simply a linear transformation of the axes $x$ and $y$ (where $y = f(x)$), i.e.,

$$x \to x' \equiv bx,$$
$$y \to y' \equiv cy,$$

© 2008 Taylor & Francis Group, London, UK

where $b$ and $c$ are the scale factors which expand each axis; for example, $x$ can be the length measured in meters and $x'$ the same quantity in mm, then $b = 1000$. It is clear that the change in the axes makes the function transform by means of the transformation $\top$ into

$$f(x) \to \top[f(x)] = cf(x'/b),$$

and then, the scale-invariance condition means that

$$f(x) = cf(x/b), \quad \forall b.$$

It is trivial to check that this functional equation has as a solution a *power law*,

$$f(x) = kx^{\alpha}, \tag{1}$$

with the exponent $\alpha \equiv \log c/\log b$ and $k$ an arbitrary constant. Note that the solution holds for all $b$, but then $c$ is not independent, $c = b^{\alpha}$. Moreover, the power law is not only a solution of the scale-invariance condition, but it is the only solution, see Appendix 1 or Refs. [3, 5]. Figure 1 illustrates the invariance of the power law under linear changes of scale, unlike to what happens for example for exponential and Gaussian functions. In some cases it is important to realize that the power-law solution is valid for complex (non-real) $\alpha$, but then not all $b$ factors are allowed, see Ref. [6].

The scale-invariance condition means that the system does not present a characteristic scale, in contrast to many phenomena in physics. Imagine that we are living on a fractal and, by means of some science-fiction procedure, our size is reduced by an unknown factor (this is equivalent to expand the $x$-axis by the

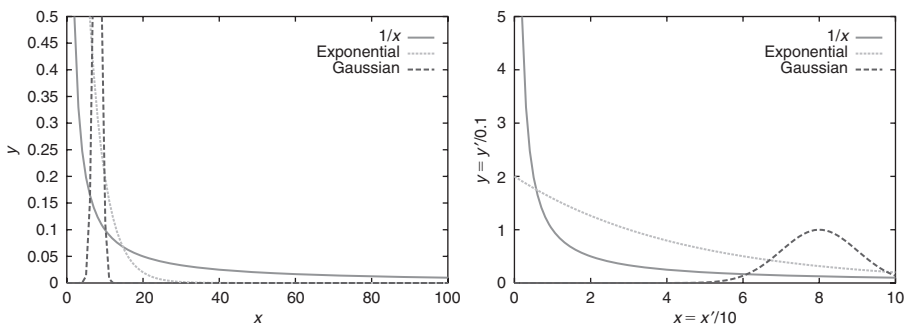



Figure 1: Scale invariance of the power law. In the left figure three functions are displayed: a power law ($1/x$), an exponential ($2 \cdot 10^{-x/10}$), and a Gaussian ($e^{-(x-8)^2/2}$). In the right figure, the same functions after expanding the $x$ and $y$ axes by factors $b = 10$ and $c = 0.1$ respectively (i.e., the $y$ axis is contracted a factor $c^{-1} = 10$). The power law remains identical, in contrast to the other functions. Note that $\alpha = \log c/\log b = -1$.

© 2008 Taylor & Francis Group, London, UK

same factor); we can try to investigate how much we have been reduced by measuring the property $f(x)$ on our (unknown) scale $x$ and compare it with the same property on a close scale $x/b$, i.e., $f(x/b)$; then, the relative change on the property is given by $f(x/b)/f(x) = 1/c$ and is therefore independent on the scale $x$. We can compare this with the case in which $f(x)$ is an exponential function, where the same procedure leads to a relation between the characteristic scale of the system and the scale of observation $x$ which allows to calculate one of them if the other is known. For this reason, we can use radioactive decay to construct clocks (changing space $x$ by time) but there is no way to define a standard of measurement in a scale-invariant system.

In fractal geometry, a power-law relation indicating self-similarity appears in the form $N(\ell) \propto 1/\ell^{d_f}$, where $d_f$ is the box-counting fractal dimension and $N(\ell)$ is the number of boxes of linear size $\ell$ necessary to cover the object, which can be interpreted as the number of structures of size $\ell$. So, in this case the exponent $\alpha$ is a fractal dimension, although the reciprocal is not true in general, not even in the case in which the function $f(x)$ is a cumulative distribution function.

In this work it will be of special importance the case in which the function that displays scale invariance depends on more than one variable, let us say, $z = f(x, y)$. We will consider a change of scale of the axes of the form

$$\begin{aligned} x &\to x' \equiv ax, \\ y &\to y' \equiv by, \\ z &\to z' \equiv cz, \end{aligned}$$

with scale factors of expansion $a$, $b$, and $c$. The scale transformation $\top$ acts now as

$$f(x, y) \to \top[f(x, y)] = cf(x'/a, y'/b),$$

and the scale-invariant condition is $f(x, y) = cf(x/a, y/b)$, $\forall a$. Although the situation is very similar to the previous case, the solution of the problem is certainly different. It can be shown that all these solutions have to be *scaling laws* [5], i.e.,

$$f(x, y) = x^{\alpha} F(y/x^{\beta}), \tag{2}$$

where $F$, the *scaling function*, is an arbitrary monovariate function, and the exponents are related to the scale factors by $\alpha \equiv \ln c/\ln a$ and $\beta \equiv \ln c/\ln b$, i.e., only one scale factor is independent. It follows that the condition of scale invariance is fully equivalent to the fact that $f(x, y)$ is a generalized homogeneous function. Note that the solution can be written in different forms, for instance, $f(x, y) = y^{\alpha/\beta} G(y/x^{\beta})$, which is identical to the previous one if $F(\theta) = \theta^{\alpha/\beta} G(\theta)$. The argument of the scaling function can also be replaced by $y^{1/\beta}/x$, for instance.

It is worth to discuss the distinction between power laws, $f(x) = x^{\alpha}$ [Eq. (1)], and scaling laws, $f(x, y) = x^{\alpha} F(y/x^{\beta})$ [Eq. (2)]. We can see that power laws are special cases of scaling laws, where the scaling function is simply a constant and

© 2008 Taylor & Francis Group, London, UK

then there is no dependence on the second variable. Although in the literature there is some confusion between power laws and scaling laws, we will keep the distinction clear in this work.

## 2 CRACKLING NOISE, CRITICALITY, AND SELF-ORGANIZED CRITICALITY

It turns out that many physical phenomena, in particular natural hazards (like earthquakes, forest fires, solar flares, etc. [7, 8]) and also similar phenomena in condensed-matter physics (as the motion of domain walls in soft magnetic materials or the sound emitted during martensitic phase transitions [9]) are constituted by bursty, episodic events whose size spans a broad-range of scales, following a power-law distribution. This behavior has been labeled as *crackling noise* [9], but notice that, in contrast to fractals, in this case it is not clear how the power law can be related to a geometrical structure, i.e., we have scale invariance (and therefore a lack of characteristic scales) but without an interpretation in terms of geometrical self similarity.

The notion of *self-organized criticality* goes one step beyond, as it proposes a mechanism for the emergence of the scale-invariant response of these systems (i.e., crackling noise) as a spontaneous organization of the dynamics of the system towards a very particular state, analogous to the critical point found in equilibrium phase transitions [7]. The idea is explained by means of the sandpile metaphor: if we add grains very slowly over a finite support, a pile starts to grow, as there is a positive balance between the added grains and the grains that fall off the pile (the former win). The growth process continues until the slope reaches a *critical* value, where the addition and the falling of grains are perfectly balanced, on average. On the other hand, if, by means of some artificial mechanism, the slope of the pile is larger than the critical value, then, the dissipation of grains at the borders predominates and the slope of the pile is reduced until it reaches the critical value. At the end, the slope of the pile fluctuates around this value, which means that the critical state can be considered an *attractor* of the dynamics.

Note that we have used the term critical as referring to a separation between two different behaviors; however, this nonequilibrium critical state of the pile should have analogous properties to equilibrium systems at the critical point of a phase transition. Let us consider a magnetic phase transition in an idealized case [5]. We assume that in a magnetic material, even if no magnetic field is applied, there exist a spontaneous (non-zero) magnetization at low temperatures (this constitutes the ferromagnetic phase). However, for high enough temperatures it is well known that there is no neat magnetization (this behavior defines the paramagnetic phase). In fact, there exists a critical value of the temperature for which an abrupt transition takes place between the spontaneous magnetic behavior and the zero-magnetization case (the transition is so sharp that magnetization

© 2008 Taylor & Francis Group, London, UK

goes to zero with infinite slope, hence analytic functions are unable to describe the magnetic behavior in this case; this is a key point in critical phenomena). It turns out that above the critical temperature, small clusters of aligned particles with a neat magnetization exist, but their magnetization cancels with each other; in contrast, below the critical temperature there exists an *infinite cluster* of aligned units, providing the neat magnetization of the material. The transition takes place in such a way that, precisely at the critical temperature, there are clusters of all sizes, but without a characteristic scale, and therefore the critical points of equilibrium phase transitions show fractal properties. Because the value of the magnetization allows to distinguish between an ordered phase (the ferromagnetic one) and a disordered one (paramagnetic), $m$ is considered an *order parameter*. This should be what happens as well in the critical state of a sandpile, providing a metaphor for the behavior of many nonequilibrium systems, which has been verified for diverse computer models. Nevertheless, for real sandpiles the picture is not always correct, but this is a different story [10].

Two remarkable properties of equilibrium systems close to their critical point are *scaling* and *universality* [11, 12]. Following with the example of a magnetic material, an equation of state of the form $m = f(T, H)$ relates the magnetization $m$ with the temperature $T$ and the magnetic field $H$. However, in the vicinity of the critical point, which is given by $T = T_c$, $H = 0$, and $m = 0$, the equation of state fulfills a scaling law, identical to Eq. (2) [5],

$$\frac{m}{h^{1/\delta}} = F\left(\frac{\tau}{h^{1/\beta\delta}}\right),$$

where $\tau \equiv (T - T_c/T_c)$ is the reduced temperature (which measures the deviation of the temperature with respect the critical temperature $T_c$ in units of $T_c$), $h$ is a dimensionless measure of $H$, as a balance between the magnetic energy and the thermal energy, and the exponents $\delta$ and $\beta$ are called *critical exponents* (for which the so-called mean-field theory yields $\delta = 3$ and $\beta = 1/2$). This means that the plots of magnetization versus reduced temperature for different applied fields yield a unique curve if $m$ is rescaled by $h^{1/\delta}$ and $\tau$ by $h^{1/\beta\delta}$. In other words, the dependence of $m$ on $\tau$ is *similar* for different $h$, except for a change of scale, at least close to the critical point, and we can say that $m$ and $\tau$ *scale* with $h$ as $h^{1/\delta}$ and $h^{1/\beta\delta}$, respectively. The unique, monovariate function describing this behavior is the scaling function $F$, for which in mean-field theory its inverse is $F^{-1}(\sigma) = 1/\sigma - \sigma^2/3$ (assuming that $m$ is dimensionless). The scaling of the equation of state close to the critical point has as a consequence that when it is restricted to particular conditions (isothermal, or zero field), the remaining variables, as well as the response functions deriving from them (the susceptibility for instance) are related by means of simple power laws.

When we compare different magnetic systems it turns out that, although the critical temperatures are different for each one, the critical exponents and the scaling function are the same. This property is called *universality*, and is valid

© 2008 Taylor & Francis Group, London, UK

even for different types of phase transition; for instance, magnetic phase transitions and liquid-gas transitions in diverse materials share as well exponents and scaling functions. If we think about it, it is astonishing how universal properties may emerge independently of the variability of microscopic, system-specific details. (In practice, the scaling of $m$ and $\tau$ with $h$ involves two extra constants that may change for different materials although the exponents and the scaling function do not change.) Nevertheless, there exist other cases for which the exponents and the functions are different, defining each group with the same properties what is (strangely) labeled as a *universality class*. In any case, microscopic details are not important to distinguish different universality classes, rather, they depend on general properties like the dimensionality of the system (one of the universality classes is the mean-field one, for which the value of two exponents and the scaling function are given above). Still it is an open question up to what point universality and universality classes are a fundamental issue for out-of-equilibrium systems.

## 3 SCALE INVARIANCE OF EARTHQUAKE SIZES

We have mentioned that earthquakes display crackling noise, and they have been proposed also as a prototypical example of a self-organized critical system. However, it is necessary to clarify that, whereas the property of crackling noise is easy to test from the response of the system (one only needs to perform the statistics of event sizes and check if it yields a power law), for the verification of the existence of self-organized criticality one has to have access to the internal variables of the system in order to measure the fluctuations of these variables around a critical state, introducing perhaps an order parameter [13].

In any case, let us start with the statistics of earthquake sizes. If we consider magnitude as a measure of size (which indeed it is), and count the number of earthquakes in a fixed region and during a sufficiently long period of time, we obtain that for each earthquake of magnitude 6 there are about 10 earthquakes of magnitude 5, 100 earthquakes of magnitude 4, and so on. This is a fundamental property of seismicity, known as the *Gutenberg-Richter law* [4, 14–16] and can be formulated more formally as,

$$n_\Delta(M) \propto 10^{-bM} \propto e^{-b \ln 10 M},$$

where $M$ is magnitude, $n_\Delta(M)$ is the number of earthquakes between $M$ and $M + \Delta$, the $b$-value is close to 1 (do not confound it with the scale factor $b$ of the first section), and the symbol $\propto$ stands for proportionality, the coefficient of proportionality would depend on the activity of the region. We can conclude that the Gutenberg-Richter law brings good news, as most of the earthquakes are very small, and only very few of them are large or catastrophic (we will see below that, unfortunately, this interpretation is not appropriate). Figure 2

© 2008 Taylor & Francis Group, London, UK

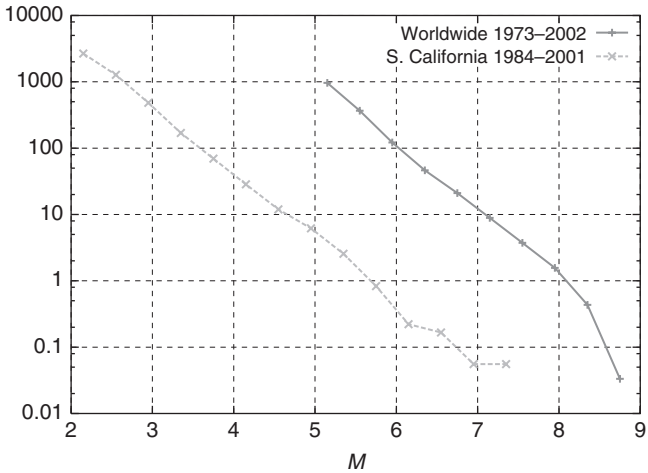



Figure 2: Average number of earthquakes per year in Southern California, for the years 1984–2001, and worldwide, for 1973–2002, for magnitude ranges of extend $\Delta = 0.4$. The straight-line behavior in the logarithmic-linear axes is an indication of exponential behavior, the slope $b$ (when the logarithm is decimal) is very close to 1. The lack of data at the left of each curve is a consequence of the incompleteness of the catalogs for small events; for regions with higher density of instrumentation the law can be shown valid well below magnitude 2. Note that $M \simeq 2/3 \log E/60$, if $E$ is measured in kJ.

illustrates the Gutenberg-Richter law for Southern California and for worldwide seismicity.

We find it more practical to describe the distribution of the size of earthquakes by means of the *probability density*, $D(M)$, defined as

$$D(M) \equiv \frac{\text{Prob}\,[M \leq \text{magnitude} < M + \Delta]}{\Delta},$$

where Prob denotes probability, and $\Delta$ should tend to zero, in the ideal case. It is straightforward to estimate $D(M)$ from $n_\Delta(M)$ as $D(M) = \Delta^{-1}N^{-1}n_\Delta(M)$, where $N$ is the total number of earthquakes (of any size); in practice, $\Delta$ should be small, in order not to modify the continuous nature of $D(M)$, but also large enough to provide statistical significance in any interval it defines. In any case, the probability density removes the dependence of the size distribution on $\Delta$, as well as on the seismic activity and extension of the spatial region under analysis, allowing the study of possible universal properties (properties that would be the same for very different systems or tectonic environment, see previous section). In this way, in terms of the probability density, the Gutenberg-Richter

© 2008 Taylor & Francis Group, London, UK

law still gives an exponential behavior. Even more, due to the special property of exponential functions, the cumulative distribution of sizes, defined by $S(M) \equiv \text{Prob}\,[\text{magnitude} > M] = \int_M^\infty D(M)\,dM$ is also an exponential function, with the same characteristic decay (given by $b \ln 10$). For this reason, many times it is not clearly stated in the literature if cumulative or non-cumulative distributions are used, but this ambiguity is only possible (and tolerable) for exponential distributions.

At the beginning of this text we have argued with great excitation about the special properties of power laws, but the distribution of earthquake magnitudes is not power law but exponential. Then, how can earthquakes be an example of scale invariance, crackling noise, and self-organized criticality? The reason is because earthquake magnitude is not a good representation of earthquake size. After all, magnitude has no dimensions, i.e., physical units. A much more natural measure of earthquake size would be the energy it releases; however, this is a quantity very difficult to obtain in practice. Nowadays, the most reliable measurement of earthquake size is *seismic moment* [16], represented by $\mathscr{M}$ here, which turns out to be equal to the product of the rigidity $\mu$, the spatially averaged slip $d$, and the fault area $A$ ruptured by the earthquake, i.e., $\mathscr{M} = \mu A d$.

The relation between seismic moment and magnitude is given, when the formed is measured in Newtons $\times$ meters by $\mathscr{M} = 10^{1.5(M+6.07)}$, which is in fact a definition of the so called moment magnitude from the seismic moment; other magnitudes, defined in many different ways, are close to the moment magnitude, except for saturation effects. Notice that $\mathscr{M}$ has units of energy ($1\ \text{J} = 1\ \text{N m}$), but it is not an energy. The energy $E$ radiated by seismic waves is believed by some authors to be roughly proportional to the seismic moment, i.e., $E \simeq 5 \cdot 10^{-5}\,\mathscr{M}$, although this question is not solved at present [16]. If we accept this proportionality as a first approximation, we obtain that the energy (in kilo-Joules) relates with the (moment) magnitude as $E \simeq 60 \cdot 10^{1.5\,M}$, i.e., the energy is an exponential function of the magnitude. (For each increase in one unit of the magnitude, the energy is multiplied by a factor $10^{1.5} \simeq 32$.) As the magnitude is exponentially distributed, it is straightforward to show that $E$ must be power-law distributed, with an exponent of the probability density equal to $1 + 2b/3$. Indeed,

$$D(M)dM = D(E)dE \quad \Rightarrow \quad D(E) = D(M)\frac{dM}{dE} \propto 10^{-bM}\frac{1}{E}$$

and then

$$D(E) \propto \frac{1}{E^{1+2b/3}},$$

where we have used the same symbol $D$ for the densities of magnitudes and energies, although of course they are different functions (exponential and power law, respectively). For the cumulative energy distribution the exponent is reduced

© 2008 Taylor & Francis Group, London, UK

in one unit, i.e., $S(E) = \text{Prob}\ [\text{energy} > E] \propto 1/E^{2b/3}$. If the proportionality between seismic moment and radiated energy were not true, the power-law behavior, with the same exponent, would at least be valid for the seismic moment. It is important to realize that there is a fundamental conflict between scale invariance and normalization of probability, and so the power law cannot hold for very small values of the variable ($E$) if the exponent of the density is larger than 1, and then a minimum cutoff is necessary in the distribution.

Other possible physical measurements of size, in addition to seismic moment and radiated energy are the rupture duration $T$ (size in time), the rupture length $\ell$, the rupture area $A$ (mentioned above), and the slip $d$ (also mentioned above). Let us assume, as a working hypothesis, that earthquakes are dynamically similar, i.e., from the evolution of the rupture it is not possible to distinguish between small and large earthquakes; this means that in particular the rupture velocity $v = \ell/T$ and the power radiated per unit of fault area $E/(TA)$ are independent of size, which implies that $\ell$ and $T$ are proportional to each other; supposing the area $A$ goes as $\ell^2$ (i.e., the earthquake propagates in the same way in all directions in the fault), this leads to the fact that the energy fulfills $E \propto T^3$ and $E \propto \ell^3$. This is in agreement with observations, at least replacing $E$ by $\mathscr{M}$ [16]. From these relations one can obtain the distributions of $T$, $\ell$, and $A$, and also that of $d$ using that of the seismic moment. It turns out that all of them are power-law distributed,

$$\begin{aligned} D(T) &= D(\mathscr{M})d\mathscr{M}/dT \propto 1/T^{1+2b}, \\ D(\ell) &= D(\mathscr{M})d\mathscr{M}/d\ell \propto 1/\ell^{1+2b}, \\ D(A) &= D(\mathscr{M})d\mathscr{M}/dA \propto 1/A^{1+b}, \\ D(d) &= D(\mathscr{M})d\mathscr{M}/dd \propto 1/d^{1+2b}, \end{aligned}$$

as power-law changes of variables preserve power-law distributions, but changing the exponent. From these power-law distributions of sizes the scale-invariance and the crackling-noise behavior of earthquakes follow directly. We need to mention that the dynamical similarity of earthquakes is however still a debatable topic.

In any case, the power-law distributions indicate that all these measures of earthquake size (radiated energy, seismic moment, duration, rupture length, etc.) do not have a characteristic scale, which has to be considered right up to the scale imposed by the size of the system, in this case the Earth crust. On the other hand, we can evaluate from the distributions the mean earthquake size, however, there is a problem for the energy and the seismic moment (and for the area if $b \leq 1$), which is that their mean values become infinite. So, despite the fact that there are no characteristic scales, mean values for durations and lengths exist, but mean values for the other variables do not. Taking the energy as an example, this means that the dissipation of energy is leaded by large earthquakes; if we try

© 2008 Taylor & Francis Group, London, UK

to calculate its mean value from the catalogs it turns out that this quantity does not converge: when a large earthquake takes place the energy it radiates is much larger than that of the rest of smaller earthquakes. In this way, the Gutenberg-Richter law expressed in terms of the energy brings very bad news: although large earthquakes are a tiny fraction of all earthquakes, they dissipate most of the energy, providing the tragic reputation of the phenomenon.

We have mentioned that a power-law distribution does not necessarily imply the existence of a spatial fractal structure. Nevertheless, in the case of earthquakes there are clear evidences for the existence of such structures. First, the distribution of earthquake hypocenters shows fractal (and even multifractal) properties [14]; and second, faults, which are the structures where earthquakes take place, form complex fractal networks [4, 17, 18]; in addition, their lengths are power-law distributed [4, 19], the same as the extension of tectonic plates (which are both responsible for and modeled by earthquakes) [20]. In conclusion, earthquakes provide a fantastic natural laboratory for the study of fractal properties.

## 4 SCALE INVARIANCE IN THE TIMING OF EARTHQUAKES

Neither in the research on earthquakes nor in the studies of crackling noise and self-organized criticality there has been a clear picture for the temporal properties of these systems. Notice for instance that crackling noise is defined only by means of the size of the response of the system, without any reference to its time evolution. In the case of self-organized critical systems it was believed that the dynamics was trivial, with the response of the system (the avalanches) following a Poisson process (i.e., at each time step a dice would decide if there is an avalanche or not). In fact, this seems to be just a pathological characteristic of very small avalanches in some popular sandpile models; larger events do not follow this trend [21].

The time properties of earthquakes are more puzzling. It is true that the Omori law, which states that the seismic rate decays as a power law after a big earthquake in a certain area around it, is well established, but when we go deeper than the measurement of rates and care about the timing of individual earthquake occurrence the issue becomes fuzzy, as there is a clear lack of a coherent phenomenology [22]. It is widely believed that fault segments produce *characteristic* earthquakes; these are events of not only the same size but also similar seismographic fingerprints that take place at more or less regular intervals, in which it is known as the *seismic cycle* [23, 24]. However, the characteristic-earthquake view has been challenged recently, mainly with the failure of the Parkfield prediction experiment [25–27], but also because paleoseismological studies do not allow to distinguish regular occurrence from a Poisson process [28]. In any case, this perspective is rooted on the assumption that faults do not

© 2008 Taylor & Francis Group, London, UK

interact with each other, or at least in the fact that the interaction is weak enough in order that the seismic cycle is not significantly altered.

Recently, an alternative, non-reductionistic approach inspired by the physics of complex systems has emerged for the study of earthquakes. Instead on concentrating on single fault segments, a more global perspective, considering large extended regions as well defined systems is necessary. It was believed that for such large regions the occurrence of mainshocks was totally random, described by a Poisson process [29]. Although other approaches have been later introduced for the statistics of mainshocks, again the complex-system perspective questions the separation of earthquakes into different processes (mainshocks and foreshocks): all earthquakes are generated by the same process, and even those events considered as aftershocks can trigger successive events and become mainshocks [30].

A major conceptual advance from this point of view has been the recent work of Bak *et al.* [31], which focused on common universal properties rather than on different peculiarities associated to particular tectonic settings, and combined the size distribution of earthquakes, the fractal structure of its spatial occurrence and its temporal occurrence into a unique unified scaling law, similar in spirit to those used to describe critical systems in statistical physics.

In the same line, we have developed a simpler approach to analyze the complexity of seismicity in time, space, and size. A fundamental advance introduced by Bak *et al.* that we take advantage of it was to consider, for a given spatial region, only events above a minimum magnitude $M_c$, and study how the dynamics of occurrence changes as a function of $M_c$. For each $M_c$-value, those events with $M \geq M_c$ define a point process, $t_0, t_1, t_2 \ldots$ where $t_i$ is the time of occurrence of the $i$-th event above the minimum magnitude in the region. Then we compute the *recurrence time* $\tau$ (also called interevent time, interoccurrence time, waiting time, etc.), which is nothing else than the time between consecutive events, i.e., $\tau_i \equiv t_i - t_{i-1}$; notice that both occurrence and recurrence times depend on $M_c$, although, for simplicity, this dependence is not reflected in the notation. In the same way, the probability density of the recurrence time will depend on $M_c$, or on the minimum radiated energy, $E_c \propto 10^{1.5M_c}$, as well as on the spatial region $\mathscr{R}$ under study; we will denote this density as $D(\tau; M_c, \mathscr{R})$, as a function of the minimum magnitude or $D(\tau; E_c, \mathscr{R})$, in terms of the minimum energy.

As we are interested in a global perspective, let us start at the largest possible scale, which is that of worldwide earthquake occurrence. The recurrence-time distributions for $M_c$ ranging from 5 to 6.5 are shown in Fig. 3(a). Obviously, the larger $M_c$, the less earthquakes there will be and the longest the recurrence times between them. However, for each $M_c$, we can measure the time in units of the mean recurrence time, this also changes the units of the density; in other words, we perform the transformation $\tau \to R(M_c, \mathscr{R})\tau$ and $D \to D/R(M_c, \mathscr{R})$, where $R(M_c, \mathscr{R})$ is the mean seismic rate, defined as the total number of earthquakes with $M \geq M_c$ in the region $\mathscr{R}$ divided by the time interval under study;

© 2008 Taylor & Francis Group, London, UK

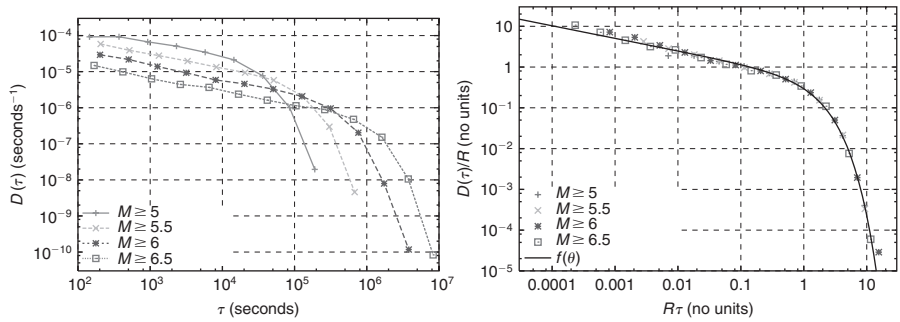



Figure 3: Left: Probability densities of recurrence times of earthquakes worldwide with $M \geq M_c$ during the period 1973–2002, for $M_c$ ranging from 5 to 6.5. Right: The same distributions rescaled by its rate. The data collapse is the signature of the scaling law. The continuous function is the gamma distribution explained in the text. $D(\tau)$ is $D(\tau; M_c, \mathscr{R})$ and $R$ is $R(M_c, \mathscr{R})$. Taken from Ref. [34].

in other words, $R$ is the inverse of the mean recurrence time. The collapse of the distributions into a unique curve shown in Fig. 3(b) is an indication of the fulfillment of a scaling law [32],

$$D(\tau; M_c, \mathscr{R}) = R(M_c, \mathscr{R}) F_{\mathscr{R}}(R(M_c, \mathscr{R})\tau),$$

where the scaling function in region $\mathscr{R}$, $F_{\mathscr{R}}$, is independent on $M_c$. Using the Gutenberg-Richter law, it turns out that $R(M_c, \mathscr{R}) \propto 10^{-bM_c}$ or $R(E_c, \mathscr{R}) \propto 1/E_c^{2b/3}$, to be concrete, $R(E_c, \mathscr{R}) = R_0(\mathscr{R})/E_c^{2b/3}$, where $R_0(\mathscr{R})$ is the rate of occurrence of events with energy greater than $E_c = 1$ in the region (in whatever units we chose for the energy, in the case in which the unit is 60 kJ this corresponds to $M_c = 0$); then the scaling law can be written as

$$D(\tau; E_c, \mathscr{R}) = \frac{R_0(\mathscr{R})}{E_c^{2b/3}} F_{\mathscr{R}}\left(\frac{R_0(\mathscr{R})\tau}{E_c^{2b/3}}\right).$$

Although it is not obvious at a first sight, this scaling law is a remarkable result. In general, when events are removed from a point process (as we do raising $M_c$), the properties of the process change; in other words, the process will *renormalize* to a new process. In many cases this renormalization leads to a Poisson process: if there are short range correlations, or if the (nonstationary) rate of the process shows a characteristic time scale, when a sufficiently large number of events have been eliminated the characteristic scales are lost and the process becomes structureless and therefore Poisson. The existence of the scaling law means that the process is invariant, or a fixed point of a renormalization-group transformation, which constitutes a very particular solution in the space of

© 2008 Taylor & Francis Group, London, UK

all possible processes [33]. The same happens at the critical points of equilibrium phase transitions [5].

As the plot indicates, the scaling function turns out to be a decreasing power law up to the largest times, where the behavior changes to an exponential decay. A gamma function can account for this behavior,

$$F_{\mathscr{R}}(\theta) = \frac{1}{\Gamma(\gamma)a}\left(\frac{a}{\theta}\right)^{1-\gamma} e^{-\theta/a},$$

where $\theta$ is the recurrence time in units of its mean, i.e., $\theta \equiv R(M_c, \mathscr{R})\tau$, $\Gamma()$ is the gamma function, $a$ is a scale parameter, and $\gamma$ is the shape parameter of the distribution. In fact, there is only an independent parameter, as the mean of $\theta$ is reinforced by the rescaling of the axes to be one, and then $\overline{\theta} = \gamma a = 1$. A fit yields $\gamma \simeq 0.7$, which implies that the exponent describing the power-law decay is about 0.3. This behavior is an indication of *clustering*, and means that there are more earthquakes separated by short recurrence intervals than what corresponds to a random, memoryless occurrence (i.e., a Poisson process with the same rate); in other words, the risk of occurrence is higher right after an earthquake, and then decreases for long times, which leads to the formation of clusters of events. This behavior was previously found by Kagan in a different approach, and is the opposite of the regularity or quasi-periodicity derived from the idea of the seismic cycle [14, 35]. One surprising consequence of clustering is the paradoxical result that *the longer it has been since the last earthquake, the longer the expected time till the next* [36].

We can explore what happens beyond worldwide seismicity, at the regional and local levels. In doing this one needs to have in mind that at the world scale seismicity is a stationary process (at least from 1973 to 2002), in the sense that the rate of occurrence is independent of the time window selected. In contrast, when we go to smaller scales, local inhomogeneities appear, due to the presence of aftershock sequences that at the global level are mixed between them and not apparent. So, at the regional and local scales seismicity is not stationary in general, and periods of variable rate exist, but followed sometimes by stationary periods. We will concentrate only on those stationary periods (as for instance 1988–1991 for Southern California). Figure 4 shows rescaled recurrence time distributions for many regions with stationary seismicity at different scales, from worldwide to small areas in Southern California and Japan, mainly. All cases in the figure, and others not shown [36], seem to be in agreement with the scaling law presented above for the worldwide case, covering a range of minimum magnitudes from 1.5 to 7.5 and from worldwide scales up to about 20 km. Therefore the scaling function can be considered the same for different regions, which means that it can be written as

$$D(\tau; M_c, \mathscr{R}) = R(M_c, \mathscr{R})F(R(M_c, \mathscr{R})\tau),$$

© 2008 Taylor & Francis Group, London, UK

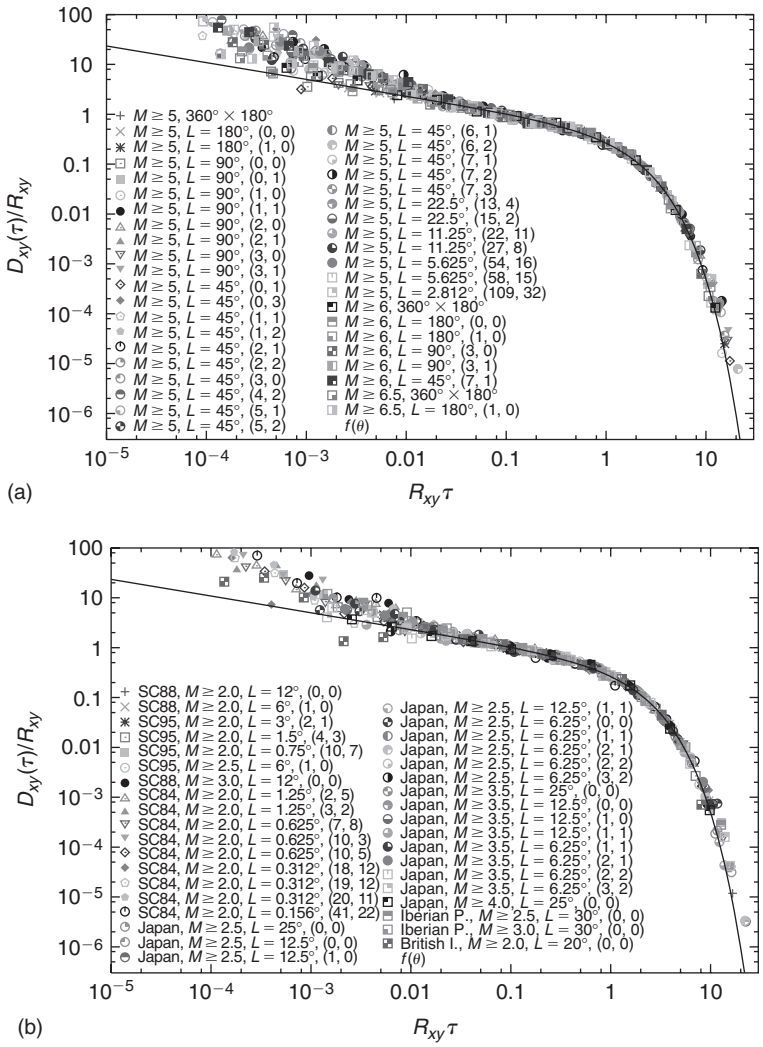



Figure 4: Rescaled probability densities of recurrence times in large regions worldwide (top) and smaller areas in Southern California (SC), Japan, the Iberian Peninsula, and the British Islands (bottom), using different minimum magnitudes and selecting time periods for which seismicity is stationary. The linear size of the region is given by $L$, $R_{xy}$ refers to $R(M_c, \mathscr{R})$ and $D_{xy}(\tau)$ to $D(\tau; M_c, \mathscr{R})$. Taken from Ref. [32].

where $F$ is independent on $\mathscr{R}$, or, simplifying the notation, $D_w(\tau) = R_w F(R_w \tau)$ with $w \equiv \{M \geq M_c, \mathscr{R}\}$. As the regions analyzed present very different tectonic properties, we may consider the results as universal, in the same sense as in equilibrium critical phenomena.

© 2008 Taylor & Francis Group, London, UK

Several authors have argued that the only possible form for the scaling function is provided by the trivial case of a Poisson process if the scaling law is exact [37], although an approximate scaling may be valid, weakly dependent on the rate [38]. These results are based on particular simple models of seismicity or on the hypothesis that contiguous regions may be considered as independent between them. In any case, this is an interesting open problem.

## 5 RELATION WITH FRACTURES: UNIVERSALITY

It is a remarkable fact that the results exposed here for earthquakes are representative of somehow related processes at a much smaller scale. Davidsen *et al.* [39] have measured the acoustic emission from laboratory rock fractures, using different materials and diverse experimental procedures. Their findings are displayed in Fig. 5 (left), showing how a scaling law for the distributions of time intervals between detected emissions holds, with a scaling function surprisingly compatible with that of earthquakes. The materials considered in the plot are a couple of sandstones (at wet conditions), three samples of granite, and Etna basalt (at dry conditions). The confined pressures were in the range from 5 to 100 MPa and the loading conditions were constant displacement rate, acoustic emission activity feedback control of loading, and punch-through loading. The authors concentrated only in the periods of stationary activity.

Another important result was found by chance during preliminary runs of the CRESST project for dark-matter search at the Gran Sasso Laboratory [40, 41]. A cryogenic detector, made by a single crystal of sapphire, recorded an unexpected series of pulses of a high rate. Initially, the researches believed that the signal was due to an unknown radioactive contamination, but the time distribution of the pulses was not Poisson but bursty, which clearly discarded radioactivity. Finally, the origin of the signal was traced to nanofractures in the crystal due to the tight clamping of the detector. The size of the fractures was rather small, involving in some cases the breaking of only several hundreds of covalent bonds. Figure 5 (right) shows the astonishing similarity between the recurrence times in nanofractures and earthquakes, where the same scaling function can describe both phenomena. Note therefore the enormous range of values for which the same law is valid, from earthquakes with estimated radiated energy larger than $2 \cdot 10^{15}$ J (magnitude larger than 7) to nanofractures of minimum absolute dissipated energy of about 5 keV, or $8 \cdot 10^{-16}$ J, which yields a range of more than 30 orders of magnitude of validity. It is noteworthy as well the profund differences between the homogeneity and regularity of a monocrystal at milli-Kelvin temperatures and the heterogeneity of fault gouge producing (and produced by) earthquakes.

Other systems outside this field verify this complex dynamics, in particular extreme climatic records [42], with a scaling function similar to the one of

© 2008 Taylor & Francis Group, London, UK

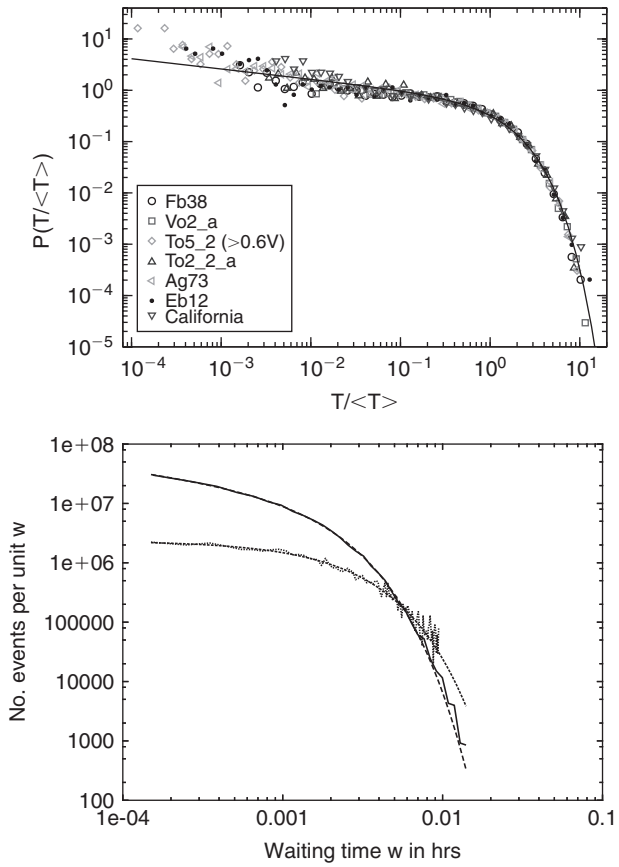



Figure 5: Top: rescaled probability densities of recurrence times of acoustic emission signals measured in laboratory experiments of rock fractures, using different samples. The continuous line is a gamma function with parameter $\gamma = 0.8$, which is compatible with the value obtained for earthquakes. Taken from Ref. [39]. Bottom, continuous curve: probability density (not normalized) of recurrence times of nanofractures in a monocrystal of sapphire at a temperature of about 10 milli-Kelvin. The fit is a gamma distribution with parameter $\gamma = 0.67$, practically the same as the value for earthquakes. Right, dashed curve: The same for radioactive induced events. The fit is an exponential (Poisson) function. From Ref. [40].

earthquakes, as well as solar flares [43] and financial time series [44], where a scaling law for recurrence times is valid but the scaling functions are different. It would be interesting to explore if they correspond to different universality classes.

In conclusion, the dynamics of point-like process representing the sudden appearance of several natural disasters and the explosive behavior of many

© 2008 Taylor & Francis Group, London, UK

nonequilibrium solid-state responses is an open field of research, that will allow a rich interchange of ideas and will certainly grow in the next years, extending perhaps to biological systems and even human behavior [45].

I am grateful to J. Davidsen and L. Stodolsky for their comments and the permission to use their figures.

## APPENDIX

We are going to demonstrate the fact that scale-invariant systems are characterized by power laws and vice versa. Let us consider a one-dimensional function $f(x)$. As we have explained in the main text, a *scale transformation* is given by the application $\top$:

$$f(x) \longrightarrow \top[f(x)] = cf(x'/b),$$

where the space expands a factor $b$ in the $x$ axis and a factor $c$ in the $y$ axis. The condition of *scale invariance* is

$$f(x) = cf(x/b) \quad \forall b, \tag{3}$$

which turns out to be a functional equation for $f(x)$ whose solutions will give the analytical form of a scale-invariant function. It means that graphs of $f(x)$ "centered" at different scales can be superimposed by a simple change of scale. To find its solutions, let us derive both sides respect $x$ and isolate $c$ to obtain [3]

$$c = b\frac{f'(x)}{f'(x/b)} \quad \forall b,$$

where the prime denotes the derivative. Substituting $c$ in the original equation (3) and multiplying both sides by $x$ one finds

$$\frac{x}{b}\frac{f'(x/b)}{f(x/b)} = x\frac{f'(x)}{f(x)} \quad \forall b.$$

As the equation holds for all $b$, it is clear that $xf'(x)/f(x)$ must be a constant, i.e.

$$x\frac{f'(x)}{f(x)} = \alpha.$$

In this way, the functional equation has been transformed into a differential one of straightforward solution, which is,

$$f(x) = kx^{\alpha},$$

with $k$ an arbitrary constant. Thus, the only scale-invariant function in one dimension is the *power law*. Substituting into the original equation (3), we find that it is required that

$$c(b) = b^{\alpha},$$

© 2008 Taylor & Francis Group, London, UK

and hence the scale-invariant condition (3) can be rewritten as

$$f(x) = b^{\alpha} f(x/b) \quad \forall b, \tag{4}$$

which means that $f(x)$ is an *homogeneous* function. Note that only when $f(x)$ is linear, i.e. in the case $\alpha = 1$, both axis are transformed by the same factor.

## References


[1] B. B. Mandelbrot. *The Fractal Geometry of Nature*. W. H. Freeman, New York, 1983.

[2] J. Feder. *Fractals*. Plenum Press, New York, 1988.

[3] H. Takayasu. *Fractals in the Physical Sciences*. Manchester University Press, Manchester, 1989.

[4] D. L. Turcotte. *Fractals and Chaos in Geology and Geophysics*. Cambridge University Press, Cambridge, 2nd edition, 1997.

[5] K. Christensen and N. R. Moloney. *Complexity and Criticality*. Imperial College Press, London, 2005.

[6] D. Sornette. Discrete-scale invariance and complex dimensions. *Phys. Rep.*, 297:239–270, 1998.

[7] P. Bak. *How Nature Works: The Science of Self-Organized Criticality*. Copernicus, New York, 1996.

[8] B. D. Malamud. Tails of natural hazards. *Phys. World*, 17 (No. 8):31–35, 2004.

[9] J. P. Sethna, K. A. Dahmen, and C. R. Myers. Crackling noise. *Nature*, 418:242–250, 2001.

[10] V. Frette, K. Christensen, A. Malthe-Sørenssen, J. Feder, T. Jøssang, and P. Meakin. Avalanche dynamics in a pile of rice. *Nature*, 379:49–52, 1996.

[11] H. E. Stanley. *Introduction to Phase Transitions and Critical Phenomena*. Oxford University Press, Oxford, 1973.

[12] H. E. Stanley. Scaling, universality, and renormalization: Three pillars of modern critical phenomena. *Rev. Mod. Phys.*, 71:S358–S366, 1999.

[13] O. Peters and J. D. Neelin. Critical phenomena in atmospheric precipitation. *Nature Phys.*, 2:393–396, 2006.

[14] Y. Y. Kagan. Observational evidence for earthquakes as a nonlinear dynamic process. *Physica D*, 77:160–192, 1994.

[15] T. Utsu. Representation and analysis of earthquake size distribution: a historical review and some new approaches. *Pure Appl. Geophys.*, 155:509–535, 1999.

[16] H. Kanamori and E. E. Brodsky. The physics of earthquakes. *Rep. Prog. Phys.*, 67:1429–1496, 2004.

[17] P. Davy, A. Sornette, and D. Sornette. Some consequences of a proposed fractal nature of continental faulting. *Nature*, 348:56–58, 1990.


© 2008 Taylor & Francis Group, London, UK

[18] I. Main. Statistical physics, seismogenesis, and seismic hazard. *Rev. Geophys.*, 34:433–462, 1996.
[19] D. Sornette and P. Davy. Fault growth model and the universal fault length distribution. *Geophys. Res. Lett.*, 18:1079–1081, 1991.
[20] D. Sornette and V. Pisarenko. Fractal plate tectonics. *Geophys. Res. Lett.,* 30:1105, 2003.
[21] M. Paczuski, S. Boettcher, and M. Baiesi. Interoccurrence times in the Bak-Tang-Wiesenfeld sandpile model: A comparison with the observed statistics of solar flares. *Phys. Rev. Lett.*, 95:181102, 2005.
[22] F. Mulargia and R. J. Geller, editors. *Earthquake Science and Seismic Risk Reduction*. Kluwer, Dordrecht, 2003.
[23] D. P. Schwartz and K. J. Coppersmith. Fault behavior and characteristic earthquakes: Examples from the Wasatch and San Andreas fault zones. *Nature*, 89:5681–5698, 1984.
[24] W. H. Bakun and A. G. Lindh. The Parkfield, California, earthquake prediction experiment. *Science*, 229:619–624, 1985.
[25] J. Murray and P. Segall. Testing time-predictable earthquake recurrence by direct measurement of strain accumulation and release. *Nature*, 419: 287–291, 2002.
[26] R. S. Stein. Parkfield's unfulfilled promise. *Nature*, 419:257–258, 2002.
[27] R. A. Kerr. Parkfield keeps secrets after a long-awaited quake. *Science*, 306:206–207, 2004.
[28] R. Weldon, K. Scharer, T. Fumal, and G. Biasi. Wrightwood and the earthquake cycle: what a long recurrence record tells us about how faults work. *GSA Today*, 14(9):4–10, 2004.
[29] J. K. Gardner and L. Knopoff. Is the sequence of earthquakes in Southern California, with aftershocks removed, Poissonian? *Bull. Seismol. Soc. Am.*, 64:1363–1367, 1974.
[30] A. Helmstetter and D. Sornette. Diffusion of epicenters of earthquake aftershocks, Omori's law, and generalized continuous-time random walk models. *Phys. Rev. E*, 66:061104, 2002.
[31] P. Bak, K. Christensen, L. Danon, and T. Scanlon. Unified scaling law for earthquakes. *Phys. Rev. Lett.*, 88:178501, 2002.
[32] A. Corral. Long-term clustering, scaling, and universality in the temporal occurrence of earthquakes. *Phys. Rev. Lett.*, 92:108501, 2004.
[33] A. Corral. Renormalization-group transformations and correlations of seismicity. *Phys. Rev. Lett.*, 95:028501, 2005.
[34] A. Corral. Dependence of earthquake recurrence times and independence of magnitudes on seismicity history. *Tectonophys.*, 424:177–193, 2006.
[35] Y. Y. Kagan. Why does theoretical physics fail to explain and predict earthquake occurrence? In P. Bhattacharyya and B. K. Chakrabarti, editors, *Modelling Critical and Catastrophic Phenomena in Geoscience*, Lecture Notes in Physics, 705, pages 303–359. Springer, Berlin, 2006.

© 2008 Taylor & Francis Group, London, UK

[36] A. Corral. Time-decreasing hazard and increasing time until the next earthquake. *Phys. Rev. E.*, 71:017101, 2005.
[37] G. Molchan. Interevent time distribution in seismicity: a theoretical approach. *Pure Appl. Geophys.*, 162:1135–1150, 2005.
[38] A. Saichev and D. Sornette. "Universal" distribution of interearthquake times explained. *Phys. Rev. Lett.*, 97:078501, 2006.
[39] J. Davidsen, S. Stanchits, and G. Dresen. Scaling and universality in rock fracture. *Phys. Rev. Lett.*, 98:125502, 2007.
[40] J. Åström, P. C. F. Di Stefano, F. Pröbst, L. Stodolsky, J. Timonen, C. Bucci, S. Cooper, C. Cozzini, F.v. Feilitzsch, H. Kraus, J. Marchese, O. Meier, U. Nagel, Y. Ramachers, W. Seidel, M. Sisti, S. Uchaikin, and L. Zerle. Fracture processes observed with a cryogenic detector. *Phys. Lett. A.*, 356:262–266, 2006.
[41] J. Åström, P. C. F. Di Stefano, F. Pröbst, L. Stodolsky, and J. Timonen. Comment on "Universal distribution of interearthquake times". *http://arxiv.org/physics/0612081*, 2006.
[42] A. Bunde, J. F. Eichner, J. W. Kantelhardt, and S. Havlin. Long-term memory: a natural mechanism for the clustering of extreme events and anomalous residual times in climate records. *Phys. Rev. Lett.*, 94:048701, 2005.
[43] M. Baiesi, M. Paczuski, and A. L. Stella. Intensity thresholds and the statistics of the temporal occurrence of solar flares. *Phys. Rev. Lett.*, 96:051103, 2006.
[44] K. Yamasaki, L. Muchnik, S. Havlin, A. Bunde, and H. E. Stanley. Scaling and memory in volatility return intervals in financial markets. *Proc. Natl. Acad. Sci. USA*, 102:9424–9428, 2005.
[45] K.-I. Goh and A.-L. Barabási. Burstiness and memory in complex systems. *Europhys. Lett.,* 81:48002, 2008.

© 2008 Taylor & Francis Group, London, UK

*Acoustic Emission and Critical Phenomena – Carpinteri & Lacidogna (eds)*
*© 2008 Taylor & Francis Group, London, ISBN 978-0-415-45082-9*

# MULTIDIMENSIONAL APPROACHES TO STUDY ITALIAN SEISMICITY

**A. Carpinteri, G. Lacidogna and G. Niccolini**
Department of Structural Engineering & Geotechnics, Politecnico di Torino, Torino, Italy

## ABSTRACT

We examine two case studies of monumental buildings analysed by the Acoustic Emission (AE) monitoring technique and located in two areas of Italy characterised by different levels of seismicity: a medieval tower rising in Alba, a characteristic town in Piedmont, and the Cathedral of Syracuse Sicily.

The motivation of this research work is twofold. On one hand, a quantitative non-destructive method for evaluating damage phenomena is of great importance given the number of ancient buildings at risk in the Italian territory, due to the intensity of the stresses to which they are subjected. In order to preserve this inestimable cultural heritage, AE technique can be highly effective for an early detection of the damage since it identifies a damaging process at the very moment it occurs. On the other hand, when we try to consider the system-environment interaction, we cannot exclude that a share of the AEs measured on a structure really comes from external sources, such as environmental vibrations or, more interestingly for our purposes, from some high-frequency geodynamical activity.

In this prospective, the relation between the AE activity on these buildings and the regional earthquakes occurred during the monitoring period is investigated in order to explore the possibility that the AEs emerging from a structure can be considered also as seismic precursors besides as signs of developing structural damage.

## 1 INTRODUCTION

The AE technique is able to analyse state variations in a certain physical system and can be used as a tool for predicting the occurrence of catastrophic events. In many physics problems – e.g., when studying test specimen failure in a laboratory, the modalities of collapse of a civil structure, the natural seismic activity of a volcano or the localisation of the epicentral volume of an earthquake – the modalities of a structural collapse are generally analysed after the event.

© 2008 Taylor & Francis Group, London, UK

This technique can be used instead to identify the premonitory signals that precede a catastrophic event, as, in most cases, these warning signs can be captured well in advance (*Zapperi et al.* [1]; *Gregori and Paparo* [2]; *Gregori et al.* [3]).

In his search for earthquake precursory phenomena, *Mogi* [4] emphasized the analogy between the AEs emerging from microcracks in brittle materials and the earthquakes: they both are elastic energy released by developing cracks inside a medium. He noticed that the fracture process strongly depends on the degree of disorder of materials: the more disordered, the more warnings one gets; the more perfect, the more treacherous is the rupture. The failure of perfect crystals is thus unpredictable while that of deteriorated materials could be forecasted. For once, complex systems could be simpler to apprehend! Therefore, the complex structure of the Earth's crust led Mogi to hope that AEs could be identified for earthquake forecasting.

## 2 FROM THE ACOUSTIC EMISSIONS TO THE EARTHQUAKES

Which are the precursors of impending earthquakes? A multitude has been suggested, such as seismic gaps or fluctuations of physical parameters in crustal rocks in the region of the epicentre (*Bolt* [5]). In recent years, some Italian researchers (*Gregori and Paparo* [2]; *Gregori et al.* [3]) criticitized the concept of *local* monitoring of some seismic or geodynamical activity, claiming that it is possible to detect not only seismic precursors occurring very close to the location of the epicentre, but also at a large distance from it.

As a matter of fact, they (*Gregori and Paparo* [2]; *Gregori et al.* [3]) observed well-defined bursts of AE activity some months before the Assisi earthquake (1997) in Central Italy, which seriously damaged the Upper Basilica of Assisi. In order to detect AE, they applied AE sensors over some rocky outcrops located at large distance, $\sim$400 km, from the site of the future epicentre, in the Apennines Mountains. These isolated sites were chosen as AE monitoring stations in order to minimize any kind of environmental disturbances except those due to possible geodynamical processes. This way of proceeding led to consider the AE bursts recorded in the period before the Assisi earthquake as likely sesimic precursors.

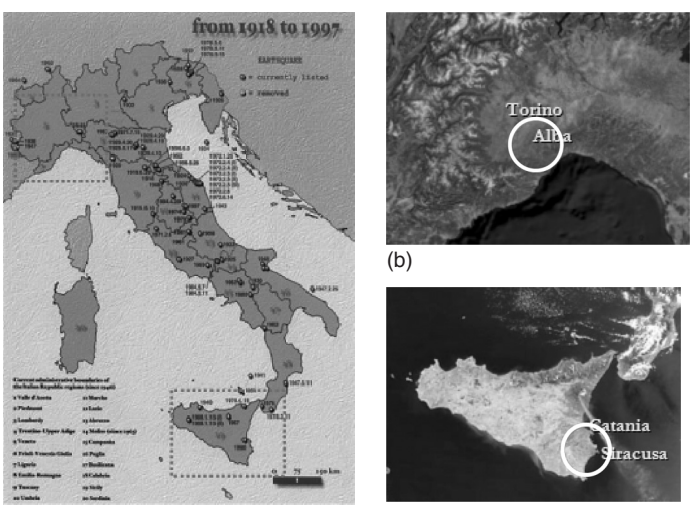
Since AEs may occur in the ultrasonic range of frequencies, any AE signal soon damps off to its emitting source, thus hardly reaching the AE sensor which generally can be at a large distance fom the source. This argument apparently makes a nonsense to investigate AE as a long-distance seismic precursor.

Actually, the process of gradual accumulation of strain and stress in some region of the Earth's crust, which suddenly turns into an earthquake failure, implies that large amounts of stress affect a wide area of the crust (extending over hundreds of kilometres and then *much larger* than the hypocentral zone, where the rupture will take place) in a period preceding the eventual occurrence

© 2008 Taylor & Francis Group, London, UK

of one earthquake. On the other hand, we know that AE derives from the not perfectly elastic behaviour of a stressed medium as the Earth's crust is. On this basis, the aforementioned authors (*Gregori and Paparo* [2]; *Gregori et al.* [3]) claimed that the accumulation of the internal stress in the Earth's crust can be detected by AE transducers. As they observe, the process of stress accumulation over time on a large region would be revealed by collecting at different sites the AEs, resulting in this case time-correlated. Obviously, this would require the simultaneous operation of a suitable network of AE monitoring sites, adequately placed in the territory, e.g. in the order of ∼1000 over one large regional area. In this sense, what we are expounding must be regarded mainly as a method of investigation, even if the results obtained correlating AE data collected during the monitoring of the two historical buildings with the data related to the regional earthquakes appear to be quite encouraging.

The first case study is that of the Sineo Tower in Alba, an ancient town of Piedmont, in the province of Cuneo, and located about 60 km far from Torino. The second one is that of the bearing structures of the Temple of Athena incorporated into the masonry walls of the Cathedral of Syracuse (investigation carried out in collaboration with the Politecnico of Milano). These two buildings are located in areas historically characterised by different levels of seismicity, as can be seen in Figure 1, where the epicentres of the strongest Italian earthquakes are mapped: looking at the two regions of interest framed by rectangles, Northwestern Italy has been characterised by a lower number of strong earthquakes




(a) (b) (c)

Figure 1: Distribution of the earthquake epicentres in Italy from 1918 to 1997 in (a) (from *Boschi et al.* [6]). Detail of the geographical position of the AE monitoring sites (Alba and Syracuse), (b) and (c).

© 2008 Taylor & Francis Group, London, UK

than Sicily. Therefore, one can wonder whether the AE sensors placed on these two buildings for integrity assessment purposes can be also influenced by the related regional seismicity.

## 3 THE CASE STUDY OF THE SINEO TOWER

### 3.1 Description of the Tower

The Sineo Tower, a masonry building from the 13th Century, is one of the tallest and mightiest medieval towers preserved in Alba (Figure 2). It is square-based, 39 m high, and leans to one side by about 1%. Wall thickness ranges from 2 m at the foundation level to 0.8 m at the top. The bearing walls are *a sacco*, i.e., consist of brick faces enclosing a mixture of rubble and bricks bonded with lime and mortar. Over a height of 15 m, the tower is incorporated in a later building.

The filling material is more organised, with brick courses arranged in an almost regular fashion, which, however, are not connected with the outer wall faces. In this case too, the total thickness of the masonry ranges from 2 m at the bottom to 0.8 m at the top. Total height is about 36 m and the tower does not lean on any side. It is also incorporated in a later building, approximately 15 m high, built when the tower had been completed.

### 3.2 Damage Detection by AE Monitoring

The cracking processes taking place in some portions of the masonry structure of the Sineo Tower were then monitored using the AE technique. The AE measurement system Atel® used by the authors (*Carpinteri and Lacidogna* [7,9,10]; *Carpinteri et al.* [8,11]) consists of eight piezoelectric (PZT) transducers,




Figure 2: The Sineo Tower in an overview of medieval towers of Alba.

© 2008 Taylor & Francis Group, London, UK

calibrated in the frequency range between 50 and 500 kHz, and eight control units. The threshold level $A_{th}$ for the signals recorded by the equipment was set equal to 100 μV. AE monitoring were carried out simply counting the occurrence of AE events during the cracking process. The principle of this procedure, termed event counting, is to count the number of times $n_0$ the threshold $A_{th}$ is exceeded by the oscillating transducer output caused by AE activity (*Brindley et al*. [12]). The event counting procedure was carried out with the adopted equipment by setting the oscillation counting capacity equal to 255 counts per each period of 120 seconds, practically equivalent to 1 count per half second. In this way each count represents at least one AE event, while the counting number $n_0$ estimates the number of the occurred AE events in a time window of 120 seconds. The number $n_0$ of counts is also proportional to the crack advancement in a given time window (*Carpinteri et al.* [13]). The difference between the event counting and another counting method, called ring-down counting, is shown in Figure 3. Major requirement to carry out this particular counting technique (not used in the present work) is a dead time as short as possible in order to capture the number of times the threshold voltage $A_{th}$ is exceeded by the burst of oscillations caused by a *single* AE event.

Two cracks visible in the inner masonry layer at the seventh floor of the Sineo Tower (Figure 4) were monitored using the AE technique (*Carpinteri and Lacidogna* [7,9,10]; *Carpinteri et al.* [8,11]). The monitoring process revealed an on-going damaging process, characterized by slow crack propagation inside the brick walls. In the most damaged zone, crack spreading had come to a halt, the cracks having achieved a new condition of stability, leading towards compressed zones of the masonry. Reaching a new stable condition is described by the decaying slope over time of the cumulative count of the AEs, illustrated by the rising staircase of Figure 5.

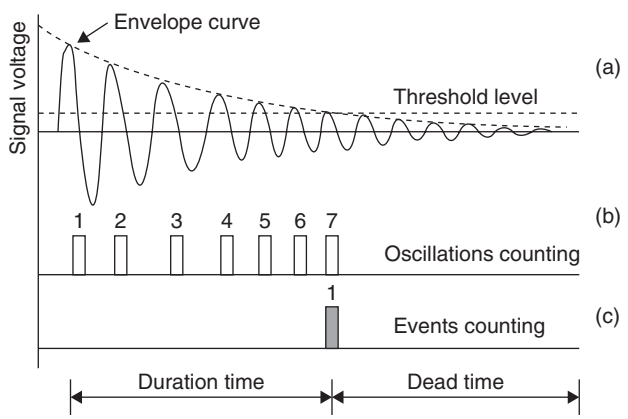



Figure 3: Counting methods from an AE signal (voltage vs. time) (a): oscillation (or ring-down) counting (b) and event counting (c).

© 2008 Taylor & Francis Group, London, UK

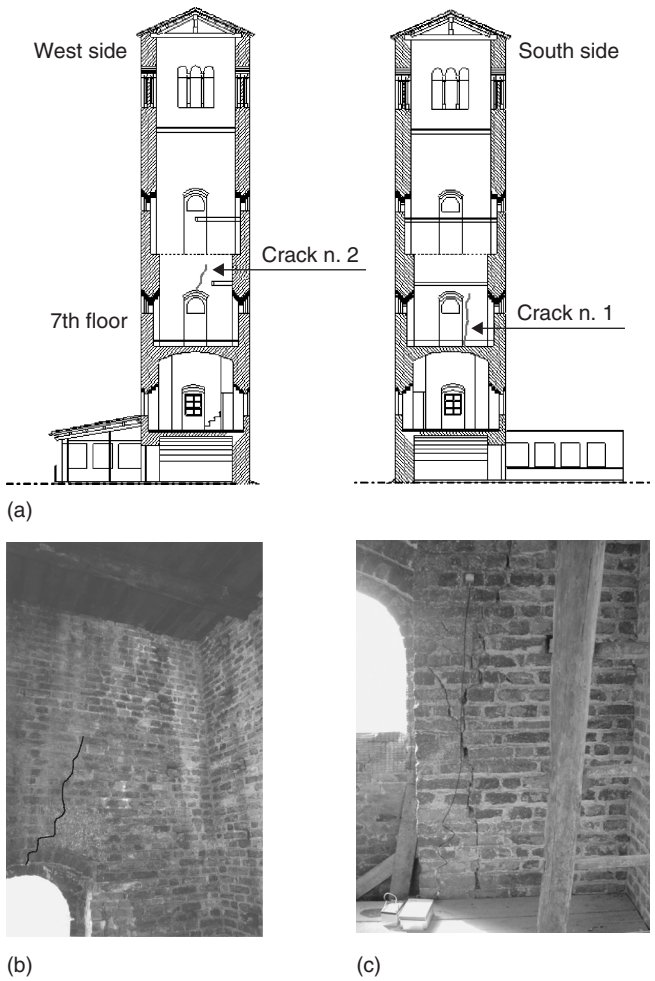



Figure 4: Cross-sections of two sides of the Sineo Tower (a). Notice the presence of two cracks near the openings at the seventh floor level (shown in detail in (b) and (c)).

### 3.3 Correlation of AEs on the Tower with the Regional Seismicity

During the monitoring of AE activity in the masonry of the Sineo Tower regional seismic activity occurred (*Carpinteri and Lacidogna* [7,9,10]; *Carpinteri et al.* [8,11]). In the diagram shown in Figure 5, the cumulative count of the AEs emerging from Crack n. 1 on the Sineo Tower and the seismic events (the grey bars) occurred in the Alba region (see the geographic map in Figure 6) are plotted as a function of time.

© 2008 Taylor & Francis Group, London, UK

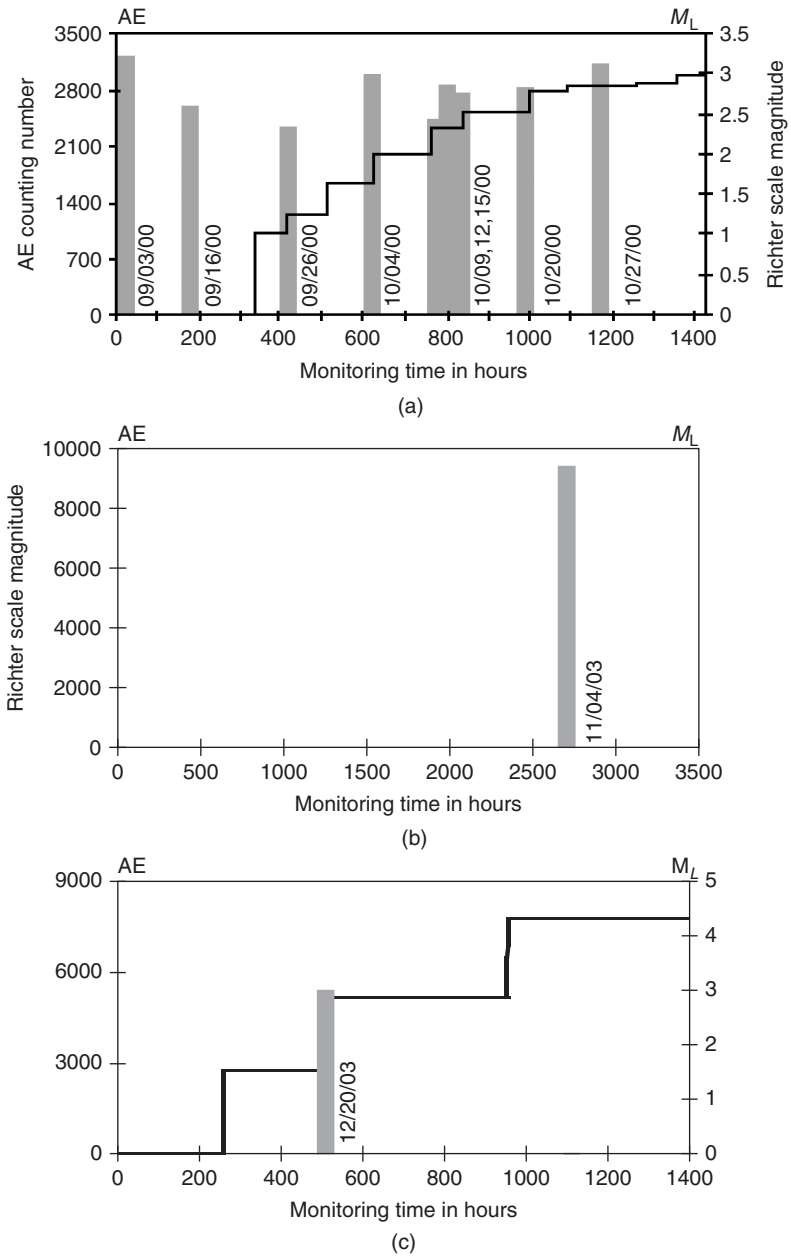



Figure 5: Cumulative count of the AEs (the rising staircase) on the Sineo Tower and the earthquakes (the grey bars) in Richter scale magnitude $M_L$.

© 2008 Taylor & Francis Group, London, UK

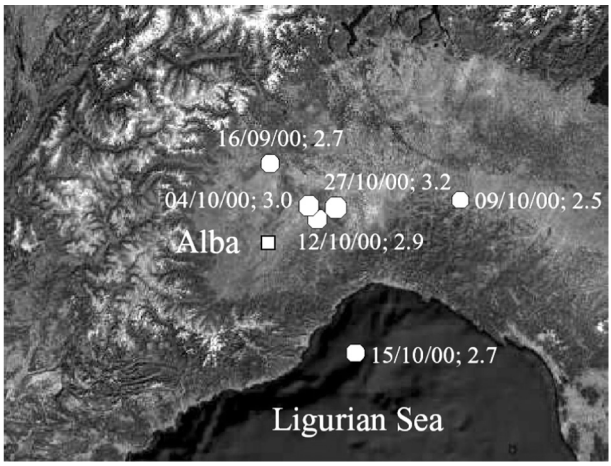



Figure 6: Geographic map showing the AE monitoring site (the Sineo Tower in Alba) and the strongest earthquakes (marked with their date and magnitude) occurred in the region during the monitoring period, from 16/09/00 to 07/11/00.

The AE activity on the Sineo Tower, recorded in several monitoring time windows, and the earthquakes in Richter magnitude $M_L$ scale occurred in the Alba region during the whole AE monitoring period are reported in Table 1.

The earthquakes with their parameters including epicentral position and hypocentral depth are listed in Table 2. The earthquake parameters have been provided by the National Institute for Geophysics and Volcanology in Rome.

The discontinuities in the graph of the available AE data (Figure 5) depends on the episodic data readings, which were performed manually by an operator. These experimental conditions have been recently improved by using a more sophisticated series of USAM® transducers which permit a finer acquisition of the AE data.

Anyway, we can see that each seismic event was often accompanied by an appreciable increment in the cumulative AE count. In this sense, we can say that, during the observation period, the Sineo Tower behaved as a sensitive earthquake receptor.

A definitive method to assess any connection between AEs and earthquakes separated in space and time probably does not exist. Along the lines of studies on space-time correlation between earthquakes, here we propose a method of statistical data analysis for calculating the degree of correlation both in space and in time between a time series of AE records and the local seismic records collected in the same time period.

The analysis is based on the space-time correlation combined generalization of the well-known Grassberger-Procaccia correlation integral (*Grassberger and Procaccia* [14]; *Tosi et al.* [15]), which leads to a visualization of both spatial and temporal correlations. The space-time combined correlation integral has been

© 2008 Taylor & Francis Group, London, UK

Table 1: Earthquakes and AE counts (the latters associated with the two visible macrocracks) during the monitoring of the Sineo Tower, from 16/09/00 to 7/11/00.

| Time Window of AE Monitoring | | Seismic events | | AE Counts | |
|---|---|---|---|---|---|
| From | To | Time | $M_L$ | Crack no.1 | Crack no.2 |
| 16/09/00 h 12:00 | 18/09/00 h 16:00 | 16/09/00 h 22:04 | 2.7 | 0 | 0 |
| 18/09/00 h 17:00 | 22/09/00 h 17:00 | | | 1052 | 712 |
| 22/09/00 h 17:00 | 26/09/00 h 11:00 | 26/09/00 h 02:41 | 2.4 | 255 | 255 |
| 26/09/00 h 11:00 | 29/09/00 h 11:00 | | | 430 | 75 |
| 29/09/00 h 11:00 | 03/10/00 h 11:00 | | | 0 | 0 |
| 03/10/00 h 11:00 | 07/10/00 h 11:00 | 04/10/00 h 16:34 | 3.0 | 405 | 1337 |
| 07/10/00 h 11:00 | 13/10/00 h 11:00 | 09/10/00 h 22:43 | 2.5 | 310 | 233 |
| | | 12/10/00 h 06:19 | 2.9 | | |
| 13/10/00 h 11:00 | 19/10/00 h 11:00 | 15/10/00 h 18:01 | 2.7 | 248 | 50 |
| 19/10/00 h 11:00 | 24/10/00 h 11:00 | 20/10/00 h 01:30 | 2.8 | 262 | 336 |
| 24/10/00 h 11:00 | 27/10/00 h 11:00 | | | 17 | 17 |
| 27/10/00 h 11:00 | 31/10/00 h 11:00 | 27/10/00 h 14:37 | 3.2 | 11 | 60 |
| 31/10/00 h 11:00 | 04/11/00 h 11:00 | | | 66 | 261 |
| 04/11/00 h 11:00 | 07/11/00 h 11:00 | | | 0 | 0 |

defined as follows:

$$C(r,\tau) \equiv \frac{1}{N_{EQ}N_{AE}} \sum_{k=1}^{N_{EQ}} \sum_{j=1}^{N_{AE}} \Theta\big(r - |\mathbf{x}_k - \mathbf{x}_j|\big) \cdot \Theta\big(\tau - |t_k - t_j|\big), \qquad (1)$$

© 2008 Taylor & Francis Group, London, UK

Table 2: Earthquakes in Richter magnitude $M_L$ scale occurred in Alba region from 16/09/00 to 7/11/00.

| Hypocentral Latitude | Hypocentral Longitude | Hypocentral Depth [km] | Epi.(1) [km] | Hypo.(2) [km] | $M_L^{(3)}$ | Date |
|---|---|---|---|---|---|---|
| 45.07 | 8.02 | 28.7 | 42.7 | 51.5 | 2.7 | 16/09/00 |
| 44.78 | 8.28 | 5.0 | 22.0 | 22.6 | 2.4 | 26/09/00 |
| 44.82 | 8.33 | 5.0 | 27.5 | 27.9 | 3.0 | 04/10/00 |
| 44.86 | 9.37 | 10.0 | 108.7 | 109.2 | 2.5 | 09/10/00 |
| 44.86 | 8.33 | 5.0 | 30.5 | 30.9 | 2.9 | 12/10/00 |
| 44.06 | 8.58 | 10.0 | 82.2 | 82.8 | 2.7 | 15/10/00 |
| 44.83 | 8.34 | 5.0 | 28.0 | 28.4 | 2.8 | 20/10/00 |
| 44.82 | 8.36 | 5.0 | 30.2 | 30.7 | 3.2 | 27/10/00 |

(1)Epicentral distance from Alba
(2)Hypocentral distance from Alba
(3)Richter magnitude

where $N_{AE}$ is the number of AE events, recorded on the Sineo Tower from 16 September 2000 to 7 November 2000, $N_{EQ}$ is the number of earthquakes in the surrounding area recorded during the same period (see Table 2), and $\Theta$ is the Heaviside step function ($\Theta(x) = 0$ if $x \leq 0$ and $\Theta(x) = 1$ if $x > 0$). The $k$-index runs over all the recorded seismic events $\{\mathbf{x}_k, t_k\}$, while $j$ runs over all the recorded AE events $\{\mathbf{x}_i, t_i\}$. Therefore, among all the possible pairs made taking an AE event and a seismic event, the sum in Eq. (1) counts those whose mutual epicentral distance is $|\mathbf{x}_k - \mathbf{x}_i| \leq r$ and whose mutual time distance is $|t_k - t_i| \leq \tau$ (see Tables 1 and 2). In practice, $C(r, \tau)$ is the probability that two events, one earthquake and one AE event, occur within a spatial region of linear size $r$ and within a time window of width $\tau$.

The condition $|t_k - t_i| \leq \tau$ does not consider the chronological order between the two events. Therefore Eq. (1) permits to assess the degree of correlation without specifying whether AE events occurring in the tower play a role as seismic precursors or as signs of developing damage.

Since time series of AEs and earthquakes are two sets strictly interwoven in the time domain, the question whether a given AE event in the tower acts as a seismic precursor or is due to possible developing micro-damage subsequent to an earthquake (in this sense we use the term 'aftershock') is open.

Here we propose a probabilistic answer, based on the available data, which can be found regarding AE events once as preceding and next as following earthquakes, and then comparing the obtained conditioned probability distributions in order to discover the prevailing trend. This analysis has been performed

© 2008 Taylor & Francis Group, London, UK

Table 3: Table of values for the cumulative probability $C_+(r, \tau)$. For example, 0.2526 is the probability (normalized to 1) that a burst of AE will be followed by an earthquake in the next 3 weeks and in a radius of 50 km around the AE monitoring site.

| $\tau$ (week) | $r$ (km) | 25 | 50 | 75 | 100 | 125 |
|---|---|---|---|---|---|---|
| 1 | | 0.0204 | 0.0944 | 0.0944 | 0.1122 | 0.1352 |
| 2 | | 0.0332 | 0.176 | 0.176 | 0.2219 | 0.2602 |
| 3 | | 0.0332 | 0.2526 | 0.2526 | 0.3087 | 0.3673 |
| 4 | | 0.0332 | 0.3112 | 0.3112 | 0.3954 | 0.4668 |
| 5 | | 0.0332 | 0.352 | 0.352 | 0.4413 | 0.5128 |
| 6 | | 0.0332 | 0.3852 | 0.3852 | 0.4745 | 0.5459 |
| 7 | | 0.0332 | 0.3852 | 0.3852 | 0.4745 | 0.5459 |

modifying the correlation integral of Eq. (1):

$$C_{\pm}(r,\tau) \equiv \frac{1}{N_{EQ}N_{AE}} \sum_{k=1}^{N_{EQ}} \sum_{j=1}^{N_{AE}} \Theta\big(r - |\mathbf{x}_k - \mathbf{x}_j|\big) \cdot \Theta\big(\tau - |t_k - t_j|\big) \cdot \Theta\big(\pm(t_k - t_j)\big). \tag{2}$$

When the function $\Theta(t_k - t_j)$ is used, all the pairs in which the AE event does not precede the seismic event are cut away from the sum. In this way, AE events are regarded as seismic precursors. Vice versa, with the function $\Theta(-(t_k - t_j))$ AE events are regarded as aftershocks. For example, $C_+(r, \tau)$ gives the probability that a burst of AE, detected at a certain time, will be followed by an earthquake in the next $\tau$ days and in a radius of $r$ kilometres around the AE monitoring site.

Varying the thresholds $r$ and $\tau$ in Eqs. (2), two cumulative distributions have been tabulated from the available data (Tables 3 and 4). From these two cumulative probability distributions the corresponding probability density functions have been derived and represented in Figures 7 and 8; it turns out that the concentration of AE events which follow an earthquake is maximum between the 5th and 20th day after the earthquake provided the epicentre lies in a radius of 28 km around the AE monitoring site (see the square in Figure 7(a)).

Vice versa, the concentration of AE events which precede an earthquake is maximum between the 23th and 6th day before the earthquake provided the epicentre lies in a strip between the 14th and 32th km around the AE monitoring site (see the square in Fig. 8(a)).

Obviously, this must be regarded simply as a proposal for the analysis of experimental data. In this sense, true progress can be realistically achieved by means of the simultaneous operation of suitable arrays of AE monitoring sites,

© 2008 Taylor & Francis Group, London, UK

Table 4: Table of values for the cumulative probability $C_{-}(r, \tau)$. For example, 0.3699 is the probability (normalized to 1) that after an earthquake, occurred in a radius of 100 km around the AE monitoring site, a burst of AE will follow in the next 5 weeks.

| $\tau$ (week) | $r$ (km) 25 | 50 | 75 | 100 | 125 |
|---|---|---|---|---|---|
| 1 | 0.0153 | 0.0944 | 0.0944 | 0.1071 | 0.125 |
| 2 | 0.0383 | 0.176 | 0.176 | 0.2041 | 0.2372 |
| 3 | 0.0561 | 0.2551 | 0.2551 | 0.2908 | 0.3367 |
| 4 | 0.0714 | 0.2985 | 0.2985 | 0.3342 | 0.3878 |
| 5 | 0.0842 | 0.3342 | 0.3342 | 0.3699 | 0.4235 |
| 6 | 0.0918 | 0.3571 | 0.3571 | 0.3929 | 0.4464 |
| 7 | 0.0918 | 0.3648 | 0.3648 | 0.4005 | 0.4541 |

adequately placed in the territory, e.g. in the order of ∼1000 over one large regional area.

### 3.4 The *b*-Value Analysis

A magnitude-frequency empirical relation, the celebrated Gutenberg-Richter (GR) relation (*Gutenberg and Richter* [16]), originally introduced to describe the earthquakes statistics, has been later successfully applied to the AE statistics (*Carpinteri et al.* [11,13,17]; *Ohtsu* [18]; *Colombo et al.* [19]; *Rao and Lakshmi* [20]):

$$\mathrm{Log}\, N(\geq m) = a - bm, \tag{3}$$

where $N$ is the number of events (either seismic or acoustic) with magnitude greater than $m$ in the monitored structural element, and $b$ and $a$ are positive coefficients to be determined subjecting the collected data to a statistical analysis. Considering the AEs, $b$ is a key parameter for assessing the damage level reached in a structure, better known as the "$b$-value". From the literature on AE tests it is well-known that the $b$-value decreases as the monitored specimen approaches impending failure (*Carpinteri et al.* [13,17]; *Ohtsu* [18]; *Colombo et al.* [19]; *Rao and Lakshmi* [20]). It is common to observe a trend of the $b$-value to the critical value $b_{\mathrm{crit}} = 1$ during final crack propagation. A theoretical basis for explaining $b_{\mathrm{crit}} = 1$ has been established, by exploiting the properties of a statistical model for a microcrack network applied to the crack advancements generating AEs (*Carpinteri et al.* [13,17]).

By means of the event counting method it is possible to estimate the $b$-value (a rigorous evaluation of $b$-value can be achieved with the USAM® AE acquisition system which captures the magnitude of a given AE event, see *Carpinteri et al.*

© 2008 Taylor & Francis Group, London, UK

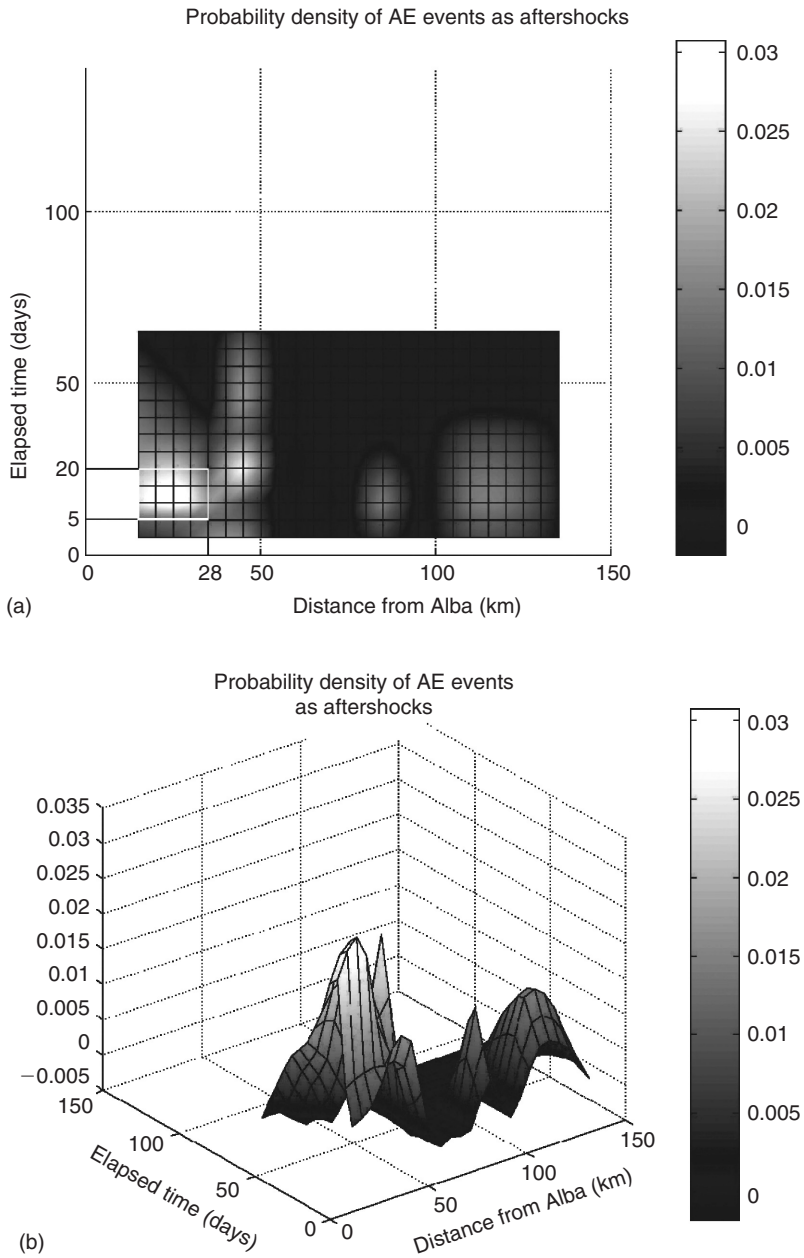



Figure 7: Probability density ($km^{-1}$ $day^{-1}$) that an earthquake followed by an AE event on the Sineo Tower occur, as a function of their spatial ("distance from Alba") and temporal ("elapsed time") separations: grayscale colour map (a), and 3D representation (b). The square in the grayscale colour map locates the space-time region with the highest probability density.

© 2008 Taylor & Francis Group, London, UK

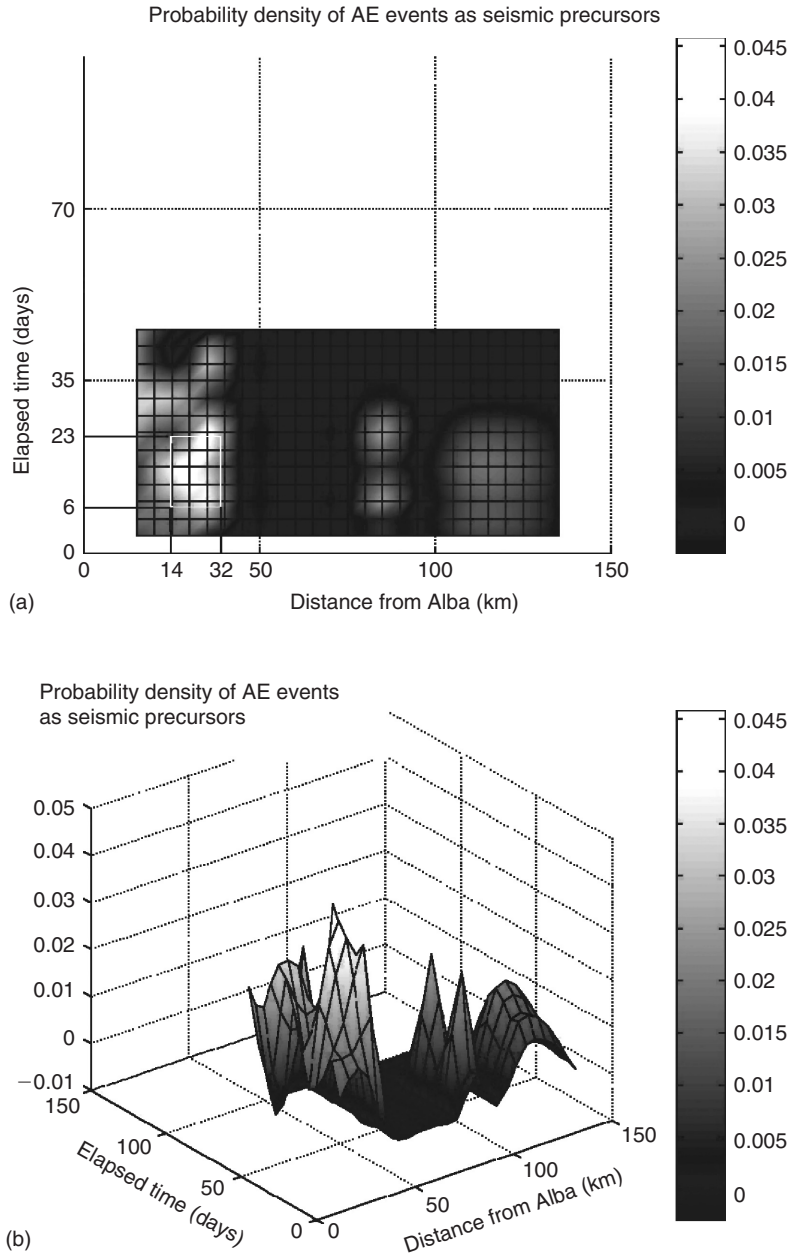



Figure 8: Probability density ($km^{-1}$ $day^{-1}$) that an AE event on the Sineo Tower followed by an earthquake occur, as a function of their spatial ("distance from Alba") and temporal ("elapsed time") separations: grayscale colour map (a), and 3D representation (b). The square in the grayscale colour map locates the space-time region with the highest probability density.

© 2008 Taylor & Francis Group, London, UK

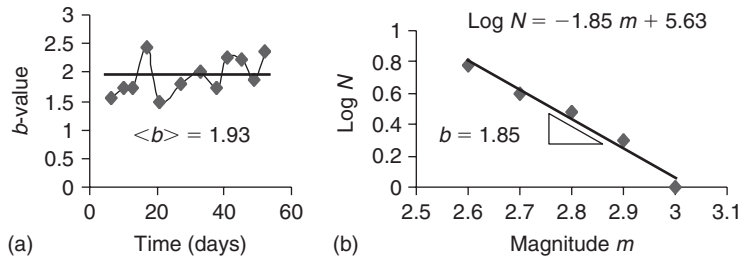



Figure 9: *b*-value trend of the monitored cracks on the Sineo Tower. The bold straight line represents the average value $< b > = 1.93$ (a). Cumulative number $N$ of earthquakes, with magnitude $\geq m$ as a function of $m$, occurred in Piedmont during the AE monitoring period with $b = 1.85$ (b).

[11]) by the formula (*Carpinteri et al.* [11,13]):

$$b^* = \frac{\text{Log}\, n_{MAX} - \text{Log}\, n_0}{\text{Log}\, A_{th}}. \tag{4}$$

Adopting the Atel® AE equipment, we have $A_{th} = 100\,\mu\text{V}$, $n_{MAX} = n \times 255$, and $n_0$ is the number of AE events counted in a time window of $n$ times 120s.

With this prescription, the "*b*-value" analysis has been carried out considering the time series, which is reported in Table 1, of the AE data collected during monitoring of the two macrocracks on the Sineo Tower shown in Figure 4. The results, depicted in the graph of Figure 9, lend themselves to a twofold reading. From the viewpoint of the integrity assessment the computed *b*-values, falling in the range (1.5, 2.5) and then far from the critical value $b_{\text{crit}} = 1$, may be interpreted as sign of stable damage evolution of the Sineo Tower.

On the other hand, there is also a remarkable similarity between the average $<b> = 1.93$ of the AE *b*-values and the seismic b-value, which is $b = 1.85$, characterising the GR statistics of the earthquakes occurred in the Alba region during the monitoring period (*Carpinteri et al.* [11]).

The intriguing observation is that, although environmental disturbances due to human activities were possibly included in the AE count, the *b*-value characterizing the statistical distribution of the AEs emerging from the tower somehow was also reflecting the regional seismic activity.

## 4 THE CASE STUDY OF THE SYRACUSE CATHEDRAL

### 4.1 Description of the Cathedral

The Cathedral of Syracuse (shown in Figure 10) rises on the remnants of the ancient Doric temple of Athena erected in the 5th century BC by tyrant Gelone

© 2008 Taylor & Francis Group, London, UK



(a) (b)

Figure 10: Facade (a) and lateral view (b) of the Cathedral of Syracuse.

on the uppermost part of the island of Ortigia. The temple had 14 columns along the sides and 6 at front, and some of them, belonging to the peristyle and the stylobate, can still be identified.

The Cathedral, which assumed its present-day appearance in the eighteenth century, in fact, was built by incorporating the ancient structures.

In the layout of the Cathedral shown in Figure 11(a), all the pillars and the columns inside the building are marked with a progressive number. Basically, the Doric columns are marked with numbers in three ranges: 1–8; 22,23; 33–40; whereas the pillars, probably obtained from the calcareous stone masonry of the temple cell, are identified with the remaining numbers.

From a survey of the cracks, it was determined that the pillars in the most critical conditions were nos. 19, 20, 30 and 31, all of them located near the end of the nave.

These pillars show an appreciable degree of deterioration, due to the presence of added layers of plaster and conspicuous cracks, which in some cases seem to cut across a major portion of their constituent stone blocks.

Pillar no. 19, selected for the application of the AE monitoring technique, is shown in the axonometric view in Figure 11(b). This element (save for a few strengthening works performed – according to the Fine Arts Board of Syracuse– during a restoration process in 1926) is entirely made of calcareous stone blocks, probably installed during the initial construction of the temple dedicated to Athena in the 5th century B.C.

## 4.2 Damage Detection by AE monitoring

The monitoring process, began at 11:00 A.M. of 11 September 2006 and ended at 12:20 P.M. of 21 January 2007, was performed on a pillar in the vertical bearing

© 2008 Taylor & Francis Group, London, UK

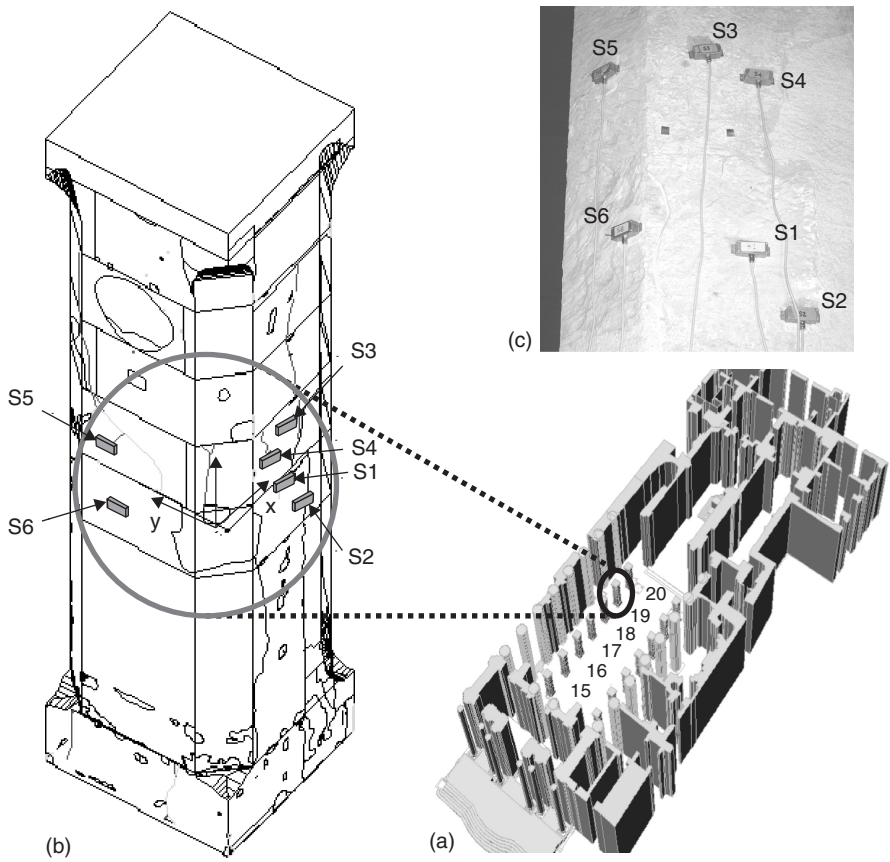



Figure 11: Layout of the Cathedral of Syracuse showing the location of the pillar subjected to AE monitoring (a); axonometric view of the monitored pillar (b); USAM® AE transducers applied to the pillar (c).

structure of the Cathedral of Syracuse by using six units USAM®, that can be synchronized for multi-channel data processing and then for localisation of the growing cracks. The AE sensors arrangement is represented in Figure 4a according to the scheme reported in Figure 4b. The sensors were glued with silicone resin on two faces of the pillar. These resins are good ultrasound conductors and have the advantage of reducing to the minimum the attenuation of signal perception in the layer between the specimen surface and the applied sensor.

The data collected were analysed mainly to interpret the evolution of damage and determine the positions of AE sources within the pillar. The most relevant parameters acquired from the signals (frequencies in a range between 50 and 800 kHz, arrival time, amplitude, duration, number of events and oscillations) are stored in the USAM® memory and then downloaded to a PC for a multi-channel data processing.

© 2008 Taylor & Francis Group, London, UK

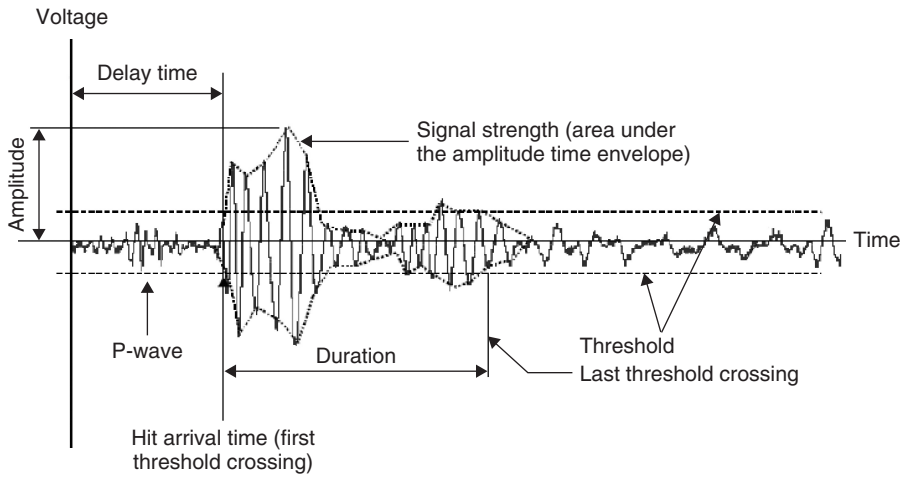



Figure 12: Waveform of an AE signal with its evaluation parameters. The threshold level $A_{th}$ for the signals recorded by the equipment was set equal to 100 μV.

Microcracks localisation is performed from this elaboration and the condition of the monitored specimen can be determined (*Carpinteri et al.* [13,17]). This procedure is usually referred to as parameter-based AE technique, and it represents a compromise between the counting techniques (ring-down and event counting) and the signal-based AE technique (which analyzes the complete waveform of the AE signal). A typical waveform of an AE signal with its most relevant parameters is shown in Figure 12.

The first stage of the AE analysis is localizing the sources of AE activity due to developing microcracks inside the specimen volume by means of the triangulation procedure coming from Seismology, where the aim was to localize the hypocenter of an earthquake from seismograms obtained at stations distributed over the Earth's surface (*Geiger* [21]). In our case, the hypocentres are typically the tips of growing cracks or newly formed microcracks.

Assuming that the AE waves propagate spherically reaching the AE sensors glued at the surface of the pillar, the solving equations for the crack localization can be trivially derived (see also Figure 13):

$$d_i - d_j = v_p \Delta t_{ij}, \tag{5}$$

where $d_i$ is the Euclidean distance between the AE source crack and the $i$-th sensor $S_i$: $d_i = [(x - x_i)^2 + (y - y_i)^2 + (z - z_i)^2]^{1/2}$, while $\Delta t_{ij} \equiv t_i - t_j$ is the measured arrival time difference for the first wave motion recorded at $S_i$ and $S_j$.

In the present work, applying the localisation procedure more than 50 AE sources have been localised. The localised sources and the cracking pattern for pillar 19 are represented in Figure 14.

© 2008 Taylor & Francis Group, London, UK

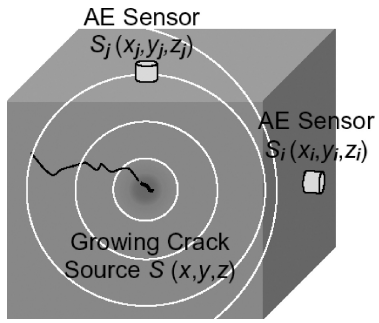



Figure 13: The first wave motion generated at $t_0$ in $S$ (an AE event generated by an opening microcrack) propagates spherically and reaches the sensor $S_i$ at time $t_i$ and $S_j$ at $t_j$.

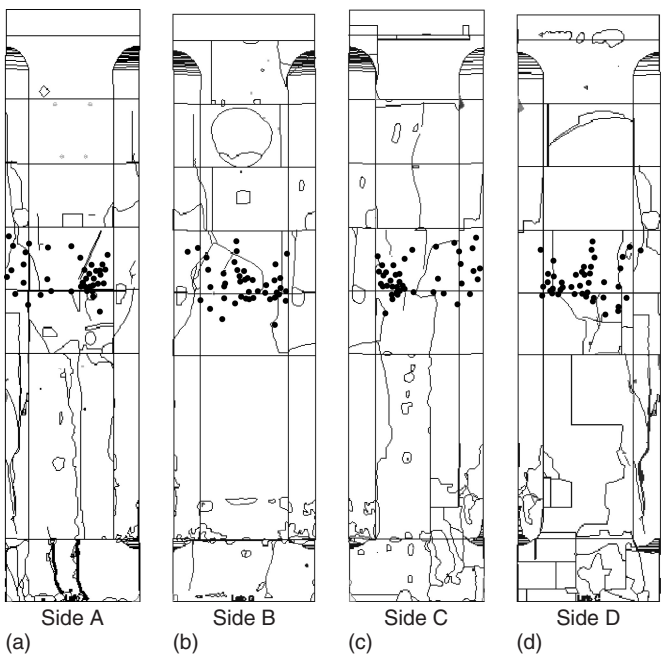



Figure 14: Cracking pattern and localisation of AE sources for pillar 19.

It can be noted that the localised sources are concentrated near the more visible crack paths. The concentration of these AE sources denounces that the pillar is subject to a damaging phenomenon in slow but progressive evolution. Within the stone blocks to which the sensors had been applied, the points were seen to concentrate along the cracks that could be discerned more clearly on the surface. The identification of these AE sources together with the oscillation counts

© 2008 Taylor & Francis Group, London, UK

shows that the pillar is indubitably undergoing a slow but incessant damage process.

### 4.3 Correlation of AEs on the Cathedral with the Regional Seismicity

As already done for the Sineo Tower, let us investigate if there is some correlation between the AE data recorded by the sensors applied to the pillar 19 and the earthquakes occurred during the monitoring period in the region surrounding Syracuse.

At this purpose, we have examined the catalogue of the earthquakes occurred in Eastern Sicily (available on the website: http://www.ct.ingv.it/Sismologia/GridSism.asp), shown in Table 5 together with the corresponding time evolution of the cumulative count of the AEs.

In this case study, we are not approaching the problem by means of the Grassberger-Procaccia correlation integral. We describe bursts of AE activity through the AE count rate $\Delta N_{AE}/\Delta t$, where $\Delta N_{AE}$ is the number of AEs counted in the time interval $\Delta t$.

In our purposes, taking long enough intervals $\Delta t$ ($\gg$1 hour) should allow to "capture" whole bursts of AE released in some geodynamical activity by the earth's crust; clearly, AE bursts are characterised by large increments $\Delta N_{AE}$ in relatively narrow time windows $\Delta t$.

In this way, we have identified four bursts of AE activity, which correspond to the grey areas subtended by the differential curve $\mathrm{d}N_{AE}/\mathrm{d}t$ (see the encircled sections in Figure 16(a)). This intense AE activity is concentrated in 25 percent of the whole monitoring period, and represents 60 percent of total subtended area (i.e., 60 percent of the total AEs).

We have associated each burst of AE with the strongest earthquake occurred immediately afterwards (compare the diagrams of Figure 16). Given an AE burst, the expression "immediately afterwards" means that we have selected the strongest earthquake occurred during the quiescent phase in the AE activity elapsing between the AE burst and the following one.

At this point, we have assumed that there exists a proportionality relationship between a burst of AEs emerging from the crust, a large value of $\Delta N_{AE}/\Delta t$, which precedes the earthquake (selected according the just described criterion) and the magnitude $M_L$ of the earthquake itself: strong earthquakes should be announced by more evident precursors.

Furthermore, since any AE geodynamical activity will necessarily extend over a large but *finite* region, we expect that the correlation of detected AEs with seismicity decays somehow as we move away from the future hypocentral zone, and in fact we talk about "regional" seismicity. Therefore, we have fitted the data (reported in Table 6) with the following relationship:

$$\frac{\Delta N_{AE}}{\Delta t} = k\frac{M_L}{r^{\alpha}}, \tag{6}$$

© 2008 Taylor & Francis Group, London, UK

Table 5: Earthquakes and cumulative count $N_{AE}(t)$ of the AEs. The time $t$, at which $N_{AE}$ is calculated, is defined by the date and the time of the earthquakes.

| Date | Time | Hypo Latitude | Hypo Longitude | Hypo Depth [km] | Hypo $r$ [km] | $M_L$ | AE counting number $N_{AE}(t)$ |
|---|---|---|---|---|---|---|---|
| 19/09/06 | 03:20 | 37.09 | 15.35 | 20.2 | 21.4 | 2.0 | 590 |
| 22/09/06 | 15:52 | 37.37 | 14.95 | 4.1 | 42.9 | 1.8 | 704 |
| 26/09/06 | 16:59 | 37.62 | 15.14 | 13.6 | 62.0 | 2.5 | 777 |
| 26/09/06 | 17:08 | 37.65 | 15.13 | 16.0 | 66.5 | 2.3 | 777 |
| 14/10/06 | 23:55 | 37.25 | 14.78 | 18.4 | 50.8 | 3.0 | 1561 |
| 16/10/06 | 02:21 | 37.14 | 15.25 | 17.9 | 19.1 | 1.3 | 1568 |
| 16/10/06 | 03:40 | 37.05 | 14.76 | 16.7 | 48.5 | 1.6 | 1570 |
| 26/10/06 | 14:28 | 38.67 | 15.41 | 208.8 | 273.4 | 5.7 | 1771 |
| 05/11/06 | 22:01 | 37.25 | 14.77 | 18.3 | 51.5 | 1.3 | 1968 |
| 14/11/06 | 23:34 | 37.81 | 14.86 | 36.3 | 95.5 | 3.0 | 2167 |
| 14/11/06 | 23:47 | 37.81 | 14.87 | 35.3 | 94.8 | 3.0 | 2167 |
| 24/11/06 | 04:37 | 36.26 | 15.76 | 11.1 | 102.2 | 4.7 | 2427 |
| 25/11/06 | 18:56 | 36.29 | 15.71 | 16.6 | 98.1 | 3.2 | 2445 |
| 05/12/06 | 05:01 | 37.06 | 15.61 | 24.3 | 38.8 | 2.9 | 3303 |
| 05/12/06 | 15:31 | 37.31 | 14.94 | 9.9 | 39.7 | 1.5 | 3309 |
| 07/12/06 | 16:23 | 37.34 | 14.93 | 0.0 | 40.9 | 1.6 | 3399 |
| 19/12/06 | 14:58 | 37.76 | 14.92 | 24.3 | 84.7 | 4.2 | 3590 |
| 20/12/06 | 01:46 | 37.77 | 14.88 | 35.0 | 90.6 | 3.3 | 3596 |
| 20/12/06 | 11:38 | 38.56 | 14.23 | 26.2 | 189.6 | 3.8 | 3599 |
| 20/12/06 | 11:45 | 38.41 | 14.21 | 10.0 | 174.7 | 3.0 | 3599 |
| 23/12/06 | 00:33 | 37.15 | 15.23 | 18.1 | 20.1 | 1.2 | 3645 |
| 25/12/06 | 08:02 | 37.23 | 15.17 | 16.1 | 24.6 | 1.8 | 3667 |
| 28/12/06 | 10:56 | 37.14 | 15.17 | 9.5 | 14.4 | 1.5 | 3702 |
| 01/01/07 | 07:58 | 38.17 | 14.86 | 24.2 | 128.2 | 3.0 | 3761 |
| 02/01/07 | 13:30 | 38.15 | 14.9 | 28.0 | 125.9 | 3.0 | 3761 |
| 09/01/07 | 09:57 | 37.08 | 15.57 | 14.0 | 30.1 | 1.9 | 3815 |
| 11/01/07 | 05:15 | 37.03 | 15.09 | 20.2 | 26.6 | 1.6 | 3838 |
| 14/01/07 | 23:23 | 36.90 | 14.98 | 17.6 | 37.2 | 1.9 | 4201 |
| 11/02/07 | 17:11 | 35.17 | 16.05 | 11.2 | 224.4 | 4.4 | 4369 |
| 11/02/07 | 20:30 | 36.85 | 14.86 | 24.7 | 51.5 | 3.2 | 4369 |

where $r$ is the distance between the earthquake hypocentre and the AE monitoring site, while $k$ and $\alpha$ are constants characterising the physics of the ongoing process. The right-hand side of Eq. (6) may be regarded as a first-order expansion in powers of $M_L$ and $r$ of a hypothetical function able to describe the complex connection between AEs and earthquakes.

© 2008 Taylor & Francis Group, London, UK

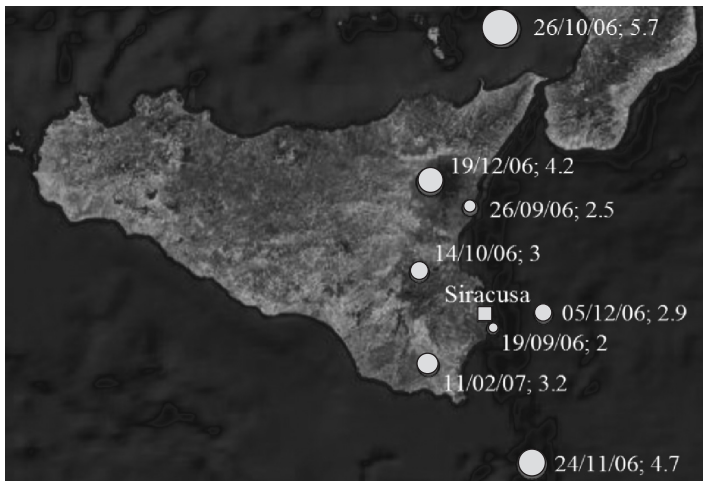



Figure 15: Geographic map showing the AE monitoring site (the Cathedral of Syracuse) and the strongest earthquakes (marked with their date and magnitude) occurred in the Eastern Sicily from 11/09/06 to 21/01/07.

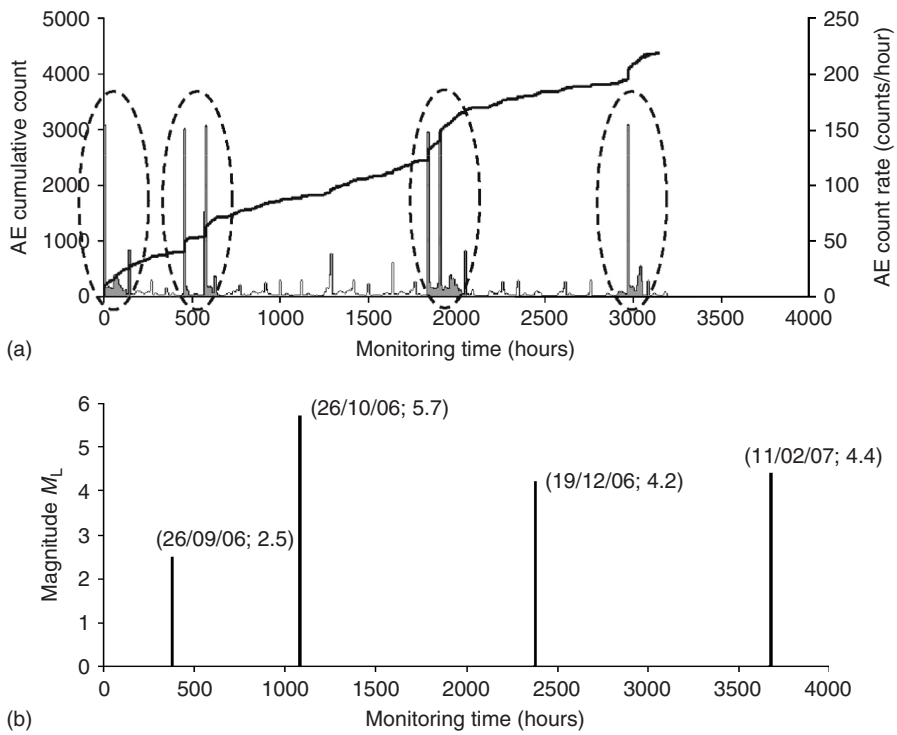



Figure 16: AE count rate in which the bursts of AE activity are encircled (a), and the strongest earthquakes occurred afterwards (b). Note the one-to-one correspondence between the four AE bursts in (a) and the four subsequent earthquakes in (b).

© 2008 Taylor & Francis Group, London, UK

Table 6: Parameters of the AE bursts and the related earthquakes. In the last column there is the rescaled magnitude $M^* \equiv M_L\,(\Delta N_{AE}/\Delta t)^{-1}$.

| Date | Time | $M_L$ | $r$ (km) | $\Delta N_{AE}$ | $\Delta t(h)$ | $M^*$ |
|---|---|---|---|---|---|---|
| 26/09/06 | 16:59 | 2.5 | 62.0 | 600 | 189 | 0.78 |
| 26/10/06 | 17:08 | 5.7 | 273.4 | 616 | 212 | 1.96 |
| 05/12/06 | 05:01 | 4.2 | 84.7 | 902 | 229 | 1.06 |
| 11/02/07 | 20:30 | 4.4 | 224.4 | 492 | 188 | 1.68 |

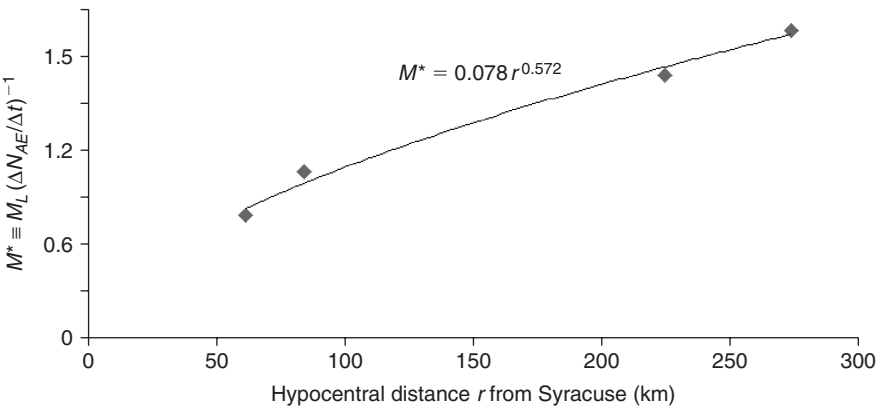



Figure 17: $M^* \equiv M_L\,(\Delta N_{AE}/\Delta t)^{-1}$ vs. $r$ diagram in which the experimental data and the fitting relation $M^* = k^{-1} r^{\alpha}$ are represented.

We have reorganized Eq. (6) in the following form:

$$M^* \equiv \frac{M_L}{\Delta N_{AE}/\Delta t} = \frac{r^{\alpha}}{k}, \tag{7}$$

in order to represent the curve fitting the experimental data in a $M^*$ vs. $r$ diagram (illustrated in Figure 17).

The best-fit parameters are $k^{-1} = 0.078$ and $\alpha = 0.572$, where $k$ can be regarded as a coupling constant between AE and seismic phenomena, while $\alpha$ describes the rate at which AE activity before an earthquake attenuates with the distance from the hypocentre. The smaller the value of $\alpha$, the larger the region in which AE activity is spread out. These values could be better understood comparing analogous values obtained from similar measurements performed in different sites. Anyway, a value of $\alpha = 0.572$, suggesting a gentle decrease of AEs with the distance $r$, seems to be consistent with our idea of AE activity involving a large region around the future hypocentre.

© 2008 Taylor & Francis Group, London, UK

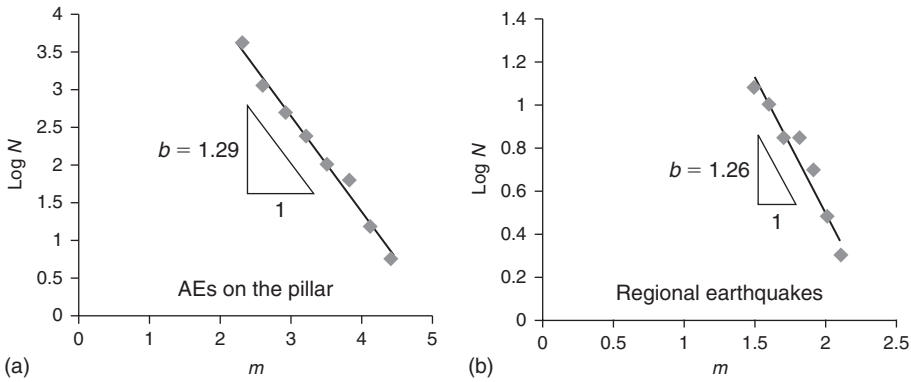



Figure 18: *b*-values characterising the AE statistics on the pillar (a) and the statistics of the regional earthquakes (b).

### 4.4 The *b*-Value Analysis

The "*b*-value" analysis has been carried out considering the statistical distribution of the AE signal magnitudes described by the GR relationship of Eq. (3) and:

$$m = \mathrm{Log}_{10} A, \tag{8}$$

relating the magnitude to the amplitude $A$ expressed in microvolts. The computed *b*-value, $b = 1.29$, is in accordance with the bad state of preservation of the pillar where several damages, consisting of detached covers and deep cracks, have been observed.

The same "*b*-value" analysis has been carried out considering the statistics of the earthquakes listed in Table 5 and the results, depicted in the graph of Figure 18, show again a remarkable similarity between the *b*-value of the AEs ($b = 1.29$) and the seismic *b*-value ( $b = 1.26$).

## 5 CONCLUSIONS

We have presented an extended application of the AE Technique, trying to correlate the AEs detected on monitored structures with the local seismic activity simultaneously occurring. Searching for precursory phenomena of the earthquakes, we propose an empirical relation connecting the bursts of AE with the magnitude of the subsequent earthquakes.

We hypothesize that this relation, which needs to be tested by means of a much richer statistics, can be used for distinguishing between AEs due to ongoing structural damage and AEs due to geodynamical activity, by comparing the values of the exponent $\alpha$.

© 2008 Taylor & Francis Group, London, UK

Furthermore, we have also observed that the *b*-value characterizing the GR distribution of the AEs emerging from the monitored buildings somehow reflects the *b*-value of the regional earthquake statistics.

The intriguing observation on the similarity of the two *b*-values suggests that the *b*-value could be considered as a universal exponent characterizing both the earthquakes distribution as well as the AE activity monitored on the urban system.

## ACKNOWLEDGEMENTS

The financial support for AE application provided by the European Union (EU) Leonardo da Vinci Programme – ILTOF Project is gratefully acknowledged.

## References

[1] S. Zapperi, A. Vespignani and H. E. Stanley, "Plasticity and avalanche behaviour in microfracturing phenomena", *Nature*, vol. 388, pp. 658–660, 1997.

[2] G. P. Gregori and G. Paparo, "Acoustic emission (AE). A diagnostic tool for environmental sciences and for non destructive tests (with a potential application to gravitational antennas)", *Meteorological and geophysical fluid dynamics*, edited by Schroeder, W., Science Edition, Bremen, pp. 166–204, 2004.

[3] G. P. Gregori, G. Paparo, M. Poscolieri and A. Zanini, "Acoustic emission and released seismic energy", *Natural Hazards and Earth System Sciences*, vol. 5, pp.777–782, 2005.

[4] K. Mogi, "Study of elastic shocks caused by the fracture of heterogeneous materials and its relation to earthquake phenomena", *Bulletin of Earthquake Research Institute*, vol. 40, pp. 125–173, 1962.

[5] B.A. Bolt, *Earthquakes*, W.H. Freeman and Company, S. Francisco and London, 1978.

[6] E. Boschi, E. Guidoboni, G. Ferrari, D. Mariotti, G. Valensise and P. Gasperini, Editors, "Catalogue of strong Italian earthquakes from 461 B.C. to 1997", Istituto Nazionale di Geofisica, vol. 43, pp. 609–868, 2000.

[7] A. Carpinteri and G. Lacidogna, "Damage diagnosis in concrete and masonry structures by acoustic emission technique", *Journal Facta Universitatis, Series: Mechanics, Automatic Control and Robotics*, vol. 3(13), pp. 755–764, 2003.

[8] A. Carpinteri, G. Lacidogna and N.Pugno, "A fractal approach for damage detection in concrete and masonry structures by the acoustic emission technique", *Acoustique et Techniques*, vol. 38, pp. 31–37, 2004.

© 2008 Taylor & Francis Group, London, UK

[9] A. Carpinteri and G. Lacidogna, "Structural monitoring and integrity assessment of medieval towers", *ASCE Journal of Structural Engineering*, vol. 132, pp. 1681–1690, 2006.
[10] A. Carpinteri and G. Lacidogna, "Damage monitoring of an historical masonry building by the acoustic emission technique", *Materials and Structures*, vol. 39, pp. 161–167, 2006.
[11] A. Carpinteri, G. Lacidogna and G. Niccolini, "Acoustic emission monitoring of medieval towers considered as sensitive earthquake receptors", *Natural Hazards and Earth System Sciences*, vol. 7, pp. 1–11, 2007.
[12] B.J. Brindley, J. Holt and I.G. Palmer, "Acoustic Emission-3: the use of ring-down counting", *Non-Destructive Testing*, vol. 6, pp. 299–306, 1973.
[13] A. Carpinteri, G. Lacidogna and G. Niccolini, "Critical defect size distributions in concrete structures detected by the acoustic emission technique", *Meccanica* (2007), in press.
[14] P. Grassberger and I. Procaccia, "Characterization of strange attractors", *Phys. Rev. Lett.*, vol. 50, pp. 346–349, 1983.
[15] P. Tosi, V. De Rubeis, V. Loreto and L. Pietronero, "Space-time combined correlation integral and earthquake interactions", *Annals of Geophysics*, vol. 47, pp. 1849–1854, 2004.
[16] B. Gutenberg and C. F. Richter, *Seismicity of the Earth and Associated Phenomena*, Princeton University Press, Princeton, 1954.
[17] A. Carpinteri, G. Lacidogna and G. Niccolini, "Critical behaviour in concrete structures and damage localization by acoustic emission", *Key Engineering Materials*, vol. 312, pp. 305–310, 2006.
[18] M. Ohtsu, "The history and development of acoustic emission in concrete engineering", *Magazine of Concrete Research*, vol. 48, pp. 321–330, 1996.
[19] S. Colombo, I. G. Main and M. C. Forde, "Assessing damage of reinforced concrete beam using '*b*-value' analysis of acoustic emission signals", *Journal of Materials in Civil Engineering ASCE*, vol. 15, pp. 280–286, 2003.
[20] M.V.M.S. Rao and K.J.P Lakshmi, "Analysis of *b*-value and improved *b*-value of acoustic emissions accompanying rock fracture", *Current Science*, vol. 89, pp. 1577–1582, 2005.
[21] L. Geiger, "Probability method for the determination of earthquake epicentres from the arrival time only", *Nachrichten von der Koniglichen Gesellschaft der Wissenschaften zu Gottingen*, vol. 4, pp. 331–349, 1910.

© 2008 Taylor & Francis Group, London, UK